UNIVERSITÉ D'ORLÉANS

ÉCOLE DOCTORALE ENERGIE – MATERIAUX – SCIENCES DE LA TERRE ET DE L'UNIVERS (EMSTU)

Conditions Extrêmes et Matériaux: Haute Température et Irradiation,

UPR3079, CNRS, Orléans

THÈSE présentée par :

Isidro Da Silva Colaço

soutenue le : **1er Octobre 2024**

pour obtenir le grade de : **Docteur de l'Université d'Orléans**

Discipline/ Spécialité : Chimie

^{52}Mn and ^{165}Er production for bimodal imaging and therapy applications

Production de ^{52}Mn et ^{165}Er pour des applications en imagerie (bimodalité) et thérapie

THÈSE dirigée par :

Dr. BESSADA Catherine	Directrice de recherche, CNRS, Orléans
Dr. ELLISON A. Paul	Assistant Professor, Université du Wisconsin, Madison (USA)

RAPPORTEURS :

Pr SEVERIN W. Gregory	Associate Professor, Université du Michigan, Lansing (USA)
Dr KUHNAST Bertrand	Directeur de Recherche, CEA, Orsay

JURY :

Dr. JAKAB TOTH Eva	Directrice de Recherche, CNRS, Orléans **(Présidente)**
Dr. SEVERIN W. Gregory	Associate Professor, Université du Michigan, Lansing (USA)
Dr. KUHNAST Bertrand	Directeur de Recherche, CEA, Orsay
Dr. HADDAD Ferid	Professeur, Université de Nantes
Dr. HAPPEL Steffen	Directeur R&D, Société TRISKEM, Bruz
Dr. DEVILLE Claire	Ingénieur de Recherche, DTU Riso, Roskilde (DK)

Adeus,

Agora o passarinho ja não cantara
nunca mais houvera o seu atrevimento
quem nao queria ouvir
botava os ouvidos ao vento
Por bem cantar,
mal não digas dos que a voz aqui levantam
pois uns cantam o que sabem
e outros sabem o que cantam
Andou aqui na roda inteira,
espalhou pelo mundo o seu sorriso,
entregou-nos o respeito dos outros,
em cima de tudo não se invejo de quem tem parelhas, éguas e montes
só se invejo de quem bebe a água em toda as fontes.

(Inspirado de Cantos Alentejanos)

Acknowledgments

First of all, I would like to thank all the members of the jury for accepting my invitation to judge and attend my thesis.

Thanks to Dr. Gregory Severin for judging my work on the production of ^{52}Mn and ^{165}Er, of which he was one of the precursors.
Thanks to Dr. Bertrand Kuhnast for agreeing to judge this work on radionuclides that are somewhat exotic in the world of nuclear medicine.
Thanks to Dr. Ferid Haddad for agreeing to lend his expertise on radionuclide production to this manuscript,
Thanks to Dr. Eva Jakab Toth, without whom this research on ^{52}Mn would not have been possible.
Thanks to Dr. Steffen Happel, with whom we had a lot of exchanges and discussions. The ^{165}Er adventure was made possible by the support of TRISKEM, your enthusiasm, and sharing from the very first meetings.
Thanks to Dr. Claire Deville for accepting my invitation to represent the Roskilde's Laboratory. Without Roskilde laboratory's publications on ^{52}Mn, what would have become of this thesis? I would also like to thank Michael Jensen for his help and encouragement over the years.
Thanks to Dr. Catherine Bessada for agreeing to supervise this thesis following Patrick Simon's departure, and for her support and encouragement over the years.
Thanks to Dr. Patrick Simon for the many discussions that led to this manuscript.
Thanks to Dr. Célia Bonnet for the ^{165}Er project and to Dr. Sara Lacerda for our many exchanges and experiences with radiolabeling.

Thanks to Dr. Conchi Ania for her support to follow my ideas about porous materials and give an opportunity to continu my works on this wonderfull area of radiochemistry. Muchas Gracias !!!
A very big thank you to the energy of the technical staff at the Orléans cyclotron (whose exact value I couldn't calculate!!!) who made these irradiations possible right up to the end, in particular, Dominique Baux for the beam development, Patrice Riffard and William Hate for the automation of separations with the ACCRA design, Thierry Sauvage for the particle physics and cyclotron operation, and the radiation protection department, David Chaulin and Sébastien Bouillon, for support on radiation protection issues.

The results set out in this manuscript are the fruit of a collective effort in which everyone played their part:
Thanks to the students who prepare the Cr pellets (Justine Vaudon, and Matthieu Gervais), determine Dw (Geoffrey Audiger, Elodie Dutilly, Emmanuel Sursin, and Charlotte Ruggeri), cross section of nuclear reaction ^{nat}V(α,x)^{52}Mn (Julius Truffier-Blanc).
Thanks to Florian Duval for the first explanations on cross sections,
Thanks to Didier Zanghi and Aurélien Canizares for the pyrometer measurements.

Thanks to Julien Sobilo for SPECT imaging from (PHENOMIN, Orléans) and Stéphanie Rétif, Marilyne Le Mée, and Sharuja Natkunarajah for animal management for biodistribution tests (PHENOMIN, Orléans).

Thanks to all the CEMHTI staff involved in one way or another (Zhiwei, Jérôme, Pierre…), whom I have forgotten to mention in this list.

This four-year project was made possible thanks to the good fortune and, above all, the support of people whom I would like to thank most warmly and deeply:
All our neighbors in Middleton, Mike, Eileen, Maureen, Mike, Julie, Sangita, Murali, Tom and Cathy, Brad for their welcome and help throughout our American year,
My dream team, gang' cyclotron, with Eduardo, Christopher, Aeli, Kaelyn, Todd, and my super Kendall.
Mr Thoret Christian, for all you taught us during our primary school, education helps us to progress and civic orientation was not only a word for you. Peace on you.
Pr. Didier Le Bars, always you gave me support and devices to follow my research in difficult contexts. Unfortunately, you left us so early before to judge this work.
Jerry and Michael, for all the documentation available on open data before it became common use. I have learned and progressed a lot thanks to this documentation.
All the people I met at WTTC (Workshop Target and Targetry Chemistry) and at Cycleur gave me ideas, help, and support in this work through discussions and exchanges on methods.

Louis Fréalle for his presence, his support, our many discussions, and his involvement in automating the separations. Our many exchanges and our complementarity have enabled our projects to move forward in the midle of many questions, but also many moments of excitement.

Jon Engle, for his constant support, right from the start, of this project, and even more so, thank you for welcoming me into your laboratory, a special one, and for letting me work with Paul. To this day, I can't believe it just happened. I'm very proud to have had the opportunity to spend a year in your laboratory in a crazy environment (yes at all levels!!!), a great place to work on radionuclide production and build projects together. And I'm keeping my fingers crossed that in a few months we'll be celebrating a 30 MeV energy cyclotron in Madison!!!!

Paul Ellison, whoa!!! I never imagine to have the opportunity to work with Bromine Man!!! You have been very patient with my poor English and answered my scientific questions and American society. I grow up in radiochemistry with your knowledge, with real exotic radionuclides, your methods, and our discussions. This thesis would never have happened without your help and I’m proud that my thesis was associated with your expertise in radiochemistry. Thanks for the help and devices.

Finally, I would like to thank my parents for their support during all my life, support me all the time as my sisters Célia and Gilda and their husbands and childrens, as my family in law for their supports.

At least, huge thanks to my children Emilio and Ianis and my wife Céline for supporting me all the time, particularly these last four years.

Semper Fi

Table of Figures

Summary of Tables

Abreviations

αHIBA: α-hydroxyisobutyric acid
ACCRA: Automatisme & Contrôle Commande Radiochimie
AE: Auger Emitter
AMA: Apparent molar Activity
CiSCoTe: Cible Solide irradiée Contrôlée en Température (Solid Target irradiated under control temperature)
CDTA: trans-1,2-Diaminocyclohexane-N,N,N',N'-tetraacetic acid hydrate
CT: Computed Tomography
RNP: RadioNucleic Purity CX: Cation Exchange
Dc: decay corrected
DOTA: 1,4,7,10-Tetraazacyclododecane-1,4,7,10-tetraacetic acid
DTPA: diethylenetriaminepentaacetic acid
Dw: Coefficient of distribution
EXC: Extraction Column
EoB: End of Beam
EoS: End of Synthesis
FDG: FluoroDeoxyGlucoseHAS: Human Serum Albumine
HEPES: 4-(2-hydroxyethyl)-1-piperazineethanesulfonic acid*)*
HPGe: High Purity Germanium
IAEA: International Atomic Energy Agency
IC: Ionic Column
ICP-MS: Inductively coupled plasma mass spectrometry
ICP-OES: Inductively coupled plasma - optical emission spectrometry
LLE: Liquid-liquid Extraction
LN1, LN2, LN3: series of extraction resin for LaNthanides
MA: Molar Activity
MP-AES: Microwave Plasma Atomic Emission Spectroscopy
MRI: Magnetic Resonance Imaging
ndc: non decay corrected
ng: nanogram (10^{-9} g)
PET: Positron Emission Tomography
pg: pictogram (10^{tendl} g)
PMT: PhotoMultiplier tube
PSMA 617: Prostate-Specific Membrane Antigen
SEM: Scanning Electron Microscope
$SF_{(Cr/Mn)}$: Cr/Mn Separation Factor
$SF_{(Ho/Er)}$: Ho/Er Separation Factor
$SF_{(V/Mn)}$: V/Mn Separation Factor
SPECT: Single Photon Emission Computer Tomography
SRIM: Stopping and Range of Ions in Matter
TAET: Targeted Auger Emitter Therapy
TLC: Thin Layer Chromatography

TPF2G: Tube Petit Format 2 Grammes (nomination of geometry calibration for a small tube with 2 mL (2g) of aqueous radioactive solutionTRIM: Transport of Ions in Matter
TRT: Targeted Radionuclide Therapy
XRD: X-ray diffraction

Elements in Mendeleiev's Periodic Table

Abreviation	Element
Ac	Actinides or Actinium according to context
Al	Aluminium
At	Astatine
Co	Cobalt
Cr	Chromium
Cu	Copper
Er	Erbium
Ga	Gallium
Gd	Gadolinium
Ho	Holmium
I	Iodine
Kr	Krypton
Ln	Lanthanides or Lanthanium to context
Lu	Lutécium
Mn	Manganese
Ni	Niobium
Rb	Rubidium
Sc	Scandium
Tb	Terbium
Tc	Technétium
Te	Tellurium
Tm	Thullium
V	Vanadium
Y	Yttrium
Zn	Zinc
Zr	Zirconium

Introduction

[^{18}F]F-FDG (fluorodeoxyglucose) is a similar molecule to glucose (a natural sugar) in which a hydroxyl group has been substituted by radioactive fluorine 18 with a short half-life (110 min), emitting positrons (e +). This chemical substitution alters glucose metabolism, causing its accumulation in cells. Because cancerous tumors consume more glucose than healthy cells, the biodistribution will be not homogenous in a patient with a cancerous tumor. This alteration of cell mechanism makes it possible to characterize and stage a wide variety of cancers using PET (Positron Emission Tomography) scans. The principle of this nuclear imaging is based on the emission of positrons, which annihilate with matter and generate two photons of 511 keV emitted in coincidence, detected by the PET scanner.

In the 2000's, a new "class" of positron-emitting radionuclides such as ^{64}Cu ($T_{1/2}$ = 12.7 h), ^{68}Ga ($T_{1/2}$ = 67.71 min) or ^{89}Zr ($T_{1/2}$ = 78.41 h) has emerged for clinical applications: the radiometals. Their benefits include longer half-lives than conventional radionuclides allowing the study of the slower biodistribution of antibodies or peptides in the body. Radiometals require new methods of production and purification. Solid targets need to be irradiated instead of liquid (^{18}F) or gas targets (^{11}C, ^{13}N, ^{15}O) and require adaptation of targetry for routine production. The preparation of target materials tends to be more complex than conventional radionuclides due to their purification before their use in radiolabeling molecules. New protocols need to be developed like a catch and release as in the case of ^{18}F (fixed on QMA cartridge and desorbed with NaCl solution in [^{18}F]NaF) or ^{11}C (frozen at 78 °C bath before releasing it at room temperature in the form of [^{11}C]CO_2). Generally, it's always necessary to use the three steps of separation: dissolution, separation, and formulation. For automatization, it appears more complex. But radiolabeling chemistry (via complexation) used for radiometals is straightforward with slight adjustment: correction of pH, the addition of chelator, reaction, and purification rather than covalent chemistry used for conventional radionuclides. Since the 80's, the number of companies that commercialize automated systems of radionuclides has drastically increased access to various radionuclides, increasing the development of targeting molecules with the emergence of radiometals. In the way that [^{18}F]FDG is associated with ^{18}F, the chelating agent DOTA (1,4,7,10-Tetraazacyclododecane-1,4,7,10-tetraacetic acid) is the leading molecule for radiolabeling with radiometals.

Nowadays, with access to numerous radionuclides, their ionizing radiation (alpha, bêta, Auger electron) proprieties are increasingly studied for therapy applications. Currently, the association of radionuclide pairs ^{44}Sc/^{47}Sc, ^{44}Cu/^{47}Cu, the terbium family (^{152}Tb for PET, ^{155}Tb for SPECT (Single Photon Emission Computer Tomography), ^{161}Tb for beta and Auger electron (AE) and ^{149}Tb for alphas) provides one radionuclide dedicated to imaging and the second for therapy applications using the same vector molecule. These pairs are being increasingly and ideally applied in preclinical research. These combinations are called theranostics pairs. In this context, the Targeted Radionuclide Therapy (TRT) is developed: a systemic treatment that uses radiolabeled cancer cell-specific molecules to first diagnostically identify, then deliver a

cytotoxic dose of radiation (alpha, beta, Auger electron) to cancer cells with limited to healthy tissues and organs [1]. In this context, some radionuclides were produced for their alpha emission ^{211}At, ^{225}Ac, or beta emission ^{177}Lu or beta/AE ^{161}Tb for clinical applications. Research on the development of AE therapy increases the need for data and the production of potential therapeutic radionuclides.

Radionuclides such as ^{18}F, ^{11}C, and ^{99m}Tc are mostly used for their imaging applications because PET or SPECT are very sensitive techniques but lack spatial resolution compared to other imaging modalities. But these nuclear imaging usually were associated to anatomical image in order to localize radioactive signal in the body. Imaging techniques with higher anatomical spatial resolution including x-ray CT (computed tomography) and MRI (Magnetic Resonance Imaging) could be useful in bimodal imaging, PET / SPECT- MRI.

Most of contrast agents used in MRI are based on Mn or Gd for their paramagnetic proprieties. Due to their toxicity, the injection of these "free" Mn or Gd is limited and requires their coordination with molecules. These contrast agents must be injected at micromolar concentration in MRI. The use of their radioactive isotope for nuclear imaging allows the use of picomolar solution avoiding at this scale the toxicity of the radiolabelled molecule for biodistribution of Mn or Gd complex molecules. Moreover, using same element in bimodal applications avoids the risk of different biodistribution if, for example, the molecule is complexed with ^{68}Ga for PET and Mn for MRI. Similar distribution is expected when using same element in the two techniques, with a nonradioactive isotope for MRI and radioactive isotope of Mn or Gd for nuclear imaging. While there exists no radioactive isotope of Gd suitable for PET/SPECT imaging, all lanthanides have very similar chemistry meaning similar biodistribution. Given this, ^{165}Er appears as a good radioactive SPECT surrogate of Gd. The purpose of this thesis was the production of ^{52}Mn and ^{165}Er at a satisfactory quality according to its imaging (PET, SPECT or bimodal SPECT/MRI) or therapy applications. For therapy applications, a high AMA (Apparent Molar Activity) is required with quality of ^{52}Mn and ^{165}Er depending on three parameters associated with the radionuclide production:

1) The target: the quality of target material and its impurities, the availability of material for irradiation, and the technique of target preparation are crucial factor on final purity of radionuclide.
2) The targetry: according to specifications of cyclotron in terms of energy and beam, characteristics of the target could be adapted (thickness, size). In this work, the research cyclotron at Orleans (France) (^{52}Mn and ^{165}Er) and two biomedical cyclotrons at Madison (Wisconsin, USA) were used.
3) The separation: a ratio above 10^5 between the radionuclide of interest and the solid target is always a minimum to consider for the radiochemical separation. The radiochemical separation needs to be easy to automatize. In these conditions the liquid-liquid extraction process were excluded, and the Solid Phase Extraction (SPE) method was preferred. For that, ion exchange resin (cation or anion resin) for their high capacity of adsorption and extraction resin for their selectivity are chosen. Moreover to increase final AMA, a step of trace metals reduction was added.

The parameters fixed the level of AMA for the produced radionuclide: low or high. This level of AMA defined its potential use in some applications where the density of receptor is limited. For that the optimization of the AMA parameters were described for ^{52}Mn and ^{165}Er with special attention on:

- Preparation of Cr target for ^{52}Mn production with proton irradiation at 14 MeV in Chapter 2.
- Determination of the cross section for nuclear reaction $^{nat}V(\alpha,x)^{52}Mn$ and the radiochemical separation V/^{52}Mn in its production by alpha irradiation of V foil at high energy (45 MeV) in Chapter 3.
- Production of ^{165}Er with low AMA for proof of concept of bimodal SPECT/MRI in Chapter 4.
- Optimization of Ho target mass, irradiation conditions according to the used cyclotron and radiochemical separation of Ho/Er for a high AMA (in vivo bimodal applications and Auger electron therapy dosimetry) in Chapter 5.

Finally, we present some preliminary results of the outlooks of this work before to conclude on the various methods of ^{52}Mn and ^{165}Er production developed in this manuscript.

1. Chapter 1: Background

1.1 MRI

Every year, millions of magnetic resonance imaging (MRI) scans are performed worldwide, and around 40 % of these examinations are enhanced by the use of a contrast agent[2]. They enable sharper images of the tissue being viewed.

1.1.1 Principle

The human body is composed mainly of water and fat, and hydrogen atoms represent around 63%. In MRI, contrasts are obtained through the density and non-uniform relaxation properties of these hydrogens through their nuclear spin (S = ½)[3]. Indeed, in the absence of an external magnetic field, the orientation of the nuclear spins of hydrogen in water molecules is random. Once the body is placed in a static magnetic field of intensity B0 (between 0.5 - 3.0 T for most clinical devices), the nuclear spins orient themselves in the direction of the field B0 vector and process individually around it at a frequency ν0 called the Larmor frequency.

The result is the appearance of a macroscopic magnetization reflecting the position of the resulting spins. By applying a 90° pulse of radio frequency ν1, from an oscillating magnetic field of intensity B1 perpendicular to field B0, the vector magnetization M0 tilts 90° in the (Oxy) plane, resulting in two components: a longitudinal component (Mz) and a transverse component (Mxy)[4,5] (Figure 1.1.).

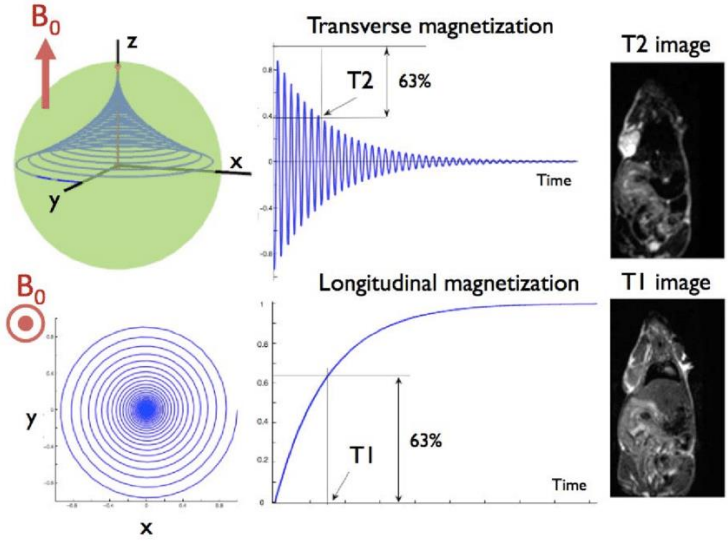

Figure 1.1: Longitudinal and transverse relaxation

Relaxation corresponds to the return to the equilibrium state of nuclear magnetization in a mono-exponential manner breaking down into two phenomena obeying very different mechanisms: longitudinal (T1) and transverse relaxation (T2). This is the principle of Nuclear Magnetic Resonance which gives a spectrum.

For MRI imaging, an equivalence between the Larmor frequency ν0 and the spatial position of the magnetizations needs to be established. In the MRI field B0, the magnetizations all have the same Larmor frequency. To introduce a dependency between spatial position and ν0, the

B0 field is varied in space using magnetic field gradients. During radio frequency emission, a "selection" gradient is applied to select a section of the body that will be the only one to emit a signal. Once the slice of interest has been selected, it remains to determine the position of the magnetizations in the plane of the slice to obtain an image. The frequency-encoding gradient is applied. Finally, images are reconstructed by two-dimensional Fourier transform after double frequency and phase coding of the slice plane and MRI images are obtained.

1.1.2 Gd or Mn contrast agent

T1 contrast agents are complexes of paramagnetic cations (e.g. Gd^{3+}, Mn^{2+}). Their effects on MRI signal intensity are positive (hyperintense signal). Most commercialized contrast agents are small Gd^{3+} complexes that diffuse rapidly from the blood into the extracellular space. They enable the detection of tumors in the brain whose blood-brain barrier (BBB) has been damaged. Recently, Gd-based MRI contrast agents have been suspected of potential *in vivo* release of free and toxic Gd^{3+}. The causal link of nephrogenic systemic fibrosis to Gd^{3+} exposure in patients[6] has led to the withdrawal of Gd^{3+} complexes formed with linear chelators[7,8]. Nevertheless, brain and bone accumulation of gadolinium remains a risk, even for highly stable and inert macrocyclic derivatives such as Gd-DOTA[9].

The paramagnetic nature of Mn makes monoaquated Mn(II) complexes safer alternatives to Gd(III) while designing MRI contrast agent candidates[7,10–13]. Mn^{2+} possesses favorable electronic properties ($S = 5/2$), and slow electron spin relaxation with T_1 values ideally on the nanosecond scale[14] to efficiently enhance the nuclear relaxation of water protons. The T1-relaxation shortening properties of bulk manganese are employed in a technique termed "manganese-enhanced magnetic resonance imaging" (MEMRI) applied to diffusion-tensor neuronal fiber tractography[15], nociceptive activity detection[16,17], functional imaging of brain activation[18], diagnosis and staging of pancreatic cancer[19], hepatocellular cell and evaluation of cardiac inotropic therapy[20]. Although MEMRI shows promise, the biological toxicity of bulk manganese[21] in terms of concentration hampers its development. MRI is a very powerful resolutive technique but has limited sensitivity due to the required concentration of injected contrast (millimolar).

In this context, nuclear imaging applications (such as PET or SPECT), being highly sensitive with the injection of nanomolar (nM) concentrations of tracer, represent a complimentary technique of imaging.

1.2 Nuclear imaging

The two major nuclear imaging techniques are positron emission tomography (PET) when the radionuclide emits a positron (e+) (^{18}F, ^{11}C, ^{64}Cu, ^{89}Zr…) (Table 1.1.). and single photon emission computed tomography (SPECT) when photon γ are emitted (^{99m}Tc, ^{111}In…) (Table 1.2.).

Radionuclide	$T_{1/2}$ (min)	Decay β+ (%)	β+ Energy (MeV)		Range in water (mm)	
			Max.	Mean	Max.	Mean
^{18}F	109.74	96,7	0.6335	0.2498	2.4	0.6
^{64}Cu	762	17.87	0.6529	0.2781	2.9	0.6
^{11}C	20.48	99.77	0.9601	0.3856	4.1	1.1
^{13}N	9.97	99.8	1.1985	0.4918	5.1	1.5
^{15}O	2.04	99.9	1.7319	0.7352	7.3	2.5

Table 1.1: Used PET radionuclides in nuclear medicine

Radionuclide	$T_{1/2}$ (h)	decay mode (%)	Photon emission (keV)	Intensity (%)
^{99m}Tc	6.02	IT (100)	141	87
^{111}In	67.9	EC (100)	247	94
			173	91
^{123}I	13.1	EC (100)	159	83
			528	1.4
^{201}Tl	73.1	EC (100)	167	10
			69-80	several X-rays

Table 1.2: Used SPECT radionuclides in nuclear medicine

The choice of imaging technique will depend on the following properties of the radionuclide:

- Radiation emission
- Half-life: sufficiently long to observe the biological process to study and not so long to limit radiation dose to the patient:
    - [^{18}F]FDG ($T_{½}$ = 110 min) is sufficient for following glucose metabolism. It's the most used radionuclide in nuclear medicine (PET). For the slow biodistribution of antibodies, radiolabeling with ^{89}Zr ($T_{½}$ = 3.3 days) is more suitable.
- Energy of gamma: enough to emerge from the tissue but well suited for absorption with detector materials (acquisition on camera via photomultiplicators (PMT) in the case of PET and collimators in the case of SPECT).

Nuclear imaging approaches have the advantages of high intrinsic sensitivity and depth penetration. PET has the additional advantages of being fully quantitative[22].

1.2.1 SPECT

The gamma camera detects and counts γ photons emitted by radionuclides. It recovers and stocks all data relative to the detected photon (energy, position in organism) (Figure 1.2.). Then standard planar projection images acquired from many angles around the patient are processed or reconstructed mathematically to obtain a three dimensional computed tomographic image.

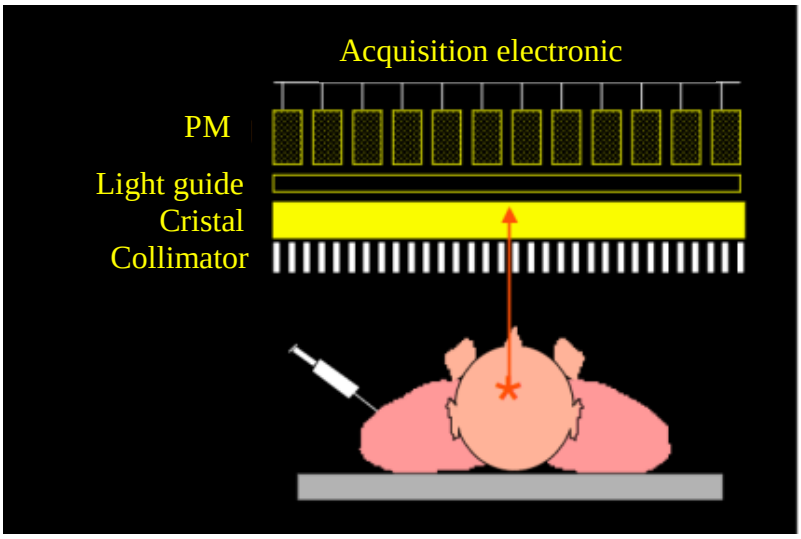

Figure 1.2: SPECT imaging

Only gamma events selected by the collimator are transformed into light energy via the photoelectric effect by a scintillator (usually sodium iodine activated with thalium (NaITl)). Then a PMT array detects this light pulse input to a position-sensing network and transfers these events to the computer. The final result is a picture of the detected photons accumulated at each point of the camera field of view during the exam. While for many years SPECT imaging was not quantitatively assessed, the field has recently begun to move toward absolute quantification[23].

1.2.2 PET

« PET involves four steps: shooting, cooking, imaging, and diagnosis ».
(Jerry Nickles, professor of medical physics and radiology at the University of Madison (WI, USA))

Positron emitters are characterized by an excess of positively charged protons. They decay to a new state (stable or not), through the transformation of a proton into a neutron, positron, and neutrino. This positron has the same mass as an electron but with the opposite charge. Once emitted, the positron travels a few millimeters losing its kinetic energy. The positron ($\beta+$) emitted from the atomic nucleus finally interacts with an electron ($\beta-$) in the stopping material and annihilates it. As a result, annihilation radiation is produced in which two photons with a 511 keV energy in opposite directions are emitted (Figure 1.3) and detected by a ring of segmented radiation detectors. The location of the annihilation reaction is determined by the the detection of the two photons in temporal coincidence (with 5 – 10 ns)[31] defining a unique line of response between the two detector elements. Many lines of response are then processed further by a reconstruction algorithms, such as filtered back projection (FBP) or ordered subset expectation maximization (OSEM), to generate a 3D image of the radionuclide distribution.

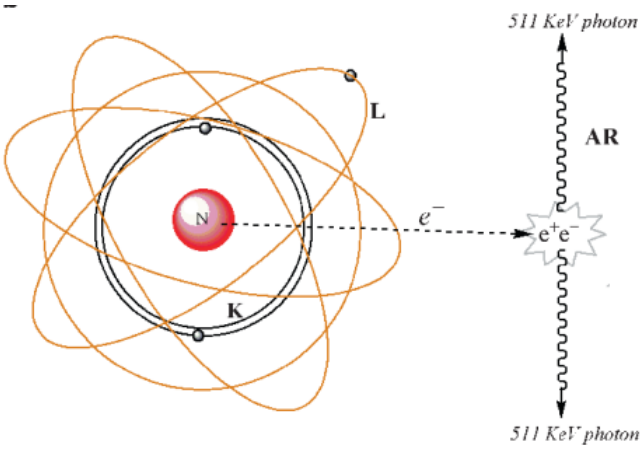

Figure 1.3: Annihilation of positron

With this definition of the concept of bimodality, how does one produce radionuclides and what radioactive Mn or Gd isotope to choose?

1.3 Production of radionuclides

To produce radionuclides for use in PET and SPECT imaging, a large diversity of nuclear reactions can be used. Research reactors and accelerators are complementary tools to access radionuclides. Research reactors provide a high neutron flux that allows the production of large quantities of neutron-rich radioisotopes, but the product radionuclides have a poor AMA (Apparent Molar Activity). This is because the neutron capture reaction does not change the atomic number Z, so the final product is an isotope of target, confounding chemical complex separation. Another point is, that access to these facilities is not easy, logistics and licenses need to be established for transport, reception, and use of radionuclides. Accelerators such as medical cyclotrons appear a complementary suitable solution for the routine production of imaging isotopes. But the radonuclide production for therapy applications is limited to research area.

1.3.1 Cyclotron

Dr. Livingston has asked me to advise you that he has obtained 1100000 volt protons. He also suggested that I add “Whoopie”!

Telegram to Lawrence, 3 August 1931

Ernest Lawrence conceived the cyclotron concept after reading the dissertation by Rolf Widerøe describing linear accelerator prototype[24]. He invented it in 1929 – 1930 at the University of California, Berkeley, and patented it in 1932[25,26]. He was awarded the 1939 Nobel Prize in Physics for this invention. The first working cyclotron had a radius of 4.5 inches (11 cm), and accelerated protons to an energy of up to 80 keV[25] (Figure 1.4).

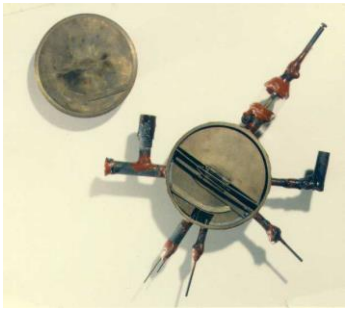

Figure 1.4: Lawrence's original cyclotron

1.3.1.1 Principle

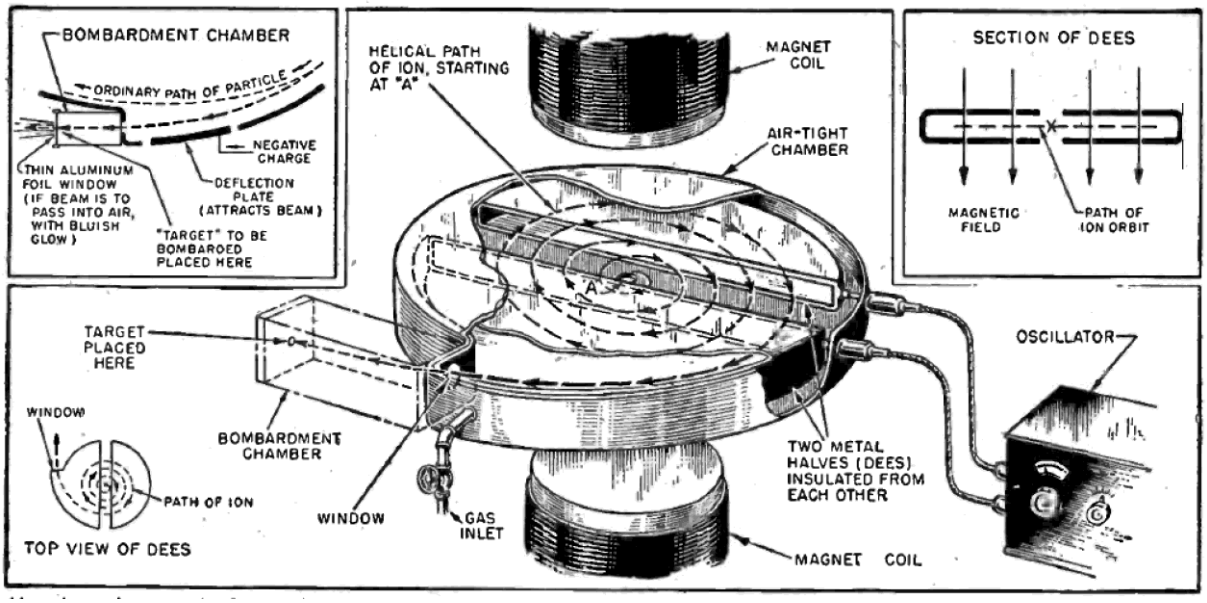

Figure 1.5: Component of cyclotron

A cyclotron is composed of three major components: an electromagnet with a field strength of 1.5 – 2.0 tesla, a pair of semicircular hollow copper electrodes, called dees, located between the poles of the magnet, and an ion source (Figure 1.5)[27].

1.3.1.2 Ion source

Initially, cyclotrons were positive ion cyclotron sources (Orleans'cyclotron), designed to accelerate positive ions ($^{1}H^{+}$ and $^{2}H^{+}$). Since the 1980s, negative ion sources have been used for all commercial and medical cyclotrons (as Madison's cyclotrons). Following ionization as negative ions in a penning ion gauge discharge of the hydrogen gas in an ion source, the ions (proton or deuteron) are injected into the center of the gap between the dees. When a 20 – 30 MHz radiofrequency alternating potential of 30 – 100 kV, generated with an oscillator, is applied to the dees, the negative ions will accelerate towards a dee that is at a positive potential. Because the magnetic field is perpendicular to the plane of the dees and particle motion, the negative ions will trace a circular path. Further, the electrical potential on the dees is alternatively positive and negative, the ions will gain energy at each crossing of the gap between the dees, as they move outward in a spiral path from the center. The magnetic force operating

on the ion is a centripetal force (Bev), which is exactly balanced by the centrifugal effect (mv^2 /r) (eq. 1).

$$Bev = \frac{mv^2}{r} \quad (1)$$

$$r = \frac{mv}{Be} \quad (2)$$

In the above equations (1) and (2), B is the magnetic field strength while m, e, and ν represent the mass, charge, and velocity of the ion, respectively. Finally, r represents the radius of the ion's orbit. For a given cyclotron, the maximum kinetic energy that an ion can attain can be estimated if B and r are kept constant (eq. 3).

$$E = \frac{B^2 r^2}{2}\left(\frac{e^2}{m}\right) \quad (3)$$

1.3.1.3 Extraction beam

Once the desired kinetic energy of the accelerating particles is achieved, the positively charged ions (H^+ and $2H^+$) are extracted from the cyclotron by passing the negative ion beam through an ultra-thin foil of carbon (graphite), which strips the electrons. The now positively charged protons will be deflected in the opposite direction in the magnetic field, which can then be directed to bombard an appropriate target to produce radioisotopes. Negatively charged electrostatic deflectors are typically used for the extraction of accelerated ions from positive ion cyclotrons. For this work, different cyclotrons were used:

- Research cyclotron located in National Center of Scientific Research, CEMHTI Laboratory in Orleans (France).
- Two medical cyclotrons located in the University of Wisconsin School of Medicine and Public Health (SMPH) in Madison,Wisconsin (WI), USA.

1.3.2 Orleans'cyclotron

➢ **Specifications**

The Orleans' cyclotron was a CGR-MeV 680 Type research accelerator (Figure 1.6) built between 1974 and 1976. From its first run on 5th November 1976 with an 11 MeV proton on an Ag target to the last irradiation on 22nd March 2023 for the production of ^{165}Er with a deuteron beam of 13 MeV on a Ho target, this research cyclotron has been used for a large number of chemical applications: studies of radiolysis, behaviors of material under irradiation (uranium oxide, metals), archeometry.

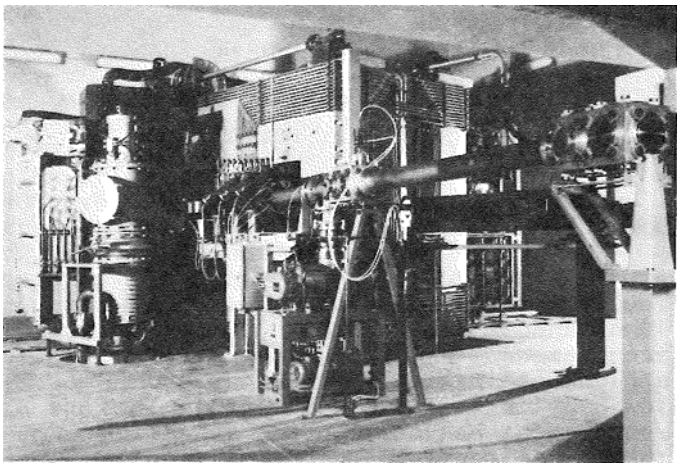

Figure 1.6 : Orléans' cyclotron in 1975

Many beam types such as the proton, deuteron, and alpha at variable energy from 10 to 45 MeV (Table 1.3) could be used giving access to numerous radionuclides with potential applications, especially for medical imaging.

Particle	**Energy (MeV)**	**Current ( )**
Proton	7 - 35	1 p/s – 40 µA
Deuteron	5 - 25	3 pA – 40µA
Alphas	10 - 45	3 pA – 25µA
HH^+	14.4	3 pA – 40µA

Table 1.3 : Particle beam at Orleans' cyclotron

1.3.3 University of Wisconsin-Madison's cyclotrons

The Cyclotron Research Group in the Department of Medical Physics makes radionuclides for medical diagnosis, disease treatment, and fundamental scientific inquiry. In the process of studying these applications, routine measurements are done that add to nuclear data repositories, develop new materials for accelerator targetry, and explore new radiochemical isolation strategies for no-carrier-added production of new and interesting radionuclides[28]. The Cyclotron Group provides radionuclides to colleagues on and off campus. In this context it has recently become a member of the U.S. Department of Energy's University Isotope Network (UIN)[29] as producers of ^{86}Y, ^{77}Br, and ^{52}Mn (Figure 1.7).

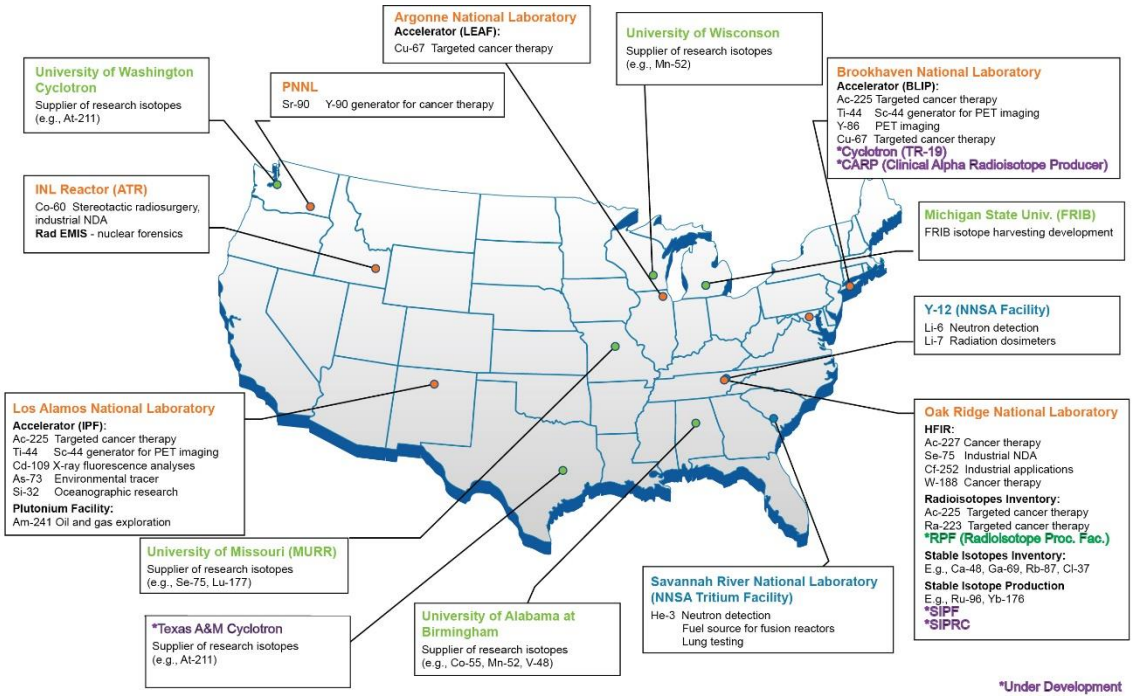

Figure 1.7 : U.S. Department of Energy's University Isotope Network (UIN)

For all these developments and production, the cyclotron group at Madison (WI) used two biomedical cyclotrons (negative ion source) (Table 1.4):

- RDS-112 (CTI Cyclotron Systems) at 11 MeV proton set up in 1985
- PETtrace (GE Healthcare) at 16 MeV proton / 8 MeV deuteron accelerator installed in 2008.

			Particle beam	
Firm	**Model**	**Type**	**Energy (MeV)**	**Current (μA)**
CTI	RDS-112	H+	11	50
GE	PETtrace	H+/²H+	16.5/8.5	75/60

Table 1.4 : Particle beam at Wisconsin-Madison's University cyclotrons

In this work, these cyclotrons were used for production of two radionuclides: ^{52}Mn and ^{165}Er.

1.4 ^{52}Mn

1.4.1 Natural Manganese

Manganese is a monoisotopic element that naturally occurs as ^{55}Mn. Manganese comprises about 1000 ppm (0.1 %) of the Earth's crust, the 12th most abundant of the crust's elements. Soil contains 7 – 9000 ppm of manganese with an average of 440 ppm. The atmosphere contains 0.01 μg/m^3.

As a transition metal with an atomic number Z = 25 with complex oxidation/reduction properties, the chemistry of manganese is different from other metals in its group, Tc and Re. In solution, the most stable oxidation state is Mn(II) with a half-reaction standard reduction potential of -1.185 V[30]. Manganese is an essential endogenous trace element that contributes to

the assimilation of lipids, proteins, and carbohydrates by our body and has a role in normal energy metabolism[31]. It is an essential constituent of many proteins and enzymes, which are therefore dependent on its presence in sufficient quantities to function properly[32,33]. This is particularly true of the endogenous enzymatic antioxidant superoxide Dismutase (Mn-SOD), whose role is to trap free radicals produced by metabolism[34]. Manganese is therefore an antioxidant that helps protect cells against oxidative stress, a key factor in skin ageing[35], and plays a role in the growth and maintenance of bones, and therefore, the main organs for receiving Mn in the body[36]. It is also in the liver, kidneys, and brain where it is bound to manganese metalloproteins. It is also found biologically in all types of bacteria, plants, and animals. It is so essential to life that the evolution of the oxygen-evolving complex (OEC) — containing four Mn atoms, responsible for catalyzing the oxidation of water to molecular oxygen — was one of the key pieces to enabling the evolution of life on earth[37].

Although it is an essential trace element in humans, roughly 10 - 20 mg in total, an excess of manganese is known to cause a variety of psychiatric and motor disturbances, which closely resemble the symptoms of idiopathic Parkinson's disease. This condition is known as "manganism" and is observed in some mining and welding populations[38].

1.4.2 Radiomanganese

Mn has five radioisotopes with half-live higher than 2 min (Table 1.5).

Isotope	$T_{1/2}$ (min)	Decay (%)	β mean (MeV)	γ > 1% (keV)	Emission 511keV	Range in water (mm)
51	46.2	β+ (97.1)	0.96	-	194.2	4.275
52^m	21.1	β+ (96.6)	1.17	1434	193.1	-
52	8049.6	β+ (29.4)	0.24	744 ; 848 ; 935 ; 1246 ; 1333 ; 1434	58.8	0.63
54	449280	EC (100)	-	834	6.00E-07	-
56	154.8	β^- (99.9)	0.83	847 ; 1811 ; 2113	-	-

Table 1.5: Mn radioisotopes

For use in PET or SPECT imaging, ^{56}Mn (β^- emitter) and ^{54}Mn (very low emission 511 keV) could not be considered. The short half-life of ^{51}Mn ($T_{1/2}$ = 46.2 min.) and ^{52}Mn ($T_{1/2}$ = 21.1 min.) require working with high activities to optimize each step of preparation of radiotracers before use (irradiation, purification, radiolabeling).

^{52}Mn is the best candidate in terms of manganese PET emitters relative to other PET emitters such as ^{11}C, ^{13}N, or ^{89}Zr because of its low average energy in β^+. With lower positron energy, the shorter positron flight path (the linear distance from the positron source to the annihilation point) reduces its impact on spatial resolution. For ^{52}Mn, its range in biological tissues (average energy of 244.6 keV, 0.63 mm)[39,40] is comparable to ^{18}F (250 keV, 0.62 mm[41]). These values are better than those of ^{51}Mn (970.2 keV, 4.275 mm) in terms of PET spatial resolution (ratio of 6).

1.4.3 Dosimetry and Imaging

Manganese-52's several high energy gamma rays (744 keV, 90%; 935 keV, 95% and 1434 keV, 100%) are its major drawbacks for its use in clinical studies[42]. Effective doses due to [^{51}Mn]$MnCl_2$ and [^{52}Mn]$MnCl_2$ in humans have been predicted using biodistribution data from animal comparison with effective dose usually done for [^{18}F]FDG. Dosimetric calculations performed in De Nardo's work demonstrate that, due to the relatively high [^{52}Mn]$MnCl_2$

effective dose, the usefulness of [^{52}Mn]$MnCl_2$ as a PET brain imaging agent is limited[43]. Moreover, the operator who manipulates high amounts of this radionuclide during production or injection will be exposed to a significant dose rate: 18.4 R × cm^2 × mCi^{-1} × h^{-1} , 2.8 times higher than ^{89}Zr (6.6 R × cm^2 × mCi^{-1} × h^{-1}) and 3.3 times higher than ^{18}F (5.6 R × cm^2 × mCi^{-1} × h^{-1})[44].

But, in some points, ^{52}Mn has advantages to be used in PET imaging:

- Its half-life of 5.6 days, similar to that of ^{89}Zr ($T_{1/2}$ = 3.3 days) and longer than that of ^{64}Cu ($T_{1/2}$ = 12.7 hours). Its use allows for carrying out imaging on a longer time scale, compatible with antibody-based targeting applications.
- ^{52}Mn emits positron at 29.4 %, a higher proportion than those of ^{64}Cu (17.9 %) and ^{89}Zr (22.7 %).
- Higher sensitivity of PET over MRI: use of low concentrations of manganese for imaging studies and biodistribution in preclinical state PET/MRI bimodality.

1.5 ^{165}Er: a radiolanthanide

1.5.1 Lanthanides Generalities

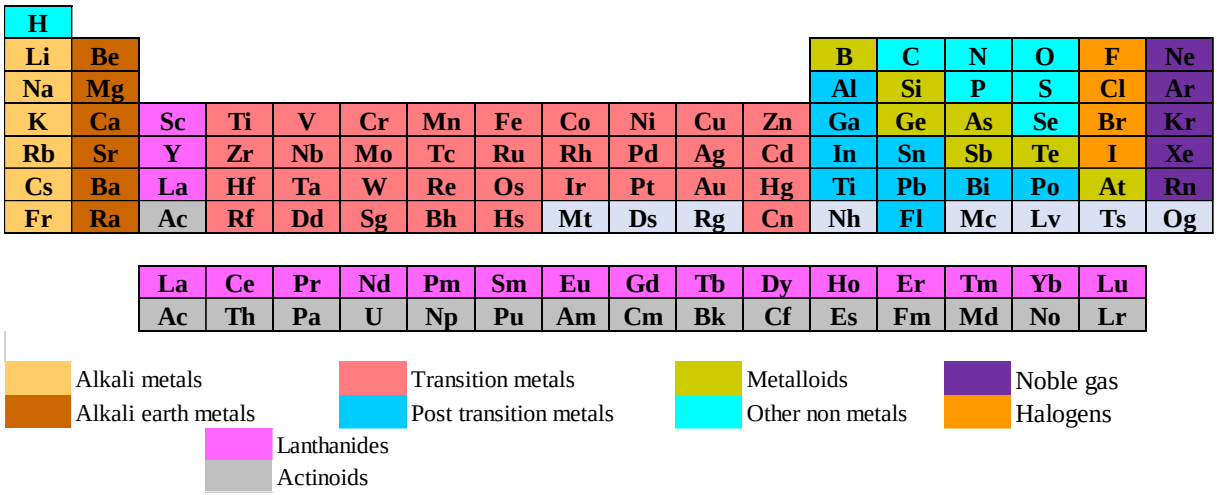

Figure 1.8: Periodic Table of Mendeleev

Rare earths perplex us in our research, baffle us in our speculations, and haunt us in our dreams. They stretch like an unknown sea before us - mocking, mystifying and murmuring strange revelations and possibilities"

Sir William Crookes.
Address to the British Association, 1887[45]

The lanthanide series of chemical elements comprises at least 14 metallic chemical elements with atomic numbers 57 – 70, from lanthanum through ytterbium. Generally, Lu (Z = 71) is also associated with this series. In the periodic table, they fill the 4f orbitals. Due to their similar proprieties, Sc and Y are considered pseudo-lanthanides (Figure 1.8). The lanthanides are therefore known as 4f-elements and the gradual filling of this 4f-subshell is what makes them unique as elements and attributes greatly to their optical and magnetic properties. More importantly, the 4f electrons are well shielded by higher electron shells (5s, 5p…) which makes them generally unhindered by chemical interaction with neighboring atoms or ions. This is in great contrast to the d-type transition elements, where the d-electrons are valence electrons

which are involved in chemical interaction. In most common compounds, lanthanides have the trivalent oxidation state. Exceptions with a some chemical stability are Eu(II), Yb(II) and Ce(IV). It is concluded that this predominant trivalent state is the result of a somewhat fortunate combination of ionization- and hydration energy (in solution) or ionization- and lattice energy (in solid compounds) rather than to any specific electronic configuration[46,47] Another interesting phenomenon is the so-called lanthanide contraction (Figure 1.9). A gradual decrease in ionic radius is observed when going through the lanthanide series from La to Lu. This is because the electrons in the 4f subshell are unable to properly shield the outer electrons (5s, 5p) from an increasing nuclear charge. These results in a gradually decreasing ionic radius, which is visible for the trivalent ions and, to some extent, for the other valences as well. Relativistic effects influence the shielding characteristics of inner electrons[48].

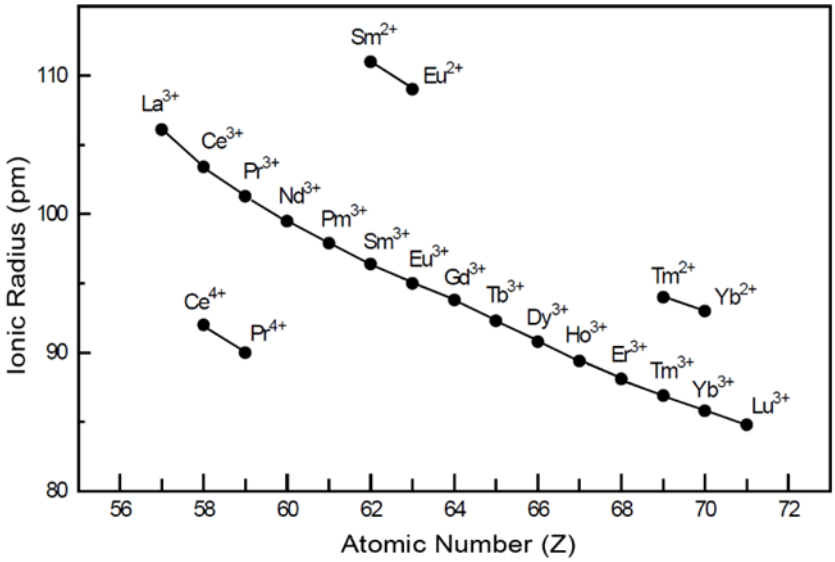

Figure 1.8 : Lanthanide contraction

Bonding on coordination is primarily ionic in character, complexes undergo rapid ligand exchange because $4f^n$ electrons are contracted into the core and unable to participate in bonding. Ln^{3+} cations display typical acid Lewis properties, preference for O-donor ligands which are more likely to be charged relative to N for example[49]. Lanthanides are luminescent in the visible under ultraviolet light for Ln^{3+} ions: lilac (Er, Nd), green (Pr, Tm), colorless (La, Ce, Gd, Yb, Lu), yellow pink (Pm, Ho), yellow (Sm, Dy), pale pink (Eu, Tb). All lanthanides form hydroxides at high pH ($Ln(OH)_3$). They have mostly a high coordination number (8 – 9).

1.5.2 Radioactive lanthanides

Due to their properties, lanhanides have lot of applications in catalysts, in the production of petroleum and glasses, metallurgy, alloys, steel alloys, ceramics (Figure 1.10), glass polishing, magnets, luminescence (lighting, lasers, telecom, displays, light conversion, security)[50–52].

Figure 1.9.: Photography of polycrystalline glasses (a) and ceramics (b) diam. 5 mm, 1 mm thickness) obtained at CEMHTI laboratory by complete crystallization of the $SrREGa_3O_7$ glass using a simple heat treatment. The samples are polished on 2 parallel faces[52].

For medical applications, gadolinium is largely used as an MRI contrast agent. Moreover, demand to produce radiolanthanides increases significantly for radiotherapy applications with ^{177}Lu and more recently ^{161}Tm for its combined proprieties of beta and Auger emission. As discussed previously with pair ^{55}Mn/^{52}Mn for manganese, it will be interesting to develop the production of a radioactive gadolinium for bimodal MRI/nuclear imaging applications. There are 33 isotopes of Gd (radioactive and stable from mass A = 136 to 169) referenced in the table of isotope decay data with 6 stables[53] and, 9 radioisotopes with half-life > 1h. Further restrictions for imaging applications need to be considered, no alpha emitter and decay time less than 10 days: only ^{159}Gd (18.479 h), ^{147}Gd (38.06 h) and ^{149}Gd (9.28 d) respect these criteria. ^{159}Gd has been proposed as a beta emitting therapeutic radionuclide [54-55]. This radioisotope is produced by thermal neutron bombardment of natural Gd_2O_3[56] in a nuclear reactor. There is no easy access to ^{147}Gd or ^{149}Gd. The only routes for production use enriched ^{151}Eu targets with proton beams in the energy range of 20 -> 35 MeV for ^{149}Gd and above 35 MeV for ^{147}Gd[57]. No radiogadolinium is easily produced from natural targets.

As previously mentioned, lanthanides have very similar chemistry because each additional electron to a lower-lying 4f orbital doesn't affect the valence shell. In this case, considering their similar biodistribution, we selected another radiolanthanide with the following characteristics: β^+ or γ emitter for PET or SPECT applications, half-life compatible with radiolabeling and imaging time (2 h to 10 days), high production yield ($MBq \cdot e\mu A^{-1} \cdot h^{-1}$) and do not require the use of the enriched target. With these criteria, two candidates have been found:

- ^{141}Nd ($T_{½}$ = 2.49 h) produced by irradiation of ^{141}Pr target[58] with deuteron beam (nuclear reaction ^{141}Pr(d,2n)^{141}Nd gives a high maximum of > 1300 mb at 16.5 MeV)
- ^{165}Er (($T_{½}$ = 10.36 h) produced by irradiation of ^{165}Ho (natural holmium) or ^{nat}Er target.

In this work, ^{165}Er was investigated due to its more favorable half-life.

1.5.3 ^{165}Er: imaging and therapy applications

1.5.3.1 Generalities on Natural Erbium

In 1787, Lieutenant Carl Axel Arrhenius found an unidentified black mineral in Ytterby (a Swedish village) fully analyzed by Finnish chemist Johan Gadolin in 1794. The chemical elements yttrium (Y), terbium (Tb), erbium (Er), and ytterbium (Yb) are all named after Ytterby[59]. Erbium's principal uses involve its pink-colored Er^{3+} ions, which have optical fluorescent properties particularly useful in laser applications. Erbium-doped glasses or crystals can be used as optical amplification media where Er^{3+} ions are optically pumped at around 980 or 1480 nm and then radiate light at 1530 nm in stimulated emission. A large variety of medical applications (e.g. dermatology, dentistry) rely on the erbium ion's 2940 nm emission (see Er: YAG laser) when lit at another wavelength, which is highly absorbed in water, in tissues, making its effect very superficia. Such shallow tissue deposition of laser energy is helpful in laser surgery[51].

1.5.3.2 Radioactive Erbium

Natural erbium is a multi-isotopic element (6 stable isotopes). One of its radioactive isotopes, ^{169}Er ($T_{1/2}$ = 9.392 d), is used in targeted therapy as a soft-β^- emitting (average energy 101 keV) radionuclide with an average soft tissue range of 0.3 mm. It is used in the treatment of rheumatoid arthritis and degenerative joint diseases. Typically, 18 – 37 MBq (0.5 – 1 mCi) ^{169}Er is administered to a patient making it a cost-effective approach in providing long-term relief of pain and deformity of the inflamed joints in compared to other therapeutic approaches[60]. Another radioactive erbium used in medical applications is ^{165}Er. In 1976, a patent was registered for [^{165}Er]Er-citrate as a cardiac infarct and tumor[61] imaging.

1.5.3.3 ^{165}Er specifications

^{165}Er has a half-life of 10.36 h decaying to a stable element ^{165}Ho (Table 1.6 and Figure 1.11), sufficient for production (irradiation, separation, radiolabeling, and injection) process and biodistribution studies. It emits low-energy X-rays (47 - 55 keV with a cumulative intensity of 73.7 %) useful for research and preclinical bimodal MRI/SPECT imaging.

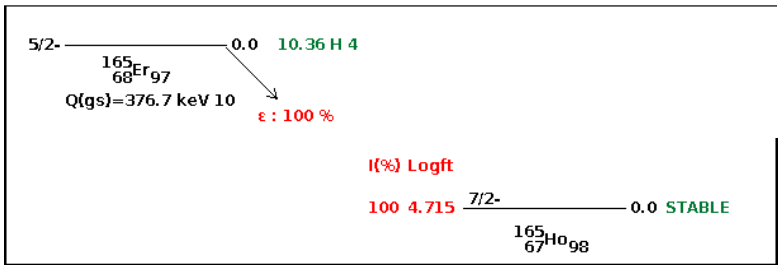

Figure 1.10: ^{165}Er decay scheme

Parent Nucleus	Parent E(level)	Parent Jπ	Parent $T_{1/2}$	Decay Mode	GS-GS (keV)	Daughter Nucleus
165 68 Er	0.0	5/2-	10.36 h *4*	ε: 100 %	376.7 *10*	165 67 Ho

Table 1.6 : Decay specifications

Energy (keV)	Range (µm)	AE per decay
0.019 - 0.222	0.001 -0.012	5.015
0.708 - 1.442	0.050 - 0140	1.556
5.309 - 7.984	1 - 2	0.658
38.255 - 52.601	25 - 45	0.047
	Total	7.3

Table 1.7: Auger electrons emission of ^{165}Er

Moreover, it has a higher number of Auger emissions (, a lower X-ray fluorescence yield, and emits no conversion electrons (CE) or gamma rays[62,63]. This lanthanide is a good candidate for Auger therapy dosimetry studies. More details about this application are provided in Chapter 5 Introduction.

2. Chapter 2: Production of ^{52}Mn by proton irradiation

2.1 Targetry of ^{52}Mn proton irradiation

2.1.1 Nuclear reaction ^{52}Cr(p,n)^{52}Mn

^{52}Mn can be produced by cyclotron via proton, deuteron or alpha beam irradiation. Chapter 3 will discuss its production via alpha irradiation. High-energy proton (30 - 100MeV) irradiation of ^{nat}Fe is viable but radionucleidic purity is lower than 99.6 %[40]. Intermediate energy deuterons (6 – 20 MeV) on ^{54}Fe gives a low cross-section. 8 – 28 MeV deuteron beam irradiation on ^{nat}Cr seems a superior option compared to proton activation regarding both yield and radionucleidic purity[64–67]. However, the parameters of Orleans'cyclotron (with 17.5 MeV maximum energy in deuteron and low current of irradiation) would limit yield of the ^{52}Mn radioactivity. Currently, ^{52}Mn is obtained by proton irradiation on a natural Cr target at 14 MeV. It is the most used route to produce ^{52}Mn using nuclear reaction ^{52}Cr (p,n)^{52}Mn up to 14 MeV[68–72]. It is also the most accessible by commercial cyclotrons. While chromium is not a monoisotopic element (^{50}Cr 4.345 %, ^{52}Cr 83.790 %, ^{53}Cr 9.501 % and ^{54}Cr 2.365 %)[73], natural chromium is composed by more than 83 % of ^{52}Cr, providing inexpensive Cr targets. However, the production of radiomanganese impurities is confounded by the ^{54}Mn ($T_{½}$ = 312 d) representing 0.1 - 0.4 % of the ^{52}Mn activity at the end of the bombardment. Its production will vary with the thickness and quality of the Cr target. High-purity Cr is available from numerous manufacturers. ^{52m}Mn ($T_{½}$ = 20.1 min), the metastable isotope of ^{52}Mn, is also produced but its short half-life is helpful. After 3 - 4 hours of decay time after end of bombardment, no traces of ^{52m}Mn remain.

2.1.2 Target preparation

2.1.2.1 State of art

Chromium is a brittle transition metal[74]. Foils of Cr with a significant thickness (500 µm) were commercially purchased on a polymer support. For this reason, usually Cr targets are designed using powder in various forms[72]: pressed on Ag backing with a hydraulic/pneumatic press, electrodeposition[67], pressed pills[75], or spark plasma sintering (SPS)[76]. This last technique, SPS, allows the sintering of a pellet starting from powder and bonding it to a different material without a need for a filler: chromium targets were prepared in 3 steps, green pellets of Cr were done from powder then an inert foil was bonded to Cu backing disc (oxygen-free high thermal conductivity) by SPS. Finally, Cr pellets were press-bonded to the backing plate system (Au/Cu) by SPS.

2.1.2.2 Compaction

At Orleans, a Cr target has been designed using chromium powder taking into account the following criteria: contamination risks during irradiation, target dissolution, and thickness of target (limitation of Cr quantity without ^{52}Mn). For these purposes, the physical characteristics of the Cr target have been studied along its preparation: mechanics, thermal resistance, porosity (closed and opened), and dissolution in acid solution. These works have been previously published as Vaudon, et al instruments article.The best conditions of compaction were determined to obtain a Cr pellet of 13 mm diameter with good visual mechanical resistance.

The 13 mm diameter was fixed by using KBr pellet die. For that, some parameters of compaction were studied: force, powder mass and time of pellets compaction. First, a force of 8.3 tons was applied to the powder for 5 min. Several mass of powder (Cr prowder, Alfa Aesar, 100 mesh, 99 %, apparent density 2.0 – 3.0 g/cm^3) were tested from 200 to 1200 mg to define what mass is necessary to obtain a complete pellet (Table 2.1).

Powder (mg)	Pictures	State of pellet
200		incomplete
400		incomplete
600		incomplete
800		perfect
1200		complete

Table 2.1: Study of compaction at 8.3tons during 5 min on Cr pellet

From these tests, 800mg of chromium was deemed necessary to have a complete pellet of 13 mm diameter. Some tests were carried out to reduce the mass of 800 mg by varying time and compaction force. The results obtained are presented in Table 2.2.

Force tons (bars)	Mass powder (mg)	Compaction time (min)	Thickness (mm)	Visual Aspect
4 (150)	649.6	5	1.08	Bad
	649.5	10	1.01	Bad
	649.8	60	1.04	Bad
	699.7	5	1.09	Bad
8,3 (300)	599.7 (3)	5	0.89	Bad
	600.2	30	0.84	Good
	650.6 (3)	2	0.88	Good (2)
	650.8 (2)	5	0.93	Good
	650.2 (4)	30	0.9	Good
	650 (2)	60	0.89	Bad
	699.6 (3)	2	0.96	Good (2)
	699.4 (3)	5	0.95	Good
	700.2	60	1.04	Bad

( ) number of tests

Table 2.2: Profile of Cr pellets prepared according to mass and thickness

The term “Bad” is associated to an irregular (non-circular shape) pellet or broken pellet (see Table 2.1, 200 – 600 mg pellets. A good pellet, it is a good uniform and compacted mass in a circular shape of 13 mm (see Table 2.1, 800 – 1200 mg pellets). The best compaction conditions were: 650 mg 30 min at 8.3 tons (300 bars). Fifteen pellets were prepared on these conditions: weight average 649.6 ± 0.6 mg (n = 15), thickness = 0.87 ± 0.02 mm yielding 13 pellets with 2 pellets broken by manipulation.

2.1.2.3 Sintering

Despite compaction, pellets remained fragile: 2 pellets have been broken by manipulation during thickness measurements. This was, therefore, a problem for the irradiation where target is in contact with a beam of strong intensity, the pellet was likely to crumble or break. To improve the mechanical strength of the pellet, a sintering process is used. It is the process of consolidating a compact powder by heating it without melting it, to ensure cohesion. Under the effect of heat, the grains move closer, until they "weld" together, forming grain boundaries. The result is a reduction in porosity. It is therefore important to pre-compact the powder so that the grains are in contact and can allow the formation of grain boundaries. The diagram below illustrates the sintering heat treatment process (see Figure 2.1).

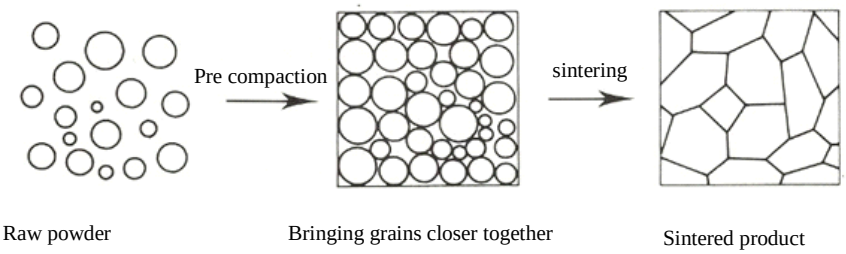

Figure 2.1: Sintering process

- **Material and Method**

Chromium is a compound that oxidizes very easily with air. For that, the sintering of Cr powder was done in an inert or reducing atmosphere in an electrical furnace (Nabertherm with controller P 320). An H_2/N_2 mixture (5 % hydrogen) has been used. In addition, to avoid a reaction between chromium and residual oxygen, Cr has been surrounded by crushed graphite. Whole has been placed in an alumina crucible and the following thermal cycle has been applied:

- Temperature rise rate: $5°C°\cdot min^{-1}$
- Peak temperature dwell time: 30 minutes
- Cooling speed: $5°C\cdot min^{-1}$

The same program was used in vacuum conditions. The vacuum was 10^{-7} mbar and the furnace was a homemade system where temperature is determined by pyrometry. The sample was put on a block next to a block of molybdenum. By measuring the emissivity of molybdenum, the temperature of the sample was determined. The study of sintering heat treatment has been carried out on the Cr pellet at various temperatures and different conditions (air, vacuum, and inert atmosphere). After sintering, bending tests were performed to determine its flexural strength or stress resistance.

- **Results**

The first tests were operated in a controlled atmosphere in oxygen on Cr pellets of 800 mg of compaction at 8.3 tons for 5 min, sintered at 500 °C, 800 °C, and 1000 °C for 30 min. Each test was repeated three times (Figure 2.3). Subsequently, we sought to determine the average

maximum stress resistance. Stress resistance increases with sintering temperature until 800 °C. After this value, no differences appeared. The stress resistance increases, while the porosity decreases as the temperature of sintering increases.

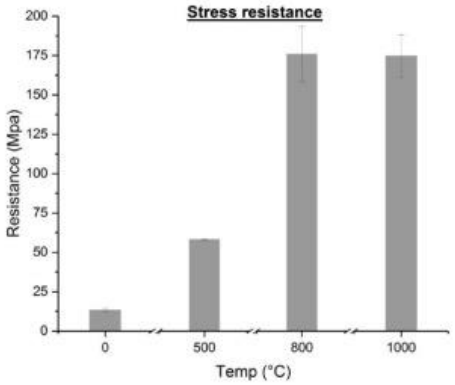

Figure 2.2: Stress resitance of Cr pellet sintered at 0, 500, 800 and 1000 °C

An optimization of conditions of sintering was made at 600 °C and 800 °C. 650 mg and 800 mg Cr pellets were used (Table 2.3). According to these results, a temperature of 800 °C was necessary to obtain a good rigid structure. The presence of oxygen or an H_2/N_2 atmosphere during the sintering made no difference in the mechanical properties. It only influences the chemical composition of the pellet. In the presence of oxygen, chromium oxide appears during the heat treatment (chromium oxide is difficult to dissolve).

Mass (mg)	Compaction Time (min)	Sintering conditions	Temperature (°)	Rupture resistance (Mpa)	STD (Mpa)
650	30	No sintering	-	12	2
		V.	600	13	1
			800	16	1
		N.C.A.	600	105	13
			800	221	29
		C.A.	600	123	14
			800	204	29
800	5	C.A.	800	211	28
	30	N.C.A.	600	100	7
			800	221	15
		C.A.	600	103	13
			800	205	13

V. Vaccuum / C.A.: Controlled Atmosphere / C.A.N.: Not Controlled Atmosphere

Table 2.3: Optimization of sintering temperature

2.1.2.4 Bending test

This test is unconventional and inspired by the "Ball on ring" test (Figure 2.2). A load (moving speed (0.5mm/min)) was applied, via a ball of alumina (9.32 mm diameter), to the center of the sample resulting in bending[77,78]. The applied force was recorded as a function of the vertical displacement of the ball. Recording measurement was stopped when the pellet was cracked. The required load to break the pellet was a mechanical parameter to evaluate each Cr pellet.

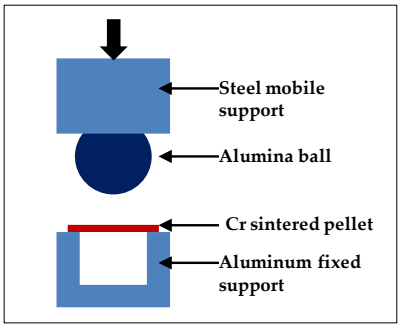

Figure 2.3: Bending test

2.1.2.5 Target dissolution

To evaluate the impact of sintering temperature on the dissolution of the Cr target, tests were made on Cr pellets of 800 mg (5 min of compaction at 8.3 tons). Dissolution has been done with 12 M HCl solution in a beaker heated at 100°C (200 °C indicated on the heating block) (Table 2.4).

Sintering T (° C)	1300	1200	100	800	650	600	600	550	500
Volume 12 M HCl (mL)	5 + 5	5 +5	10	10	10	10	10	10	10
T (°C) heating	100	200	200	200	200	200	200	200	200
Dissolution	P.	P.	P.	P.	P.	P.	C. (20 min)	C. (10 min)	C. (10 min)
% weigh dissolved in 30 min	65	75	76	80	80	80	100	100	100

P. Partial / C. Complete

Table 2.4: Dissolution of Cr pellet target

Cr pellets sintered up to 1000 °C were difficult to completely dissolve in 10 mL of 12 M HCl. Cr pellet sintered at 600 °C were dissolved in 20 mL of 12 M HCl but at this sintering temperature, the resistance to rupture of the Cr target are two times lower than at 800 °C (see table 2.4.). For these reasons, a sintering temperature of 800 °C was selected for the design of the Cr target. The dissolution of the Cr pellet by HCl starts at grain boundaries and increases the porosity of the pellet. SEM (Scanning Electron Microscope) observations confirm that grain boundaries are attacked and the material becomes more porous after the dissolution step (Figure 2.4).

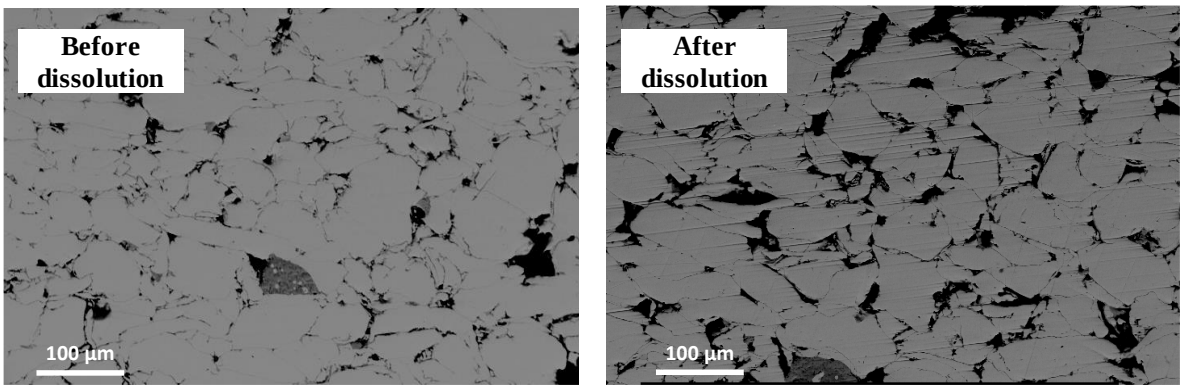

Figure 2.4: Micrograph SEM (mode BSE) of sintered pellet at 800°C, before and after dissolution

For temperatures higher than 600 °C, the densification is important. The residual porosity is too low, the reactive surface is therefore too small and the acid cannot penetrate the core of the material. Otherwise, chromium oxidizes very easily: a small amount of chromium oxide could crystallize during the sintering step or dissolve in contact with 12 M HCl. Then, chromium oxide is hard to dissolve because it is a stable compound [79,80]. During dissolution, 12 M HCl is charged with chromium ions. For the Cr pellet sintered at 600 °C with 10 mL of 12 M HCl, the dissolution is incomplete whereas with 20 mL complete dissolution happened. During the process of sintering, the Cr pellet is in the presence of carbon to avoid oxidation. Chromium carbide could be formed and limit the dissolution of the Cr pellet (Figure 2.5)[81]. Nevertheless, it should be noted that the higher the density is, the more difficult is the acid attack during dissolution because the grains are too close. Indeed, a pellet sintered at 650 °C or 800 °C does not dissolve completely while a pellet sintered at 600 °C dissolves completely.

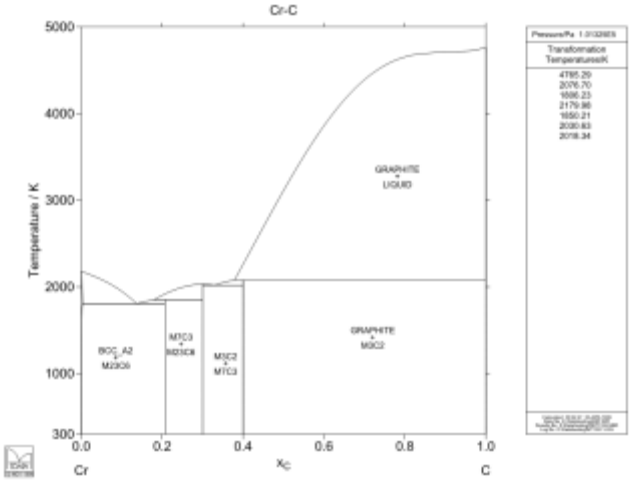

Figure 2.5: Phase diagram Cr-C

2.1.2.6 Porosity of target

2.1.2.6.1 Open and closed porosity

To validate these explanations, more investigations are made. First, the average density of 800 mg Cr pellet was determined at different conditions of sintering (by weighing pellets and measurement of thickness and diameter) (Table 2.5):

Temperature (°C)	**500**	**550**	**600**	**650**	**800**
Density (%)	76	80	75	77	82

Table 2.5: Evolution of Cr pellet density relative to sintering temperature

Before sintering, the density of the 800 mg pellet was 73 % of the theoretical density of Cr for the same volume. After sintering, the material was densified. In Figure 2.15. Grains appear closer or even welded (Figure 2.6).

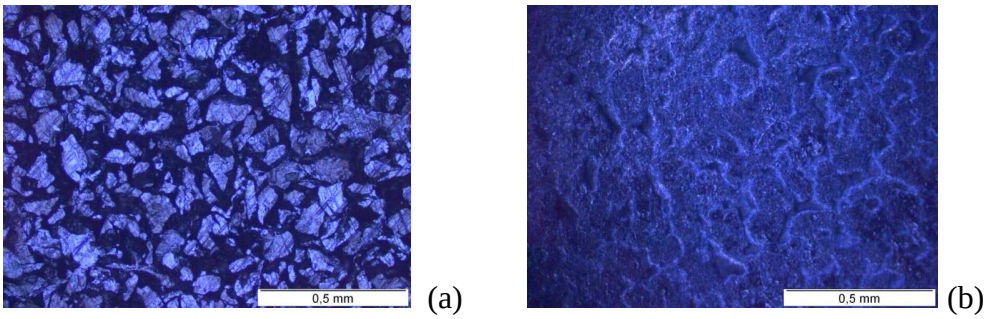

Figure 2.6: Micrography of non-sintered pellet (a) and sintered pellet at 1300 °C (b)

We define the porosity of the pellet as either: open or closed. The closed porosity corresponds to a pore that is isolated from the others and does not communicate with the outside. On the contrary, opened porosity was observed when pores communicated with the outside. The results obtained are summarized in the following Figure 2.7.

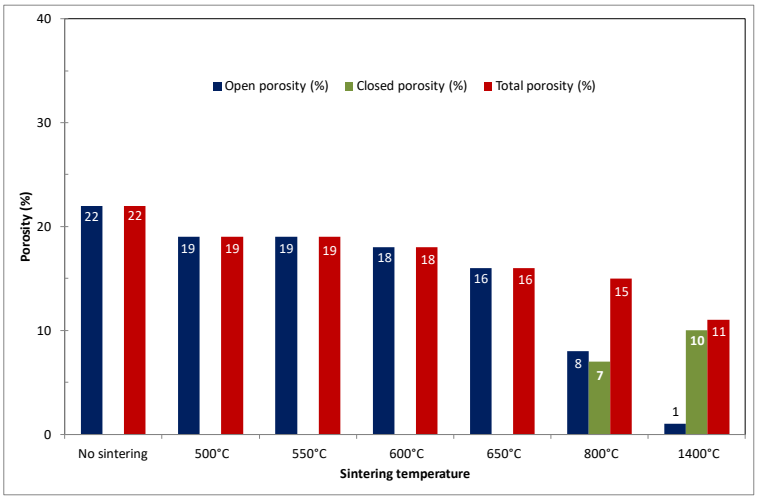

Figure 2.7: Evolution of the Cr pellet porosity with the sintering temperature

2.1.2.6.2 Porosity versus sintering temperature

These results show that the non-sintered chromium pellet is very porous: the higher the sintering temperature is, the lower the porosity is. Therefore, when the porosity is very low, the attack of the acid for dissolution becomes difficult because the acid cannot penetrate the pellet core to attack grain boundaries and grains. This may also explain why a pellet sintered at 600 °C dissolved easily while sintering at 800 °C did not completely dissolve. To try to understand the ability to dissolve as a function of the sintering temperature, the microstructure evolution is followed as a function of temperature. For this, observations in optical microscopy and scanning electron microscopy (SEM) were performed. Some micrographs are presented in the following Figures 2.8 and 2.9

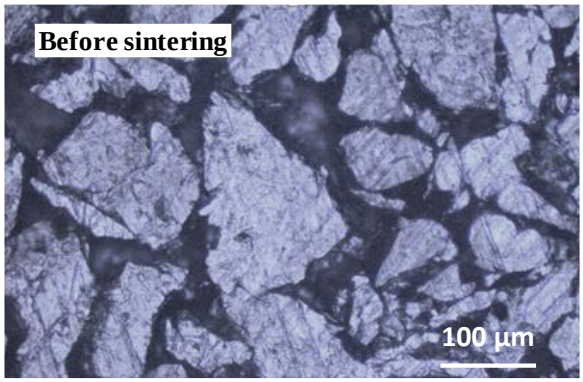

Figure 2.8: Micrography of 800 mg Cr pellet before sintering (optical microscope)

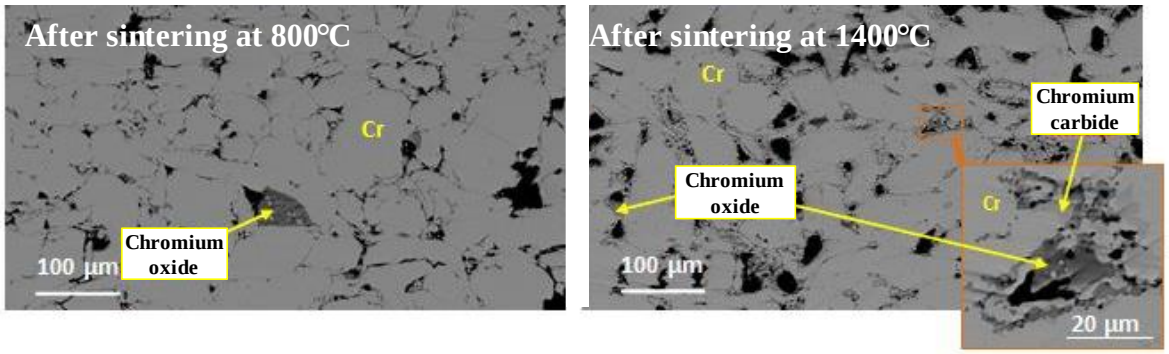

Figure 2.9: Micrography of 800 mg Cr pellet after sintering and polished (SEM) at 800 °C and 1400 °C

The heat treatment of the Cr pellet in an N_2/H_2 atmosphere and a crucible containing graphite powder induces the formation of small areas of chromium oxide (because of residual oxygen adsorbed in the porosity) and the formation of a chromium carbide, when the temperature is higher, for example 1400 °C: chromium carbide is formed from the pellet chromium and the carbon powder. During the dissolution step, these two compounds will not facilitate the attack of the pellet with hydrochloric acid.
(Just an aside: these pellets are essentially "frits", with a porosity that could be quantified by their impedance to gas flow. Imagine a fixture to measure the pressure difference across the pellet as a function of the gas (eg He) flowing through it.)

2.1.2.7 Polishing

2.1.2.7.1 Interest

After all these tests, a first target was designed: a Cr pellet of 800 mg compressed at 8.3 tons (300 bars) for 30 min. and sintered at 800 °C. This Cr pellet has a thickness of around 900µm. According to SRIM 2008, a 14 MeV beam proton was completely stopped in a 420 µm thickness of Cr target (with an angle of 60°). At an energy of 5.5 MeV (390 µm effective thickness), ^{52}Mn production is stopped, and half of the Cr thickness of the pellet is not irradiated (no ^{52}Mn). The thickness of the Cr pellet should be reduced by polishing it. Four advantages would benefit from polishing:

- reduction of the thickness,
- reduction of no-irradiated Cr mass (mass of metal traces impurities)
- increasing efficiency of cooling target: the flat surface of the Cr pellet improves contact between the Cr pellet and Al support of irradiation compared to a rough surface. Moreover, the reduction of the thickness of the Cr pellet improves the thermal transfer of cooling water

- removal of the oxide layer on the surface of the Cr pellet.

2.1.2.7.2 Method

Figure 2.10: Polishing instrument (ESC 200 GTL (ESCIL company)

The polishing protocol starts with low polishing grits and utilized a ESC 200 GTL (ESCIL company) polishing instrument. (Figure 2.10). With this technique, an optimized protocol was created:

- 30 minutes with a 120 grit belt at 100 rpm
- 8 - 10 minutes with a new belt from 120 grit at 100 rpm
- 5 minutes with a 320 grit belt at 100 rpm
- 10 minutes with a 600 grit belt at 100 rpm
- 20 minutes with a 1200 grit belt at 100 rpm

Finally, the 900 µm thickness of 650 mg Cr pellet (13 mm diameter) sintered at 800 °C was reduced to 300 – 400 µm with this protocol in 1 – 2 h. It remains to be determined whether polishing has completely removed the oxide layer formed during sintering. For this purpose, an X-ray diffraction study was carried out.

2.1.2.7.3 Surface analysis

It was determined visually (color change) that after sintering, the sample had oxidized. Polishing removed a large outer layer of the pellet and thus the surface oxidation. However, it is impossible to know whether or not the sample has oxidized in depth during sintering. X-ray diffraction (XRD) analysis can answer this question. XRD analysis was performed on pellet sintered at 800 °C without (Figure 2.11a) and with polishing 2.11b). These results highlight the presence of chromium metal in the majority phase and the presence of traces of eskolaïte Cr_2O_3.

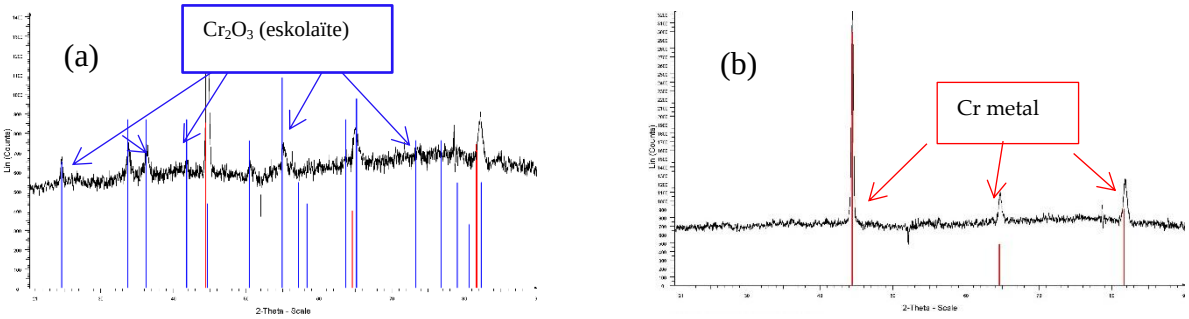

Figure 2.11: XRD diffractograms of Cr pellet sintered at 800 °C (a) no polished (b) polished

(a), these three peaks are present, other peaks correspond to chromium oxide (eskolaite Cr_2O_3). (b) shows three peaks corresponding to metallic chromium.

This analysis shows that polishing removes all the oxide formed during sintering. A controlled atmosphere during sintering step is not necessary due to polishing stage, which is mandatory to reduce the thickness of the target.

2.2 Radiochemical Separation

For using ^{52}Mn in radiolabeling studies it is crucial to obtain a high purity radiomanganese. For that, it will be essential to minimize the quantity of Cr due to its toxicity, particularly in hexavalent form. For the extraction of ^{52}Mn from a Cr target, some radiochemical separation methods have been published: Topping and his collaborators used anion exchange chromatography in 2013, achieving poor separation, and a large quantity of acid used[68]. Lahiri in 2006 used solvent extraction with trioctylamine solvent but this method is time-consuming and leads to poor chemical yield[82]. A good method will be a « trap-and-release » chromatography where Mn will be fixed on resin and Cr has no retention. A small volume (< 1 mL) to elute ^{52}Mn will be adapted. Stephen Graves[40] and his colleagues developed a semi-aqueous anion exchange method with good separation factor $SF_{(Cr/Mn)}$ = 601 ± 31 after one column and a cumulative $SF_{(Cr/Mn)}$ (after three columns) of (2.0 ± 0.3) x 10^6.

2.2.1 Coefficient of distribution (Dw) of resin AG1-X8

To confirm these conditions, coefficients of distribution (Dw) of this anion exchange have been determined using the radiotracer method.

2.2.1.1 Radiotracer Method

This method is based on following the element in a chemical process using one of its radioactive isotopes. It was developed by the Hungarian radiochemist Georges Hevesy. In 1923 when he published the first study on the use of the naturally radioactive ^{212}Pb as a radioactive tracer to follow the absorption and translocation in the roots, stems, and leaves of Vicia faba[83]. He won the 1943 Nobel Prize for Chemistry[84] for the radiotracer method. He later invented the neutron activation analysis technique in 1936[85]. The radiotracer method has been used to define the distribution coefficient (Dw) on AG1-X8 resin with ^{51}Cr for Cr and ^{52}Mn for Mn.

2.2.1.2 Protocol

Different concentrations of HCl (1, 4, 8, and 12 M) were done by dilution of 12 M HCl (SCP Sciences) and various percentages of ethanol (0 and then 93 to 98% by step of 1%) (Fisher Chemical) in eluted solution (Ethanol/HCl) were tested. A solution of ^{51}Cr and ^{52}Mn was prepared according to the following protocol (Figure 2.12): a Cr pellet (Alfa Aesar, 99.9%) (∅ 13 mm, thickness ≈ 800 µm, 800 mg compressed at 8.3 tons (300 bars), sintered at 800 °C) was irradiated by 0.2 µA, 23 MeV proton beam for 30 min to obtain significant activity of ^{51}Cr. In these experimental conditions, nuclear reactions ^{nat}Cr(p,n)^{52}Mn and ^{nat}Cr(p,x)^{51}Cr occur. Then after 4 h to permit the decay of ^{52m}Mn, the target is dissolved in 5 mL of 12 M HCl and then evaporated to dryness. At this point, ^{52}Mn is in the [^{52}Mn]$MnCl_2$ form. ^{52}Mn/^{51}Cr were dissolved in 2 mL of 2 M HCl: this is the ^{51}Cr/^{52}Mn stock solution with [^{51}Cr] = 1.3 MBq/mL

and [^{52}Mn] = 1.45 MBq/mL. 75 mg of AG1-X8 resin is weighed for each test (all tests were triplicated see Figure 2.12). AG1-X8 resin is mixed with 970 µL of elution solution in every tube. Then 30 µL (containing ≈ 3 mg Cr) of crude solution was added. Every tube was shaken for 1 hour then allowed to rest and finally centrifugate for 10 min. 500 µL of each solution are extracted and analyzed by ɣ spectroscopy in a defined geometry: tube 2G geometry for spectrogamma analysis (addition of 1.5 mL of water in each tube). The activity of ^{51}Cr and ^{52}Mn was assessed by gamma spectrometry with an HPGe detector. For the data acquisition, the samples were placed 5 cm from the detector. The HPGe detector was calibrated with ^{133}Ba and ^{152}Eu solution on Tube 2G geometry homemade with certified standard radioactive sources (Cerca France) in energy and efficiency. For activity measurements, γ-ray spectrum analysis software package Genie 2000 (Canberra, USA) was used.

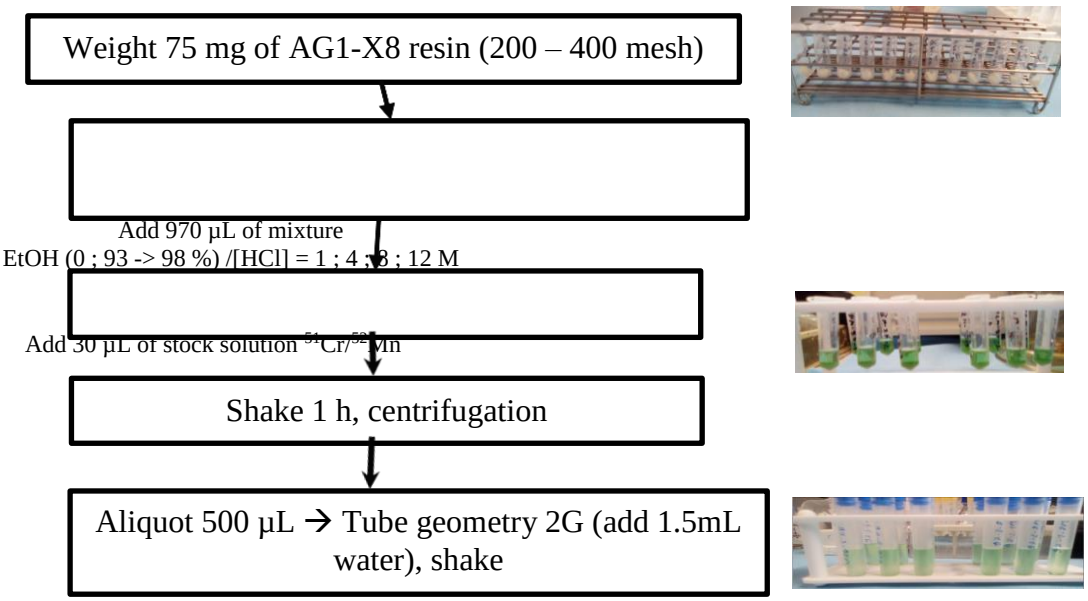

Figure 2.12: Protocol for determination of Mn and Cr

2.2.1.3 Results

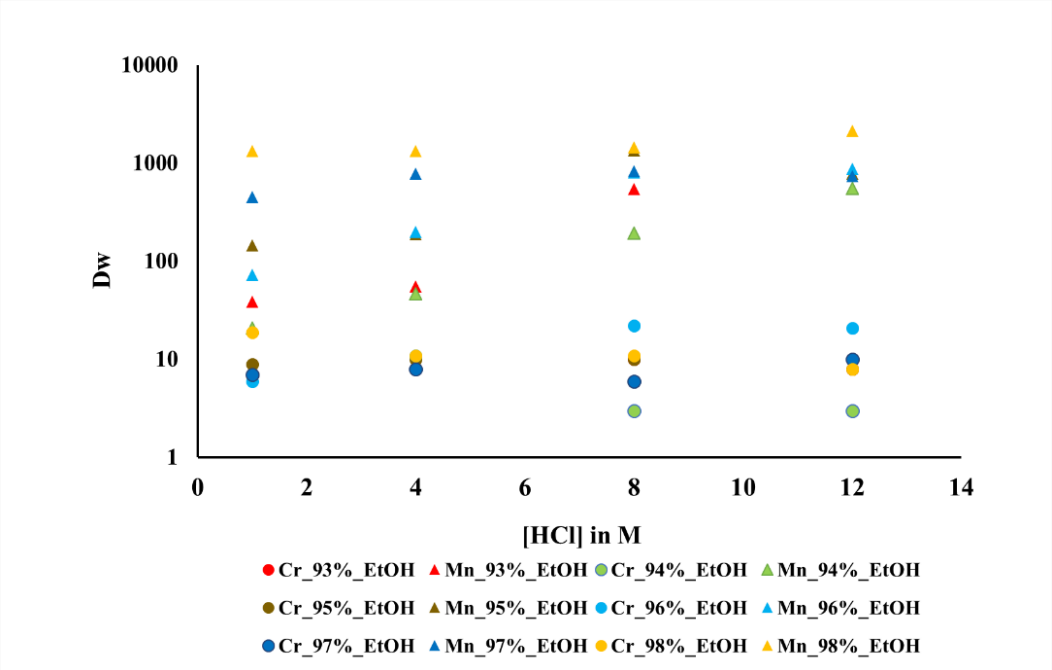

Figure 2.13: Dw of Cr and Mn for AG1-X8 with mixture Ethanol/HCl at various % (V/V)

For aqueous HCl solution at each concentration (1, 4, 8, 12 M), there was no retention for Cr and Mn (Figure 2.13). The higher concentrations of ethanol provided higher retention of Mn on the resin without a change in Cr retention. These results confirmed that Stephen Graves' method was useful and adapted to ^{52}Mn[70].

2.2.2 Separation on column

2.2.2.1 Manual Separation

A multistep column separation to isolate ^{52}Mn from irradiated Cr targets was implemented manually then semi-automated using homemade software ACCRA (Automatisme & Contrôle Commande Radiochimie)[86] and a remote controlled system. In all the cases, a Cr pellet (350 mg, 400 µm thickness, ∅ 13 mm) was irradiated for 30 min at 0.2 µA with a 14 MeV proton beam. Irradiation was done at limited current intensity and time to reduce dosimetry of ^{52}Mn for these preliminary tests. In this way, the production of ^{51}Cr was limited but sufficient to use the radiotracer method for Cr in the first step of each experiment. After a decay time of 4 h, the target was dissolved in 5 mL of HCl 32 – 35 % and put under reflux during 4 h. After cooling, 200 mL of ethanol was added to obtain a final solution of HCl 11 M / ethanol (97/3 (v/v)). This was the crude solution to load on the column. A first column of 300 mg of AG®-1-X8 was conditioned (same protocol for each AG®-1-X8 column) with 5 mL of 10 M HCl then 20 mL water and finally 5 mL mixture 11 M HCl/ethanol (97/3 (v/v)). After that, the crude solution was loaded on a column by gravity (Mn is fixed on the column whereas Cr is not retained) then the column was rinsed with 30 mL of solution of 11 M HCl/ethanol (97/3 (v/v)) to eliminate traces of Cr. Finally, ^{52}Mn was eluted with 1 mL or 2 mL of 8 M HCl solution in respectively experiments 1 (exp.1) and 2 (exp.2). After that the solution of ^{52}Mn was evaporated to 1 mL, cooled and 33 mL of ethanol were added. The solution was shaken before being loaded in a

second column of 200 mg AG®-1-X8 resin. Then the same protocol of separation was used as in column 1. Finally, the ^{52}Mn solution was evaporated to 1 mL, cooled and 33 mL of ethanol was added. The solution was shaken before loaded in a third column of 100 mg AG®-1-X8 resin. Then ^{52}Mn was eluted with 1 mL or 2 mL of 0.1 M HCl solution in respectively experiments 1 (exp.1) and 2 (exp.2). In this case, to apply this method for future production of ^{52}Mn, a lower concentration in hydrochloric acid will be help radiolabel molecules. The γ yield of extraction for Cr and Mn in each column was determined by gamma spectrometry. An aliquot of each recovered solution on each column was collected and prepared at a specific geometry tube 2G measured at 5 cm of the detector. Results of ^{52}Mn and Cr recovery yield in the final tube of each column are listed in Table 2.8. Excellent separation between ^{52}Mn and Cr was accomplished. An $SF_{(Cr/Mn)}$ > 300 000 in the first experience is obtained (assuming a 1 % Cr recovery yield for columns 2 and 3). Because of the low ^{51}Cr activity produced, its signal was under the limit of detection for gamma measurements in the samples from columns 2 and 3 (Table 2.6).

Column	**Step**	**Exp.1 Distribution (%)**		**Exp.2 Distribution (%)**	
		^{52}Mn	**^{51}Cr**	**^{52}Mn**	**^{51}Cr**
1	loading	0	85	1	85
	rinsing	0	13	0	12
	^{52}Mn elution	100	1	98	3
2	loading	0	ND	0	ND
	rinsing	0	ND	0	ND
	^{52}Mn elution	100	ND	100	ND
3	loading	0	ND	0	ND
	rinsing	0	ND	0	ND
	^{52}Mn elution	100	ND	100	ND

ND : No detected

Table 2.6: Distribution of ^{51}Cr/^{52}Mn in exp.1 and 2.

In experiment 2, the higher cumulative yield of recovery can be explained by the higher volume of 0.1 M HCl (2 instead of 1 mL) used to recover ^{52}Mn in the final fraction but these were preliminary results obtained on low activity of ^{52}Mn (5 MBq). Nevertheless, these results confirm the validation of this method to produce ^{52}Mn in a more adequate media for radiolabeling molecules (Table 2.7).

Column	**Yield of ^{52}Mn recovery (%)**		**Yield of ^{51}Cr recovery (%)**	
	Exp.1	**Exp.2**	**Exp.1**	**Exp.2**
1	69	74	1	3
2	84	84	ND	ND
3	67	97	ND	ND
Cum. Yield (%)	43	60		

Table 2.7: Results of ^{52}Mn/^{51}Cr recovery yield (%)

2.2.2.2 Semi-automated separation:

2.2.2.2.1 ACCRA system

Due to its high dosimetry, manipulation of ^{52}Mn needs to be automated in case of regular use of high activities. The CEMHTI laboratory developed a polyvalent and easy-to-customize tool for radiochemists. Easy use and versatility of ACCRA have been demonstrated in its application of ^{89}Zr production[87] or ^{165}Er developments. This system has been developed with homemade software, ACCRA to remote control all operations. The system has 22 input-output switches controlled by Siemens ET200s automaton. The radiochemist defines the functionality of each switch (valves, flow sensor, etc.) to integrate into the process. For that, he program very easily in three steps the software adapted to his radionuclide. First, he creates a sketch of the design of the separation in a paint file (1200 * 700 pixels) with an extension .bmp. The picture must use a dedicated object from the ACCRA library (Figure 2.14).

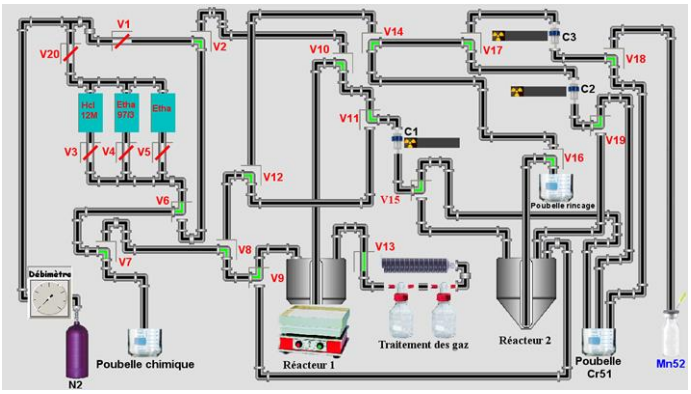

Figure 2.14: Screen control of ^{52}Mn separation in ACCRA software

Then a word file was recorded in a .txt file where the status and position (in pixels) of each element are indicated to coordinate the real command of switches with its position on sketch. For example Switch V2 (valve number 2): 3 way (valve with 3 ways), horizontal position (orientation on the sketch), and normally open position (status of the valve when the system is off). The third action of programming is writing the sequence (in a .txt file) of the process with the status of each object (in state 0 or 1) for each separation step (switch, sensor etc.). For example, step (Elution of Cr), V1: 1, V2: 0 ….V22: 1. Although radiochemical separation is a "catch and release" method in the case of ^{52}Mn production, the multicolumn process needs an intermediary dilution in ethanol. It's a good point to evaluate the flexibility of the ACCRA system and its versatility. The dissolution of the irradiated chrome target was not integrated into the automated process.

2.2.2.2.2 Tests

After writing different files to use ACCRA for ^{52}Mn purification, some adaptations of the method have been done mostly to reduce the time of process: evaporation to dryness between each column, the addition of 1 mL of 12 M HCl (dissolve ^{52}Mn) and 33 mL of ethanol to dilute ^{52}Mn in mixture 11 M HCl/ethanol (3/97 (v/v)) on dry reactor before depositing solution on next column of process.

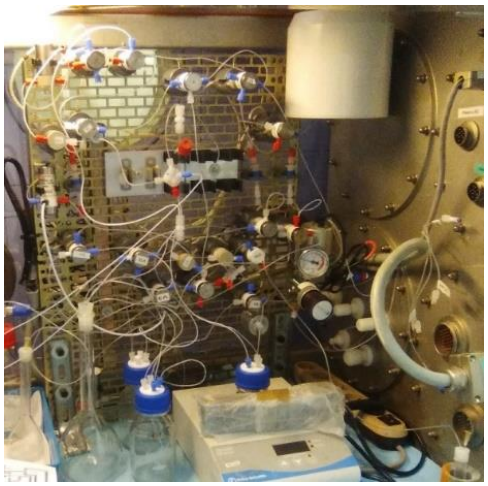

Figure 2.15: Set-up for automatization of ^{52}Mn production

Column	Step	Distribution (%)	
		^{52}Mn	^{51}Cr
1	loading	0	96
	rinsing	0	4
	^{52}Mn elution	100	0
2	loading	0	ND
	rinsing	0	ND
	^{52}Mn elution	100	ND
3	loading	0	ND
	rinsing	0	ND
	^{52}Mn elution	100	ND

Table 2.8: Distribution of ^{51}Cr/^{52}Mn in semi automated system

Column	Yield of ^{52}Mn recovery (%)	Yield of ^{51}Cr recovery (%)
1	77	ND
2	82	ND
3	84	ND
Cum. Yield (%)	53	

Table 2.9: Results of ^{52}Mn/^{51}Cr recovery yield (%)

The automated results agreed with the results obtained manually (Table 2.8 and 2.9). Adding dissolution of target and loading solution on column 1 need to be included in the automatization process. The robust separation of ^{52}Mn/^{51}Cr has been done without major troubles in the execution of the program (Figure 2.15). For the rest of ^{52}Mn production, separations were performed manually because they were quicker and more suitable for the small activity used for radiolabeling (< 20 MBq). For safety reasons, the manual operation required all components (columns, tubings, collection) to be shielded with 10 cm of lead.

2.3 ^{52}Mn radiolabeling applications

The study of bispidine-type ligands for Mn^{2+} complexation, namely Bisp1 (Fig 2.16), revealed some very interesting physicochemical properties, inertness, and good relaxivity[88]. These good results lead us to explore the radiolabeling Bisp1 with radioactive ^{52}Mn.

2.3.1 [^{52}Mn]Mn-Bisp1

2.3.1.1 MRI proprieties of MnBisp1

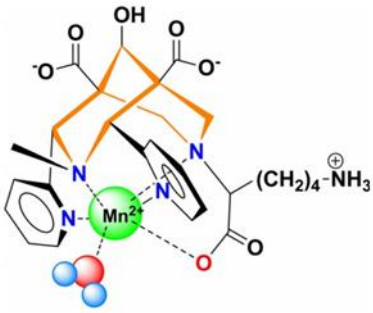

Figure 2.16: Three-dimensional representation of the Mn-Bisp1structure

Our collaborators from IPHC (Institut Pluridisciplinaire Hubert Curien, Strasbourg) and CBM (Centre de Biophysique Moléculaire, Orléans)synthesized and characterized a strongly preorganized structure of the 2,4-pyridyl disubstituted bispidol ligand Bisp1 which endows its Mn^{2+} complex with exceptional kinetic inertness[88]. They demonstrated that despite a relatively modest thermodynamic stability, the Mn-Bisp1 (Figure 2.16) complex has an exceptional resistance to dissociation. At 37 °C, pH 6.0, and in the presence of Zn^{2+}, MnBisp1 remained intact and did not show any relaxivity change for at least 140 days. In vivo MRI experiments performed in mice indicated quick renal clearance. To evaluate its potential in bimodal PET/MRI, [^{52}Mn]Mn-Bisp1 was synthesized and its stability on biological media has been studied.

2.3.1.2 Source of ^{52}Mn

A Cr pellet of around ~300 mg (~400 µm thickness) was irradiated for 2 h at 7 µA with a 14 MeV proton beam. Upon irradiation, the irradiated chromium pellet was dissolved in 5 mL HCl 32 – 35 %, for 4 h under reflux, followed by the addition of 200 mL of ethanol to obtain a final solution of HCL 11 M/ethanol (97/3 (v/v)). ^{52}Mn was purified from the bulk chromium by a double separation as described above (see section 2.3.1.3.1. Manual Separation) of the column with anion exchange resin AG©-1-X8, ultimately providing [^{52}Mn]Mn-Cl_2. The ^{52}Mn is recovered as [^{52}Mn]$MnCl_2$ solution at pH≈1.

2.3.1.3 Synthesis of [^{52}Mn]Mn-Bisp1

For the radiolabeling, the pH of the ^{52}Mn solution was adjusted to 7 with NaOH in the presence of ascorbic acid. Bisp1 was added at $1:10^4$ ^{52}Mn:L molar ratio and the mixture was incubated for 1 h at 70 °C. Bisp1 was radiolabeled under different conditions of pH, temperature, and ^{52}Mn/Bisp1 ratio. The radiochemical purity was followed at 5, 15, 30, and 60 min by thin-layer chromatography (TLC) (aluminum sheets covered with silica gel 60 F254, Merck) developed with5 % (w/v) ammonium acetate in a 1:1 mixture of methanol and water as mobile phase. The TLCs are exposed by impregnation on a multisensitive phosphor screen (Packard, Perkin Elmer, Meriden, USA) and imaged on a Cyclone Storage phosphor system Packard, Perkin Elmer, Shelton, USA). In this system, the free ^{52}Mn does not migrate (R_f = 0 – 0.1) while the [^{52}Mn]Mn-Bisp1 has an R_f = 0.8.

2.3.1.4 Lipophilicity of [^{52}Mn]Mn-Bisp1

Lipophilicity, most commonly referred to as the LogP, represents the ratio at the equilibrium of the concentration of a compound between two phases, an oil, and an aqueous phase[89]. Lipophilicity is a physicochemical parameter that has to be widely taken into account when developing new drugs since it has been reported to have a significant influence on various pharmacokinetic properties such as absorption, distribution, permeability, as well as routes of drug clearance. Lipophilicity[90] was assessed through the determination of the octanol/saline partition coefficients (log P values), by the ‘‘shake flask’’ method: an aqueous solution of a compound is mixed in a flask with an organic solvent (usually water-saturated n-octanol). Then, the flask is shaken to equilibrate the sample between the two phases, and the phases are then separated. Afterward, the concentration of the analyte is measured in both phases.

Briefly, 100 µL of each radiocomplex was added to a solution containing 1 mL saline (pH = 7.4) and 1 mL of n-octanol (obtained from a saturated n-octanol solution), in triplicate. The resulting solutions were vortexed and centrifuged at 3000 rpm for 10 min. Aliquots of 100 µL were removed from the n-octanol phase and the water phase. The activity was measured in gamma spectrometry. The lipophilicity was calculated as the average log ratio value of the radioactivity in the organic fraction and the aqueous fraction from the three samples. Optimized reaction conditions were obtained for pH = 7, 70 °C, 1 h, achieving 99% radiolabeling yield. [^{52}Mn]Mn-Bisp1 is highly hydrophilic with a logP = -1.96 ± 0.06.

2.3.1.5 Stability of [^{52}Mn]Mn-Bisp1

The in vitro stability of the radiocomplex [^{52}Mn]Mn-Bisp1 (pH = 7) was studied in the presence of different media: water, saline (0.9 % NaCl), phosphate-buffered saline (PBS, Dubelcco, pH 7.4, without Ca and Mg) and 0.6 mM human serum albumin (HSA). For this, 20 µL aliquots of the complex were mixed with 200 µL of the medium, the tubes were kept at room temperature, and the complex stability was followed by radioTLC (0.3 µL aliquots). The studies were performed in duplicate. All reactions were performed in the presence of ascorbic acid to prevent any oxidation reaction. This complex is stable in all media up to 18 h, and a slightly lower to moderate stability at 24 h (Figure 2.17).

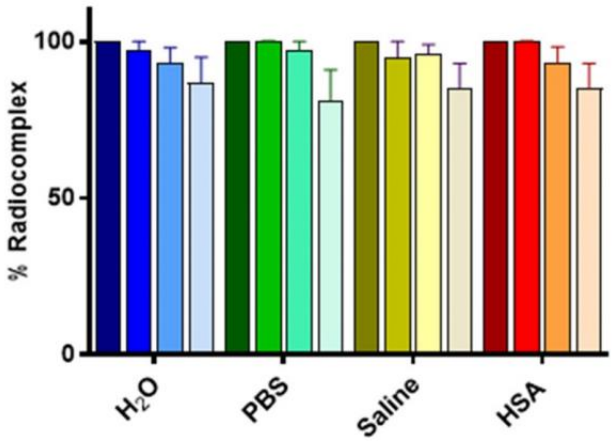

Figure 2.17: In vitro stability of [^{52}Mn]MnBisp1 in different media at pH = 7.4 (water, PBS, and saline (0.9 % NaCl)) and in the presence of 0.6 mm HSA, at different time points: 0, 1, 18, and 24 h (darker to lighter color, respectively).

Finally, Bisp1 was successfully radiolabelled with ^{52}Mn and the radiocomplex showed good stability for at least 24 hours in various biologically relevant media. Taken together, these

features and in particular the excellent kinetic inertness of the complexes make bispidine ligands highly interesting for Mn^{2+} chelation and confirm the great potential of Mn^{2+}-bispidines for the development of MRI and PET imaging agents[91].

2.3.2 [^{52}Mn]Mn-Bisp1-RGD

2.3.2.1 Synthesis of [^{52}Mn]Mn-Bisp1-RGD

Based on these preliminary radiolabeling experiments, a biological validation of the bifunctional bispidine Bisp1 was done. The ligand was functionalized with a cyclic RGD peptide known to target integrins overexpressed on tumor cell membranes[3]. Then it was radiolabeled with ^{52}Mn (Figure 2.18). The choice of cyclic RGD as a targeting motif allows us to target several types of integrins, including αvβ5 and αvβ6, overexpressed by this cell type[92]. However, we are aware that this targeting motif is not the most suitable for $^{52}Mn^{2+}$-based radiocomplexes (its long half-life would be more suitable for long-distribution motifs such as antibodies), but on the occasion it is what we had it at our disposal.

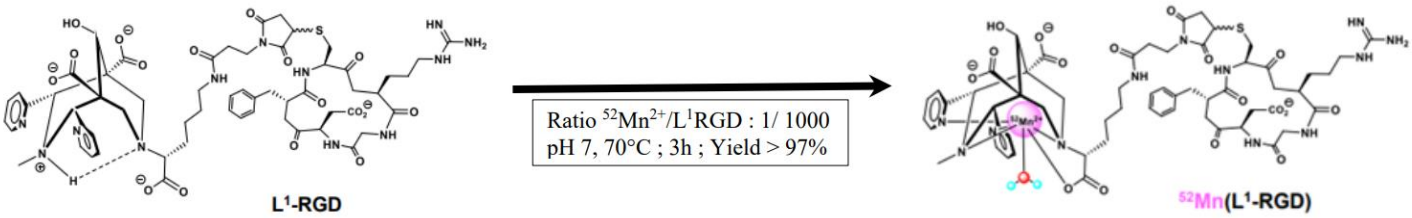

Figure 2.18: synthesis of [^{52}Mn]Mn-Bisp1-RGD

2.3.2.2 Biodistribution of [^{52}Mn]Mn-Bisp1-RGD

A biodistribution study on three mice bearing colorectal tumors was conducted at CIPA (Centre d'imagerie du petit Animal, CNRS Orléans). To achieve this, 4 h after injection of the radiocomplex [^{52}Mn]Mn-Bisp1-RGD (2 MBq/mouse), tumors and major organs were harvested, weighed and their activity measured. Figure 2.19 shows the percentage of injected dose per gram of organ. The tumor/intestine ratio is the crucial point of this study. Here, the ratio is 6:2 means that the activity is well localized in the tumor and that the vectorization is effective (Figure 2.28).

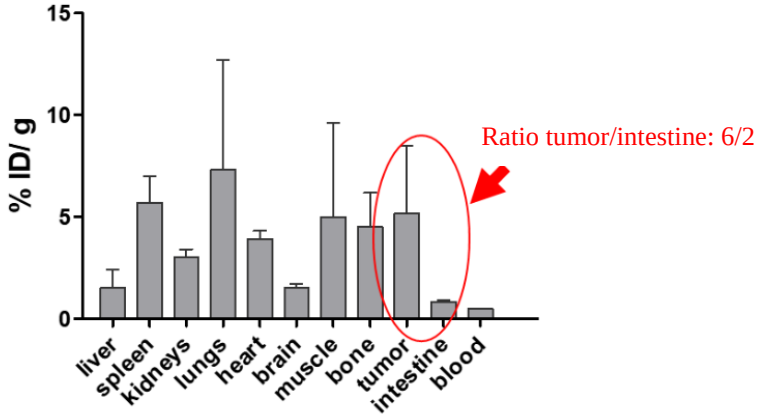

Figure 2.19: [^{52}Mn]MnBisp1RGD Biodistribution

A rapid clearance was accompanied by predominantly renal excretion of the radiocomplex, suggesting low uptake in the liver, intestines, and spleen. The biodistribution profile shows no particular accumulation in blood, heart, and liver, typical binding organs for $^{52}Mn^{2+}$ [93]. Promising tumor binding was obtained.

2.3.3 [^{52}Mn]Mn-Bisp2

2.3.3.1 Ligand H_4Bisp2

Due to its very interesting physico-chemical proprieties, my collaborators expanded their research to other bispidines which differ in the nature and position of the functional groups carried by the N7 positions of the piperidine rings. Depending on the nature of this functional group, the bispidines synthetized fall into three families could be classified into three groups derived: "lysine" (Bisp1), "phosphonate" (Bisp2), and "glycine" (Bisp3). To investigate the influence of substituents at the N7 position of the bispidine skeleton on the thermodynamic stability and the kinetic inertness of the corresponding Mn^{2+} complexes, Bisp2 (Figure 2.20) and Bisp3 were synthesized (Figure 2.21).

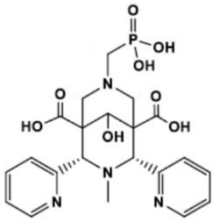

Figure 2.20: Bispidine Bisp2

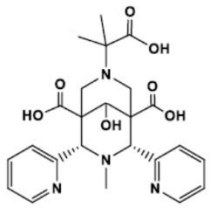

Figure 2.21: Bispidine Bisp3

This functionalization is expected to strongly influence ligand basicity, the formation and dissociation kinetics of the Mn^{2+} complex, and on parameters impacting the relaxivity group[91]. Ligand H_4Bisp2 was obtained according to the procedure described previously[94]. To complete its study for potential bimodal PET/MRI probe, radiolabeling of H_4Bisp2 with ^{52}Mn has been realized, log P (lipophilicity) was determined, and the stability of [^{52}Mn]Mn-Bisp2 was investigated.

2.3.3.2 Synthesis of [^{52}Mn]Mn-Bisp2

For the radiolabeling ^{52}Mn was prepared according to the conditions described in section 2.4.1.3. with Bisp2 added at a $1:10^4$ 52Mn:Bisp2 molar ratio and the mixture was incubated for 15 min. at room temperature achieving > 99 % labeling yield. Lowering the ^{52}Mn:Bisp2 ratio by 10-fold increased the labeling reaction time from 15 to 20 min which was fully achieved at 70 °C. The radiolabeling is faster than that observed for the bispidine analogue Bisp1 for a similar ratio ($1:10^4$), the radiolabeling of Bisp1 required the use of higher temperature and longer reaction times (1 h, 70 °C)[95]. The free ^{52}Mn does not migrate (R_f = 0 – 0.1) while the [^{52}Mn]Mn-Bisp2 complex has an R_f of 0.7.

2.3.3.3 Lipophilicity of [^{52}Mn]Mn-Bisp2

[^{52}Mn]Mn-Bisp2 is highly hydrophilic with a log*P* = -2.80 ± 0.05. As expected, [^{52}Mn]Mn-Bisp2 is more hydrophilic than the previously studied [^{52}Mn]Mn-Bisp1.

2.3.3.4 In vitro stability of [^{52}Mn]Mn-Bisp2

The *in vitro* stability of the radiocomplex was assessed in different media at pH = 7.4 (water, PBS, and saline (0.9 % NaCl)) and in the presence of 0.6 mM HSA (Figure 2.22), revealing its stability in all media up to 24 h. Bisp2 was successfully radiolabelled with ^{52}Mn and its radiocomplex has shown very good stability for at least 24h in various biologically relevant media.

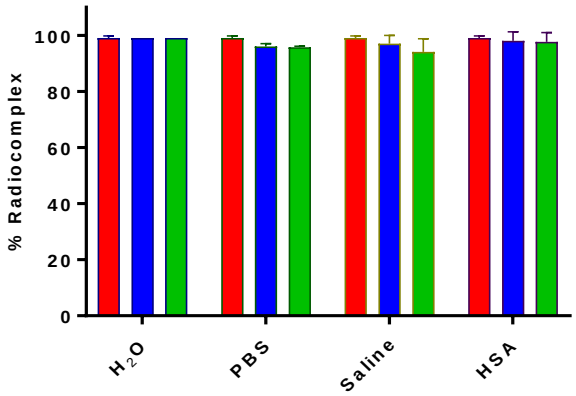

Figure 2.22: *In vitro* stability of [^{52}Mn)]Mn-Bisp2 in different media at pH 7.4 (water, PBS, and saline (0.9% NaCl)) and in the presence of 0.6 mM HSA, at different time points: t_0 (red bars), 2 h (blue bars) and 24 h (green bars).

2.3.4 Stability of [^{52}Mn]Mn-Bisp3

In parallel stability of complexes of [^{52}Mn]Mn-Bisp3 was compared with the one of [^{52}Mn]Mn-DOTA and [^{52}Mn]Mn-CDTA.

2.3.4.1 Choice of DOTA and CDTA

In vitro, the stability of [^{52}Mn]Mn-Bisp3 has been evaluated and the results of its stability were compared to two other ^{52}Mn complexes :

- [^{52}Mn]Mn-DOTA: it was recognized already in the early nineties that the tetraazacyclododecane-1,4,7,10-tetraacetic acid (DOTA) ligand is a robust chelator that forms stable and inert complexes that remain extremely chemically stable under neutral pH and room temperature conditions without chemical dissociation with a large variety of metal ions[96].
- [^{52}Mn]MnCDTA : CDTA(trans-1,2-Diaminocyclohexane-N,N,N',N'-tetraacetic acid hydrate form) forms fast and kinetically complexes with the Mn^{2+} ion. CDTA displayed the best features for the in vivo applications in the past[97].

2.3.4.2 Quality of ^{52}Mn : AMA

Three targets have been done to realize this study. AMA (apparent molar activity) was determined in each batch to compare its purity. But what is AMA ?

2.3.4.2.1 Definition: Apparent Molar Activity

According to the System International Convention, the term ‘specific’ refers to a physical property as a function of the mass of the material in question. In chemistry, the amount of material (mass) is denoted in moles. Thus, the following terms are to be used correctly:

- Specific activity: the measured activity per gram of compound in Bq/g or GBq/mg symbol: A_s.
- Molar activity: the measured radioactivity per mole of the compound in Bq/mol or GBq/µmol; symbol: A_m.

Due to the radioactive decay, the measurement time needs to be associated to the determination of these terms (End of Bombardment, (EoB), End of Synthesis (EoS))[98].

The highest possible molar activity, A_m, of a radionuclide is its carrier-free Am (CFMA: Carrier-free molar activity). When stable isotopes of an element are present along with the radioactive isotope, the stable isotopes are called carriers. In this case, A_m is reduced to the amount of stable isotope in the sample.

CFMA could be calculated using the following mathematical relationships[99] :

- Decay constant (λ) can be calculated as $\lambda = 0.693/ T_{½}$
- Knowing the activity (Bq) and λ, the number of atoms (*N)* in a radioactive sample can be determined based on the activity law, $A = \lambda N$
- One mole of any element contains 6.022×10^{23} atoms (Avogadro's number)

For ^{52}Mn, $T_{½}$ = 5.591 d. then activity (Bq) in 1 mol is equal to:
$0.693/ (5.591 \times 24 \times 60 \times 60) \times 6.022 \times 10^{23} = 864$ GBq/µmol or MBq/nmol
Because 1 Ci = 3.7×10^{10} Bq then CFMA (^{52}Mn) = 23 Ci/µmol or mCi/nmol

CFMA (^{52}Mn) = 864 MBq/nmole or 23mCi/nmole

However, the metal trace presence or precursor molecules in a radiolabeled compound preparation give a lower measured molar activity than CFMA (^{52}Mn) In such cases, the term apparent molar activity (AMA) is more appropriate to describe the ^{52}Mn quality.

2.3.4.2.2 Determination of AMA

AMA was measured for each ligand: Bisp3, DOTA, and CDTA. The apparent molar activity (AMA) of the ^{52}Mn solution was determined by titration using tetraazacyclododecane-1,4,7,10-tetraacetic acid (DOTA, Macrocyclics Inc)[100]. The chelator, DOTA, has a high affinity for a metal variety, many which are present in the final fractions of each separation, therefore chelation can serve to determine chemical purity of the final solution[101]. The AMA for radiochemical isolated ^{52}Mn was determined through titration by reaction with solutions of varying concentrations of Bisp3, DOTA and CDTA. It is expressed as the ratio of. the radioactivity of ^{52}Mn per micromole of chelator required to complex 100 % of the manganese.

To polypropylene tubes, 20 µL of ^{52}Mn in 0.1 M HCl (≈ 70 kBq), 1 M NaOAc (100 µL, pH = 4.7) 99.995 % metal traces basis, Aldrich), and ligand (100 µL, 0.03 – 3 µg/mL) in 18 MΩ·cm water were added. Following incubation at 85 °C for DOTA for 1 hour, each tube was assayed by TLC using a silica-based stationary phase (J.T. Baker) and 0.1 M citrate solution as the mobile phase. Radioactivity distribution on the TLC plates was visualized using a MiniGabi Star plate reader (Elysia Raytest, (Angleur, Belgium)). Free ^{52}Mn had an R_f of ~0.9, while the [^{52}Mn]L (Bisp3, DOTA, and CDTA) has a Rf = 0.2 - 0.4. To compute the AMA, ^{52}Mn activity in MBq was divided by twice the number of moles of DOTA, Bisp3 or CDTA required to complex 50% of the radioactivity. The value was reported as MBq of ^{52}Mn per µmol of ligand, or MBq/µmol. For L6, 10 – 30 – 50 µL of a 30 µg/ mL. Three batches of ^{52}Mn were used (3 different targets irradiated and treated according to the process described in section 2.4.1.2. Source of ^{52}Mn), one by media. For CDTA, solution of 1mg/mL was used: at pH = 4.5, 1h, and

85°C the reaction was not complete and only 9 – 17 % yield. At pH = 6.0 (0.5 M Acetate solution) this value increased to 81 – 88 % and at pH = 7 (HEPES solution) achieved 90 – 93 % of complexed CDTA. The pH was set to 5.0 with 10 M NaOH solution and after 24 h > 96 % for each sample target. These conditions will be used to obtain 100 % of [^{52}Mn]Mn-CDTA.

2.3.4.2.3 Results

Weight (mg)	Act.(1) EoB (MBq)	^{52}Mn recovery in final fraction of each column (%)					Act. (2) (MBq)	Ligand	AMA EoB (MBq/ µmole)
		C1	C2	C3	Yield ^{52}Mn (%)	V. ^{52}Mn batch (ml)			
267.5	11.56	81.4	83.2	98.4	66.6	1.1	0.2	DOTA	31.2
								Bisp3	31.9
								CDTA	< 0.3
245,0	7.67	80,0	84.9	99.3	67.4	1.1	0.1	DOTA	18.7
								Bisp3	45.4
								CDTA	1.1
291.9	13.34	82.3	85.8	99,0	69.9	1.1	0.2	DOTA	75.1
								Bisp3	> 56.9
								CDTA	< 1.4

Table 2.10: AMA (MBq/µmole (EoB)) obtained from Cr target proton irradiation

For DOTA, an AMA = 42 ± 30 MBq/µmole (n = 3) was obtained. This value seems low when compared to the literature but the ^{52}Mn activity employed is significantly lower (Table 2.11.). A discussion on the impact of ^{52}Mn radioactivity on AMA is detailed in section 3.3.2AMA. Even though the variation of AMA was significant between targets 1, 2, and 3, their low value will not impact this study only lowering by a factor 2 the radiolabeling to have 100 % radiolabeling. AMA obtained with Bisp3 results are in about the same order. For CDTA, AMA is very low compared to the other two ligands used. AMA was also affected by the type of ligand used for titration.

2.3.4.3 Stability studies

Then*in vitro* stability of [^{52}Mn]Mn-DOTA, [^{52}Mn]Mn-CDTA, and [^{52}Mn]-MnBisp3 in various media were evaluated: pH, biological media, and transmetalation conditions were studied.

2.3.4.3.1 Biological media

In each batch, 0.29 MBq (100 µL) of ^{52}Mn were buffered to pH = 5.2 and added to the ligand at a concentration of 1 mg/mL. All quantities needed for a yield of 100% of complexation were indicated in Table 2.11.

Ligand name	Volume (µl)			moles	
	^{52}Mn	Buffer pH = 5.2	Ligand (L)	^{52}Mn (pmol)	(L) (mmol)
DOTA	100	125	35	88	0.3
Bisp3	100	125	15	88	0.3
CDTA	100	125*	100	190	0.3

*for 100 %, pH need to be fixed at 5.0 and one night of reaction (no intermediary measurements)

Table 2.11: Conditions of radiolabelling Bisp3, DOTA, and CDTA in case of biological media

In these conditions, for each ligand, no dissociation was observed until 168 h on biological media (Table 2.12).

		Media of dissolution				
	Time (h)	PBS	HSA 0.6 mM	Human Serum	RPMI	MEM
Bisp3	1	100	100	100	100	100
	6	100	100	100	100	100
	78	100	100	100	100	100
	172	100	100	100	100	100
	final pH	4.3	4.5	5.5	4.5	4.7
DOTA	1	100	100	100	100	100
	6	100	100	100	100	100
	78	100	100	100	100	100
	172	100	100	100	100	100
	final pH	4.3	5.0	5.2	4.7	4.7
CDTA	1	100	100	100	100	100
	72	100	100	100	100	100
	168	100	100	100	100	100
	final pH	4.9	5.5	6.4	5.5	6.1

RPMI: Roswell Park Memorial Institute
MEM: Minimum Essential Media

Table 2.12: Percent dissociation of [^{52}Mn]MnBisp3, [^{52}Mn]Mn-DOTA and [^{52}Mn]Mn-CDTA according to the biological media and time

2.3.4.3.2 pH

In each batch, 0.98 MBq (100 µL) of ^{52}Mn were buffered to pH = 5 and added to the ligand at a concentration of 1 mg/mL (Table 2.14.). Complexation results are indicated in Table 2.13.

Ligand name	Volume (µl)			moles	
	^{52}Mn	Buffer pH = 5.2	Ligand (L)	^{52}Mn (pmol)	(L) (mmol)
DOTA	200	250	70	175	4
Bisp3	200	250	30	175	4
CDTA	200	250*	200	578	4

*for 100 %, pH need to be fixed at 5.0 and one night of reaction (no intermediary measurements)

Table 2.13: Conditions of radiolabelling Bisp3, DOTA, and CDTA for pH study

	Time (h)	pH 1 - 2	2	3	4.5	5	6	8	10
	1	59	100	100	100	-	100	100	100
	4	50	-	-	-	-	-	-	-
	18	-	68	100	100	-	100	100	100
Bisp3	42	-	61	100	100	-	100	100	100
	46	-	-	100	100	-	100	100	100
	120	0	17	100	100	-	100	100	100
	216	0	0	97	100	-	100	100	100
	1	0	-	100	100	-	100	100	100
	18	0	-	100	100	-	100	100	100
DOTA	42	0	-	100	100	-	100	100	100
	46	0	-	100	100	-	100	100	100
	120	-	-	100	100	-	100	100	100
	216	-	-	100	100	-	100	100	100
	1	6	34	29	62	100	100	100	100
CDTA	72	15	53	52	83	100	100	100	100
	168	0	0	0	38	100	99	100	100

Table 2.14: % of dissociation of [^{52}Mn]MnL6, [^{52}Mn]Mn-DOTA, and [^{52}Mn]Mn-CDTA according to the pH and time

2.3.4.3.3 Transmetalation

In each batch, 0.48 MBq (200 µL) of ^{52}Mn were buffered to pH = 5 and added to the ligand at a concentration of 1mg/mL (Table 2.15). Complexation results are indicated in Table 2.16.

Ligand name	Volume (µl) ^{52}Mn	Buffer pH = 5.2	Ligand (L)	moles ^{52}Mn (pmol)	(L) (mmol)
DOTA	200	250	70	175	1
Bisp3	200	250	30	175	1
CDTA	200	250*	200	578	1

*for 100 %, pH need to be fixed at 5.0 and one night of reaction (no intermediary measurements)

Table 2.15: Conditrions of radiolabelling Bisp3, DOTA, and CDTA for transmetalation study

	Time (h)	Transmetalation conditions EDTA 5 mM	Zn 2 x nl = 3.5 mM	Zn Phys. 50 µM	Cu 2 x nl = 3.5 mM	Cu Phys. 1 µM
	1	100	100	100	100	100
Bisp3	6	100	100	100	100	100
	72	100	100	100	100	100
	1	100	100	100	100	100
DOTA	6	100	100	100	100	100
	72	27	31	93	37	100
	1	ND	0	87	0	95
CDTA	72	ND	-	72	-	75

nl: normal level
ND : Not determined

Table 2.16: % of dissociation of [^{52}Mn]MnBisp3, [^{52}Mn]Mn-DOTA and [^{52}Mn]Mn-CDTA according transmetalation conditions and time

2.4 Conclusion on the production of ^{52}Mn by proton irradiation

^{52}Mn could be produced by irradiation of a Cr target with a 14 MeV proton beam at Orleans' cyclotron for radiolabeling applications. However, the ratio of radiolabeling between ^{52}Mn to chelator was very high around 1:30000 - 60000 (^{52}Mn: chelator) calculated on three samples used for Bisp3 stability (see section 2.4.4.3. Quality of ^{52}Mn: AMA). Moreover considering that there is 1 ppm of natural Mn present as an impurity in Cr powder used for the targets, a limit ratio of 800 - 1200 could be calculated between ^{52}Mn/Mn. Stable Mn as an impurity is not the drawback for low AMA, radiochemical separation seemed efficient which is why the low ^{52}Mn activity produced is the highest parameter to correct to obtain a high AMA. Also, ^{54}Mn was present in all ^{52}Mn batches in small quantities (< 1 %). These quantities don't affect the quality of ^{52}Mn PET imaging but its half-life, $T_{½}$ = 312 days, is a drawback for regulatory authorities and developments of ^{52}Mn for clinical applications. The contamination with ^{54}Mn in the Cr-target approach results from the presence of ^{54}Cr (reaction ^{54}Cr(p,n)^{54}Mn)[71].

Moreover, the preparation of the Cr target takes time, 2 days in our process presented above[102] even with the reduction of mass from ≈ 800 mg to ≈ 300 mg multiplied by 2-3 times the target mass and associated trace metals. The Cr pressed directly on silver doesn't give a best control of the quantity of Cr dissolved (automation improve it)[70]. The use of electrodeposition is a potential solution to simplify and control more impurities sources but in any case, it won't solve the presence of ^{54}Mn if natural chromium is used. Using enriched ^{52}Cr gives some significant advantages in production yields and quality[103], due to the minor presence of ^{54}Mn contaminant but it requires the use of more expensive materials and specific technologies to recover enriched ^{52}Cr. It increases significantly the cost of production. All these considerations give us arguments to investigate the production of ^{52}Mn by alpha irradiation at high energy (45 MeV)[104].

3. Chapter 3: Production of ^{52}Mn by alpha beam irradiation

Introduction

Using an alpha beam to irradiate a vanadium foil via nuclear reaction $^{51}V(\alpha,x)^{52}Mn$ is another way to produce ^{52}Mn. This approach has major advantages: (1) the target is a commercially available vanadium foil, (2) vanadium is a practically monoisotopic target (^{51}V 99.75% and ^{50}V 0.25%), while natural chromium used in the previous method is a mixture of different isotopes (^{50}Cr 4.345 %, ^{52}Cr 83.790 %, ^{53}Cr 9.501 % and ^{54}Cr 2.365 %)[73]. This alleviates the preparation of the Cr target.

We propose to determine the cross-section of $^{nat}V(\alpha,3n)^{52}Mn$ at Orleans' cyclotron with an incident energy alpha beam of 45 MeV using two different targetries types. The irradiation of the spot-welded V target was realized. The physical yield ($MBq \cdot \mu A^{-1} \cdot h^{-1}$) was determined, and for the first time, radiochemical separation ^{52}Mn/V with IC (ionic chromatography) or EXC (extraction chromatography) column was realized. After the separation of the majority of V from ^{52}Mn by cation exchange resin, anion exchange, and extraction exchange columns were tested to reduce metal traces in the final ^{52}Mn batch. Finally, AMA and ^{52}Mn radionuclidic purity from ^{54}Mn by this alpha irradiation were determined and compared to values obtained by proton irradiation.

3.1 Cross sections

3.1.1 $^{51}V(\alpha,3n)^{52}Mn$

First, we consider the fact that vanadium possesses 2 isotopes: 50 and 51. Production of ^{52}Mn by irradiation of natural vanadium target comes from nuclear reaction $^{50}V(\alpha,2n)^{52}Mn$ and $^{51}V(\alpha,3n)^{52}Mn$. But assuming the isotopic ratio of vanadium, the nuclear reaction $^{51}V(\alpha,3n)^{52}Mn$ should dominate the $^{nat}V(\alpha,x)^{52}Mn$ yield. The cross-section of nuclear reaction $^{50}V(\alpha,2n)^{52}Mn$ and $^{51}V(\alpha,3n)^{52}Mn$ have been calculated with TENDL2021 library[105] and are plotted in Figure 3.1. TENDL is a nuclear data library which provides in ENDF format the output of the TALYS nuclear model code system for direct use in both basic physics and applications.

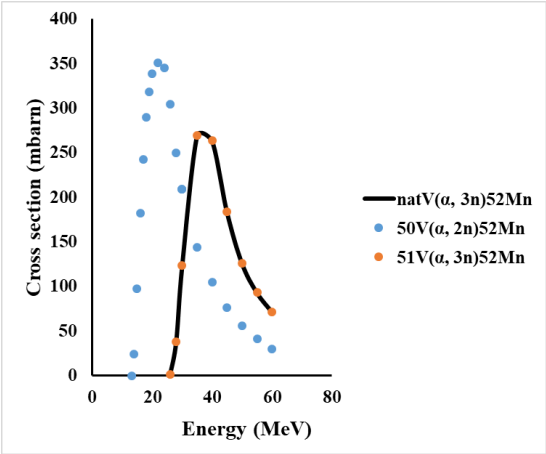

Figure 3.1: Nuclear reaction to produce ^{52}Mn considering 100 % isotopy of each V isotope

For this production, an alpha beam with a minimum energy of 35 MeV is necessary. Only a few cyclotrons in the world can accelerate alpha particles at such high energy[106]. Limited ^{51}V(α,3n)^{52}Mn cross-section data (with alpha beam energy > 40 MeV) have been published in 1969[107–110], two in the 1980's[111,112], various in 1990's[112–119] and most recently in 2022 by Gantumur and collaborators[120]. Results from Smend's experiments are not considered (no clear data is available in their article)[109]. Moreover, results are very dispersed and need to be improved[121]. These experimental results were compared with the theoretical calculations obtained from the TENDL 2021 library (Figure 3.2.).

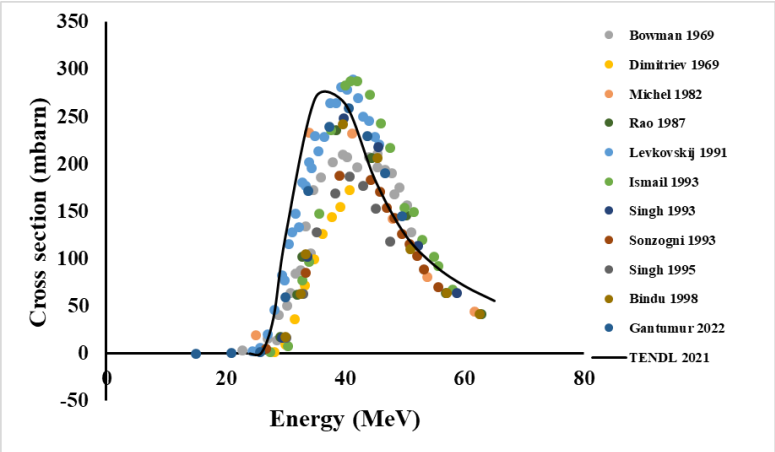

Figure 3.2: Cross section of ^{51}V(α,3n)^{52}Mn

3.1.2 ^{nat}V(α,x)^{54}Mn

^{54}Mn was produced at a lower alpha energy: high cross-section of the reaction ^{51}V(α,n)^{54}Mn (666 mbarn) at 13 MeV (TENDL2021)). Above 30 MeV, cross-section of nuclear reaction ^{51}V(α,n)^{54}Mn is weak (Figure 3.3).

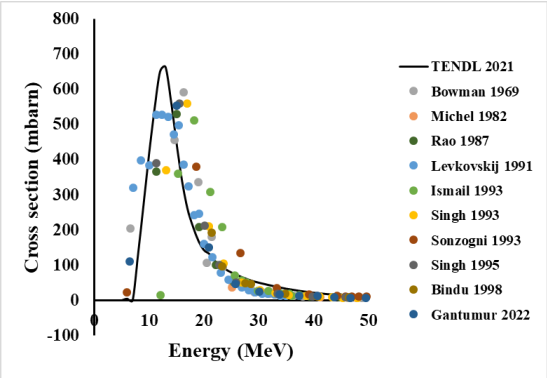

Figure 3.3: nuclear reaction $^{nat}V(\alpha,x)^{54}Mn$

3.1.3 Irradiations

3.1.3.1 Targetries

3.1.3.1.1 Hatch tip targetry

The cross-section measurements were duplicated, using the two different solid targetries available at Orleans'cyclotron. The first, called "hatch tip" (Figure 3.4), is dedicated to the low intensity (< 2 µA) current of irradiation. The target needs to be dismantled manually and has a 90° incident beam angle to the target.

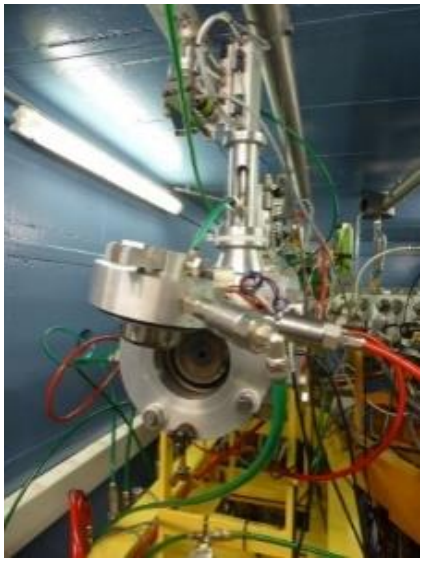

Figure 3.4**:** Targetry "hatch tip" low current (< 2 µA)

3.1.3.1.2 CiSCOTe targetry

The second is the called CiSCoTe (Cible Solide irradiée Contrôlée en Température (Solid Target irradiated under control temperature by thermocouple and pyrometer)[122]) targetry adapted for irradiation with higher current intensity with a cooling system and shuttle for remote recovery of the target (Figure 3.5 and 3.6). The beam has a 60° incident angle with the target. The foil target could be irradiated with a 10 – 15 µA intensity beam.

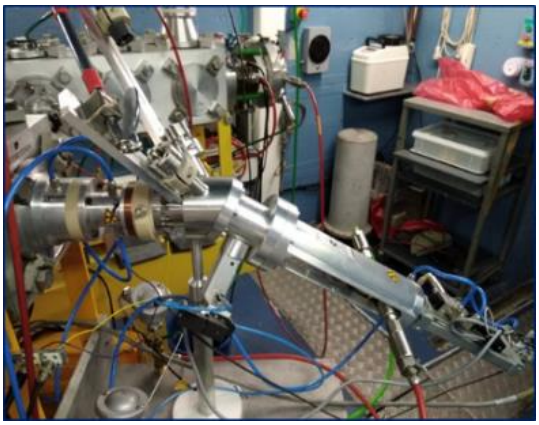

Figure 3.5: CiSCoTe Targetry on irradiation vault

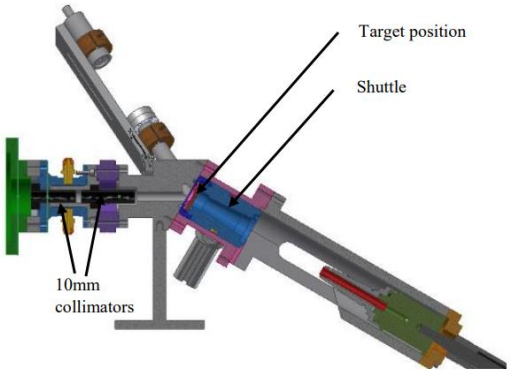

Figure 3.6: CiSCoTe targetry description

Note: in the case of a 60° incident angle, effective thickness needs to be considered for cross-section calculations. Using this targetry, the real thickness of the used target needs to be corrected by a factor of 1.16 (1/cos(30°)). In the manuscript, only real thickness will be mentioned but if necessary, these calculations will be supposed.

3.1.3.1.3 Foil materials

The foils of V (25 µm), Cu (20 µm), and Ti (25 µm) were purchased at Alfa Aesar with 99.9%. Foils were irradiated between 5 – 45 MeV by the alpha beam during 2 min at low current intensity (I = 200 - 500 nA). After irradiation, a cooling time of 3 hours was observed to allow for the decay of short half-life radionuclides particularly ^{52m}Mn ($T_{½}$ = 21.1 min) due to its high emitted radiation dose.

3.1.3.2 Stacked-foil technique

3.1.3.2.1 Alpha monitor foils

The methodology of the stacked-foil technique has been used[123]. Some monitor foils will be introduced in stacked-foil sandwiches at various points to evaluate intermediary energy and fluence of the alpha beam. Due to variations in the foil thickness and/or beam current, an examination of the radioactivity of two isotopes produced simultaneously via competing reactions (i.e. (α,2n) and (α,3n)) within a monitor foil can be beneficial[124]). For alpha beam particles, recommended IAEA monitor foil are Al, Ti, and Cu (Table 3.1)[125-126].

Reaction	product nucleus half-life $T_{1/2}$	Main γ line		α-particle energy range (MeV)
		Eγ (keV)	Iγ (%)	
$^{27}Al(\alpha,x)^{22}Na$	2.6 y	1274.5	99.94	29 - 100
$^{27}Al(\alpha,x)^{24}Na$	14.96 h	1368.6 2754.0	100 99.94	50 - 100
$^{nat}Ti(\alpha,x)^{51}Cr$	27.70 d	320.1	9.83	5 - 40
$^{nat}Cu(\alpha,x)^{66}Ga$	9.49 h	1039.3	37.9	5 - 40
$^{nat}Cu(\alpha,x)^{67}Ga$	63.26 d	93.3 184.6	37.0 20.4	15 - 50
$^{nat}Cu(\alpha,x)^{65}Zn$	244.10 d	1115.5	50.75	15 - 50

Table 3.1: Specifications of alpha beam recommended IAEA monitor foil

First Al foil is not a good choice in our experiments with an 8 – 45 MeV range energy beam. Nuclear reaction $^{27}Al(\alpha, x)^{22}Na$ and $^{27}Al(\alpha, x)^{24}Na$ have poor cross-sections respectively 30 mb and 1.4 mb at 45 MeV and no significant signal at energy below 35 MeV (Figure 3.7 and 3.8).

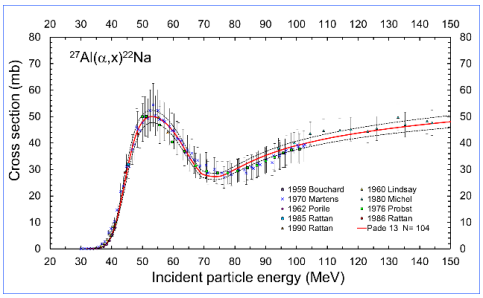

Figure 3.7: nuclear reaction $^{27}Al(\alpha, x)^{22}Na$

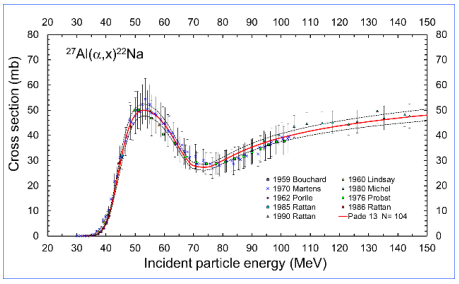

Figure 3.8: nuclear reaction $^{27}Al(\alpha, x)^{24}Na$

Then Cu foils were considered with the production of Ga isotopes 66 and 67 (Figures 3.9 and 3.10).

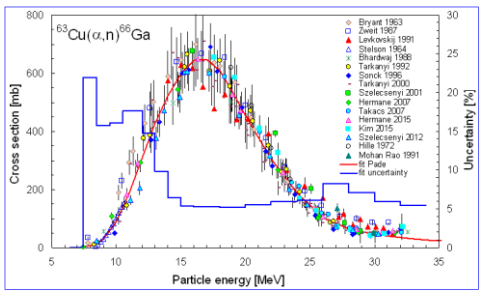

Figure 3.9: $^{63}Cu(\alpha,x)^{66}Ga$

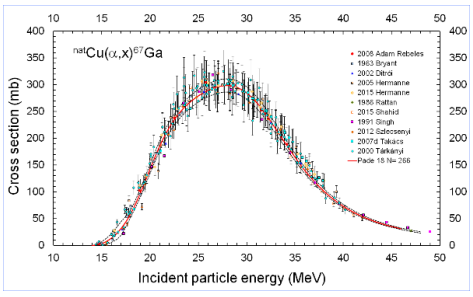

Figure 3.10: $^{nat}Cu(\alpha,x)^{67}Ga$

For a lower energy (under 20 MeV), the Ti foils are suitable than the Cu foil. They have been introduced in stacked-foil sandwiches for nuclear reaction $^{nat}Ti(\alpha,x)^{51}Cr$ (Figure 3.11) with higher cross-section.

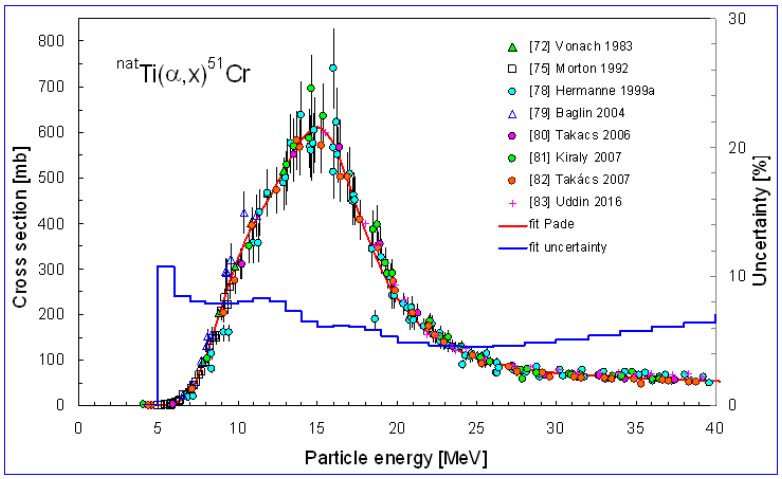

Figure 3.11: Nuclear reaction $^{nat}Ti(\alpha,x)^{51}Cr$

3.1.3.2.2 Stacked-foil sandwich

Two stacked-foil sandwiches were prepared. Using the SRIM software version 2013[127], energy in (E_{in}), out (E_{out}), and the average energy (E0) in each foil was calculated for each irradiation. The sandwich irradiated on the "hatch tip" targetry (at 90°) was composed of 16 foils: 12 V foils, monitor Cu foil in positions 6 and 10, and monitor Ti foils in position 13 and 16 (see Table 3.2). The energy estimated on foil 17 is low and was not utilized in the following analysis.

Foil		Irradiation at 90°				Irradiation at 60°			
n°	Element	Th.real (µm)	E_{in} (MeV)	E_{out} (MeV)	E0	E_{in} (MeV)	E_{out} (MeV)	E0	Th.eff.* (µm)
1	V	25	45.0	43.4	44.2	45.0	43.1	44.1	29
2	V	25	43.4	41.7	42.6	43.1	41.1	42.1	29
3	V	25	41.7	40,0	40.9	41.1	39.1	40.1	29
4	V	25	40.0	38.2	39.1	39.1	37.0	38.1	29
5	V	25	38.2	36.3	37.3	37.0	34.8	35.9	29
6	Cu	20	36.3	34.2	35.3	34.8	32.2	33.5	23
7	V	25	34.2	32.2	33.2	32.2	29.7	31.0	29
8	V	25	32.2	30.1	31.2	29.7	27.1	28.4	29
9	V	25	30.1	27.9	29.0	27.1	24.3	25.7	29
10	Cu	20	27.9	25.3	26.6	24.3	20.9	22.6	23
11	V	25	25.3	22.7	24.0	20.9	17.4	19.2	29
12	V	25	22.7	19.9	21.3	17.4	13.3	15.4	29
13	Ti	25	19.9	17.6	18.8	13.3	9.5	11.4	29
14	V	25	17.6	14.1	15.9				
15	V	25	14.1	9.9	12.0				
16	Ti	25	9.9	5.6	7.8				

Th.eff* effective thickness

Table 3.2: Composition of stacked-foil sandwiches irradiations at 90° and 60°

The sandwich irradiated on CISCoTe targetry (at 60°) was composed of 13 foils: 10 V foils, monitor Cu foil in position 6 and 10 and Ti foil in position 13, current intensity I = 200

nA and irradiation time: 2 min (see Figure 3.12. and Table 3.2). Energy estimated beyond foil 14 suggests vanishing yields.

Figure 3.12: Stacked-foil sandwich for irradiation at 60°

3.1.3.2.3 Gamma-ray spectrometry

After cooling time (3 hours), foils were assayed at first for 120 s via high-purity germanium (HPGe) gamma spectrometry. Then, they were counted repeatedly to reduce uncertainty on the net peak area. Radionuclides were identified according to their gamma ray (Table 3.3).

Radionuclide	Half-life $T_{1/2}$			Main γ ray Eγ (keV)			Iγ (%)			Eγ (keV) considered for quantification
^{52}Mn	5.591	±	0.003	744.233	±	0.013	90	±	1.2	x
				935.544	±	0.012	94.5	±	1.3	
				1434.092	±	0.017	100	±	1.4	
^{54}Mn	312.20 d	±	0.2	834.848	±	0.003	99.976	±	0.001	x
^{51}Cr	27.704 d	±	0.003	320.0824	±	0.0004	9.91	±	0.01	x
^{66}Ga	9.49 h	±	0.03	1039.22	±	0.003	37	±	2	x
^{67}Ga	3.2617 d	±	0.0005	93.31	±	38.81	38.81	±	0.03	x
				184.576	±	21.41	21.41	±	0.01	
^{65}Zn	243.93 d	±	0.09	1115.539	±	0.002	50.04	±	0.1	

Table 3.3: Identification of radionuclide by γ spectrometry

Radionuclides were quantified by gamma-ray spectroscopy from an HPGe detector (model: GC1319. Cryostat 7500SL, Preamp 2002 CSL, serial number b 93081; relative efficiency: 13 %). It was connected to a digital spectrum analyzer (DSA; model: DSA-1000 operated by the Gamma Acquisition & Analysis module of the Genie 2000 spectroscopy software package (v3.3)). The detector resolution was 2.34 keV full width at half maximum (FWHM) at the 1434.1 keV peak of ^{52}Mn and 0.8 keV (FWHM) at the 93.3 keV peak of ^{67}Ga. The detector was calibrated with calibrated ^{133}Ba and ^{152}Eu (about 4000 kBq) point source at 5 cm from the end-cap Ge sensor to avoid coincidence losses and assure low dead time. A dual efficiency curve was obtained: a low energy range from 35 keV to 356 keV with essentially ^{133}Ba peaks and a high energy range from 356 to 1402 keV (Figure 3.13).

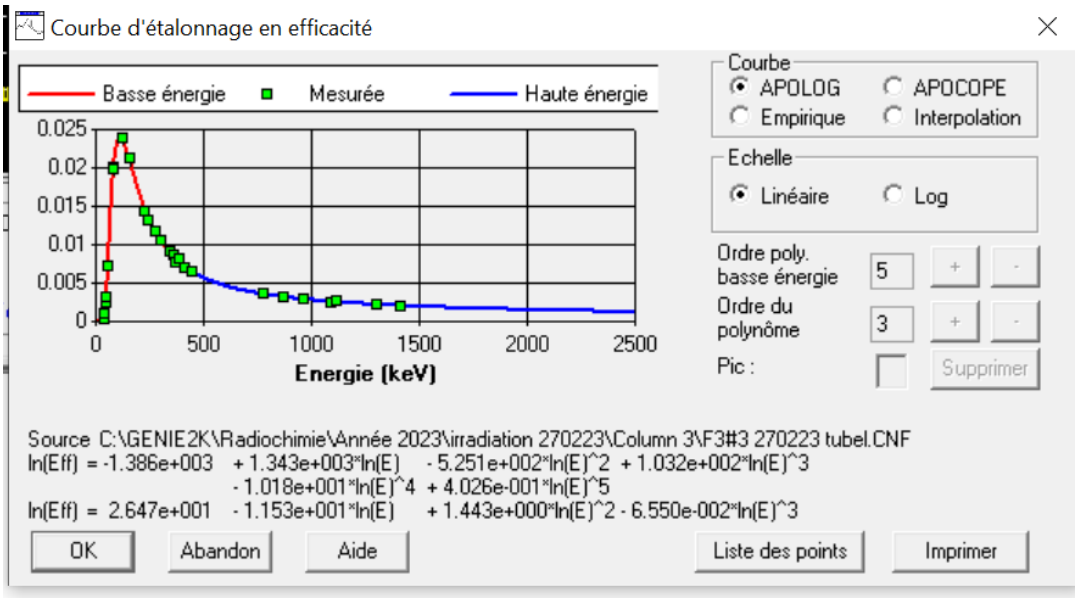

Figure 3.13: Example of dual efficiency curve calibration

3.1.4 Determination of key parameters in irradiations

3.1.4.1 Activity

The signature gamma rays were used to calculate the activity of radionuclide at the end of bombardment (EoB) using equation (4):

$$A_c = \frac{Nc}{\epsilon c * Iy * Cd * tt} \quad (4)$$

Where A_c is activity at the beginning of the measurement (Bq), N_c is the net peak area in each peak of interest (cps), I_y branching ratio of the gamma-ray, ε_c is the detector efficiency, t_t is the live time measurement (s) and C_d is the correction factor for the decay during counting.
The C_d was calculated using equation (5):

$$C_d = \frac{1 - e^{-\lambda i * tr}}{\lambda i * tr} \quad (5)$$

Where λ is the decay constant ($\lambda = \ln(2)/T_{½}$) of the considered radionuclide and t_r is the real measurement time (s).

3.1.4.2 Energy

The average value of energy alpha beam on Cu foil in position 6 and 10 was calculated using equation (6)[128] :

$$\frac{A_{66Ga}}{A_{67Ga}} = \frac{\sigma_{66Ga} * (1 - e^{-\lambda_{66Ga} * tb})}{\sigma_{67Ga} * (1 - e^{-\lambda_{67Ga} * tb})} \quad (6)$$

Where A_{66Ga} and A_{67Ga} are measured activity at end of bombardment (EoB), σ_{66Ga} and σ_{67Ga}, value of cross-section from IAEA for each reaction, λ_{66Ga} = 2.029E-05 s^{-1} and λ_{67Ga} = 2.46E-06 s^{-1} (decay constant) and t_b = 200 s, irradiation time for our experiments. After simplification, we can reduce the equation (6) to the following formulation in the case of our experiments:

(7) $$\frac{\sigma 66Ga}{\sigma 67Ga} = 0.12136 * \frac{A66Ga}{A67Ga}$$

The ratio of cross-section $^{nat}Cu(\alpha,x)^{66}Ga$ and $^{nat}Cu(\alpha,x)^{67}Ga$ was obtained. This value is associated with energy established on recommended and tabulated IAEA values for these nuclear reactions. By linear interpolation of function E(energy)= f(ratio (σ_{66Ga} / σ_{67Ga})), average energy in foil 6 and 10 were calculated[129,130].

3.1.4.3 Intensity beam

With calculated energy on foil 6 and 10, cross-section values for $^{nat}Cu(\alpha,x)^{66}Ga$ and $^{nat}Cu(\alpha,x)^{67}Ga$ will be established by linear interpolation of σ_{66Ga} = f(Energy) and σ_{67Ga} = f(Energy) from tabulated IAEA values. For each radioisotope of Ga, the beam intensity (ϕ in particles per second) was determined according to equation (8) (here for ^{66}Ga):

(8) $$\phi = \frac{A_{66Ga}}{n\sigma_{66Ga\ *}(1 - e^{(-\lambda_{66Ga} * tb)})}$$

Where: *n* is the number of target atoms per unit area (nuclei·cm^{-2}) and calculated according to equation (9):

(9) $$N_A{*}(\frac{\rho_A}{M}) = n$$

Where N_A is the Avogadro constant: 6.022 * 10^{23} (mol^{-1}), ρ_A areal target density (g/cm^2) and M molar mass (g/mol).

3.1.4.4 Cross-section

Finally, for each V foil, cross-section σ_x (x = ^{52}Mn or ^{54}Mn) will be calculated with equation (10):

(10) $$\sigma_x = \frac{A_x}{n_x\phi * (1 - e^{-\lambda_x * t_b})}$$

Where A_x is the measured activity of foil *x* at EoB (Bq), n_x is the number of target atom per area unit for measured radionuclide at foil *x*, λ_x decay constant for measured radionuclide at foil *x* (s^{-1}) and ϕ the flux (particles per seconds).

3.1.5 Calculation of Uncertainties

3.1.5.1 Activity

Activity was measured by gamma spectrometry using a calibrated curve of efficiency for geometry measurement. Uncertainty on each activity incorporates all uncertainties related to

the measurement of activity (detector efficiency, decay constant, branching ratio of the gamma-ray, net peak area in peak of interest). It is a measured uncertainty.

3.1.5.2 Energy

3.1.5.2.1 Individual uncertainties at 90° and 60° angle

To determine an uncertainty on average energy on each foil, we consider three parameters:

1- beam angle of target
2- energy of the extracted beam
3- thickness of monitor foil (Cu, Ti, and V)

- For point 1: variation of beam angle of target was considered as negligible. With SRIM 2008, an angle of 60° has been used directly on the program with the theoretical thickness of foil.
- For point 2: without measurements of initial energy, we consider a theoretical value of beam of 45.0 ± 0.5 MeV as energy irradiating foil 1 (E in). Energy out (E out) was determined on each foil for 44.5, 45.0, and 45.5 MeV with TRIM 2008 and an average of E_{in} and E_{out} is called average energy on foil. For each calculation, 10000 ions are used to simulate the beam and evaluate the standard deviation of E_{out} (by Excel file). This variation is negligible (less than 0.4 % until foil 9) relative to the propagation of uncertainty on the initial energy beam and thickness of foils. Moreover, E_{out} obtained on each foil was used in foil (n + 1) without considering the SD (standard deviation) of E_{out} on foil n. For each foil, the uncertainty of average energy with a beam energy of 45.0 MeV is determined by the difference between Energy (beam 45.5 MeV: E455) and (beam 44.5 MeV: E445) divided by 2. (Table 3.4, and 3.5)

Foil	Eaverage (MeV)	E - ΔE445 (MeV)	E + ΔE455 (MeV)	± ΔE (MeV)	± ΔE (%)
1	44.2	43.7	44.7	0.5	1.2
2	42.6	42.0	43.1	0.5	1.3
3	40.9	40.1	41.5	0.7	1.7
4	39.1	38.3	39.7	0.7	1.8
5	37.3	36.4	38.0	0.8	2.2
6	35.3	34.2	36.1	0.9	2.6
7	33.2	32.0	34.1	1.1	3.2
8	31.2	29.7	32.2	1.2	3.9
9	29.0	27.4	30.1	1.4	4.7
10	26.6	24.8	27.9	1.6	5.8
11	24.0	21.9	25.5	1.8	7.4
12	21.3	19.0	23.0	2.0	9.4
13	18.8	16.1	20.6	2.3	12.0
14	15.9	12.7	18.0	2.7	16.7
15	12.0	7.8	14.7	3.4	28.5
16	7.8	2.5	11.3	4.4	56.8

Table 3.4: Uncertainties on the energy of extracted beam (MeV) on irradiation at 90° for each sandwich foil

Foil	Eaverage (MeV)	E - ΔE445 (MeV)	E + ΔE455 (MeV)	± ΔE (MeV)	± ΔE (%)
1	44.1	43.6	44.6	0.5	1.1
2	42.1	41.6	42.7	0.6	1.4
3	40.1	39.4	40.8	0.7	1.7
4	38.1	37.2	38.8	0.8	2.1
5	35.9	35.0	36.8	0.9	2.5
6	33.5	32.5	34.5	1.0	3.0
7	31.0	29.9	32.1	1.1	3.6
8	28.4	27.2	29.8	1.3	4.5
9	25.7	24.3	27.3	1.5	5.8
10	22.6	20.9	24.4	1.7	7.6
11	19.2	17.1	21.3	2.1	10.8
12	15.4	12.7	17.9	2.6	17.1
13	11.4	7.7	14.6	3.5	30.5

Table 3.5: Uncertainties on the energy of extracted beam (MeV) on irradiation at 60° for each sandwich foil

These results have been obtained with theoretical thickness for Cu (20µm), Ti (25µm), and V (25µm) foil.

- For point 3: The thickness for foil Ti and V was 25 µm ± 5 % (1.25 µm) and for Cu foil, 20 µm ± 5 % (1.0 µm). To evaluate uncertainty on energy due to variation of thickness, TRIM 2008 calculations have been done considering two extreme conditions of experiments on each foil (Table 3.6 and 3.7):
    - lower thickness : 19 µm for Cu, 23.7 µm Ti/V
    - higher thickness : 21 µm for Cu, 26.3 µm Ti/V

Foil	Eaverage (MeV)	E - ΔE26_3 (MeV)	E + ΔE23_7 (MeV)	± ΔE (MeV)	± ΔE (%)
1	44.2	43.6	44.2	0.3	0.7
2	42.6	41.8	42.6	0.4	0.9
3	40.9	40.0	41.0	0.5	1.3
4	39.1	38.1	39.4	0.7	1.7
5	37.3	36.1	37.6	0.8	2.0
6	35.3	34.0	35.7	0.9	2.5
7	33.2	31.7	33.8	1.0	3.1
8	31.2	29.5	31.8	1.2	3.8
9	29.0	27.1	29.8	1.4	4.7
10	26.6	24.4	27.5	1.6	5.9
11	24.0	21.5	25.1	1.8	7.6
12	21.3	18.4	22.6	2.1	10.0
13	18.8	15.3	20.3	2.5	13.2
14	15.9	11.7	17.7	3.0	19.1
15	12.0	5.8	14.5	4.4	36.3
16	7.8	-	11.1	-	-

Table 3.6: Uncertainties on the energy of extracted beam (MeV) considering the uncertainty of Cu, Ti, or V foil thickness on irradiation at 90°

Foil	Eaverage (MeV)	E - ΔE26_3 (MeV)	E + ΔE23_7 (MeV)	± ΔE (MeV)	± ΔE (%)
1	44.1	44.0	44.1	0.1	0.1
2	42.1	42.0	42.3	0.1	0.4
3	40.1	39.8	40.4	0.3	0.7
4	38.1	37.6	38.4	0.4	1.1
5	35.9	35.3	36.4	0.5	1.5
6	33.5	32.8	34.1	0.7	2.0
7	31.0	30.1	31.8	0.9	2.7
8	28.4	27.3	29.4	1.1	3.8
9	25.7	24.3	26.9	1.3	5.2
10	22.6	20.8	24.1	1.6	7.2
11	19.2	16.9	20.8	1.9	10.1
12	15.4	12.4	17.0	2.3	15.0
13	11.4	7.2	13.4	3.1	27.4

Table 3.7: Uncertainties on the energy of extracted beam considering the uncertainty of Cu, Ti or V foil thickness on irradiation at 60°

3.1.5.2.2 Global uncertainty at 90° and 60° angle

To conclude on the uncertainty of energy in each foil taking in count variation of initial energy 45.0 ± 0.5 MeV and ± 5 % of the variation of thickness in each foil, we established conservative values for uncertainty on average energy in each foil for irradiation at 90° (Table 3.8) and 60° (Table 3.9) by adding the two individual uncertainties in quadrature.

Foil	Eaverage (MeV)	± ΔE (E) (%)	± ΔE (thickness) (%)	± ΔE (%)
1	44.2	1.2	0.7	1.4
2	42.6	1.3	0.9	1.6
3	40.9	1.7	1.3	2.1
4	39.1	1.8	1.7	2.4
5	37.3	2.2	2.0	3.0
6	35.3	2.6	2.5	3.6
7	33.2	3.2	3.1	4.5
8	31.2	3.9	3.8	5.4
9	29.0	4.7	4.7	6.6
10	26.6	5.8	5.9	8.3
11	24.0	7.4	7.6	10.6
12	21.3	9.4	10.0	13.7
13	18.8	12.0	13.2	17.8
14	15.9	16.7	19.1	25.4
15	12.0	28.5	36.3	46.1
16	7.8	56.8	-	-

Table 3.8: Global uncertainty on energy beam (MeV) at 90°

Foil	Eaverage (MeV)	± ΔE (%)	± ΔE (thickness) (%)	± ΔE (%)
1	44.1	1.1	0.1	1.1
2	42.1	1.4	0.4	1.4
3	40.1	1.7	0.7	1.9
4	38.1	2.1	1.1	2.4
5	35.9	2.5	1.5	2.9
6	33.5	3.0	2.0	3.6
7	31.0	3.6	2.7	4.5
8	28.4	4.5	3.8	5.9
9	25.7	5.8	5.2	7.8
10	22.6	7.6	7.2	10.5
11	19.2	10.8	10.1	14.8
12	15.4	17.1	15.0	22.7
13	11.4	30.5	27.4	41.0

Table 3.9: Global uncertainty on energy beam (MeV) at 60°

3.1.5.3 Intensity beam

For established the uncertainty on cross-section of nuclear reaction $^{nat}V(\alpha,3n)^{52}Mn$ and $^{nat}V(\alpha,x)^{52}Mn$, we use the formulation (8) where :

- Uncertainty on the decay constant λ_x, t_b irradiation time will be negligible.
- Uncertainty on n atomic number by unit area (nuclei.cm^{-2}) (see equation (9)), only foil thickness (th.) needs to be considered in the calculation of ρ_A areal density (g/cm²).

With these hypotheses, we reduce the calculation of cross-section uncertainty to:

$$\Delta\sigma = \sigma \sqrt{\left(\frac{\Delta A}{A}\right)^2 + \left(\frac{\Delta th.}{th.}\right)^2 + \left(\frac{\Delta \Phi 0}{\Phi 0}\right)^2} \quad (8)$$

Where σ cross-section of radionuclide (barn), ΔA = uncertainty on activity (Bq), A = activity of radionuclide (Bq), $\Delta_{th.}$ = uncertainty of foil thickness (5 %), th. = thickness of foil (µm), $\Delta\Phi_0$ = uncertainty on average intensity beam (p/s) and Φ_0 = average intensity beam (p/s). To establish uncertainty on cross-section, it is necessary to have the uncertainty on the intensity of the beam (p/s).

Considering that the beam intensity is constant along the foil sandwich, the average intensity beam, Φ_0, is the average intensity beam calculated on foil 6 and 10 for radionuclides ^{66}Ga and ^{67}Ga.

$$\Delta\Phi_0 = \Phi_0 \sqrt{\left(\left(\frac{\Delta\Phi 66.6}{\Phi 66.6}\right)^2 + \left(\frac{\Delta\Phi 66.10}{\Phi 66.10}\right)^2 + \left(\frac{\Delta\Phi 67.6}{\Phi 67.6}\right)^2 + \left(\frac{\Delta\Phi 67.10}{\Phi 67.10}\right)^2\right)/4} \quad (9)$$

Where $\Delta\Phi_{66.6}$, $\Delta\Phi_{66.10}$, $\Delta\Phi_{67.6}$, $\Delta\Phi_{67.10}$ = uncertainties on intensity beam calculated with radionuclide ^{66}Ga and ^{67}Ga on foil 6 and 10. According to equation (8), uncertainty on intensity beam calculated is (for example, here ^{66}Ga on foil 6):

(10) $$\Delta\Phi_{66.6} = \Phi_{66.6}\sqrt{\left(\frac{\Delta A66.6}{A66.6}\right)^2 + \left(\frac{\Delta th.Cu}{th.Cu}\right)^2 + \left(\frac{\Delta\sigma 66.6}{\sigma 66.6}\right)^2}$$

Where $\Delta A_{66.6}$ = uncertainty of activity for ^{66}Ga on foil 6 (Bq), $A_{66.6}$ = Activity for ^{66}Ga on foil 6 (Bq), $\Delta\sigma_{66.6}$ = uncertainty of cross-section of ^{66}Ga on foil 6 (linear interpolation) (mbarn) and $\sigma_{66.6}$ = cross-section of ^{66}Ga on foil 6 (linear interpolation) (mbarn). $\sigma_{66.6}$ is calculated as explained in section 3.1.4.2. Energy. Then to determine $\Delta\sigma_{66.6,}$ it's necessary to calculate uncertainty on average energy obtained by linear interpolation of ratio of the cross-section. For that, uncertainty on cross-section ratio is applied to the obtained energy:

(11) $$\frac{\Delta\,\sigma 66.6\,/\sigma 67.6}{\sigma 66.6\,/\sigma 67.6} = \sqrt{\left(\frac{\Delta A66.6}{A66.6}\right)^2 + \left(\frac{\Delta A67.6}{A67.6}\right)^2}$$

-Δσ66.6 and + Δσ66.6 are estimated by linear interpolation, with values respectively associated to E – ΔE and E + ΔE (in %).

3.1.5.4 Ti foil monitor foil

According to the large energy uncertainty calculated (see section 3.1.5.2.2 Global uncertainty on energy at 90° and 60° angle) for foils higher than 13, they were not considered in the following results. Nevertheless, for comparison to obtained results with monitor foil 6 and 10, two methods have been used to calculate the beam intensity and average energy on Ti foil 13 (production of ^{51}Cr):

1. The beam intensity calculated for Cu foil (^{66}Ga and ^{67}Ga) is constant until position 13: cross-sections are calculated with equation (10). A linear interpolation is done using tabulated IAEA values to estimate the average energy on foil.
2. Average energy calculated with SRIM 2008 on position 13 Ti foil is considered to estimate the alpha energy. This IAEA recommented ^{51}Cr production cross-section at this energy is then used to calculate intensity beam using an analogous to equation (8). Uncertainties of cross-section will be estimated similarly to ^{66}Ga and ^{67}Ga.

3.1.5.5 ^{52}Mn and ^{54}Mn Cross section

For uncertainty of cross-section for ^{52}Mn and ^{54}Mn, equation is:

(12) $$\Delta\sigma_{Mn} = \sigma_{Mn}\sqrt{\left(\frac{\Delta AMn}{AMn}\right)^2 + \left(\frac{\Delta th.V}{th.V}\right)^2 + \left(\frac{\Delta\Phi 0}{\Phi 0}\right)^2}$$

Where $\Delta\sigma_{Mn}$ = uncertainty of cross-section for ^{52}Mn or ^{54}Mn (mbarn), σ_{Mn} = cross-section for ^{52}Mn or ^{54}Mn (mbarn), $\Delta_{th.V}$ = uncertainty of vanadium foil thickness (5 %), th. V = thickness of vanadium foil (µm), $\Delta\Phi_0$ = uncertainty on average intensity beam (p/s) and Φ_0 = average intensity beam (p/s).

3.1.6 Results and Discussion

3.1.6.1 Activity

The counting results of foils 6 and 10 in irradiation at 90° and 60° were based on 3 measurements at least (Table 3.10). Energies are values from SRIM 2008 calculations.

Foil	E av. (MeV)	66Ga A (EoB) (Bq)	66Ga ΔA (Bq)	66Ga ΔA (%)	67Ga Act EoB (Bq)	67Ga ΔA (Bq)	67Ga ΔA (%)
6 (90°)	35.3	5.18E+04	8.81E+03	17	1.04E+04	7.76E+02	7
10 (90°)	26.6	2.70E+04	4.68E+03	17	2.19E+04	1.50E+03	7
6 (60°)	33.5	1.67E+04	3.01E+03	18	6.83E+03	4.82E+02	7
10 (60°)	22.6	3.14E+04	5.23E+03	17	9.92E+03	6.89E+02	7

Table 3.10: Activities in foils 6 and 10, irradiation at 90° and 60°.

3.1.6.2 Energy and intensity beam

With a ratio of activities $A^{66}Ga/A^{67}Ga$ (R1), the ratio of cross-section (R2) was determined (Table 3.11) using equation (7).

Foil	R1	R2	R2 (E1)	R2 (E2)	E1 (MeV)	E2 (MeV)	(E0) (MeV)
6 (90°)	4.974	0.604	0.564	0.665	35.5	36.0	35.7
10 (90°)	1.230	0.149	0.149	0.168	28.0	27.5	28.0
6 (60°)	2.450	0.297	0.275	0.331	33.5	34.0	33.7
10 (60°)	3.160	0.384	0.349	0.408	25.0	24.5	24.7

Table 3.11: Determination of average energy in foil 6 and 10 for irradiation at 90° and 60°

Where R1 ratio of activity $A^{66}Ga/A^{67}Ga$, R2 = ratio of cross-section $\sigma^{66}Ga/\sigma^{67}Ga$, R2 (E1) = lower ratio obtained at Energy (E1) on recommended IAEA table, R2 (E2) = higher ratio obtained at Energy (E2) on recommended IAEA table and E_0 = Energy for R2 obtained by linear interpolation. At energy E_0, the intensity beam for each radioisotope of gallium 66 and 67 was calculated by linear interpolation (Table 3.12).

Foil	E0 (MeV)	σ 66Ga (E0)	σ 67Ga (E0)	ϕ 66Ga (p/s)	ϕ 67Ga (p/s)	ϕ0 (p/s)
6 (90°)	35.7	88.8	147.5	1.41E+12	1.41E+12	1.44E+12
10 (90°)	28.0	44.5	198.4	1.47E+12	1.47E+12	
6 (60°)	33.7	59.02	199.1	5.97E+11	5.95E+11	6.10E+11
10 (60°)	24.7	105.74	275.4	6.24E+11	6.25E+11	

Table 3.12: Intensity beam (p/s) for foils 6 and 10 on the irradiation at 90° and 60°

3.1.6.3 Uncertainties

Considering R2 for each foil, we estimate its uncertainty as below:

Foil	R2	ΔR2 (%)	R2 - ΔR2	R2 + ΔR2
6 (90°)	0.6036	18.6	0.492	0.716
10 (90°)	0.1493	18.7	0.121	0.177
6 (60°)	0.2973	19.3	0.240	0.355
10 (60°)	0.3835	18.1	0.314	0.453

Table 3.13: Uncertainty on ratio of cross-section $\sigma^{66}Ga/\sigma^{67}Ga$

Using the tabulated IAEA table of monitor Cu foil, by linear interpolation of curve ratio $\frac{A\ 66Ga}{A\ 67\ Ga}$ = f(Energy), exact energies associated with extreme (low and high) ratio R2 value were determined (Table 3.13).

Foil	E0 (MeV)	E0 - ΔE0 (MeV)	E0 + ΔE0 (MeV)	± ΔE0 (MeV)	± ΔE0 (%)
6 (90°)	35.7	35.1	36.2	0.6	1.6
10 (90°)	28.0	27.3	29.3	1.0	3.5
6 (60°)	33.7	33.1	34.2	0.5	1.6
10 (60°)	24.7	24.2	25.3	0.6	2.3

Table 3.14: Uncertainty on Energy (MeV) on foil 6 and 10

Using uncertainty on E_0 energy (Table 3.14), uncertainty Δσ of ^{66}Ga and ^{67}Ga were determined by linear interpolation (Table 3.15).

Foil	E0 (MeV)	σ 66Ga (mbar)	Δσ 66Ga (%)	σ 67Ga (mbar)	Δσ 67Ga (%)
6 (90°)	35.7	88.6	9.6	148.0	9.0
10 (90°)	28.0	47.2	21.2	295.7	4.2
6 (60°)	33.7	59.5	12.1	198.9	7.4
10 (60°)	24.7	106.8	15.3	274.7	4.4

Table 3.15: Uncertainty on the cross-section of ^{66}Ga and ^{67}Ga

Finally, uncertainty on the intensity beam was calculated according to equations (12) and (13) (Table 3.16.).

Foil	ϕ 66Ga (p/s)	Δ ϕ 66Ga (%)	ϕ 67Ga (p/s)	Δ ϕ 67Ga (%)	ϕ ave. (p/s)	Δ ϕ (%)
6 (90°)	1.41E+12	20.2	1.41E+12	12.7	1.44E+12	18.9
10 (90°)	1.47E+12	27.9	1.47E+12	9.4		
6 (60°)	5.97E+11	22.3	5.95E+11	11.4	6.10E+11	17.7
10 (60°)	6.24E+11	23.2	6.25E+11	9.6		

Table 3.16: Uncertainty on intensity beam (p/s)

3.1.6.4 Position 13: Ti foil

After evaluating the intensity beam and energy on Cu foil, the same was done on Ti foil number 13 using two methods. By Method 1, the intensity beam is constant between foil 6, 10, and 13. By Method 2, the average energy is estimated by the software SRIM 2008.

3.1.6.4.1 Comparison Method 1 and 2

Method	Foil	Energy		Intensity beam	
		E0 (MeV)	E0 (%)	ϕ0 (p/s)	Δ ϕ0 (%)
1	13 (90°)	21.0	0.9	1.44E+12	18.9
	13 (60°)	15.4	1.6	6.10E+11	17.7
2	13 (90°)	18.8	17.8	9.23E+11	48.0
	13 (60°)	11.4	41.0	8.74E+11	72.2

Table 3.17: Estimation of intensity beam and energy on foil 13 by 2 methods

By method 2, a huge uncertainty on the beam intensity was obtained due to the large uncertainty on energy (Table 3.17.). For the calculation of the cross-section of ^{52}Mn and ^{54}Mn, the following values for the intensity beam will be considered:

At 90° Φ = 1.44E+12 p/s ± 18.9 %

At 60° Φ = 6.10E+11 p/s ± 17.7 %

3.1.6.4.2 Variation of energy on foil 6, 10 and 13

Values of average energy on foil 6, 10, and 13 were compared assuming a constant intensity beam (Table 3.18).

Foil	Energy									
	Irradiation at 90°					Irradiation at 60°				
	E1 (MeV)	±ΔE1 (%)	E0 (MeV)	±ΔE0 (%)	Δ(E1-E0)/E1 (%)	E1 (MeV)	±ΔE1 (%)	E0 (MeV)	±ΔE0 (%)	Δ(E1-E0)/E1 (%)
6	35.3	3.6	35.7	1.6	- 1.3	33.5	3.6	33.7	1.6	- 0.6
10	26.6	8.3	28.0	3.5	- 5.3	22.6	10.5	24.7	2.3	- 9.3
13	18.8	17.8	20.7	5.2	- 10.4	11.4	41.0	14.5	17.7	- 27.2

Table 3.18: Energy calculated at constant intensity beam on foil 6, 10, and 13

Where E1 = Energy calculated with SRIM 2008 at 45.0 MeV and ΔE1 = uncertainty of energy E1 (see section 3.1.5.2.2 Global uncertainty on energy at 90° and 60° angle). Energies calculated with monitor foil are in good agreement with SRIM 2008 calculations (from 0.6 % to 10.4 %). Only for irradiation at 60° on foil 13, higher uncertainty was observed at 27.2 %. It is explained by the higher crossed thickness of the target increasing the straggling of the beam and oblique pathway of the beam. As a last point, the uncertainties on energy are very conservative, estimating variation, particularly for thickness. For the cross-sections of ^{52}Mn and ^{54}Mn, E1 values and their uncertainty are associated to the result.

3.1.7 Cross-section results

3.1.7.1 $^{nat}V(\alpha,3n)^{52}Mn$

Considering values of intensity beam notified in section 3.1.6.4.1 Comparison Method 1 and 2 .The cross-section of ^{52}Mn has been calculated (Table 3.19 and 3.20) and Figure 3.14.

➢ Irradiation at 90°

A (Bq)	±	ΔA (Bq)	ΔA (%)	E (MeV)	±	ΔE (MeV)	ΔE (%)	σ (mbarn)	±	Δσ (mbarn)	Δσ (%)
9978	±	443	4.4	44.2	±	0.6	1.4	223	±	45	20.1
12061	±	493	4.1	42.6	±	0.7	1.6	270	±	54	20.0
11159	±	461	4.1	40.9	±	0.9	2.1	249	±	50	20.0
12541	±	507	4.0	39.1	±	1.0	2.4	280	±	56	20.0
12094	±	489	4.0	37.3	±	1.1	3.0	270	±	54	20.0
9005	±	310	3.4	33.2	±	1.5	4.5	201	±	40	19.9
6337	±	312	4.9	31.2	±	1.7	5.4	142	±	29	20.2
3177	±	205	6.4	29.0	±	1.9	6.6	71	±	15	20.6
30	±	1	4.0	24.0	±	2.5	10.6	1	±	0	20.0
44	±	14	32.5	21.3	±	2.9	13.7	1	±	0	37.9

Table 3.19: Cross section of $^{nat}V(\alpha,3n)^{52}Mn$ at 90°

➢ Irradiation at 60°

A (Bq)	±	ΔA (Bq)	ΔA (%)	E (MeV)	±	ΔE (MeV)	ΔE (%)	σ (mbarn)	±	Δσ (mbarn)	Δσ (%)
4513	±	202	4.5	44.1	±	0.5	1.2	205	±	37	18.3
5305	±	270	5.1	42.1	±	0.5	1.3	241	±	44	18.4
5553	±	302	5.4	40.1	±	0.7	1.7	252	±	47	18.5
5614	±	273	4.9	38.1	±	0.7	1.8	255	±	47	18.4
5122	±	268	5.2	35.9	±	0.8	2.3	233	±	43	18.5
2635	±	175	6.7	31.0	±	1.1	3.5	120	±	23	18.9
1256	±	78	6.2	28.4	±	1.2	4.3	57	±	11	18.8
204	±	36	17.9	25.7	±	1.4	5.4	9	±	2	25.2
12	±	2	20.8	19.2	±	1.8	9.3	1	±	0	27.4
7	±	2	33.3	15.4	±	2.0	13.0	0	±	0	37.8

Table 3.20: Cross section of $^{nat}V(\alpha,3n)^{52}Mn$ at 60°

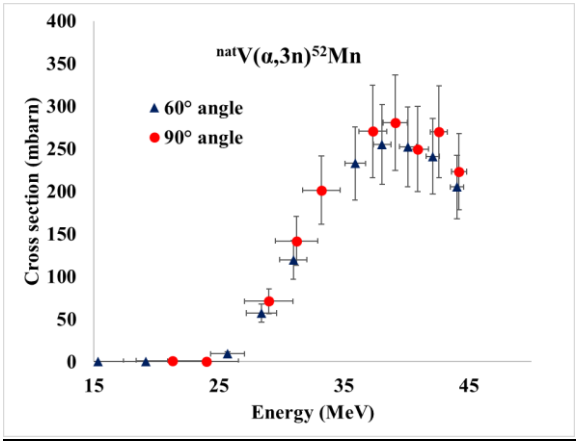

Figure 3.14: cross-sections of $^{nat}V(\alpha,3n)^{52}Mn$

3.1.7.2 $^{nat}V(\alpha,x)^{54}Mn$

All calculated activities of ^{54}Mn (EoB) are reported in Table 3.21, and 3.22.

➢ Irradiation at 90°

A (Bq)		ΔA (Bq)	ΔA (%)	E (MeV)	±	ΔE (MeV)	ΔE (%)	σ (mbarn)	±	Δσ (mbarn)	Δσ (%)
28	±	16	57.1	31.2	±	1.2	3.8	35	±	21	60.2
27	±	12	44.4	29.0	±	1.4	4.8	34	±	16	48.3
40	±	2	5.0	24.0	±	1.8	7.5	50	±	10	19.6
57	±	9	16.1	21.3	±	2.0	9.4	71	±	18	24.9

Table 3.21: $^{nat}V(\alpha,x)^{54}Mn$ at 90°

➢ Irradiation at 60°

A (Bq)		ΔA (Bq)	ΔA (%)	E (MeV)	±	ΔE (MeV)	ΔE (%)	σ (mbarn)	±	Δσ (mbarn)	Δσ (%)
7	±	4	50.7	28.4	±	1.3	4.6	19	±	10	53.7
11	±	2	19.7	25.7	±	1.5	5.8	27	±	7	26.5
44	±	5	11.4	19.2	±	2.1	10.9	112	±	24	21.1
35	±	15	42.9	15.4	±	2.6	16.9	89	±	41	46.4

Table 3.22: $^{nat}V(\alpha,x)^{54}Mn$ at 60°

3.1.7.3 Discussion

For the production of ^{52}Mn, the cross-section is in good agreement with the published cross-sections in the energy range of 30 – 45 MeV (Figure 3.15). We notice a drift of all published (higher cross-section around E = 40 MeV) compared to TENDL 2021 (around E = 35 MeV) simulation along the energy axis. Uncertainties on energy don't justify this variation for our work.

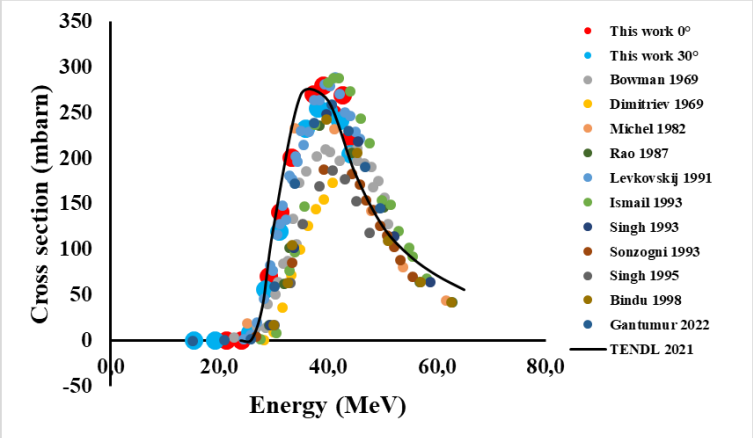

Figure 3.15.: Comparison of our work to the state of the art of $^{nat}V(\alpha,3n)^{52}Mn$

Relative to the production of ^{54}Mn, above 31.2 MeV, no ^{54}Mn was detected, in agreement with previous data published on this topic. Below this energy, the results have a very high uncertainty and the activity detected is very low to consider these results are representative of ^{54}Mn. A more precise evaluation of the quantity of ^{54}Mn will done on the ^{52}Mn batch with higher levels of radioactivity.

In conclusion, ^{52}Mn production is effective for an energy beam > 30 MeV, and no significant quantity of ^{54}Mn was detected. Target thickness will chosen to result in the desired ^{52}Mn production and ^{54}Mn impurity. After determining the best irradiation conditions for producing ^{52}Mn, its extraction from the V target will be investigated for a high AMA (Apparent Molar Activity).

3.2 Purification of ^{52}Mn from V

3.2.1 Targetry ^{nat}V/^{52}Mn

3.2.1.1 Optimization of target

The produced ^{52}Mn needs to have the highest possible AMA for radiolabeling molecules for PET imaging. An estimation of AMA[131] was done with the following equation:

(13) $$AMA = \frac{A_{EoB} * Y_{52Mn}}{\left(\frac{A_{EoB} * 10^6 \frac{Bq}{MBq} * Y_{52Mn}}{\lambda * N_{Av}}\right) + \left(\frac{m_V * F_{Mn\ imp} * Y_{52Mn}}{MW_{Mn}}\right) + \left(\sum \frac{m_{Met}}{MW_{Met}}\right)}$$

With A_{EoB} = ^{52}Mn EoB radioactivity in MBq, Y_{52Mn} = fractional radiochemical yield of ^{52}Mn, λ = ^{52}Mn decay constant in s^{-1}, N_{Av} = Avogadro's number in atoms/nmol, m_V = V target mass in ng, $F_{Mn\ imp}$ = fractional natural manganese impurity in V target, MW_{Mn} = molecular weight of manganese in ng/nmol, m_{Met} = metals (Met.) mass in V target in ng, MW_{Met} = molecular weight of metals in ^{52}Mn final solution in ng/nmol.

For metals, we consider the most relevant metals in cation form in solution with +2 degree of oxidation that could compete with Mn^{2+} during radiolabeling: Cu, Zn, Fe. V needs to be considered because of a huge mass of target compared to the ^{52}Mn mass. The overall amount of ^{52}Mn radioactivity will be limited (50 MBq) due to the license restrictions of ^{52}Mn radioactivity and radiation safety at Orleans'cyclotron. Thus improving AMA will depend on decreasing the denominator of this equation. Efficiency of radiochemical separation between Mn and V target, percent of "cold" (natural) manganese in V foil (and other relevant metals if their quantities are significant), and limited metal traces contamination in ^{52}Mn final solution are factors to study and optimize.

3.2.1.2 Irradiations

3.2.1.2.1 Efficient cooling system

Nielsen *et al*. produced ^{52}Mn at 40 MeV with the alpha beam at Birmingham's cyclotron. For that, they irradiated an in-house designed solid target with a V foil air-cooled on the front side and placed on Al support water-cooled on the back side. With a 2.5 µA alpha beam, they observed a burned discoloration of the V foil indicating insufficient cooling. At a higher current (9.1 µA) the beam burned a hole in the V foil[132].

3.2.1.2.2 Spot-welded target

Considering these results and that V has a lower heat conductivity compared to Cr, the target was redesigned to support a higher intensity of current. For that, the spot welding method developed by Ellison *et al.* (University of Wisconsin) has been applied to the V target: V foil (diameter 3 to 12.7 mm, thickness: 75 to 127 µm) was spot welded on a Ta support (diameter 14.7 mm, thickness 500 µm)[133]. Then the target was inserted in a previously described Al support adapted to CiSCoTe targetry. The spot-welding method allows the control of target size. The AMA depends in part on the V target mass irradiated as well as its impurities. Reducing this mass has no significant modification of physical yield ($MBq \cdot e\mu A^{-1} \cdot h^{-1}$) and improves AMA. For all experiments, the largest thickness used was 127 µm resulting in the 45 MeV incident alpha beam degrading to 36.3 MeV (90° incident angle) or 34.8 MeV (60° incident angle). All targets were irradiated with a 45 MeV alpha beam during 0.25 – 6.2 h at 0.5 - 5.0 µA, then after a cooling time of 4 hours, targets were dissolved in 0.7 mL of 15 M HNO_3 and then diluted to 50 mL with water. An aliquot of 2 mL was measured in a dose calibrator (Capintec CRC-15R, setting# 696/2). The ^{52}Mn activity of the V target at EoB was calculated.

3.2.1.3 Physical yield

3.2.1.3.1 Diameter target

To define the optimal diameter of the target, five targets were designed with a thickness of 127 µm (Alfa Aesar, 99.8 % purity). For this thickness (E_{out} < 35 MeV), ^{54}Mn was not detected. Each target was spot-welded and V foil centered in the middle of Ta support. For these experiments, each target was irradiated for 30 min with 0.5 eµA of 45 MeV $^{4}He^{2+}$ on a 90° incident angle (Figure 3.16).

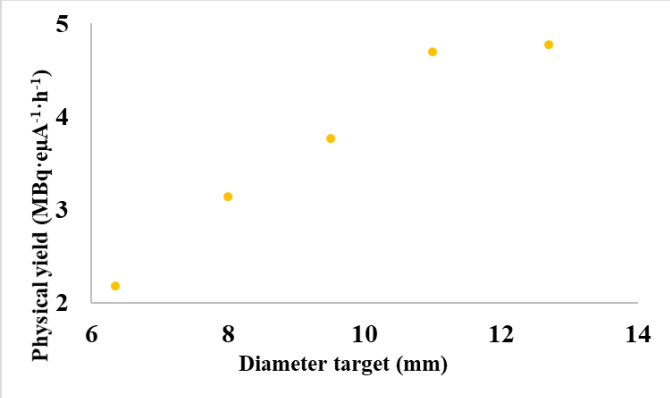

Figure 3.16: Physical yield of ^{52}Mn versus diameter of target

The 11 mm diameter target seems to be the best size for our targetry, yielding 4.7 $MBq \cdot e\mu A^{-1} \cdot h^{-1}$. These results agree with the fact that a 10 mm collimator upstream from the target limits the beam spot size and divergence (Figure 3.16). Despite its lower yield, 9.5 mm diameter targets were utilized for the majority of irradiations due to their smaller vanadium mass.

3.2.1.3.2 Activity versus mass target

Table 3.23 shows the results of all irradiations from various sizes of targets. As expected, the physical yield increased with the thickness of the target from 0.9 ± 0.1 $MBq \cdot e\mu A^{-1} \cdot h^{-1}$ (25 µm) to 4.2 ± 0.5 $MBq \cdot e\mu A^{-1} \cdot h^{-1}$ (126 µm) (on preliminary test below, 4.8 was measured). For

9.5 mm diameter, no significant differences were observed between physical yield at 75 and 96 µm whereas at 126 µm physical yield (3.6 ± 0.7 MBq·eµA^{-1}·h^{-1}) was higher than 75 µm (2.5 ± 0.1 MBq·eµA^{-1}·h^{-1}). These results show that the higher physical yields can be achieved with larger targets, but at the expense of a higher target mass. These variations will have an impact on radiochemical separation: increasing thickness from 96 to 126 µm (9.5 mm diameter) will increase of target mass by 43% and physical yield by 28%. On the other hand, increasing target diameter from 9.5 to 12.7 mm will increase target mass by 77% and increase physical yield by only 17%. As shown in equation (16), ^{52}Mn AMA may be more lower when using the 12.7 mm diameter target compared with 9.5 mm of 126 µm thickness. A choice of 126 µm V foil has been done over ≈ 100 µm because the latter foils are not commercially available. Moreover, uncertainty on µm is obtained from the analysis certificate of V foil or measured in 10 points of rolled foil (75 – 100 µm) (Table 3.23.). Some details are not considered in this evaluation as spot welding technique, which doesn't give a perfectly flat surface.

Number irradiation	thickness (µm)	diameter (mm)	weight (mg)	spot welded	Physical yield (MBq·eµA-1·h-1)
4	25	12.7	18.4 ± 0.1	no	0.9 ± 0.1
4	75	9.5	34.3 ± 0.3	yes	2.5 ± 0.1
1	125	8	37	yes	3.1
3	96 ± 3	9.5	37.7 ± 1.1	yes	2.8 ± 0.3
14	126 ± 1	9.5	53.9 ± 2.8	yes	3.6 ± 0.7
3	126 ± 1	12.7	95.4 ± 0.4	no	4.2 ± 0.5

Table 3.23: Physical yield (MBq·eµA^{-1}·h^{-1}) of ^{52}Mn obtained by irradiation of 45 MeV alpha beam on V target

3.2.2 Radiochemical separation V/^{52}Mn

As we do for the purification of ^{52}Mn from a chromium target, various steps will be used to purify as much as possible the ^{52}Mn from V target irradiation. For that, first, extraction of the bulk mass of vanadium by one or two steps was done then purity was increased by a more selective method to isolate ^{52}Mn from potential metal traces (reducing m_{Met} term in equation 16 see section 3.2.1.1. Optimization of target).

3.2.2.1 Historical separation V/^{52}Mn

Relative to radiochemical separation, no previous publications about nuclear cross-section described the purification of ^{52}Mn from target ^{nat}V. Using nuclear reaction ^{nat}V(^{3}He,x)^{52}Mn, Sastri dissolved the V target in "hot" HNO_3 and added a saturated solution of potassium iodate to the solution and the mixture was boiled. After correcting pH to 10 with sodium hydroxide solution, a liquid-liquid extraction (LLE) with 0.1 M 8-hydroxyquinoline in chloroform was done two times. The chemical yield was 50 – 60 % and the radiochemical purity was greater than 99.9 %. The ^{52}Mn was in the oxinate complex in chloroform[134]. More recently, this method has been modified to inject the product in the form of chloride [^{52}Mn]$MnCl_2$ into the rat and monkey models. The extracted chloroform-hydroquinone solution containing only ^{52}Mn was reduced to dryness. The dried organic layer was back-extracted with a mixture of 0.1 M HCl

and 10 % v/v ethanol. The pH was adjusted and the manganese-52 solution was diluted and buffered with 1 M bicine. The yield was 11 – 41 MBq (0.3–1.1 mCi) ^{52}Mn/mL[135]. No information was provided about percent recovery or radionuclidic purity (RNP). At least, no ^{54}Mn impurity percent was noted in the final product. However, due to the high dosimetry of ^{52}Mn, in routine production, an automated separation is needed for radiation safety: LLE is not the best-adapted protocol for that. The radiochemical separation needs to be modified by introducing IC (Ionic Chromatography: cation or anion exchange resin) (high capacity) or SLE (Solid-Liquid Extraction) resins (high selectivity) to reduce these drawbacks.

3.2.2.2 Cation exchange resin

Commercially available ion exchange resins are insoluble, organic polymer materials in the form of very small beads[136]. Cation resins have negatively charged functional groups, which adsorb positively charged ions. Conversely, the positively charged functional groups of anion resins adsorb negatively charged ions. These ions are referred to as counterions. The resin used in this study was Dowex 50W-X8, hydrogen form, 200 - 400 mesh cation exchange resin. This is a strong cation exchanger with sulphonic acid functional groups attached to a styrene divinylbenzene copolymer lattice. Cations in solution are covalently bonded to the negatively charged sulphonic acid groups on the resin. The mesh value of the resin refers to the size of the resin beads. In the case, 200 - 400 mesh, the diameter of each resin bead is 38 – 75 µm, thereby having a relatively large total surface area compared to larger beads, which maximises the separation resolution. The resin also contains 50 – 56 % water content (moisture). The amount of cross-linkage between resin beads (X8) is 8%; thereby having an approximate exclusion limit, for globular molecules of molecular weight (MW) no greater than 1000 i.e. allowing smaller ions to pass through and react with the resin but not larger molecules such as large metal complex ions or proteins[137]. Switching between solutions of extreme pH values should be avoided as it may cause osmotic shock to the resin beads, which physically alters the resin and therefore its functionality. Further importance is the ion exchange capacity of a resin, which is defined as the number of exchangeable groups per unit volume of resin, as milli-equivalents per mL of resin (meq/mL)[138,139]. The ion exchange capacity for Dowex 50W-X8 is 1.4 meq/mL. Therefore, the amount of total ions to be exchanged should not exceed this amount or effective separation will not be attained.

3.2.2.3 Dw for V/Mn on Dowex 50W-X8 with HNO_3

Vanadium(IV) or (V) can be separated from other metal ions by elution from a cation exchange column with dilute acid containing 1 % or less hydrogen peroxide : small amounts of vanadium quantitatively have been separated from 25 other metal ions with Dowex 50W-X8 (H+-form)[140]. But maximum yields can be challenging for elements with multiple oxidation states, such as V, whereby the affinity of particular ions for the ion exchange resins is dependent on the oxidation state of the ions and charge of complexes formed. It is unclear what effect the variable oxidation state of V would have on the ability of H_2O_2 to complex V but using strong oxidising acids such as HNO_3 should convert all V into the pentavalent form[132].

Distribution coefficients (Dw) for cation in nitric acid with a sulfonated polystyrene resin (AG 50W-X8) were published in 1965 by Strelow and his collaborators[141]. A complementary study in dilute nitric acid (0.1 M and 0.2 M) had shown some discrepancies where the Dw values vary by 50 – 70 % between the two studies[139]. In these dilute solutions, almost all of the analytes were absorbed onto the resin and therefore extremely low concentrations (< 1 ppb) remained in the solution to be analysed. With the advent of more advanced instrumentation such as inductively coupled plasma mass spectrometry (ICP-MS), it was possible in 2012[139] to analyse such dilute solutions more precisely and accurately than in previous studies and this

most likely explains the discrepancy between the two studies. For Mn, values are not comparable because degree of oxidation is not the same. For vanadium, Dw for V(IV) and V(V) were measured in 1965 study whereas only value of V(V) was reported in 2012 (Table 3.24).

year of study		HNO_3 (M)							
		0.1	**0.2**	**0.5**	**1**	**2**	**4**	**6**	**9**
1965	**Mn (II)**	1240	389	89	28.4	11.4	3.0	-	-
	V (IV)	495	157	35.6	14	4.7	2.5	-	-
	V (V)	20	10.9	4.9	2	1.2	0.5	-	-
2012	**Mn (IV)**	3490	991	135	33	9.8	4.7	3.9	4.2
	V (V)	1480	356	51	14	5.3	3.1	2.8	3
	Cr (III)	277	262	199	96	19	4.4	2.9	2.7
	Fe (III)	1290	2550	762	167	24	6.3	4.4	5
	Co (III)	3730	901	118	29	8.2	3.4	2.6	2.4
	Ni (II)	1270	751	115	29	8.5	3.6	2.8	2.6
	Cu (II)	2140	836	111	26	7	2.6	2	1.8
	Zn (II)	289	390	77	21	7	2.4	1.8	1.6

Table 3.24: Comparison of Dw from 1965 and 2012 studies

Considering the Dw obtained in the 2012 study, separation at 0.5 M HNO_3 seems difficult, and at 0.1 M, it will take a long time to correctly separate each of the elements assuming that Dw of Mn (II) was not lower than 3490 (Mn (IV)). In this context, no catch and release of ^{52}Mn in an acceptable time and volume of solution will be possible. But using the fact of large Dw difference between Mn(IV) and V(V) at 0.1 – 0.5 M with weak retention of Mn, a final dissolution in 0.1 M nitric acid solution was considered then an elution at 0.5 M was experimented in first approach.

3.2.2.4 Determination of V and ^{52}Mn

3.2.2.4.1 Vanadium

The radiotracer method will not used for V (with ^{48}V) because alpha irradiation at 45 MeV doesn't produce this radionuclide. Access to ICP-MS was limited because samples must not be radioactive, so a 10-fold decay time of ^{52}Mn (55 days) needs to be respected and the instrument needs to be available (planning 3 months before the day of analysis). Fortunately, in aqueous solution, vanadium complexes have different colors according to their degree of oxidation related to pH: lilac $[V(H_2O)_6]^{2+}$ (II), green $[V(H_2O)_6]^{3+}$(III), blue $[VO(H_2O)_5]^{2+}$(IV), yellow-orange oxides $[VO(H_2O)_5]^{3+}$(V). Elution of V will follow in part by the color blue on the column. A NaI probe at the column outlet follows the signal of ^{52}Mn online. For the last irradiations, a recently purchased ICP-OES (Inductively coupled plasma-optical emission spectrometry) on site helped us to confirm the initial analysis with ICP-MS.

3.2.2.4.2 ^{52}Mn

^{52}Mn was produced by alpha irradiation of V targets (mass ≈ 30 to 100 mg). After irradiation and a minimum of 3 hours of decay time, the target was put in a 50 mL cylindric tube and 0.7 mL of 15 M HNO_3 was added to dissolve the V target generating brown-orange fumes. After 5

min and complete dissolution, 50 mL of water was added to obtain a brown-dark solution which quickly turned to blue/green when adding water. The blue final solution has an approximate 0.25 M HNO_3 concentration. Before loading the solution onto the column, an aliquot of 60 µL was held back for estimation of the total activity of irradiation. The activity of the aliquot was measured by a dose calibrator (Capintec CRC-15R setting#676/2 for ^{52}Mn) and following dilution to standard calibrated volume for HPGe gamma spectrometry measurements. All fractions were measured by dose calibrator and Ge spectrometry in a determined geometry: TPF2G (small polypropylene tube (5 mL) filled with 2 mL of the solution to analyzed).

3.2.3 Cation exchange method with Dowex 50W-X8 resin

3.2.3.1 Column 1

3.2.3.1.1 Preliminary experiments

In preliminary experiments, V foils of 25 µm thickness (≈ 18 mg; ∅ 12.7 mm) were irradiated and radiochemically separated with ≈ 800 mg of Dowex 50W-X8 (Bio-Rad, 200 – 400 mesh). Larger targets (35 – 100 mg) were treated as follows: dissolution in 15 M HNO_3, dilution of solution with water to [HNO_3] ≈ 0.2 M then loading the solution onto a 5.3 g Dowex 50W-X8 resin (200 – 400 mesh) column, and elute with 0.5 M HNO_3 to recover the V (blue color) before switching to 5 M HNO_3 to recover ^{52}Mn.

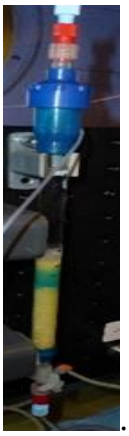

Figure 3.17: Elution of loading solution on Dowex 50W-X8

This first protocol was applied to spot-welded vanadium targets of ≈ 50 and ≈ 95 mg (126 µm thickness; ∅ 9.5 and 12.7 mm) (Table 3.25.). Briefly, the target was dissolved in 0.7 mL of 15 M HNO_3 then volume completed to 50 mL with water to obtain the expected concentration of HNO_3. The solution is loaded onto a 4.0 g (Sigma Aldrich) or 5.3 g (Bio-Rad) of Dowex 50W-X8 resin (200 - 400 mesh) column preconditioned with 15 mL of 5 M HNO_3, 80 mL of water, and 15 mL of 0.1 M HNO_3. 129 to 190 mL of 0.5 M HNO_3 was used to recover vanadium (blue color on column (see Figure 3.17)). After the blue band eluted from the column, the concentration of HNO_3 was switched to 5 M to recover ^{52}Mn in 9 to 28 mL.

Note: Resin mass (4.0 g) used in the case of Sigma Aldrich's resin was lower than in the case of Bio-Rad's resin (5.3 g) to obtain the equal height of column (≈ 100 mm) (glass column external ∅ 13 mm, internal ∅ 10 mm). We suppose that Bio-Rad's resin (historical resin in the laboratory) had an excess of water absorbed to explain the difference in mass for the equal height of column.

Target mass (mg)	Resin mass (g)	Loading		HNO_3 0.5 M		HNO_3 5 M		Colmn
		V. (ml)	^{52}Mn (%)	V. (ml)	^{52}Mn (%)	V. (ml)	^{52}Mn (%)	^{52}Mn (%)
96.8	4.0	53	0.7	155	4.3	9.4	94.9	0
95.5	4.2	37.5	0.4	154	0.5	13.4	98.7	0
95.5	5.3	43.5	0	190	11.5	14.5	86.6	1.8
54.8	5.3	50	0.2	186	26.6	14.4	73.2	0
53.8	5.1	51	0	149	1.1	28	98.9	0
55.0	5.1	51	0	160	5.7	15	94.1	0.1
51.5	5.1	50	0	162	31.4	18	68.7	0

Table 3.25: ^{52}Mn recovery according to volumes of 0.5 M and 5 M HNO_3

With a volume of 0.5 M HNO_3 < 140 mL, no ^{52}Mn was recovered at this step, while more than 95 % was isolated in the following 5 M HNO_3 aliquot (Table 3.25.). But these conditions are not optimized: it's necessary around 2.5 – 3 h to recover ^{52}Mn in 16.8 ± 5.8 mL (n = 7) of 5 M $HN0_3$. To reduce time of 52Mn, solution of 1.5 M were used in association with 0.5 M: at lower concentration vanadium is more eluted than 52Mn but required higher time for separation. A 7 M HNO3 was used too to reduce recovery volume of 52Mn (for the second step this solution need to be diluted to 0.2 M HNO_3).

3.2.3.1.2 ^{52}Mn recovery along 0.5 M / 1.5 M HNO_3 volume

For these experiments, solutions of dissolved V target (∅ 9.5 mm, thickness 75 µm (≈ 36 mg) and 127 µm (≈ 55 mg)) were loaded on 6.6 g Dowex 50W-X8 resin (Bio-Rad, 200 - 400 mesh). The mass of cation exchange resin was increased from 5.3 g to 6.6 g to limit loss of ^{52}Mn: reducing the volume of 0.5 M HNO_3 and using 1.5 M HNO_3 solution decrease the volume necessary to recover the V. ^{52}Mn will be eluted more quickly with 1.5 M HNO_3 solution. By increasing the resin mass (Dowex 50W-X8) eluted with 0.5 M HNO_3, ^{52}Mn will spend more time in contact with the resin. The amount of mass added was a compromise between elution time reduction and residence time in the resin. The 6.6 g Dowex 50W-X8 resin was eluted first with 0.5 M HNO_3 (0 to 55 mL), then with 1.5 M HNO_3 (2 to 54 mL), and at last with 7 M HNO_3 (7 to 25 mL) (Table 3.26). Finally, the column was rinsed with 15 mL of 7 M HNO_3 and 80 mL of water (Rinsing).

Id.	V target mass (mg)	Volume (mL)						^{52}Mn (%)						
		Loading	0.5 M HNO_3	1.5 M HNO_3			7 M HNO_3	Loading	0.5 M HNO_3	1.5 M HNO_3			7 M HNO_3	Rinsing
				(1)	(2)	(total)				(1)	(2)	(total)		
A	**39.1**	40	48	42	9,7	52	10	0	0	0	20	20	80	0
B	**37.1**	38	45	40	12,5	53	12	0	0	0	18	18	82	0
C	**34.4**	51	41	10	0	10	7	1	5	47	0	47	43	3
D	**34.4**	53	40	12	0	12	9	0	3	26	0	26	66	4
E	**33.5**	50	51	2	0	2	11	0	13	13	0	13	73	1
F	**35.0**	51	48	5	0	5	7	0	8	11	0	11	76	6
G	**53.0**	40	49	40	10	50	10	0	0	0	0	0	86	15
H	**56.4**	50	38	6	0	6	13	0	0	0	0	0	92	6
I	**53.6**	37	14	25	10	35	11	0	0	0	20	20	80	0
J	**54.1**	40	15	26	6,2	32	13	0	0	0	13	13	88	0
K	**37.0**	39	15	25	15	40	14	0	0	0	8	8	92	0
L	**34.4**	50	0	51	3,9	54	8	0	0	9	15	24	74	2
M	**33.9**	51	0	49	0	49	10	0	0	4	0	4	93	4
N	**55.7**	41	0	52	0	52	25	0	0	0	0	0	99	0
O	**59.6**	55	0	43	0	43	25	1	0	0	0	0	98	2
P	**53.9**	48	0	54	0	54	20	0	0	0	0	0	92	0
Q	**50.9**	50	0	44	6,5	50	14	1	0	4	11	15	84	1

Id. = Identification of sample

Table 3.26: Percentage of ^{52}Mn in different fractions of elution on 6.6 g of Dowex 50W-X8 resin

In the best conditions, where only ≈ 50 mL of 1.5 M HNO_3 were used, 93 ± 6 % (n= 5 see samples M to Q) of ^{52}Mn were recovered in 19 ± 7 mL of 7 M HNO_3 no much better than using 5 M HNO_3. For the second step, a 20-fold dilution of 7 M HNO_3 recovered at step one will be necessary to employ it. For that, a volume of 7 M HNO_3 of about 10 mL or less will be indicated. Conditions of elution with ≈ 48 mL of 0.5 M HNO_3 then ≈ 50 mL of 1.5 M HNO_3 used for samples A, B, and G gave this result but the yield of ^{52}Mn recovery decreases to 83 ± 3 %. Perhaps, looking for different fractions of 1.5 M HNO_3 recovered for A, B, and G samples, and reducing the 1.5 M HNO_3 volume to 45 mL could be a good compromise between increasing yield recovery without significantly increasing the volume of 7 M HNO_3. For similar sample conditions (I, J, and K) variations of ^{52}Mn yield recovery (80 to 92%) could be associated with the volume of 1.5 M HNO3. For example, the separation of C, D, and H samples was successively eluted on the same or the next day using the same column. ^{52}Mn yield recovery increased successively with columns (43% for sample C, 66% for sample D, and 92% for sample H). Probably the columns had been stocked in the dry state. Usually between two irradiations occurring in different days or weeks, the columns were rinsed with 15 mL of 5 M HNO_3 then 80 mL of water and stored wet. Compared to the previewed results, the presence of ^{52}Mn in the 0.5 M HNO_3 solution (5 to 13%) in samples C, D, E, and F confirms a potential breakthrough for these separations, particularly for samples C and D with respectively 43 and 66% yields. The wet storage of the columns is crucial for the repeatability of separations. The transition between 1.5 M HNO_3 to 7 M HNO_3 is sensitive for ^{52}Mn yield recovery: limit the 7 M HNO_3 volume for the second step. Equilibrium needs to be found between using a small volume of 0.5 M HNO_3 and less than 50 mL of 1.5 M HNO_3, regardless of the mass of the target. A direct elution of the column with a solution of 1.5 M HNO_3 reduces the time of elution but creates some breakthrough as well as difficulty in the reproducibility of the separation with a fixed volume of 1.5 M HNO_3.

3.2.3.1.3 Elution of Vanadium

The distribution of V on different elution fractions was determined by ICP-OES (Table 3.27).

Mass target (mg)	Loading	HNO_3 0.5 M	HNO_3 1.5 M (1)	HNO_3 1.5 M (2)	HNO_3 7 M	Rinsing	Recovery yield (%)
50.9	9.9	0.0	74.9	0.5	0.2	0.0	85.4
34.4	12.8	0.0	84.2	0.0	0.0	0.0	97.1
34.4	28.0	71.0	1.0		0.0	0.0	100.0
34.4	19.1	77.9	2.4		0.1	0.0	99.5
56.4	29.3	65.5	2.8		0.5	0.0	98.2
13.0	9.0	86.7	0.1		0.1	0.0	95.9
41.4	16.3	79.8	0.2		0.1	0.0	96.4
33.5	11.2	86.3	0.1		0.2	0.0	97.9
35	15.1	78.9	0.2		0.0	0.0	94.2
33.9	18.4	80.6	0.8		0.2	0.0	100.0
Mean (%)	16.9	78.3	79.5	0.3	0.2	0.0	96.5
STD (%)	7.1	7.2	6.6	0.3	0.1	0.0	4.3

Table 3.27: Composition in V for each separation fraction for various targets

These results confirm that the blue color is a good indicator of V presence. After loading, the initial ^{52}Mn solution 17 ± 7 % (n = 10) was eluted in 40 – 50 mL, and 79 ± 7 % (n = 10) of V was recovered in 0.5 M HNO_3 or 1.5 M HNO_3. Only 0.2 ± 0.1 % of the total Vanadium was measured on the final solution 7 M HNO_3.

3.2.3.1.4 Separation factor (SF) for V/^{52}Mn

V/Mn separation factor ($SF_{(Cr/Mn)}$) is a good indicator of the separation quality between vanadium and manganese. For its determination, equation (17) was used in the case of V/^{52}Mn separation:

(14) $$SF = \frac{\frac{m_{Vbefore}}{m_{Vafter}}}{\frac{A_{52Mn\,before}}{A_{52Mn\,after}}}$$

with $m_{V,before/after}$ being the ICP-OES-quantified vanadium mass before/after the separation step 1 eluted in 7 M HNO_3. Its average is 0.2 ± 0.1 % (Table 3.26.) and $A_{52Mn,before/after}$ being the dose-calibrator-quantified ^{52}Mn activity before/after the separation step 1 (Table 3.26). Excluding sample C ($SF_{(V/Mn)}$= 215) for high breakthrough with only 43% of ^{52}Mn recovered, an average $SF_{(V/Mn)}$ = 423 ± 47 (n = 15) was obtained for the separation step 1 of V/^{52}Mn.

3.2.3.2 Column 2

3.2.3.2.1 Results

A second separation on DOWEX 50W-X8 resin was realized to increase the $SF_{(V/Mn)}$. 500 mg of Dowex 50W-X8 resin (200 - 400mesh) was used. The 7 M HNO_3 fraction recovered in step 1 was diluted to 0.2 M HNO_3 and then loaded on a column filled with Dowex 50W-X8 preconditioned with 5 mL of 5 M HCl, 15 mL of water, and 5 mL of 0.1 M HNO_3. HCl was used instead of HNO_3 for rinsing and elution in step 2 to facilitate the potential evaporation of ^{52}Mn final solution or its use at this step for radiolabeling. Due to the large volume of loading solution, no rinsing volume of 0.5 M or 1.5 M HNO_3 was used to elute V. We consider that this large volume could be sufficient to elute the rest of V. Before changing the nitrate to chloride form of ^{52}Mn, a solution of 0.1 M HCl was used (2 mL). Finally, ^{52}Mn was recovered from column (C2) in about 6 mL of 10 M HCl solution (Table 3.28).

7 M HNO_3 fraction step 1 (ml)	V. Loading (mL)	^{52}Mn repartition in fraction (%)				10 M HCl (ml)
		Loading	0.1 M HCl	C2	10 M HCl	
11.0	213	0	0	*	99.8	8.4
11.0	248	14.3	0.2	0.9	84.7	5
9.8	206	26.2	0.3	0.1	73.4	5
14.2	186	3.1	0	8.6	88.3	5
8.4	288	19.3	0.3	5.8	74.7	5
12.6	485	2	0.2	7.4	90.5	5
9.4	362	3.2	0.1	2.5	94.2	5.9
7.1	269	6.1	0	4.5	89.4	6
7,0	260	3.1	0	5.3	91.6	6
10.2	377	31.7	0	0	68.3	5.9
6.9	275	0.9	0	3.9	95.2	6

* no measured

Table 3.28: Distribution of ^{52}Mn in fractions on DOWEX 50W-X8 resin step 2

86.4 ± 11.6% (n = 10) of ^{52}Mn was recovered in 5.7 ± 1.0 mL 10 M HCl and up to 90.7% by increasing the elution volume from 5.7 mL to 7 – 8 mL. However, the reproducibility of the loading step is critical in this process. The larger volume of loading solution wasn't justified by the higher % of ^{52}Mn recovery from column 1, for 485 mL of loading, 2% of ^{52}Mn recovered whereas for 248 mL, 14.3 % of ^{52}Mn recovered (Table 3.29). Due to the limited volume of flasks (≈ 200 mL) used for 7 M HNO_3 dilution recovered from step 1, the loading solution was divided into 2 or 3 fractions according to global volume. During the loading process, the solution was recovered on 2 or 3 fractions (F1, F2, and F3).

Loading (mL)	F(1)		F(2)		F(3)	
	(mL)	% ^{52}Mn	(mL)	% ^{52}Mn	(mL)	% ^{52}Mn
213	102	0	111	0	-	-
248	100	0	148	14.3	-	-
206	72	0.1	134	26.1	-	-
186	117	0	69	3.1	-	-
288	150	0	138	19.3	-	-
485	164	0	161	0.2	160	1.8
362	132	0	140	0	90	3.2
269	133	0	136	6.1	-	-
260	132	0	128	3.1	-	-
377	115	0	142	4.9	120	26.8
275	138	0	137	0.9	-	-

Table 3.29: Distribution of loading solution in each fraction and % ^{52}Mn recovery associated

For the first fraction F1, < 0.2 % ^{52}Mn recovered in 72 – 164 mL then this % of ^{52}Mn recovered varied. During recovery of fraction 2 (F2), flasks need to be changed. However, if column was dried during the process, the retention of ^{52}Mn would be affected, thus could explain the high percent breakthrough of ^{52}Mn recovered in some solutions F2 or F3.

3.2.3.2.2 $SF_{(V/Mn)}$ on column 2

After separation, the composition of V in each fraction of step 2 was determined by ICP-OES. 39.4 ± 8.9 % of V loaded in column 2 were recovered in ^{52}Mn final fraction. A lower percentage was observed when a significant part of ^{52}Mn was eluted in the loading fraction (target 34.4 and 33.5 mg). An average column 2 $SF_{(V/Mn)}$ = 2.3 ± 0.4 was obtained (Table 3.30). With a low concentration of V in the solution, no color blue acted as an indicator to define the volume of 0.5 M HNO_3 to rinse the column after loading the solution.

Reference mass target	Fraction 10 M HCl		SF
	V (%)	^{52}Mn (%)	
48.3	51.7	88.3	1.7
34.4	29.7	74.7	2.5
56.4	39.7	90.5	2.3
33.9	41.5	94.2	2.3
13,0	41.5	89.4	2.2
41.4	42.4	91.6	2.2
33.5	23.3	68.3	2.9
35,0	45.5	95.2	2.1
Mean	39.4	86.5	2.3
STD	8.9	9.7	0.4

Table 3.30: Recovery yield (%) of V and ^{52}Mn in 10 M HCl fraction

But with ICP-OES analysis to follow the quantity of V in fraction, future works will be done with rinsing the column after the loading process with various volumes of 0.5 M HNO_3, based on C1 experiments. The chemistry of vanadium was complex and sensitive to the reaction conditions. In the case of radiolabeling molecules with ^{52}Mn perhaps the $SF_{(V/Mn)}$ obtained in step 1 could be sufficient for vanadium but other trace metal contaminants could compete with ^{52}Mn in the radiolabeling step.

3.2.4 Trace metal reduction

Looking for equation (16), to increase AMA it's necessary to limit contaminants on each step of production of ^{52}Mn source (target, solvent, column, resin, fitting…). Some metals with an oxidation state +2 in solution were considered contaminants: Co, Cr, Cu, Fe, Mn, Ni, and Zn. First, these elements can occur in the V foil used for the target (Figure 3.18) and the spot welding method (copper electrode).

Product No.: 13783

Product: Vanadium foil, 0.127mm (0.005in) thick, 99.8% (metals basis)

Lot No.: N24D050

V 99.8%

Al	250	B	< 5	C	80
Cd	< 1	Co	< 50	Cr	< 50
Cu	< 50	Fe	< 200	H	< 3
Hf	< 100	Mg	< 10	Mn	< 1
Mo	84	N	91	Na	< 10
Nb	< 100	Ni	< 50	O	300
P	< 30	Pb	< 1	S	< 10
Si	180	Sn	< 50	Ta	< 100
Ti	< 50	U	< 1	W	< 40
Zr	< 50				

Values given in ppm unless otherwise noted

Figure 3.18: Certificate of Analysis of V foil used in spot welding method

V foils contain < 1 ppm of Mn. Fe, Cr, Cu, Co, Ni, and Cr are not listed in the analysis certificate, but limited concentration values are as high as 200 ppm for Fe and 50 ppm for other elements. While Cu is the spot welding electrode, no results on ICP-OES showed any Cu in the subsequent solutions from the spot welding process. Two purification methods used in irradiated Cr target for ^{52}Mn production were applied to reduce metal traces: employing anion exchange or extraction chromatography column.

3.2.4.1.1 Anion exchange AG1-X8 resin

The first method was described in section 2.2.2.1 Manual separation. The separation on column (proton irradiation of Cr target) uses an anion exchange resin AG1–X8 200 – 400 mesh. Two columns of AG1–X8 resin, 200 mg (first separation) and 100 mg (second separation) were used. Fractions were evaporated to dry, then after cooling the residue, 1 mL of 10 M HCl was added to dissolve the residue then 30 mL of ethanol was added to obtain a solution of ethanol/10 M HCl (97/3 % (V/V)). The solution was then loaded onto an anion exchange column pre-conditioned (5 mL of 8 M HCl, then 15 mL of UP (ultra-pure) water, and finally 5 mL of mixture ethanol/10 M HCl 97/3 % (V/V)). Columns were then rinsed with 3 mL of mixture ethanol/10M HCl 97/3 % (V/V), then the ^{52}Mn was recovered in 8 M HCl solution from the first column and 0.1 M HCl from the second column. The following ^{52}Mn yield of recovery was obtained (Table 3.31).

Reference mass target (mg)	AG1-X8 resin	
	200 mg (%)	100 mg (%)
55.7	96.6	99.5
59.6	96.9	100
53.9	96.1	96.5
48.3	95.9	99.2
50.9	92.2	96.5
34.4	95.4	97.7
34.4	95.2	99.0
34.4	95.1	99.2
56.4	95.7	100
33.9	95.2	99.3
Mean	95.4	98.7
STD	1.3	1.3

Table 3.31: ^{52}Mn recovery yield (%) on anion exchange resin AG1-X8 (200 mg then 100 mg)

For the evaluation of various metals, no decontamination was calculated because ICP-OES measurements were not consistent. In the case of ^{52}Mn similar results were obtained by spectrometry gamma. For other elements, the chloride presence in the solution could affect the measurements by ICP.

3.2.4.1.2 Extraction resin: AC resin

The second method to reduce metal traces and particularly Cr uses an extraction AC resin[103]. No available data exists about D_w for V. For this reason, the D_W values were measured for concentration of HNO_3 between 0.1 and 2 M in static mode (on batch) contrary to dynamic conditions used in Kendall Barrett's article.

3.2.4.1.2.1 Determination of Dw

- **Material**

Standard solutions of Cr, V, Mn, Fe, Co, Zn, Cu, Al, Ni, (SCP Sciences) at 1000 ppm were diluted to desired concentration with 2 M HNO_3 (SCP Sciences). HNO_3 solutions (0.1 M, 0.2, 0.3, 0.5, 1, and 2 M) were all prepared from HNO_3 concentrated (SCP Science) and diluted with 18 MΩ water. Extraction Actinide (AC) Resin ® (TRISKEM, 50 – 100 µm, density = 0.35 g/mL, capacity Fe (III) = 32.1 mg by g of resin) was used for Dw determination.

- **Method**

Ten-fold lower concentrations of trace metals (Fe, Co, Zn, Cu, Al, Ni) were used compared to major constituents (Cr, V, and Mn) to be more representative of the V target. In these conditions, 3 % of AC resin capacities were used for separation. 50 mg of AC resin® is weighed for each test (all tests were triplicated). In every tube, AC resin® is mixed with 50 or 100 µL of standard solution (Cr-V-Mn (each 130 ppm)) and metal traces (Fe, Co, Zn, Cu, Al, Ni (13 ppm)), 150 to 1000 µL of 1 M or 3 M HNO_3 (to fix the correct nitric acid concentration of each sample) and additional volume of water to complete the volume to 1.5 mL. Every tube was shaken for 1 hour then allowed to rest, and finally, centrifugee (9 G RCF (Relative Centrifugal force)) for 10 min. 300 or 600 µL of each solution are extracted and diluted to 5 mL with 1.7 mL of 1 M HNO_3 and 2.7 or 3.0 mL of water. Sample were triplicated, and concentrations measured by ICP-MS. Dw and its standard deviation were calculated by the following equation (18).

(15) $$D_W = \frac{M_s}{M_l} * \frac{V_l}{m}$$

Where D_W weight distribution (mL/g), V_l is the volume of the eluent (mL), m is the element mass (g) and M_s (element mass (g) in solid phase = $M_i - M_l$), M_l (element mass (g) in liquid phase) and M_i initial mass of the element in solution before contact with the resin).

- **Dw: results**

Results of major components for ^{52}Mn production were obtained with good reproductibility (Table 3.32).

$[HNO_3]$	Cr (mL/g)			Mn (mL/g)			V (mL/g)		
(M)	Dw	±	STD	Dw	±	STD	Dw	±	STD
0.1	213.4	±	10.6	1431.8	±	128.9	348.8	±	4.9
0.2	22.7	±	4.7	328.1	±	93.4	200.9	±	15.6
0.3	6.9	±	1.4	161.6	±	7.2	135.5	±	6.0
0.5	0.7	±	0.1	60.4	±	1.2	84.6	±	1.8
0.8	0.6	±	1.7	24.4	±	3.1	55.9	±	5.4
1	0.8	±	0.6	18.1	±	1.7	51	±	3.6
2	0.9	±	0.4	5	±	1.7	33.3	±	2.8

Table 3.32: Dw of AC resin for V, Mn and Cr in nitric acid

For a V target, no easy separation is expected with this AC resin for the pair V/Mn in nitric acid conditions. At lower nitric acid concentration (0.1 M), it seems possible to separate Cr, Co, Zn, Cu, and Ni from Mn every V could be eluted. Fe and Al data are not sufficiently precise to evaluate eventual separation. In these conditions the levels of Fe and Zn were very low (< 5 (Fe) or 10 ppb (Al): below its LD (Limit of Detection)) (Table 3.33).

$[HNO_3]$	Fe (mL/g)			Co (mL/g)			Zn (mL/g)			Cu (mL/g)			Al (mL/g)			Ni (mL/g)		
(M)	Dw	±	Std	Dw	±	Std	Dw	±	Std	Dw	±	Std	Dw	±	Std	Dw	±	Std
0.1	> 233	±	4.0	30.9	±	0.7	56.7	±	3.3	228.2	±	6.2	> 103	±	1.7	73.0	±	45.5
0.2	> 249	±	13.3	9.8	±	1.5	14.0	±	4.4	58.0	±	4.4	> 110	±	6.6	80.4	±	42.6
0.3	> 235	±	3.8	4.6	±	0.2	5.2	±	1.1	26.1	±	1.0	> 104	±	1.7	91.6	±	13.0
0.5	> 126	±	185.1	3.9	±	1.2	0.1	±	0.8	12.4	±	1.3	> 231	±	1.4	68.7	±	13.4
0.8	> 227	±	4.6	0.4	±	0.3	2.4	±	1.3	5.9	±	0.6	> 229	±	4.6	0.4	±	0.2
1	> 231	±	6.7	1.2	±	0.8	5.3	±	1.5	2.9	±	0.8	> 233	±	6.7	1.8	±	0.9
2	> 234	±	1.5	1.8	±	0.8	4.0	±	0.9	1.5	±	0.5	> 236	±	1.5	2.2	±	0.9

Table 3.33: Dw of trace elements (Fe, Co, Zn, Cu, Al, Ni) with AC resin in nitric acid

Our D_w values can be compared with those measured by Barrett *et al* (Table 3.34.) in the production of ^{52}Mn by proton irradiation[142]. While the Dw values measured in this work for Cr and Mn are different from those measured by Barret *et al*, they have the same trends overall.

conc. [M]	Dw (mL/g) Cr	Mn	Fe
0.01	14.4 ± 1.5	297.5 ± 2.2	(1.8 ± 0.6) x 10^6
0.05	16.6 ± 1.3	234.9 ± 1.4	(1.8 ± 0.3) x 10^6
0.1	8.2 ± 1.0	120.8 ± 0.6	(5.5 ± 2.7) x 10^4
1.0	5.3 ± 0.8	21.6 ± 0.1	(1.3 ± 0.3) x 10^4
3.0	2.3 ± 3.4	5.5 ± 0.1	(9.3 ± 1.4) x 10^3
5.0	5.7 ± 1.4	6.8 ± 0.1	(6.6 ± 0.8) x 10^3

Table 3.34: Dw for AC resin in HNO_3 reported by Barrett *et al*[142].

3.2.4.1.2.2 AC resin in dynamic mode: 2 columns

- **Material and Method**

Tests were done with an irradiated target (test 1 and 2: same target but partial dissolution). For the tests 3 and 4 targets (∅ 9.5 mm, 75 mm thickness not irradiated) were used and 0.6 MBq of ^{52}Mn were added to follow it. After applying 2 separations with Dowex 50W-X8 (≈ 6.7 g then 500 mg) as described above, two columns with 250 and 150 mg of AC resins were used. AC resins were pre-conditioned with 5 M HNO_3 (5 mL) then water until pH = 6 - 7 then rinsing with 0.01 M HNO_3 (5 mL). For AC resin 250 mg, the final solution of step 2 Dowex 50W-X8 was dried and was taken up in 2.0 mL of 0.01 M HNO_3. The solution was loaded on the column and an additional 100 mL of 0.01 M HNO_3 was passed over the column to wash residual materials and metal traces from Mn. Finally, ^{52}Mn was recovered in 2 mL of 3 M HNO_3. This solution was diluted with 38 mL of water to change the acid concentration to 0.15 M HNO_3. The solution was loaded on 150 mg AC resin column and an additional 50 mL of 0.01 M HNO_3 was passed over the column to wash residual materials and metal traces from Mn. Finally, ^{52}Mn was recovered in 2 mL of 3 M HNO_3. Additional evaporation of ^{52}Mn solution was done to reduce the acidy of the solution. The final dried solution was dissolved in 1 mL of 0.1 M HCl.

- **Results**

Reference mass target (mg)	^{52}Mn recovery (%) Column 1 (C1) : 250 mg				Column 2 (C2) : 150 mg			
	Loading solution	0.01 M HNO_3	3 M HNO_3	C1	Loading solution	0.01 M HNO_3	3 M HNO_3	C2
13.0	0	0	87.0	13.0	0	0	100	0
41.4	0	0	91.7	8.3	4.3	0	94.1	1.6
33.5	0	0	94.0	6.0	4.1	0	91.8	2.1
35.0	0	0.3	92.8	6.9	0	0	92.8	6.9
	Mean		91.4				94.7	
	STD		3.1				3.7	

Table 3.35: ^{52}Mn recovery yield (%) using AC resin (250 mg in C3 and 150 mg in C4)

These results confirmed that ^{52}Mn was fixed on the column at a lower concentration (Table 3.35) and 2 mL of 3 M HNO_3 to desorb it. Yield of ^{52}Mn recovery was > 90 % for each column. In the case of the first column with AC resin, increasing the volume of 3 M HNO_3 for elution to 3 mL probably gives a yield of recovery of 100 %. In the second column, 150 mg is too low to avoid some breakthrough of ^{52}Mn because conditions as similar to column 1 (C1). Targets used to evaluate the separation of metals by AC resin had a low mass (13.0 to 41.4 mg) to limit metal impurities for AMA determination. Considering the limited metal impurities of interest

in V foil (see Figure 3.18.), quantities of metal to analyze by ICP-OES are about limit of quantification (LQ) or limit of detection (LD). In these conditions no equilibrated balance of mass of each metal was obtained: results were not consistent. For a good elution profile of elements such as Fe, Cu, Zn, or Ni during AC resin's protocol, spiking these elements in small quantities (limiting the metal quantity adding Mn and V to 10% of the capacity of AC resin) will be a good approach to validate AC resin.

3.2.5 Comparison of trace metal reduction methods

The two methods are equivalent to recovering ^{52}Mn (> 90%) but comparison is challenging in terms of quality. One option will be to compare the AMA of each method. Some AMA were estimated on a protocol using 2 cation exchange columns (Dowex 50W-X8 resin, ≈ 6.7 g, and 500 mg) and, then two anion exchange columns (AG1-X8 resin, 250 and 150 mg).

3.2.5.1 AMA

The used method for AMA's determination was described in details in section 2.3.4.2.2. Determination of AMA. AMA increased with higher produced ^{52}Mn activity (Table 3.36). For 30.2 ± 11.1 MBq EoB (n = 7), an AMA of 20.9 ± 4.5 MBq/µmole (EoB) was obtained with two columns (C3, C4) of anion exchange AG1-X8. For low produced ^{52}Mn activity 3.8 ± 1.1 MBq (n = 8), AMA = 3.1 ± 1.5 MBq/µmole. In this last case, every separation was done with two anion exchange columns (C3 and C4). These results of AMA are similar to the ones we obtained by proton irradiation on the Cr target (Table 2.10.).

Weight (mg)	Act. (EoB) (MBq)	^{52}Mn recovery in final fraction of each column (%) C1	C2	C3	C4	Global ^{52}Mn Recoverv (%)	Volume ^{52}Mn final batch (mL)	Act. used for (MBq)	AMA (EoB) (MBq/µmole)
55.0	50.3	82.9	38.4	79.8	-	25.4	1.0	0.19	0.8
53.8	38.7	97.0	27.8	93.6	-	25.2	0.9	0.34	13.6
38.6	31.3	96.6	99.8	98.4	-	94.9	1.0	0.43	17.3
51.5	28.0	56.9	69.3	85.2	-	33.6	1.0	0.2	2.7
53.9	23.4	88.2	73.4	96.1	96.5	62.2	0.6	0.2	17.7
54.8	20.9	69.4	93.2	95.7	-	61.9	1.1	0.25	9.96
37.0	18.8	88.7	86.4	84.2	-	64.5	2.2	0.08	24.0
56.4	5.7	92.1	90.5	95.7	100.0	79.8	1.0	0.07	2.3
50.9	4.6	83.8	40.8	92.2	96.5	31.5	1.1	0.02	3.3
59.6	4.2	96.7	65.3	96.9	100.0	61.2	1.1	0.04	5.5
48.3	4.1	58.8	88.3	95.9	99.2	49.8	1.1	0.03	4.0
34.4	3.2	74.0	50.7	95.4	97.7	35.8	1.1	0.02	2.2
34.4	3.2	43.4	45.6	95.2	99.0	18.8	0.9	0.01	0.4
34.4	2.9	66.2	74.7	95.1	99.2	47	1.0	0.02	3.3
55.7	2.1	96.1	84.7	96.6	99.5	78.6	0.9	0.03	3.5

Table 3.36: AMA (EoB) of ^{52}Mn obtained by V irradiation

In literature, natural chromium powder targets were irradiated with an incident proton beam energy of 17.5 MeV on the degrader (12.8 MeV on the Cr target material) at 15 µA for 2 – 8 h giving high yields of 336.7 ± 44.4 MBq (9.1 ± 1.2 mCi[72]). AMA depends on the concentration of the eluant, especially for the natural chromium powder targets[72]: 185 ± 22.2 MBq/µmol (5.0 ± 0.6 mCi/µmol) for final elution of ^{52}Mn with 0.1 M HCl, in case of elution with 6 M HCl, the AMA increased to 999 ± 88 MBq/µmol (27.0 ± 2.4 mCi/µmol)[72]. In our cases, two experiments are not presented in Table 3.36 where 6 M HCl was used in the final AX column elution of ^{52}Mn instead of 0.1 M HCl. In these conditions, AMA of 22.0 and 60.0 MBq/µmole for 23.4 and 9.4 MBq product (EoB) were obtained. No sufficient experiments were done to confirm this point in our work. However, these results are not astonishing: HCl

concentration reduction from 8 M to 2 M (Cu) or less (Zn) improves the elution of elements such as Fe, Cu, or Zn. This concept was used for example in the production of ^{64}Cu to separate Ni from Cu[143,144]. Considering a factor of ≈ 10 between values of AMA= 185 MBq/µmole for 337 MBq produced in literature and our AMA= 21 MBq/µmole obtained for 30 MBq, we can estimate in first approach that these results are similar. The method with cation exchange resin (Dowex 50W-X8) associated with an anion exchange column (AG1-X8) gives good results in ^{52}Mn separation from V target. The low activity of ^{52}Mn produced (for radiation safety at Orleans) and low concentration of used HCl on final elution are the more justified reasons of low AMA obtained.

3.2.5.2 AC resin versus AG1-X8 resin protocol

To compare separation using AC resin or cation exchange resin Dowex 50W-X8, the average composition of the final ^{52}Mn sample for each protocol was determined by ICP-OES. Their composition in Mn, V, and metals (Co, Cr, Cu, Fe, Ni, Zn) are calculated in moles (nmol). Only individual quantities for Cu, Fe, and Zn were reported in Table 3.37.

resin	n	Moles (nmoles)																		
		V			Mn			Metals												
								Total			Cu			Fe			Zn			
AG1-X8	7	< 3,1*	±	4	3,3	±	1,3	144,3	±	79,1	59,3	±	50,9	65,1	±	31,4	17,2	±	9,3
AC	3	< 1,4*	±	0,6	2	±	0,8	43,4	±	27,6	22,8	±	25,6	1	±	0,4	18,4	±	0,5

* LD (limit of Detection)
Total Metals : nmoles in Co, Cu, Cr, Fe, Ni, Zn

Table 3.37: Composition of final ^{52}Mn sample in V, Mn, and Metals for the protocol using AG1-X8 resin and AC resin.

Considering the average target mass for each protocol 41.8 ± 9.7 mg (n = 7) for AG1–X8 resin and 29.3 ± 14.7 mg (n = 3) for AC resin, the number of moles for V and Mn could be considered similar. In the case of metals, a variation in a metal mole number was observed between two protocols 144.3 nmoles (anion exchange) versus 43.4 nmoles (extraction exchange). More than 2 times lower number of moles (59.3 versus 22.8 nmoles) of Cu and a drastic reduction of Fe (65.1 to 1 nmoles) by the extraction exchange process explain the variation of metal amount. In this way, the AC resin method appears as a cleaner solution of ^{52}Mn. Why a higher Fe in the anion exchange process and lower scale metals? If we look for protocols used in two cases (Figure 3.19), more different reagents and concentrated acids were used in the anion exchange process (Ethanol, 10 M HCl, 8 M HCl, and 0.1 M HCl) whereas only diluted nitric and hydrochloric acid and water were used for AC resin. These arguments could justify the observed difference in quantities of metals in the final batch of ^{52}Mn. In the first approach, for purification of metals for the ^{52}Mn production by alpha irradiation, the AC resin protocol was indicated to be used for steps after cation exchange step with Dowex 50W-X8.

	AG1-X8	AC resin
	Dry solution from step 2	
Column 1	+ 1 mL 10 M HCl	+ 2 mL 0.01 M HNO_3
	+ 30 mL Ethanol	cooled in an ice water
	loading on 200 mg column	loading on 250 mg column
	+ 3 mL mixture Ethanol/10 M HCl 97/3 (% (v/v))	+ 100 mL water
	+ 2 mL 8 M HCl	+ 2 mL of 3 M HNO_3
	dry	---------
Column 2	+ 1 mL 10 M HCl	+ 38 mL water
	+ 30 mL Ethanol	
	loading on 100 mg column	loading on 150 mg column
	+ 3 mL mixture Ethanol/10 M HCl 97/3 (% (v/v))	+ 50 mL of water
	+ 2 mL 0.1 M HCl	+ 2 mL of 3 M HNO_3
	---------	dry
		+ 1 mL 0.1 M HCl

Figure 3.19: Comparison of protocols with anion exchange resin (AG1-X8) and extraction exchange resin (AC resin)

3.3 Comparison of Cr and V target production

Some criteria have been defined to compare the quality of ^{52}Mn produced by the proton beam on the Cr target and alpha beam on the V target: physical yield (MBq·eμA^{-1}·h^{-1}), AMA, and ^{54}Mn impurities.

3.3.1 Physical yield

For proton irradiation at 14 MeV, two measurement series have been done to determine the Physical yield and % of ^{54}Mn impurities produced (Table 3.38).

Thickness (μm)	Weight (mg)	Activity EoB (MBq)	Physical yield (MBq·eμA^{-1}·h^{-1})
388	282	2.22	2.9
337	256	4.41	6.1
337	255	4.35	5.7
347	267.5	11.56	6.2
354	245	7.67	4.0
382	291.9	13.34	2.2
		Mean	4.5 ± 1.7

Table 3.38: Physical yield (MBq·eμA^{-1}·h^{-1}) of Cr target irradiation with 14 MeV proton beam

For alpha irradiation, similar results have been obtained 2.8 ± 0.3 MBq·eμA^{-1}·h^{-1} (n = 3) (96 μm thickness, ∅ 9.5 mm), 3.6 ± 0.7 MBq·eμA^{-1}·h^{-1} (n = 14) (126 μm thickness, ∅ 9.5 mm) and 4.2 ± 0.5 MBq·eμA^{-1}·h^{-1} (126 μm thickness, ∅ 12.7 mm) (n = 3) with lower mass (37 to 97 mg).

3.3.2 AMA

In all cases, the obtained AMA for each irradiation is much lower than the published values. However, this can be explained by the low activity produced and the use of diluted acid to

extract ^{52}Mn to realize tests. For proton irradiation, a method with an anion exchange column was used by various teams working on the production of ^{52}Mn. For alpha irradiation, this is the first work with radiochemical separation. Even though some modifications need to be added for a robust method, low AMA is not due to separation method.

3.3.3 ^{54}Mn impurity

3.3.3.1 Proton irradiation

Determination of ^{52}Mn and ^{54}Mn activities were measured (30 min – 24 h counting time) by spectrometry gamma on representative separation points: solution of target dissolution (initial solution), column C1, C2, and C3 after separation and final fraction. In some cases, it was possible to measure percent ^{54}Mn in fraction 1 of the separation step 1 and fraction 2 or 3 from step 2 of V Target separation (every point of measurement is considered n = 1, for various measurements on the same point only average of values has been retained for estimation). Because some measurements have a dead time > 20 % ever we calculated a ratio (series 1), and we proceeded at a second series of measurements with a below 8% dead time (Table 3.39). No significant variation in results has been observed, only a lower measurement uncertainty. 0.39 ± 0.15 % (n = 3) was in good agreement with TENDL 2021 calculations 0.41 % for conditions on series 2. The average value obtained with series 2 was compared with results from alpha irradiation.

	mass (mg)	**eff. thickness (µm)**	**E_{out} (MeV)**	**%**	**±**	**unc. (%)**	**(n)**
	267.5	403	5	0.44	±	0.22	3
Serie 1	245	412	4.7	0.42	±	0.31	5
	291.9	444	3.4	0.38	±	0.26	2
	281.4	374	6	0.38	±	0.15	6
Serie 2	255.6	392	5.4	0.41	±	0.13	7
	254.6	392	5.4	0.37	±	0.16	7
		Mean Serie 2		0.39	±	0.15	

Table 3.39: Measurements of EoB ^{54}Mn radionuclidic percent on two series of ^{52}Mn production by 14 MeV proton irradiation (E_{in})

3.3.3.2 Alpha irradiation

For alpha irradiation, measurements are done on 3 types of samples on every irradiation: Initial solution, Column 2 after elution, and final solution of ^{52}Mn (Table 3.40).

Mass (mg)	eff. thickness (µm)	E_{out} (MeV)	%	±	unc. (%)	(n)
48.3	148	34.4	0.08	±	0.02	2
50.9	148	34.4	0.10	±	0.02	3
56.4	148	34.4	0.09	±	0.01	3
54.1	145	34.7	0.09	±	0.02	2
53.0	145	34.7	0.11	±	0.02	2
53.6	145	34.7	0.09	±	0.01	2
39.1	116	36.9	0.07	±	0.01	2
37.0	109	37.4	0.07	±	0.01	2
37.1	109	37.4	0.07	±	0.02	1
34.4	101	38.0	0.08	±	0.02	3
34.4	101	38.0	0.09	±	0.02	3
34.4	101	38.0	0.11	±	0.02	3
33.9	101	38.0	0.08	±	0.02	2
		Mean	0.09	±	0.02	13

Table 3.40: Measurements of ^{54}Mn radionuclidic percent on production of ^{52}Mn by alpha irradiation at 45 MeV (E_{in})

Two V thicknesses have been tested (≈ 125 and ≈ 100 µm corresponding respectively to effective ≈ 145 and ≈ 116 µm due to a 60° incident angle of targetry). No difference in percent ^{54}Mn was observed between these various targets: 0.09 ± 0.02 % (n = 6) for E_{out} < 34.7 MeV versus 0.08 ± 0.02 % for E_{out} > 36.9 MeV (n = 7), the global result is 0.09 ± 0.02 % (n = 13). TENDL 2021 calculations for 45 MeV alpha beam give 0.23 % for E_{out} < 34.7 MeV and 0.20 % for E_{out} > 36.9 MeV. In our conditions, percent ^{54}Mn produced by alpha irradiation for E_{out} < 34.7 MeV is between 2 to 5 lower than in the case of proton irradiation at 14 MeV. In proton irradiation, the beam was stopped on the Cr target.

3.3.4 Equivalence of irradiation methods

Two methods of ^{52}Mn production are equivalent in separation time, yield, and AMA (Table 3.41). Relative to the target preparation, the vanadium method is less time-consuming and easier to do with the usual tools to prepare it. A precise control of target mass is obtained with the alpha irradiation process reducing contamination of the final product (percent ^{54}Mn lower in alpha case 0.09% versus 0.39% in case of proton irradiation). This difference appears insignificant but could impact dosimetry[121]. However, in all cases, ^{54}Mn was produced. In the case of proton irradiation using enriched ^{52}Cr target could solve this point but this solution is not cheap. For V target irradiation, the reduction of thickness and higher beam energy (50 – 55 MeV) will be some alternatives to investigate.

Material	Cr powder	V foil
isotopy (%)	83.8 (^{52}Cr)	99.8 (^{51}V)
reaction	^{52}Cr (p,n)^{52}Mn	^{51}V(α,3n)^{52}Mn
Form	sintered and polished pellet	spot welded method
Time	2 days	30 min,
mass (mg)	266.8 ± 17.8 (6)	30 - 95
Physical yield (MBq. E.µA.h)	4.5 ± 1.7 (n = 3)	3.6 ± 0.7 (n = 14)
Number of column	3	4*
Yield (%)	66.9 ± 10.7 % (n = 3)	73.8 ± 6.8 % *
Time (h)	4	5
AMA (MBq/nmole)	41.7 ± 29.6 (n = 3)	20.9 ± 4.5 (n = 8)
% of ^{54}Mn	0.39 ± 0.15 (n = 3)	0.09 ± 0.02 (n = 13)

* results with 2 columns of anion exchange resin AG1-X8

Table 3.41: Comparison of ^{52}Mn production by proton and alpha irradiation

3.4 Conclusion on the ^{52}Mn production by an alpha irradiation

For the first time, ^{52}Mn was produced by alpha irradiation on a V target at 45 MeV in France. The physical yield obtained 3.6 ± 0.7 MBq·eµA^{-1}·h^{-1} (n = 14) for mass target = 53.9 ± 2.8 mg is similar to that obtained proton irradiation. However, a simplified preparation process for the V target was used. The purification happens in two steps, the first eliminates the maximum of V mass by a cation exchange column 6.6 g of Dowex 50W-X8 (first separation: 89.7 ± 6.6 % (n = 8) of ^{52}Mn recovered for m = 54.6 ± 2.6 mg, $SF_{(V/Mn)}$ = 448 ± 33), and, then 500 mg of Dowex 50W-X8 for the second rough separation V/^{52}Mn 87.4 ± 11.8 % (n = 12) of ^{52}Mn recovered, $SF_{(V/Mn)}\approx$ 2. The average yield of recovery after the cation exchange column (1 and 2) step is good 78.4% with $SF_{(V/Mn)} \approx$ 900 (between V and Mn). The optimization of 0.5 M, 1.5 M, and 7 M HNO_3 volume will improve this yield in step 1. For the second separation, the use of 0.5 M HNO_3 will increase the $SF_{(V/Mn)}$. Nevertheless only 0.2 ± 0.1 % (n = 10) of the V target was recovered for step 2 (equivalent to 70 µg (35 mg) – 190µg (95 mg)). For extraction of metals, two methods have been used with similar purification results of ^{52}Mn recovery yield: 94.2 ± 1.3% for anion exchange resin AG1-X8 versus 86.6 ± 3.4% for extraction AC resin. However, the AC resin method gives a cleaner ^{52}Mn solution with less metals, particularly iron. About the separation time and quality of the ^{52}Mn final solution, the AC resin experiments (Dw in nitric acid and dynamic mode) demonstrated its capacity to remove V whereas ^{52}Mn is fixed on resin and could be used instead of a second column of Dowex 50W-X8 resin. Finally, percent ^{54}Mn in the product (EoB) was weak at 0.09 ± 0.02 % by alpha irradiation in a range of energy (34.4 - 45.0 MeV). At the time, in all cases, ^{54}Mn will be produced at a weak percentage which is a crucial point relative to French regulatory authorities particularly in terms of waste management. However, the use of ^{52}Mn in clinical studies is limited due to its harmful dosimetry. It could be used in preclinical studies for the biodistribution of new Mn-labelled drugs. Although the radiochemical separation process is good, a high AMA needs a high activity that anticipates an automation process for regular manipulation to limit radiation to personnel (operator, researcher). In this context, this work facilitated access to the production of ^{52}Mn for the development of bimodal MRI/PET imaging using pair ^{52}Mn/^{55}Mn.

4. Chapter 4: Production of ^{165}Er for "in vitro" bimodal MRI/SPECT imaging

Dr. Célia Bonnet develops molecular imaging probes sensitive to concentration of Zn impacting relaxation of Gd. However, in MRI, it's impossible to quantify the concentration of Gd related to signal relaxation connected to [Zn]. That why using a radioactive cocktail of naural Gd/ radioactive Gd we can determine the quantity of radioactive Gd in tumor by quantification of its PET or SPECT signal then knowing the ratio ^{nat}Gd/^{rad}Gd, deduce the[^{nat}Gd] in tumor. Then in MRI, a mixture will be injected in a mouse, and for each [Zn] a relaxation signal will be associated and correlated to known [Gd]. As discussed in Chapter 1, section 1.5.2 Radioactive lanthanides, there does not exist a radionuclide of gadolinium that is suitable for PET or SPECT imaging, and so ^{165}Er will be used as a radiolanthanide surrogate. This chapter describes production, isolation, and *in vitro* proof of concept experiments utilizing ^{165}Er for bimodal MRI/SPECT applications.

4.1 Production of ^{165}Er

4.1.1 Generalities

^{165}Er can be produced by a cyclotron or a neutron reactor. The neutron pathway leads to a large range of activities and the result is "carrier added" (i.e. presence of other isotopes of Erbium). However, a "no carrier added" pathway is the best way for radiolabelling ligand in efficient yield and applications. Therefore, irradiation with a cyclotron, starting from a different element is useful. Proton, deuteron, or alpha particle irradiation of erbium or holmium targets produces no-carrier-added ^{165}Er through a nuclear reaction routes according to the chart of the Nuclides (Figure 4.1).

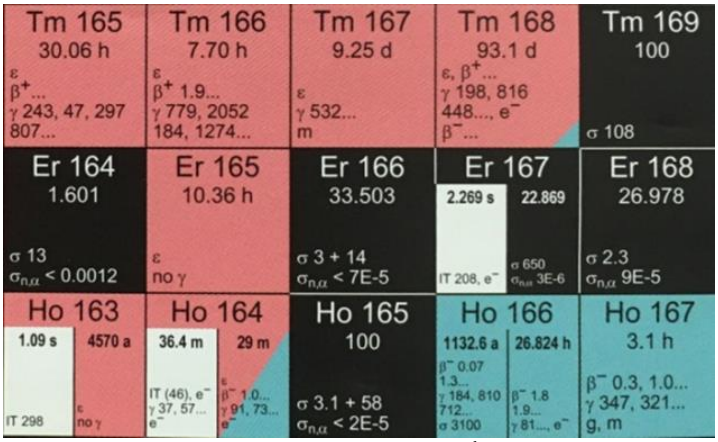

Figure 4.1: Chart of the nuclides (10th Edition 2018)

Proton or deuteron irradiation of erbium produces ^{165}Tm ($T_{1/2}$ = 30.06 h) via ^{nat}Er(p,xn)^{165}Tm [145,146,147] or ^{nat}Er(*d,xn*)^{165}Tm [148] respectively, which can be chemically isolated before its β^- decays to ^{165}Er. While these routes offer high ^{165}Er yields, they require a medium energy, multiparticle research cyclotron, and expensive, isotopically enriched targets for the highest yields. Irradiation of naturally monoisotopic holmium targets produces ^{165}Er using 35 – 70 MeV alpha particles via ^{165}Ho(*α,4n*)^{165}Tm (β^- decay)^{165}Er [149,150], 10 – 20 MeV deuterons via ^{165}Ho(d,2n)^{165}Er [151,152], or 6 – 16 MeV protons via ^{165}Ho(*p,n*)^{165}Er [63,153,154]. All these

irradiations can be done at Orleans'cyclotron due to its broad energy and particle capabilities (see 1.3.2. Orleans'cyclotron, table 1.3). The alpha irradiation to produce a generator ^{165}Tm/^{165}Er will be treated on the Outlooks part of this work (section 6.1.2. Generator ^{165}Tm/^{165}Er). The existence of more than 1000 cyclotrons capable of accelerating low-energy protons (< 20 MeV) makes the latter route particularly accessible to the research community worldwide[155].

4.1.2 Irradiation

For *in vitro* bimodal MRI/SPECT imaging, irradiations were done at Orleans'cyclotron using proton (16 MeV) and deuteron (17.5 MeV) irradiation of a Ho foil target. Hatch tip targetry was used for these experiments (see Chapter 3 section 3.1.3.1.1), and because there is no cooling on this system only particle intensity on target was limited to 3 µA. ^{165}Ho is the single stable isotope of holmium (100% abundance). ^{165}Er is produced via ^{165}Ho(p,n)^{165}Er nuclear reaction and decays by EC (Electron Capture) to ^{165}Ho. Another nuclear reaction happens, producing the ^{166}Ho ($T_{1/2}$ = 26.8 h) in a low amount. It is produced by ^{165}Ho(n,g)^{166}Ho from prompt neutrons produced by proton scattering in the beamline and target assembly. For optimization of separation, the radiotracer method was applied to pair ^{166}Ho/^{165}Er to follow ^{nat}Ho and ^{nat}Er, respectively. The deuteron nuclear reaction ^{165}Ho(d,2n)^{165}Er was also used to increase the amount of ^{166}Ho ((produced via ^{165}Ho(d,p) in addition to ^{165}Ho(n,g)) and facilitate its detection by gamma spectrometry.

4.2 Separation Ho/Er

4.2.1 Separation of lanthanides

Because lanthanides have very similar chemistry, separation between them is challenging. Due to lanthanide contraction, they could be divided into two sub-groups: light lanthanides (La to Eu) with higher similarity with actinides and heavy lanthanides, with smaller ionic radius, and this aspect is used to improve separation between these elements. Ho and Er are heavy rare earths (Figure 4.2).

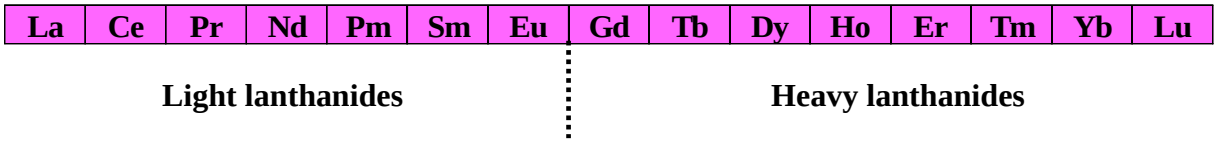

Figure 4.2: Division of lanthanides, light and heavy

The complexing agent, alpha-hydroxyisobutyric acid (α-HIBA) was first used in 1956 as a superior reagent to separate individual members of the lanthanide series from a complex mixture using a cation-exchange resin Dowex 50 [156,157]. It is widely used in the separation of lanthanides[136]. Two aspects further complicate the necessary ^{nat}Ho/^{165}Er separation: first, they are neighbouring rare earths, second, there is a huge mass ratio between Ho target and ^{165}Er. Usually, a demonstration of such separation is made at the analytical level with an online chromatographic system (HPLC: High-Performance Liquid Chromatography) on balanced mixtures or traces (some ng (nanogram) or pg (pictogram)) for each lanthanide. Separation of a few ng of ^{165}Er from 100 mg of natural holmium requires more attention to the separation parameters. In addition, the acidity and volume of the final solution need to agree with the ^{165}Er application (bimodal MRI/SPECT imaging in vivo, Auger emission therapy)[158]. Some radiochemical separations of adjacent lanthanides (heavy rare earth) using the complexing

agent, α-HIBA, have been recently reported effectively separating Gd/Tb[159,160], Dy/Ho[161], Ho/Er [63,153], and Er/Tm [162,163]. Alternatively to cation exchange chromatography with its high capacity but low selectivity, extraction chromatography (EXC) combines the selectivity of liquid-liquid extraction with the ease of operation of column chromatography. It was introduced to the field of radiochemistry through the pioneering work of Winchester[164] of use of classical bis(2-ethyl-1-hexyl) phosphoric acid (HDEHP)-based solvent extraction system to separate the lanthanides elements from each other in the USA, and Siekierski and Kotlinska in Poland, in the late 1950's[165,166].

Extraction chromatographic systems consists of three major components: 1) an inert support, made of porous organic polymer ('resin') particles packed into a column: in general, 20 – 200 mm particle-size is used for gravity flow columns, 2) a stationary phase, consisting of water immiscible liquid extracting agent (here HDEHP) coating and impregnating as a thin film the porous inert support, 3) a mobile phase, made of aqueous acid solutions, flowing down around the porous beads coated with the stationary phase, and containing the solutes to be separated. Extraction-chromatographic materials based on acidic organophosphorus extractants are conventionally used for rare-earth element separation. Some extraction resins[167,168] impregnated with acidic organophosphorus extractants including bis(2-ethylhexyl) phosphoric acid (HDEHP, LN resin)[169,170], 2-ethylhexyl phosphonic acid mono-2-ethylhexyl ester (HEHEHP, LN2 resin)[102,158,171,172], and bis(2,4,4-trimethyl-1-pentyl)phosphinic acid (H[TMPeP], LN3 resin)[172,173] have been used to separate adjacent heavy lanthanides. These resins have also been applied for the microcomponent separation from a macrocomponent[174,175] in a mixture of lanthanides. These extraction resin series (LN, LN2, LN3) are commercialized by TRISKEM company (Figure 4.3).

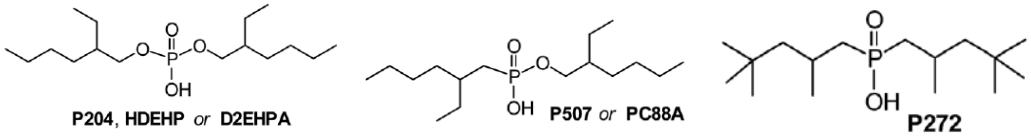

Figure 4.3: Chemical structures of extractants used in LN (P204), LN2 (P507) and LN3 (P272) resin.

HDEHP has been widely used for primary separation because the distribution coefficients of the rare earth elements differ markedly from impurities in leach groups (e.g. in spent fuel actinides and rare earth elements)[176]. According to data sheets about series of LN extraction resin (LN, LN2, LN3)[177] confirmed with work of Salla Tapio[172], under the same concentration of nitric acid, retention percentages of Ho and Er decrease in order LN1 > LN2 > LN3. For this reason, LN2 resin based on mono-2-ethylhexyl ester of 2-ethylhexyl phosphonic acid (HEHEHP) was chosen because rare earths can be stripped at lower acidities than from HDEHP[184].

4.2.2 Extraction with LN2 resin

There are two different methods to determine distribution coefficients (Dw), batch (static method) and column (dynamic method). In the batch method, the resin is added to a solution that contains ions of the element for which Dw is determined. The mixture is stirred until equilibrium is reached. Finally, the resin and solution are separated and the concentration (mass) of the ion in both phases is determined. In the column method, the resin is packed into a column and a solution containing the ions is passed through the column[179].

4.2.2.1 Dw for Ho/Er separation

4.2.2.1.1 Materials and Methods

To establish conditions of separation of ^{165}Er from the Ho target, first distribution coefficients $Dw_{(Ho)}$ and $Dw_{(Er)}$ were determined for LN2 [(20 – 50 µm), density: 0.37 g/mL; capacity: 0.16 mmol (trivalent actinides and lanthanides)/ Conversion factor Dw/k' :1.75] in contact with [HNO_3] = 0.1, 0.2, 0.3, 0.4, 0.5, 0.8, 1, 2, 5 M. In previous unpublished experiments, particle size was found to significantly affect the dynamic column separation of radiolanthanides Dw being similar, as determined by static tests (for example in the case of LN2 20 – 50 µm and 50 – 100 µm). Briefly, a target of natural Ho (0.3 mm thickness, 196 mg) was irradiated for 2 h at 2 µA at 17.5 MeV deuteron resulting in end of bombardment activities (A_{EoB}): ≈ 800 MBq ^{165}Er and 100 MBq ^{166}Ho. The irradiated foil was dissolved in 1 mL of 5 M HNO_3 solution and diluted with water to 5.5 mL giving the crude solution. Around 100 mg of LN2 (20 – 50 µm) resin was weighed for each test performed in triplicate. In every tube, LN2 resin was mixed with 1.4 mL HNO_3 taking into account the 100 µL of crude solution added (around 14.6 MBq of ^{165}Er / 1.8 MBq of ^{166}Ho, 3.5 mg Ho mass, 50% capacity of resin). For a concentration of 0.4 M HNO_3, two supplementary batches were done with 7 mg (100 % of resin capacity) and 14 mg of Ho (200 % of resin capacity). Every tube was shaken for 30 min, then allowed to rest and centrifuged for 20 min. 500 µL of each solution were extracted and measured at an acceptable dead time (<8 %) by high HPGe spectrometry in a calibrated geometry (see section 3.1.3.2.3. gamma-ray spectrometry).

4.2.2.1.2 Determination of Dw

4.2.2.1.2.1 Concept of distribution coefficient

The distribution coefficient describes the degree to which an analyte is retained on the solid phase (resin) under chosen experimental conditions (pH, molarity of acid, analyte concentration). High distribution coefficients (>1000) indicate that the element of interest is strongly retained on the resin. When the distribution coefficient is in the 100 < Kd < 1000 interval, the element of interest is moving slowly with the mobile phase. Distribution coefficient between 0 and 10 represent a situation where an analyte is has a low affinity for the resin. Dw (mL/g) is equal to the activity of an element in the solid phase divided by its activity in the liquid phase according to Equation (19):

Equation (16)
$$D_w = \frac{A_s}{A_l} * \frac{V_l}{m} = \frac{(A_0 - A_l)}{A_l} * \frac{V_l}{m}$$

Where V_l is the volume of the eluent (mL), m is the resin mass (g), A_s is the activity of element in the solid phase, A_0 initial activity in solution without contact with resin, and A_l activity in the liquid phase. A_s A_0 and A_l are measured in Bq.

A Ho/Er selectivity factor α can be calculated as the ratio between the distribution coefficients of two elements using equation (20):

Equation (17)
$$\alpha = \frac{D_{W\,(Ho)}}{D_{W\,(Er)}}$$

The higher the selectivity factor is, the more readily the elements can be separated under the given conditions. These values depend on the experimental conditions and are calculated in batch experiments. In a previous study by Horwitz et al.[180], the following selectivity factors

were obtained: 2.0 for Nd/Pm separation on LN1 resin, 1.9 and 1.6 for Sm/Eu and Eu/Gd pairs on LN1 resin, respectively, 2.5 for Dy/Ho separation on LN2 resin and 2.2 for Yb/Lu on LN2 resin. The selectivity factor is sometimes also called separation factor. The use of this nomenclature is discouraged[181]. A more appropriate definition for separation factor (SF) is introduced for the column-based radionuclide separation experiments in section 5.3.1.

4.2.2.1.2.2 Results

Until 0.3 M HNO_3, $Dw_{(Ho)}$ and $Dw_{(Er)}$ decrease identically. At 0.4 M, $Dw_{(Ho)}$ for 50% capacity = 11.2, meaning that Ho is not retained at this concentration, whereas Er with Dw = 30.8 will be fixed on resin. Increasing the mass of holmium to (100%) and above (200%) the capacity of the resin significantly decreases Dw of Ho (by 48 – 58%) and Er (by 49 – 66%), indicating that saturating resin with Ho will impact Ho/Er separation. To limit the volume of ^{165}Er recovery, the concentration of HNO_3 needs to be ≥ 1 M. At this concentration, Ho is completely eluted when Er desorbs slowly (Table 4.1). In all cases, values of $Dw_{(Ho)}$ and $Dw_{(Er)}$ for LN2 demonstrate the challenge of separating two adjacent lanthanides (Table 4.1).

[HNO_3]	**Dw (mL/g)**					
	Ho			**Er**		
0.1	44.7	±	0.6	108.4	±	3.2
0.2	21.5	±	2.3	59.3	±	7.7
0.3	16.7	±	0.4	45.7	±	1.3
0.4 - 50 %	11.2	±	0.5	30.8	±	2.0
0.4 - 100 %	5.8	±	0.4	15.7	±	1.2
0.4 - 200 %	4.7	±	0.2	10.5	±	1.1
0.5	8.6	±	3.5	23.4	±	1.5
0.8	3.9	±	0.1	10.4	±	0.2
1	2.6	±	0.1	5.4	±	0.2
2	1.8	±	0.4	3	±	1.0
5	- 0.4	±	0.3	0.1	±	0.4

Table 4.1: $Dw_{(Ho)}$ and $Dw_{(Er)}$ in LN2 resin (20 – 50 µm) at various [HNO_3]

Values of $Dw_{(Ho)}$ and $Dw_{(Er)}$ are not sufficiently different to elaborate a « catch and release » protocol at a defined concentration of eluent as we used for Cr in the production of ^{52}Mn. Here, using directly 1 M HNO_3 to elute Ho is not very efficient because most of Er will be eluted with Ho due to a small difference in Dw. A gradient of nitric acid concentration is more beneficial. For that, the Ho target was dissolved in 0.1 M of HNO_3 and loaded on LN2 resin creating an initial variation of Ho from Er due to its Dw (45 versus 108 at 0.1 M). Then 0.4 M HNO_3 solution increases progressively [HNO_3] in the column until most of Ho is recovered in 0.4 M HNO_3 whereas in these conditions Er will be eluted more slowly. Finally, 1 M HNO_3 is used to desorb the rest of Er from the resin. Even with this protocol, because Dws are not much different, the lost of part of Er is unavoidable. A compromise is necessary between an acceptable time of elution of ^{165}Er relative to its half-life, its quality ([Ho] as low as possible), and volume and acidity for the recovered solution of ^{165}Er.

4.2.3 Elution of LN2 (resin 20 – 50 µm)

4.2.3.1 Manual separation

A 100 mg Ho target was irradiated with a proton beam at 16 MeV, then dissolved to 15 M nitric acid, evaporated to dryness and reconstituted in 2 mL of 0.1 M HNO_3. A radiochemical separation using a ≈ 4 g column of LN2 resin (20 – 50 µm, 14 cm height, 1 cm inner diameter, flow of 1 - 2 drops/second (1 mL/min) under 1 bar of nitrogen) was performed. The column was preconditioned with 15 mL of 5 M HNO_3, 50 mL of water until neutral pH and 15 mL of 0.1 M HNO_3. After deposition 2 mL of ^{165}Er on the column, Ho was eluted with ≈ 110 mL of 0.4 M HNO_3, and then ^{165}Er was recovered in 1 M HNO_3. By this process, 75 – 80 % of ^{165}Er was isolated in a 1 M HNO_3 (7 – 26 mL) solution with less than 1% of Ho, as determined by HPGe spectroscopy of ^{165}Er/^{166}Ho in the eluted fractions. Using higher nitric acid concentration would reduce the final volume of ^{165}Er solution. The profiles of three replicated separations are shown below in Figure 4.4.

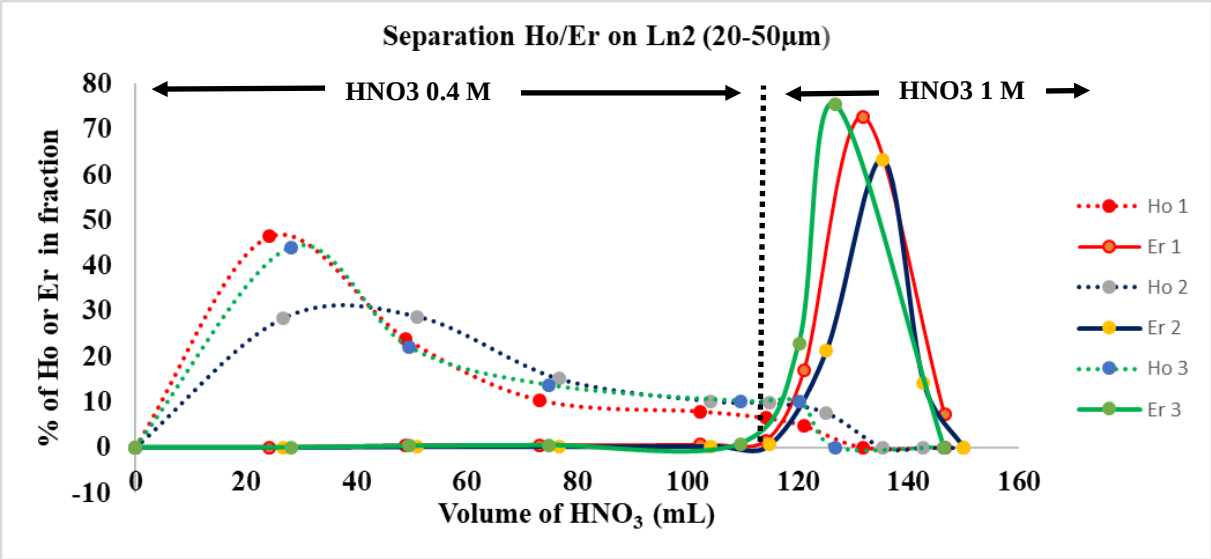

Figure 4.4: Profile of the three separations of Ho/Er using ^{165}Er/^{166}Ho as a tracer

The separation of Er/Ho by the LN2 resin extraction (Triskem) gave good separation results using an step-wise elution gradient. Using 1 M HNO_3, the first 10 mL need to be excluded because 1) the dead volume of the column is equivalent to this volume, 2) <10% of Ho will be on the column and are eluted together with ^{165}Er reducing its purity. Volume variation of 1 M HNO_3 needs to be optimized or higher concentration of nitric acid used after eluting the column with 10 mL of 1 M HNO_3. The ratio of $^{166+165(nat)}$Ho/Er before and after extraction (on ^{165}Er batch) goes from more than 2.10^7 to less than 40000. Estimations are made with an initial ratio of ^{166}Ho/^{165}Ho where the target weight (^{165}Ho) is known and the weight of ^{166}Ho is defined by relationship activity-weight.

4.2.3.2 Semi-automatized

To anticipate a high activity of ^{165}Er in the future (produced via deuteron instead of proton irradiation) and protect the operator during the radiochemical separation, the separation was automated using the ACCRA system (described in section 2.2.2.2.1) were done using control sketch below (Figure 4.5) from the dissolution step of target until to final evaporation of 1 M HNO_3.

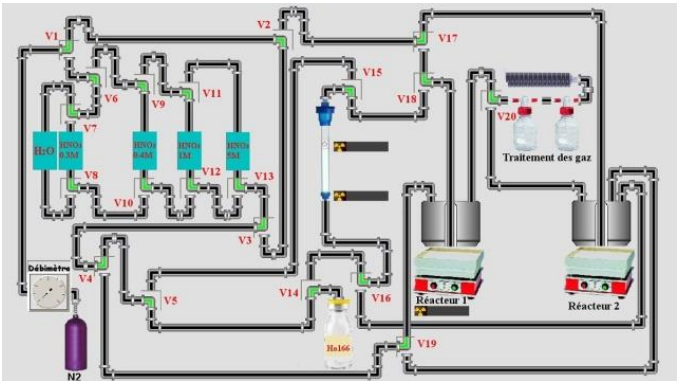

Figure 4.5: Remote control of Ho/Er separation

Automation has proved necessary for radiation protection with increased activity of ^{165}Er and more with multiplication of deuteron irradation experiments. A more sensitive evaluation of the quality of a ^{165}Er batch and its ratio $^{166+165(nat)}$ Ho/Er must be performed regarding the quality of the irradiated target and the generated by-products. At least, this Ho/Er separation protocol can readily be adapted as it answers issues on radiolanthanides extraction where the separation of micro from macro component is crucial.

4.3 Validation of bimodal MRI/SPECT imaging (^{155}Gd/^{165}Er)

4.3.1 Concept of Zn^{2+} sensitive molecule

The quantitative in vivo mapping of endogenous metal ions would be highly important as their spatial and temporal distribution is often not well known. Zn^{2+} is the second most important transition metal ion in the body, required for over 300 different cellular processes, including enzyme activities, DNA and protein synthesis or signaling. The brain, prostate, breast, and pancreas have a particularly high content of zinc (mM to µM depending on the physiological or pathological state), in a range accessible by MRI[182]. Misregulation of zinc has been associated with cancers[183], diabetes[184], and neurodegenerative diseases[185]. Nevertheless, its role is not completely understood and remains an active area of research. There is a clear need for quantitative assessment of zinc via non-invasive imaging techniques. The development of "smart" or responsive MRI contrast agents is a new area that emerged several years ago. Chemistry developments have been very active with several examples of such agents reported in the literature. Despite progress in their *in vivo* use, it is not possible to access the local zinc concentration. The MRI response of the contrast agent is dependent not only on the biomarker but also on the concentration of the agent which prevents quantitative assessment. Therefore there is an urgent need for methods allowing quantitative detection[158]. Quantitative detection using small molecule bimodal agents can be achieved, either by combining an MRI and a PET/SPECT reporter in the same molecule, or by injecting a cocktail of imaging agents for each technique. Both approaches have been applied to pH mapping[186,187] but cannot systematically be translated to cation detection. The second approach where a cocktail can be tuned to respect the sensitivity of each imaging technique was applied to our case assuming that the biodistribution of the two molecules complexed with ^{155nat}Gd (MRI) and ^{165}Er (SPECT) are similar. Gianolio et al[187] took advantage of the similar chemical properties of Ln^{3+} ions and used the mixture of a pH-responsive Gd^{3+} complex and its radioactive $^{166}Ho^{3+}$ analogue. With the production method used to obtain ^{166}Ho, their samples were diluted in a high amount of ^{165}Ho. Although they achieved pH detection, this approach would be unrealistic to detect biomarkers in µM or even mM concentration, as the high quantity of bulk ^{165}Ho present would

strongly limit the attainable MRI response. The combination of the two techniques has already proven powerful to achieve both good resolution and sensitivity.

4.3.2 Materials and Methods

4.3.2.1 Ligand L1

Here, we propose to use $^{165}Er^{3+}$ and demonstrate the quantification of Zn^{2+} using a cocktail of the Zn^{2+}-responsive MRI agent GdL1 and its [^{165}Er]Er-L1 analogue[188].

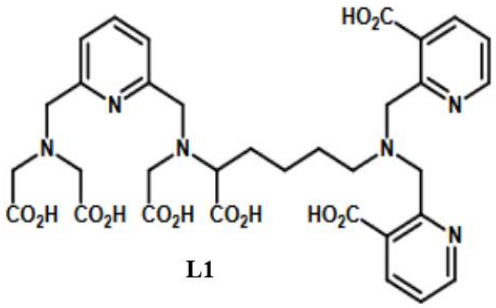

Figure 4.6: Ligand L1

The ligand 2,2'-(((5-((((6-((bis(carboxymethyl)amino)methyl)pyridin-2-yl)methyl) (carboxymethyl)amino)-5-carboxypentyl) azanediyl)bis (methylene))dinicotinic acid (called L1) consists of a polyaminocarboxylate unit with a pyridine backbone to chelate the Ln^{3+}, a linker, and a Zn^{2+} binding unit (Fig. 4.6). It was synthesized by Dr Bonnet et al.[158]. The relatively good thermodynamic stability and kinetic inertness of LnPy complexes ensure their safe use in animal studies, as previously demonstrated. The Ln^{3+} has two inner sphere water molecules which are not replaced by physiological anions and confer high relaxivity to the Gd^{3+} complex. The complex responds to Zn^{2+} in the presence of human serum albumin (HAS).

4.3.2.2 Cocktail ([^{155}Gd]Gd-L1/[^{165}Er]Er-L1)

A cocktail with a known GdL1/[^{165}Er]Er-L1 mole ratio (1/2.4 x 10^{-7}), set according to the relative sensitivities of MRI and SPECT detection, was prepared in HSA solution (0.6 mM, physiological concentration). For the radiolabeling, the pH of the ^{165}Er solution was adjusted between 5 - 7 with NaOH and 1:30,000 molar ratio of ligand added (the excess of L1 is used to complex the remaining $^{165}Ho^{3+}$) using the following procedure: 27 µL of L1 at 1.1 mM (29.7 nmol) were added to 13 MBq (415 µL) of $^{165}Er^{3+}$ ($n_{(Er)}$ = 1.15 x 10^{-12} mol). The mixture is incubated for 10 min at room temperature. The radiochemical purity was followed by thin-layer chromatography (TLC, silica plates), using Water/Methanol/Acetic Acid (4:4:0.2) as the mobile phase. The TLCs are exposed on a multisensitive phosphor screen (Packard, Perkin Elmer, Meriden, USA, and imaged on a Cyclone Storage phosphor system Packard, Perkin Elmer, Shelton, USA). In this system, the free ^{165}Er has Rf = 0 – 0.1 and the [^{165}Er]Er-L1 has an Rf = 0.8[3]. This solution was then diluted to give five samples, to which unknown concentrations of Zn^{2+} were added while keeping the HSA concentration constant at 0.6 mM for all samples. The activities were measured by gamma spectrometry. Then the samples were imaged using a high-resolution gamma camera (Biospace Mesures, Paris, France) equipped with a position-sensitive photomultiplier tube and a parallel collimator (20 mm thickness) with 1.7 mm holes. Images were recorded with a 128 x 128-pixel and 16 - bit matrix, with a spectral window centered 20 % on the photopeaks of the ^{165}Er, shown in Figure 4.7a. The concentration of $^{165}Er^{3+}$ was calculated from the signal intensity, giving access to the Gd^{3+} concentration (by knowing the

Gd/Er ratio). These Gd^{3+} concentrations correspond within 6% to those calculated according to the dilutions and the concentrations of the Gd^{3+} stock solution (which was determined by bulk magnetic susceptibility shifts (BMS)[189] (Figure 4.7b). This is within the range of the experimental uncertainty calculated to be ca. 16%. Finally, after total decay of the samples (ca. 1 – 2 weeks), a T1-weighted MR image was recorded on a 1.5 T scanner (Signa HDxt, General Electric, Milwaukee, USA). The longitudinal relaxation times measured were translated into relaxivity using the Gd^{3+} concentration calculated for each sample.

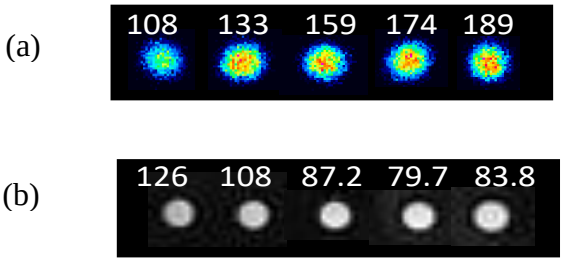

Figure 4.7: T1-weighted images of the five samples (T1 values are in ms) at 1.5 T using a spin echo sequence with TE = 9 ms and TR = 100 ms; T1 values measured with variable TR from 20 to 2000 ms (a)corresponding images from the gamma camera (activities are in kBq) (b).

4.3.3 Comparison of $[Zn^{2+}]$: bimodality versus ICP-OES

The $^{165}Ho/^{165}Er$ ratio is estimated to be between $3 \cdot 10^4$ (measured from the purification issued from a deuteron production) and 10^6 (maximum estimation from the proton production using the limit of detection of the HPGe detector). Indeed, the presence of $^{165}Ho^{3+}$ is detected through the activity of $^{166}Ho^{3+}$ knowing the $^{165}Ho/^{166}Ho$ ratio after irradiation of the foil. ^{166}Ho activity produced via deuteron reaction is always measured allowing us to calculate the ratio $^{165}Ho/^{165}Er$ precisely. From the proton production, due to lower quantities of $^{166}Ho^{3+}$, ^{166}Ho is below detectable limits in the ^{165}Er fraction. The limit of detection of the HPGe detector gives an estimation of the ratio $^{165}Ho/^{165}Er$ of 10^6. The concentration of $^{165}Er^{3+}$ produced being 10^{-10} M, $^{165}Ho^{3+}$ concentration should be around $3 \cdot 10^{-6}$ and lower than 10^{-4} M, which should indeed not impact the MRI response in the presence of $3 \cdot 10^{-4}$ M of Gd^{3+} complex. Based on a calibration curve recorded on the same MRI scanner and at the same temperature, the experimental Zn^{2+} concentrations were calculated from the measured relaxivities (Table 4.2).

- **MRI Imaging** :

All acquisitions were performed on a 1.5 T MRI scanner (Signa HDxt, General Electric, Milwaukee, USA) with a homogenous emitting/receiving single-element head coil. Acquisitions consisted of a series of conventional single slice (7 mm thickness) spin echo sequences with short echo time (TE = 9 ms) and different repetition times (TR = 20, 40, 60, 80, 100, 120, 140, 160, 180, 200, 500, 1000, 1500 and 2000 ms), and a 256 x 256 matrix. Samples were previously stored in the acquisition room, to avoid temperature variation during scanning.

The experimental error on the Zn^{2+} concentrations was calculated to be 23%. We also determined the Zn^{2+} concentration of each sample via ICP-OES, and a good agreement was obtained (the difference between the concentration measured via ICP-OES and determined via relaxivity measurements is a maximum of 16.1 %, within the experimental error)[158] (Table 4.2).

	$[Zn^{2+}]_{exp}$ (mM)	$[Zn^{2+}]_{th.}$ (mM)	Error (%)
Sample 1	0.33	0.32	2.6
Sample 2	0.29	0.29	1.7
Sample 3	0.54	0.49	11.0
Sample 4	0.62	0.55	13.1
Sample 5	0.10	0.12	16.1

Table 4.2: Zn^{2+} concentration determined by the use of the bimodal cocktail of GdL/[^{165}Er]Er-L (exp.) and by ICP(th.)

4.3.4 Conclusion

These experiments demonstrated the potential application of ^{165}Er in vitro bimodal MRI/SPECT imaging. Nevertheless, the high molar ^{165}Er /ligand ratio (1:30000) and estimation of $SF_{(Ho/Er)} \approx 1000$ are indicators of a low AMA according to equation (16) (see section 3.2.1.1. Optimization of target). This work also lays the foundation for Chapter 5 where we produce and isolate ^{165}Er with even higher AMA.

5. Chapter 5: High apparent molar activity ^{165}Er

Introduction:

Radiopharmaceuticals Lutathera® ([^{177}Lu]DOTATATE) for neuroendocrine tumors[190] and [^{177}Lu]PSMA-617 for prostate cancer[191] show receptor-targeted, medium-energy-electron-emitting radiopharmaceuticals are effective in treating these solid tumors. However, for the treatment of micrometastatic or disseminated cancers, radiopharmaceuticals emitting shorter range, higher linear energy transfer (LET) radiations, such as Auger electrons (AE), show potential in preclinical studies[192–194]. Following decay, AE-emitting radionuclides release a cascade of 0.02 – 50 keV electrons that stop with high LET over subcellular, nano- to micrometer ranges. These properties give AE-based radiopharmaceuticals reduced cross-irradiation of healthy tissues and off-target dose burden compared with β⁻-emitting radionuclide therapeutics. Furthermore, when tumor-specifically localized to radiation-sensitive subcellular structures such as DNA[195], this may result in higher maximum tolerated doses and expanded therapeutic windows.

The biological impact of these AEs is also evident in comparison studies of ^{177}Lu- and ^{161}Tb-based radiopharmaceuticals[196–198] which are biologically, chemically, and physically matched, with the exception that ^{161}Tb has ten times larger AE emission yields (Table 5.1.)[199]. Fundamental radiation biology studies of the effects of AEs require a pure AE-emitting radionuclide, with minimal concomitant medium/high energy electron or photon emissions. Erbium-165 decays by electron capture with only low energy x-rays and AE emissions (Table 5.1)[199]. As a heavy lanthanide, ^{165}Er can radiolabel the same biological targeting vectors used to deliver ^{177}Lu and ^{161}Tb [200], allowing for comparative studies of pure AE-emitting (^{165}Er), β⁻-emitting (^{177}Lu), mixed AE- and β⁻-emitting (^{161}Tb) radiopharmaceuticals. Thus, ^{165}Er is a useful tool for fundamental studies on the biological effects of AEs and, if incorporated into an appropriate biological targeting vector, for the targeted radionuclide therapy of metastatic and disseminated disease.

R.	Half-life (d)	Avg. AEs per decay	Avg. Energy per AE (keV)	Avg. β⁻ per decay	Avg. Energy per β⁻ (keV)
^{177}Lu	6.64	1.1	1	1	133
^{161}Tb	6.89	11	5.7	1	154
^{165}Er	0.43	7.3	11	0	0

Table 5.1: Comparison of AEs and β⁻-particles emitted by ^{165}Er, ^{161}Tb, and ^{177}Lu

For application in receptor-targeted therapeutic radiopharmaceuticals, a high molar activity (MA) is necessary to achieve good radiolabeling yield of small pharmaceutical masses with large amounts of radioactivity. This high molar activity ensures that the biologically administered mass of radiopharmaceutical is sufficiently small to not saturate the targeted receptor on diseased cells. When prepared for human use, [^{177}Lu]PSMA-617 and [^{177}Lu]DOTATATE are radiolabeled with high yield at a molar activity of 60 MBq/nmol[201,202]. To accomplish this MA for biomedical cyclotron produced ^{165}Er, the radionuclide must be chemically isolated from the holmium target material with a high (> 10^5) separation factor ($SF_{(Ho/Er)}$) due to residual target material competition with ^{165}Er during radiolabeling chemistry. To define the MA of produced ^{165}Er, an estimation was calculated, called AMA (apparent molar activity). After describing the equation (21) of AMA adapted to the production of ^{165}Er, the impacts of cyclotron target, irradiation conditions (Orleans'cyclotron, Madison's cyclotron,

targetry, type of beam (proton, deuteron)) and radiochemical separation parameters will be investigated. AMA will be determined by MP-AES or ICP-OES analysis and DOTA/DTPA titration by radiolabeling for each optimal production at Orleans (F) and Madison (WI, USA) conditions. Next, a radiolabeling of PSMA-617 with ^{165}Er demonstrates the ^{165}Er product's suitability for AE emitter therapy applications. Finally, a preliminary radiolabeling ligand with high AMA ^{165}Er for "in vivo" bimodal MRI/SPECT imaging will be presented. Some irradiations and separation parameters need to be evaluated and upgraded to access a high AMA of ^{165}Er, a crucial point for specific targeting of tumor cells *in vivo*.

Note: AEs are sometimes also known as Auger-Meitner or Meitner-Auger electrons[203,204] but these terms have unfortunately no scientific sense. Today it is known that Lise Meitner never observed AE in the radioactive decays she had studied. What Lise Meitner[205], who was one of those responsible for the discovery of nuclear fission, observed conversion electrons, not AE. Both types of electrons are emitted in different physics processes and should not be confounded. This fact has been explained in detail, e.g. by H.E. Mahnke[206], and this finding was confirmed by an international expert group that has reviewed all relevant historical documents, recently presented at the 10th International Symposium on the Physical, Molecular, Cellular and Medical aspects of Auger Electron processes, September 6-8, 2023, Historial session, the Discoveries of Auger Electron Processes. A written summary of these findings will be published.

5.1 ^{165}Er AMA

5.1.1 Formulation of Apparent Molar Activity for ^{165}Er

AMA described in section 2.3.4.2.1. Definition: Apparent Molar Activity was applied to ^{165}Er with $T_{½}$ = 10.36 h. The activity (in Bq) in 1 mol is equal to :

$0.693/(10.36 \times 60 \times 60) \times 6.022 \times 10^{23} = 11190$ GBq/µmol or MBq/nmol

Because 1 Ci = 3.7×10^{10}Bq then CFMA ($_{165Er}$) = 302 Ci/µmol or mCi/nmol

CFMA (^{165}Er) = 11190 MBq/nmole or 302 mCi/nmole

AMA is effectively the number of chelator molecules necessary to chelate a given amount of ^{165}Er radioactivity. Non-radioactive elements may compete with ^{165}Er for the chelator during the radiolabeling reaction. As lanthanides, Ho, and Er have similar chemistry, Er mass impurity in the Ho target and residual holmium mass (incomplete isolation of erbium) in the final radionuclide preparation will lower AMA. Usually, the AMA was determined by titration using tetraazacyclododecane-1, 4, 7, 10-tetraacetic acid (DOTA) or diethylenetriaminepentaacetic acid (DTPA). Thus, transition trace metal impurities can lower AMA of ^{165}Er solution in case of no selective lanthanide chelator. Considering ^{165}Er mass, non-radioactive erbium impurity from the Ho target, and residual holmium mass, the maximum achievable EoB AMA (AMA_{EoB} in MBq ^{165}Er per nmole of Ho/Er) of a final formulation of ^{165}Er can be calculated with the following equation (21):

Equation (18)
$$AMA_{EoB} = \frac{A_{EoB} \cdot Y_{165Er}}{\left(\frac{A_{EoB} \cdot 10^6 \frac{Bq}{MBq} Y_{165Er}}{\lambda \cdot N_{Av}}\right) + \left(\frac{m_{Ho} \cdot F_{Er\,imp} \cdot Y_{165Er}}{MW_{Er}}\right) + \left(\frac{m_{Ho}}{MW_{Ho} \cdot \frac{SF_{Er}^{Ho}}{Y_{165Er}}}\right)}$$

with A_{EoB} = ^{165}Er radioactivity in MBq, Y_{165Er} = fractional radiochemical yield of ^{165}Er, λ = ^{165}Er decay constant in s^{-1}, N_{Av} = Avogadro's number in atoms/nmol, m_{Ho}= Ho target mass in ng, $F_{Er\ Imp}$= fractional erbium impurity in Ho target, MW_{Er} = molecular weight of Er in ng/nmol, $MW_{Ho)}$ = molecular weight of Ho in ng/nmol Ho/Er, $SF_{(Ho/Er)}$ (defined in section 5.3.1) = separation factor.

5.1.2 ^{165}Er: what are the parameters to study?

Unless otherwise stated, AMA will be calculated at EoB. According to equation (21), higher AMA will be available by increasing the numerator (produced ^{165}Er activity and high yield recovery of ^{165}Er) and/or reducing denominator values (non-radioactive erbium, residual Ho, and trace metal impurities). For that, some optimization of the following parameters will be done:

- Target: quality of Ho foil (% of natural erbium), mass of Ho target (thickness (µm) and diameter (mm)), preparation.
- Targetry: physical yield ($MBq \cdot e\mu A^{-1} \cdot h^{-1}$), a cross-section of nuclear reaction (beam particle), specifications of cyclotron (biomedical or research), cooling system
- Radiochemical separation: $SF_{(Ho/Er)}$, recovery yield of ^{165}Er (%), time, cation exchange process with complexing ligand versus extraction resin, metals impurities.

5.2 Irradiation of Ho target

Direct water-jet cooled spot-welded targets were utilized for ^{165}Er production by proton beam (20 – 40 µA) in two biomedical cyclotron of Madison and indirectly-cooled on Al support of target by deuteron beam (6 – 10 µm) in Orleans' cyclotron. The power (in Watt) deposited in Ho target is 250 W (12.5 MeV * 20 µA: 12.5 MeV proton) or 350 W (17.5 MeV * 20 µA: 17.5 MeV deuteron). As mentioned in chapter 3 section 3.2.1.2.2., the spot welding preparation technique allows a good control of target size, second parameter impacting significantly the AMA.

5.2.1 Spot welding Ho target

5.2.1.1 Purity of Ho foil

All holmium metal foils contain some erbium metal impurities. Because it is not chemically possible to separate the cold Er impurity from the ^{165}Er radionuclide product, the percentage of cold impurity of Er in Ho foil has a crucial impact on AMA as shown in equation (21). For example, applications on Auger therapy require an AMA > 7.4 MBq/nmol (0.2 Ci/µmole) at the end of synthesis (EoS). To evaluate the impact of Ho foil quality (i.e. the percent Er impurity) on AMA, two parameters must be considered: mass of Ho target and produced ^{165}Er activity. The following realistic hypothetical values were assumed for calculations (Table 5.2.):

- Mass of Ho target: 100 mg
- Product activity of ^{165}Er (EoS): 370 MBq (10 mCi)

		AMA (MBq/nmole)		
	Er impurity in Ho foil	**0.06 %**	**< 0.01 %**	**0.5 ppm**
$SF_{(Ho/Er)}$	10^{4}	0.7	3.0	5.9
	10^{5}	1.1	5.6	57.7
	10^{6}	1.1	6.3	394.4

Table 5.2: Estimated AMA (MBq/nmol) according to ratio of Er impurity of Ho foil

According to the purity of Ho foil, use of ^{165}Er in Auger therapy microdosimetry might be foreseen:

- 0.06 %: no application, cold erbium too much even with a very high Separation Factor ($SF_{(Ho/Er)}$)
- 0.01 %: application in some cases ($SF_{(Ho/Er)} > 10^5$)
- 0.5 ppm: application regardless $SF_{(Ho/Er)}$

5.2.1.2 From a block to a foil

Cyclotron targets were prepared from holmium metal foils. Initially, 300 – 640 µm thick holmium foils (Alfa Aesar, 99.9%) were used. Based on certificates of analysis, two differing foil lots contained 0.06% (600 ppm) or < 0.01% (< 100 ppm) erbium. High purity 0.5 mm thick, 10 mm diameter holmium metal discs with 0.5 ppm Er were purchased from the Department of Energy (DOE) Ames Laboratory Materials Preparation Center (MPC), USA. Based on proton energy loss calculations[127], a 300 µm holmium degrades 12.5 MeV protons to 7.1 MeV, below which the ^{165}Ho(p,n)^{165}Er nuclear reaction cross-section vanishes[63]. Holmium foils were wrapped in 25 µm thickness stainless steel foil and rolled to the desired thickness (190 – 400 µm) using a commercial rolling mill. A commercial disc cutter (Pepetools) was used to punch holmium discs of desired diameter (3 – 9.5 mm). The holmium target disc was centered and spot-welded on a 0.5 mm thick, 19 mm diameter tantalum disc using a variable transformer-controlled (60 – 75% power) commercial 115 V spot welder fitted with a copper or silver electrode, as previously described[133]. Roughly 6 – 10 individual spot welds uniformly covered the 7 to 70 mm² holmium target.

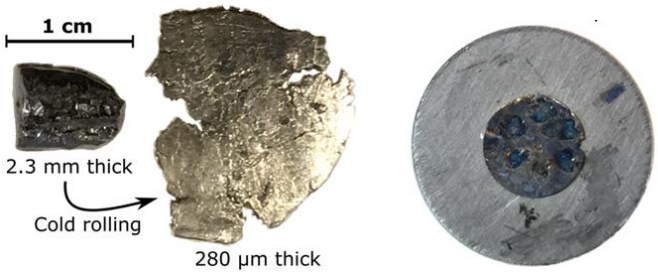

Figure 5.1: Bottom: Holmium (122.2 mg, 7.9 mm diameter, 280 µm thick, 0.5 ppm Er impurity) spot welded to 19 mm diameter, 500 µm thick Ta. Top: 9.1 x 7.3 x 2.3 mm thick Ho piece before and after cold rolling to 16.5 x 19.7 x 0.28 mm thick foil with visible cracking around edges.

Cold rolling, disc cutting, and spot-welding methods were well suited for the fabrication of cyclotron irradiation targets of tightly controlled dimensions and mass from a variety of commercial holmium metal sources. The malleability of holmium allowed for the dramatic thinning of metal foils through rolling. While thickness reduction by factors of two or three was

readily achieved, when an eight-fold change in thickness was attempted, cracking around the edges was observed, as shown in Figure 5.1. Spot-welded holmium was well adhered to the tantalum backing and withstood proton/deuteron irradiation at all investigated intensities.

5.2.2 Proton irradiations

5.2.2.1 Relation thickness/proton energy beam

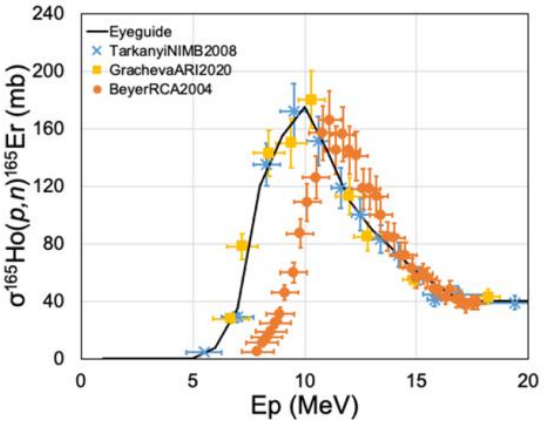

Figure 5.2: ^{165}Ho(p,n) ^{165}Er excitation function with experimental data from Tarkanyi (2008), Gracheva (2020), and Beyer (2004). Cross sections displayed in the black line eye guide were used for theoretical ^{165}Er yield calculations.

The following published or calculated cross-sections for nuclear reaction ^{165}Ho(p,n)^{165}Er TENDL2015, Beyer (2004)[153], Tarkanyi (2008)[154] and Gracheva (2020)[63] were studied. Considering their standard deviation between each other, a combination of Tarkanyi's and Gracheva's cross-section (Figure 5.2, eyeguide) was used to calculate the physical yield (MBq·eμA^{-1}·h^{-1}) of ^{165}Er for a 1 h irradiation of 127 – 750 μm thick of Ho foils at 11, 12.5, 14 and 16 MeV incident proton energies (Figure 5.3).

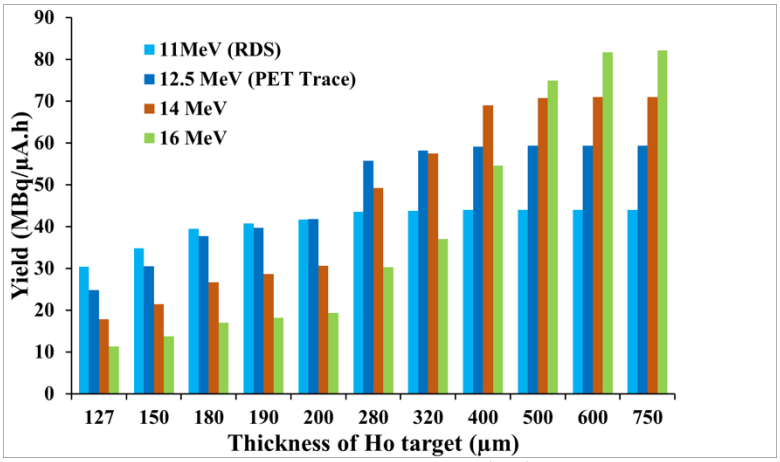

Figure 5.3 : Evaluation of physical yield (MBq·eμA^{-1}·h^{-1}) versus thickness of Ho target

Using an incident beam proton of 11 MeV, a 400 μm thickness will be sufficient to maximize yield. But in these conditions, Ho target mass is two times higher than a target of 200 μm thick for only a 5.2 % increase of produced ^{165}Er activity. Because the separation of lanthanides is challenging, increasing the used Ho mass target increases Er impurities, time of separation, and $SF_{(Ho/Er)}$. The benefit of Ho mass increase is justified by a relevant increase of ^{165}Er activity. For each energy beam, a compromise between Ho thickness (indirectly Ho mass) and expected ^{165}Er activity need to be established: ≈ 300 μm for 12.5 MeV, 325 μm < > 400

µm for 14 MeV, and 450 < > 500 µm for 16 MeV. But in the case of 14 and 16 MeV protons, such used Ho thickness will affect ^{165}Er AMA. Using a smaller thickness of 200 µm halved the produced ^{165}Er activity, nevertheless access to 40 µA current intensity in routine irradiation by biomedical cyclotron limits its impact.

These previous estimations were obtained considering a perfect beam with a sufficient surface of the target to recover all the beam. In practice, especially with the case of the PETtrace cyclotron, only a fraction (~50%) of the proton beam will be incident on a 10 mm diameter target disc[207]. This phenomenon will result in lower measured physical yields relative to calculated values. In all case evaluation of experimental physical yields need to be done.

5.2.2.2 Biomedical cyclotron for irradiations

Spot welded holmium metal targets were proton irradiated at the University of Wisconsin using two biomedical cyclotrons: a CTI-RDS-112 (CTI Cyclotron Systems) and a PETtrace (GE Healthcare), see section 1.3.3 University of Wisconsin-Madison's cyclotrons. For low-intensity irradiations, ^{165}Er was quantified by high purity germanium (HPGe) gamma spectrometry (Canberra, full width at half maximum at 1333 keV = 1.6 keV) of the irradiated target disc, while correcting for the self-attenuation of the 46 – 55 keV x-rays. The HPGe low energy range (30 – 300 keV) was energy and efficiency calibrated using ^{133}Ba and ^{241}Am calibration standards (Amersham).

5.2.2.2.1 CTI-RDS-112 cyclotron

For CTI RDS-112 irradiations, the target disc was clamped to a water-jet-cooled target support fixture with a 12.7 mm apertured aluminum ring and irradiated with 10 – 20 µA of undegraded 11 MeV protons. Target with 3.2 to 7.6 mm diameters were irradiated on CTI-RDS-112 cyclotron. The diameter spot beam was estimated on smaller diameter of target with GAFChrom film (Figure 5.4).

Figure 5.4: GAFChrom film of target 3.2, 4.8, and 6.5 mm diameter irradiated on CTI-RDS-112

5.2.2.2.2 GE-PETtrace cyclotron

For PETtrace irradiations, a commercial solid target irradiation and transfer system (ARTMS QIS, Vancouver, Canada)) was used. Holmium target discs were assembled into the water-jet cooled transfer capsule, positioned 3.6 cm down-beam from a water-cooled 480 ± 20 µm thick aluminum degrader, and irradiated with 20 – 40 µA of 12.5 MeV protons. The reliable and compact pneumatic transfer system allowed delivery and retrieval of the target directly to the cyclotron from a hot cell. A proton irradiation energy of 12.5 MeV centers the ^{165}Ho(p,n)^{165}Er excitation function peak within the energy loss window of the protons traversing a 200 – 300 µm thick holmium target. Experimental end-of-bombardment (EoB) ^{165}Er physical yields were measured via attenuation-corrected HPGe of target discs or dose calibrator measurements of dissolved target aliquots, or CX elution fractions (Table 5.3). The yields show a significant dependence on the holmium target dimensions and the irradiating cyclotron. According to calculations using literature cross-sections[173,208], a 1–2 hour proton irradiation of 275 µm thick holmium results in physical ^{165}Er yields of 50 MBq·eµA^{-1}·h^{-1} at

12.5 MeV and 39 MBq·eμA^{-1}·h^{-10}at 11 MeV. Experimental ^{165}Er physical yields were significantly lower than these theoretical maxima likely because the cyclotron-integrated charge includes protons impinging on the target outside the holmium diameter. This is especially problematic for the PETtrace cyclotron, which has an oblong beam spot with full width at half maxima of 11 and 8.7 mm, as measured by autoradiography of irradiated aluminum discs. One hour irradiations of 40 μA protons resulted in minimal discoloration of the spot-welded Ho disc (see figure 5.2).

Figure 5.5 : Representative image of a 7.9 mm ø, 270 μm thick, 106 mg holmium disc spot-welded to tantalum, before and after 68 minutes, 40 μA·h PETtrace irradiation.

5.2.2.3 Conclusion

The CTI RDS-112 cyclotron provides a significantly smaller beam spot than PETtrace resulting in a higher overall ^{165}Er physical yield, despite the lower irradiation energy and smaller target diameter (Table 5.3). However, the CTI-RDS-112 cyclotron is limited to 20 μA irradiation current, a factor of 2 below that routinely used with the GE PETtrace cyclotron.

Cyclotron	Ho dimensions			Ein (MeV)	Eout (MeV)	^{165}Er physical yield (MBq·μA^{-1}·h^{-1})	n
	diam. (mm)	thick. (mm)	mass (mg)				
PETtrace	9.5	280 - 300	174 ± 8	12.5	7.5	24.1 ± 0.5	5
PETtrace	9.5	200 - 240	125 ± 6	12.5	8.4 - 9.1	19.1 ± 1.1	3
PETtrace	7.9	270 - 280	108 ± 4	12.5	7.8	14.1 ± 1.4	3
PETtrace	7.9	190	69 ± 1	12.5	9.3	12.0 ± 0.9	4
RDS-112	7.9	190 - 280	84 ± 22	11	5.3 - 7.5	28.0 ± 1.8	5
RDS-112	6.4	320 - 620	121 ± 75	11	< 4.8	30.0 ± 6.1	2
RDS-112	4.8	320	48	11	4.2	23	1
RDS-112	4.8	180	23	11	7.7	13	1
RDS-112	3	320	22	11	4.2	16	1
RDS-112	3	180	10	11	7.7	9	1

Table 5.3: Erbium-165 physical yields for various Ho targets dimensions irradiated on CTI-RDS-112 or Ge PETtrace cyclotron

5.2.3 Deuteron irradiations

5.2.3.1 Relation thickness/ deuteron energy beam

Like with the proton experiments (section 5.2.2.1), for deuteron irradiations there is a balance between produced ^{165}Er activity at a beam energy and Ho target mass. In this case, to

define the best ratio between the deuteron beam energy and Ho target mass, the AMA was calculated for each deuteron energy beam (12, 13, 14, 15, 16, 17.5 MeV) and various thicknesses of ∅ 9.5 mm diameter Ho target (25, 62, 127, 200, 300, 400, 500, 700 µm). Some realistic assumptions have been made: $SF_{(Ho/Er)}$ was fixed at 10^5, a ^{165}Er recovery yield after Ho/Er separation of 60%, and a Ho target with 70 ppm of erbium impurity. All estimations of ^{165}Er activity were calculated for an irradiation of 1 h with a current intensity of 10 µA. An average of physical yield (MBq·eµA^{-1}·h^{-1}) ^{165}Ho(d,2n)^{165}Er cross sections from 2008 Tarkanyi's work[151] and 2013 Hermanne's work[152] was applied at ^{165}Er activity calculations. A Ho density of 8.8 g/cm^3 was employed for calculations. Results are shown in Table 5.4.

				Target ∅ 9,5mm				
thickness (µm)	**25**	**62**	**127**	**200**	**300**	**400**	**500**	**700**
mass (mg)	**15.6**	**38.7**	**79.2**	**124.7**	**187**	**249.4**	**311.7**	**436.4**
Energy beam (MeV)				AMA (MBq/nmole) (EoB)				
17,5	12.1	13.5	17.1	19.9	22.0	20.1	16.3	11.7
16	20.3	21.7	23.4	24.5	22.6	17.6	14.1	10.1
15	23.6	24.1	25.1	25.1	19.9	15.0	12.0	8.6
14	26.3	25.9	26.2	23.0	16.4	12.3	9.8	7.0
13	27.3	26.3	24.1	18.4	12.5	9.4	7.5	5.3
12	27.1	25.0	19.2	13.1	8.8	6.6	5.3	3.8

Table 5.4: Estimation of AMA (MBq/nmol) (EoB) for a ∅ 9.5 mm diameter Ho target with 70 ppm Er impurity and ^{165}Er recovery of 60% according to energy deuteron beam (12 to 17.5 MeV)

Optimal AMA versus energy beam is highlighted in yellow in Table 5.4. Higher AMA are obtained for 25 µm (27.3 MBq/nmol) and 62 µm (26.3 MBq/nmol) at 13 MeV energy beam. But considering for preclinical studies that 500 MBq (EoS) of ^{165}Er radiolabeling molecule are necessary, ≈ 800 MBq (EoB) (at least 7 h after EoB for preparation of ^{165}Er) must be produced. To that, 1 h of irradiation with I = 10 µA on a ∅ 9.5 mm diameter Ho target with a thickness ≥ 127 µm (994 MBq for 14 MeV (AMA = 26.1 MBq/nmol) and 914 MBq for 13 MeV (AMA= 24.1 MBq/nmol for physical yield = 91.4 MBq·eµA^{-1}·h^{-1})). A 13 MeV deuteron energy was chosen for experiments with 127 µm thickness Ho target on section 5.2.3.3 13 Mev deuteron beam because historical records of Orleans' cyclotron tuning parameters were available for this energy, while cyclotron developments would have been necessary for a 14 or 15 MeV deuteron beam.

At least, a target of 300 µm thickness will be more adapted for high AMA when using a 17.5 MeV deuteron beam (physical yield 196.8 MBq·eµA^{-1}·h^{-1}), the most used deuteron beam at Orleans' cyclotron.

5.2.3.2 17.5 MeV deuteron beam

Using the spot-welding method for deuteron irradiation at Orleans'cyclotron, 17.5 MeV irradiations were done at high current intensity using CiSCoTe targetry.

First, four spot welded Ho targets (thickness = 300 µm; mass ≈ 198 mg and ∅ 9.5 mm and Ta foil support (thickness 500 µm, ∅ 14.7 mm) were irradiated during 1 – 4 h at 7 - 16 µA. No targets were melted but the physical yield 136 ± 48 MBq·eµA^{-1}·h^{-1} has a significant standard

deviation. Looking for the target after irradiation, some brown spots were observed on the edge of the target (Figure 5.3). The spot beam seems uncentered and Al piece be irradiated.

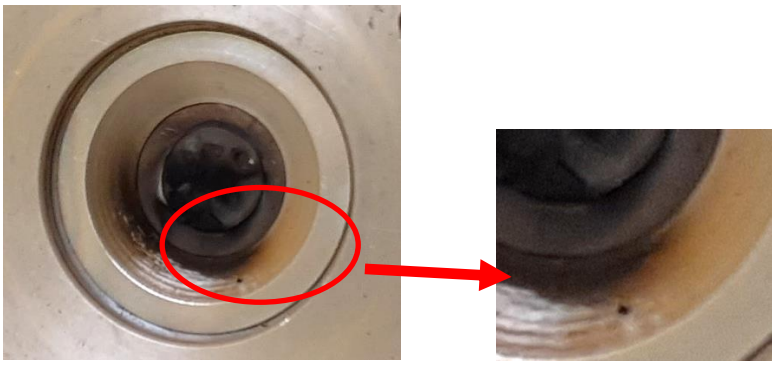

Figure 5.6: Spot beam uncentered, traces on the Al support

To verify this hypothesis, the position of the spot beam was determined by irradiation of 5 spot welded targets (Ho foil centered thickness = 127 µm and ∅ = 3, 4.75, 6.35, 8, and 9.5 mm, Ta support thickness 500 µm and ∅ 14.7 mm) by a 17.5 MeV deuteron beam at I = 2 µA for 30 minutes (Figure 5.4).

Figure 5.7: Determination of spot-beam by irradiation of 5 spot-welded targets with various diameter

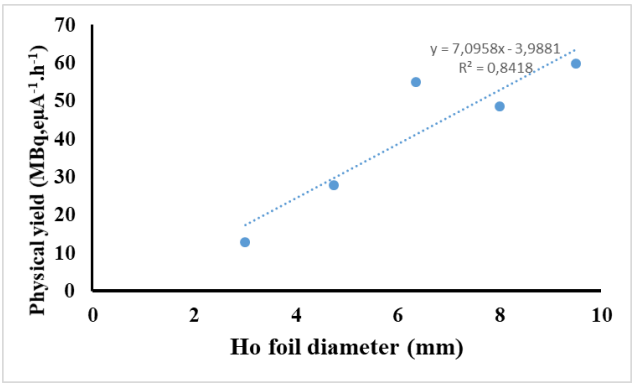

Figure 5.8: Physical yield (MBq·eµA^{-1}·h^{-1}) = diameter of Ho foil

Excluding the point of Ho foil with 6.35 mm, linearity was obtained between the diameter of Ho foil and physical yield (MBq·eµA^{-1}·h^{-1}) (R= 0.997) (Figure 5.5). 86 % of the theoretical physical yield for the Ho target (thickness 127 µm) with 9.5 mm diameter was obtained. All targets were scanned with Radio-TLC scanner (Radio Thin Layer Chromatography, Raytest Elysa Gina Star) (Figure 5.6). The profile of activity on targets demonstrated that the spot beam was off-center for all irradiations.

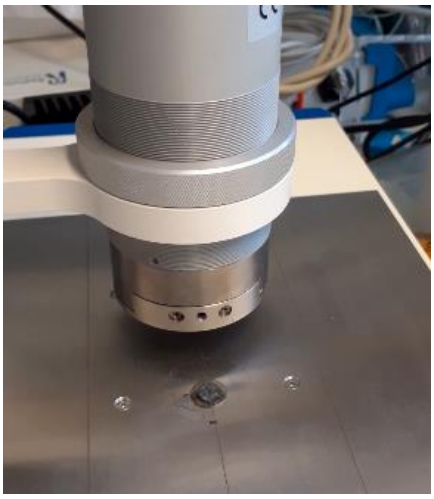

Figure 5.9: Scanning of Ho target with Radio-TLC system

Nine uncentered Ho foils (∅ 8 mm and thickness 300 µm) were irradiated by a 17.5 MeV deuteron beam at 6 - 15 µA during 3 – 6 h. Physical yield was 63 ± 55 $MBq \cdot e\mu A^{-1} \cdot h^{-1}$ (n = 9) but 3 targets melted and in two other irradiations physical yields were very low: ^{165}Er recovered was less than 25 % of expected production according to TENDL 2017 calculations. Excluding these 5 results, physical yield increased up to 117 ± 24 $MBq \cdot e\mu A^{-1} \cdot h^{-1}$ (n = 4) for I = 6 – 9 µA similar to 136 ± 48 $MBq \cdot e\mu A^{-1} \cdot h^{-1}$ obtained for a centered 9.5 mm diameter target. Nevertheless, the reproducibility was very bad.

5.2.3.3 13 MeV deuteron beam

The manual clamping of the shuttle was not sufficient to have a reproducible contact between the Ta disc, Al support, and cooling system: partial or complete loss of target when high heating (intensity or focalization of the beam).

Limited to irradiation intensity < 10 µA, we made the following changes: wrench tightening of target assembly, lower deuteron energy, and thinner Ho targets. The power (in W) deposited into Ho at 10 µA irradiation intensity for the two energy/thicknesses were compared. Considering effective Ho target thickness (for more information see back at section 3.1.3.1.2. CiSCoTe targetry) at 60° angle, 147 µm for 13 MeV and 348 µm for 17.5 MeV, energy out (E_{out}) of Ho target were respectively 9.1 MeV (E_{in} = 13 MeV) and 9.5 MeV (E_{in} = 17.5 MeV) (Figure 5.7.). Power (in W) deposited in the Ho target was 4.1 MeV * 10µA = 41 W for 13 MeV (127 µm thickness at 60° of incident beam angle) versus 8 MeV * 10µA = 80 W for 17.5 MeV for a 300 µm thickness (at 60° of incident beam angle). The thermal load on the Ho target was divided by two when a 13 MeV deuteron was used instead of a 17.5 MeV beam.

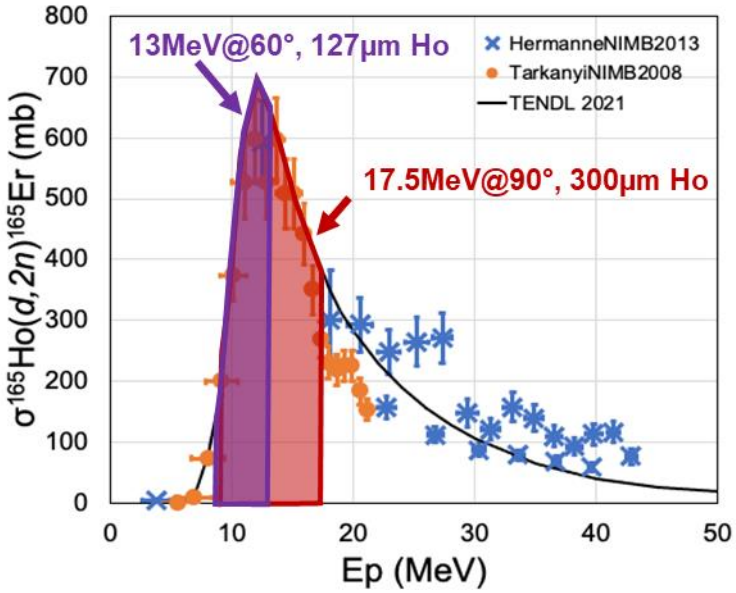

Figure 5.10: cross-section of nuclear reaction ^{165}Ho(d,2n)^{165}Er (0-50 MeV)

Twelve irradiations were done on Ho target with a mass = 90.4 ± 2.3 mg for 6.0 ± 0.4 h at 6.0 ± 0.3 µA for giving an ^{165}Er physical yield of 75.1 ± 10.1 MBq·eµA^{-1}·h^{-1}. It represents roughly 80% of the theoretical physical yield obtained for a 127 µm Ho target (∅ 9.5 mm) (91.4 MBq·eµA^{-1}·h^{-1}. No melted target on these reproducible conditions was observed.

5.2.3.4 Conclusion

Physical yield for a 9.5 mm centered ∅, and 300 µm thickness spot welded target irradiated by 17.5 MeV deuteron (Orleans' cyclotron) is 6 times higher than results obtained by 12.5 MeV proton on PET-Trace (136 ± 48 (n = 4) versus 24 ± 1 MBq·eµA^{-1}·h^{-1} (n = 5)) in complete agreement with theory. However, no satisfactory reproducibility has been observed: 45 % to 93 % of theoretical physical yield was obtained. Due to limited times for irradiations on Orleans'cyclotron planning, drastic modifications have been done to have reproducibility of irradiations for in vivo MRI/SPECT imaging applications: power deposited in Ho target divided by two in reducing energy beam from 17.5 MeV to 13 MeV and wrench tightening. Good reproducibility at 13 MeV deuteron has been found for a 127 µm thickness and 9.5 mm centered ∅ resulting in a physical yield of 75.1 ± 10.1 MBq·eµA^{-1}·h^{-1} (3 - 4 times higher than proton).

These results suggest that the lack of reproducibility of 17.5 MeV irradiations at I > 6µA is likely associated with the low efficiency of the cooling system on the CiSCoTe solid target system. Implementation of a water-jet cooled target system with cooling water directly on the back of the Ta foil would significantly improve the beam tolerance of the target. With these conditions, no melting trouble would be expected, and higher current intensity could be used more to reduce the irradiation time from 6 h to an acceptable time (1 – 2 h) for routine use of ^{165}Er.

5.3 Radiochemical separation

After defining optimal conditions for high AMA in terms of preparation of the holmium cyclotron target and targetry, the challenging point of Ho/Er separation is investigated. A high $SF_{(Ho/Er)} > 10^5$ is necessary to access to high AMA. In the first evaluation, $SF_{(Ho/Er)}$ was ≈ 1000 (1294 ± 1183 (n= 3)) for experiments on one single column LN2 (20 - 50 µm) see chapter 4 section 4.2.3.1[209]. A multi-column process is necessary to obtain $SF_{(Ho/Er)} > 10^5$. A protocol in three steps was studied. First step extraction of bulk Ho from ^{165}Er was done with cation exchange column (CX) for proton irradiations and extraction column (EXC) for deuteron irradiations. Then EXC with LN2 (20 – 50 µm) resin was used in the second step and various chromatographic parameters were optimized. Finally, a third step using EXC with b-DGA resin was added to concentrate the final ^{165}Er solution and eliminate traces of transition metals.

5.3.1 Ho/Er Separation factor

The $SF_{(Ho/Er)}$ were calculated according to equation (22) with $m\ or\ A_{Ho,before/after}$ being the ratio holmium mass (^{nat}Ho) /activity (^{166}Ho) before/after the separation step and $A_{165Er,before/after}$ being the ratio of dose-calibrator-quantified ^{165}Er activity before/after the separation step.

Equation (19)
$$SF(Ho/Er) = \frac{m\ or\ A_{Ho,before} \Big/ m\ or\ A_{Ho,after}}{A_{165Er,before} \Big/ A_{165Er,after}}$$

For proton irradiations (Madison's cyclotrons), holmium mass across the separation procedure was quantified using microwave plasma atomic emission spectrometry (MP-AES, Agilent MP4200). Holmium standard solutions of 0.1 – 50 ppm were made by dissolving holmium chloride hydrate (REaction® 99.99 % (REO), Alfa Aesar) in water or holmium metal (US DOE Ames Laboratory MPC) in 11 M HCl, followed by dilution in 0.1 M HCl. The limit of detection for holmium was determined to be ~ 0.1 ppm in an undiluted sample solution. MP-AES analyzed samples were typically diluted by a factor of 2 – 10 in 0.1 M HCl.

For deuteron irradiation (Orleans'cyclotron), the tracer method was used with ^{166}Ho for ^{nat}Ho and ^{165}Er for Er (radioactive and ^{nat}Er target impurity). ICP-OES (Agilent 5880) or ICP-MS (Thermo element XR) were used for holmium quantification in some cases for deuteron irradiations.

5.3.2 Step one: a rough separation of Ho from ^{165}Er

5.3.2.1 Cation exchange Dowex 50W-X8 with αHIBA

A publication of the biomedical cyclotron production and radiochemical isolation of ^{165}Er from holmium reported the production of 1.6 GBq ^{165}Er in a 10 h, 10 µA proton irradiation[63]. The ^{165}Er was isolated in a 10 hour process through a CX/αHIBA (α-hydroxyisobutyric acid) column using a proprietary resin with 12 – 22 µm particle size followed by an extraction column (EXC) using LN3 resin to concentrate the product. While the isolation of ^{165}Er from macroscopic Ho was achieved, neither the residual mass of Ho in the ^{165}Er product, nor the $SF_{(Ho/Er)}$, nor radiopharmaceutical labeling results were reported[63]. Although many chelating agents have been tested and used for lanthanide chromatographic separations, HIBA remains the usual separating reagent[210]. The dual hydroxyl and carboxyl functionality enables various coordination modes for HIBA (Figure 5.8), in which the hydroxyl group could either be protonated or deprotonated[210].

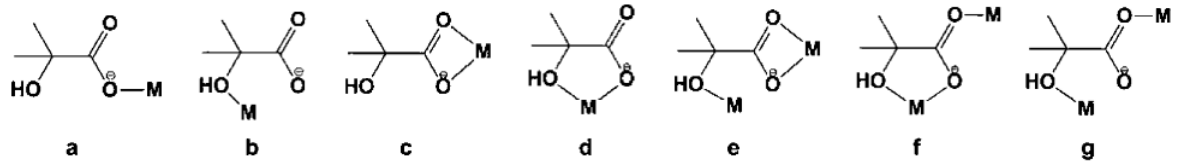

Figure 5.11: Possible Coordination Modes of HIBA with Metal Ions

After irradiation, holmium cyclotron targets were dissolved in 11 M HCl (2 mL, Trace Select Ultra, Fluka Analytical), followed by evaporation to dryness at 130 °C under Ar flow. The resulting yellow/pink salts were dissolved in 70 mM αHIBA (2 mL, pH = 4.7). The αHIBA solution was freshly prepared by dissolving α-hydroxyisobutyric acid (99 %, Sigma Aldrich or 98 %, Acros Organics) with 18 MΩ·cm ultrapure water (Milli-Q) and pH adjusted with 25 % ammonia solution (Fisher Scientific) using a pH probe (Checker® pH tester, Hanna Instruments). A 30 – 60 µL aliquot of the dissolved, reconstituted target was assayed for ^{165}Er radioactivity by ionization chamber dose calibrator (Capintec CRC-15R, setting #260). The dose calibrator setting #260 was experimentally determined by cross-calibration with HPGe gamma spectrometry. The ^{165}Er activity in highly concentrated (50 – 90 mg/mL) holmium solutions was corrected by the 46 – 55 keV x-rays self-attenuation.

A 1 cm diameter, 25 cm long CX column (Bio-Rad AG50W-X8, 230 - 400 mesh, 63 – 150 µm, 1.7 meq/mL, NH_4^+ form) was equilibrated with water (~100 mL), then 70 mM αHIBA (pH = 4.7, ~100 mL), followed by injection of the ^{165}Er/Ho/αHIBA solution and elution with 5 mL/min 70 mM αHIBA (pH = 4.7, 440 – 820 mL). Under these conditions, ^{165}Er elutes before holmium and the first ~90% of eluted ^{165}Er was collected (150 – 350 mL) for secondary purification, as determined by monitoring the column effluent using a shielded inline radiation detection system consisting of a CsI(Tl) scintillator (1 x 1 cm, Hilger Crystals Ltd, UK) coupled to a photomultiplier tube (E849-35, Hamamatsu Photonics, Japan) powered and processed with bench-top electronics (925-SCINT, Ortec, USA) and logged using a digital counter (USB-6008, National Instruments Corp). Then, the mobile phase was changed to 0.5 M αHIBA (pH = 4.7, 250 mL) for stripping the remaining bulk holmium from the cation exchange column followed by water (200 – 500 mL) for column storage. The ^{165}Er radioactivity eluting in each collected CX fraction was quantified by dose calibrator immediately after elution.

The first step of the ^{165}Er isolation procedure accomplishes a bulk holmium/erbium separation while accommodating 180 mg holmium loading masses through CX/αHIBA column chromatography with commercially available CX resin in a standard stainless steel semipreparative high-pressure chromatography column housing. This 19.6 mL column has a theoretical capacity of 1.8 grams of trivalent Ho^{3+}, ten times larger than the intended holmium loading masses. Based on the Dy/Ho separation process of Mocko *et al.*[161], 70 mM αHIBA (pH = 4.7) was used as the mobile phase. When the mobile phase was freshly prepared and carefully pH adjusted to within 0.05 pH units, consistent retention times were observed with 90 % of the total ^{165}Er radioactivity eluting in a Gaussian-shaped peak 40 – 90 minutes after injection, as shown in the representative Radiochromatogram (Figure 5.12). Holmium elutes after ^{165}Er with its leading edge beginning at ~350 mL as seen through the diminishing $SF_{(Ho/Er)}$ with increasing ^{165}Er fraction collection volume. The use of a mobile phase that was not freshly prepared or incorrectly adjusted to too low of a pH resulted in significantly longer retention times and diminished separation of ^{165}Er and Ho.

With 5 mL/min flow, the column pressure was routinely 17 – 19 MPa. Following ^{165}Er elution, the column was stripped with freshly prepared 0.5 M αHIBA (100 mL, pH = 4.7), followed by water (250 mL). The column was re-used until the flow pressure significantly increased (> 22 MPa), upon which it was disassembled and repacked with fresh resin slurry, every ~10 uses. As determined by dose calibrator measurements of ^{165}Er and MP-AES

measurements of Ho in the eluted CX fractions, the CX/αHIBA column accommodated 180 mg Ho loading mass and effectively removed bulk Ho with an acceptable ^{165}Er yield. Loading 111 ± 17 mg Ho and recovering 94.7 ± 2.5 % of ^{165}Er resulted in a $SF_{(Ho/Er)}$ of 320 ± 210 (n = 6). Loading 174 ± 8 mg Ho and recovering 95.3 ± 1.8 % of ^{165}Er resulted in a $SF_{(Ho/Er)}$ of 130 ± 60 (n = 5). For the larger loading masses, decreasing ^{165}Er recovery to 90.5 ± 1.4 % resulted in an $SF_{(Ho/Er)}$ of 250 ± 150 (n = 5), and further decreasing ^{165}Er recovery to 80 % resulted in an $SF_{(Ho/Er)}$ of 1000 ± 400 (n = 1). These results indicate the sensitivity of the CX/αHIBA separation to Ho loading mass and demonstrate the challenging balance between ^{165}Er recovery and $SF_{(Ho/Er)}$. To ensure a reproducible, optimal balance between yield, and $SF_{(Ho/Er)}$ for this step, an online radiation detector was used to determine when to stop collecting the ^{165}Er fraction. Following loading ≤ 120 mg Ho, ^{165}Er fraction collection was ended when the radioactivity signal was ~1/10th maximum value, resulting in ~95 % ^{165}Er recovery. Following loading ~180 mg Ho, ^{165}Er fraction collection was ended when the radioactivity signal was ~1/4th maximum value, resulting in ~90 % ^{165}Er recovery (Figure 5.9).

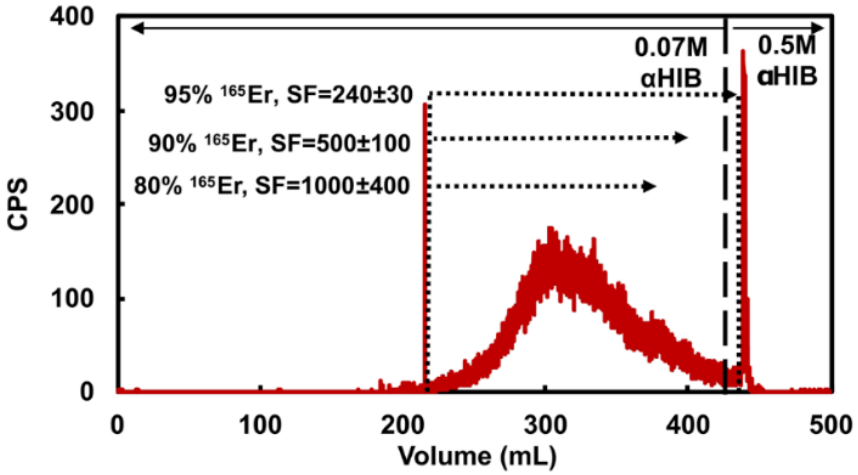

Figure 5.12: Representative ^{165}Er radioactivity elution profile from a CX column loaded with 178 mg holmium and eluted with 5 mL/min 0.07 M αHIBA (pH = 4.7). Dotted lines and corresponding text highlight three possible ^{165}Er-rich fraction collection volumes demonstrating the balance between ^{165}Er recovery and $SF_{(Ho/Er)}$. The 0.5 M αHIBA (pH = 4.7) rapidly elutes the remaining ^{165}Er along with bulk holmium.

5.3.2.2 Extraction Chromatography: LN2 resin with HNO_3 gradient

- **Methods**

For the first step using EXC with LN2 resin (20 – 50 µm), conditions were optimized relative to the first results obtained for in vitro bimodal MRI/SPECT imaging (see section 4.2.3).

^{165}Er from 13 MeV deuteron irradiated spot welded Ho target with mass = 90.4 ± 2.3 mg (n = 12) was isolated using a 4 g of LN2 resin column preconditioned with 15 mL of 5 M HNO_3 then 80 mL of water and finally 15 mL of 0.1 M HNO_3. After target dissolution in 2 mL of 10 M HCl and evaporation to dryness, the pink powder was dissolved in 2 mL of 0.1 M HNO_3. Then after removing a 60 µL holdback of this solution as a reference, the rest of the solution was deposited on top of the preconditioned column and loaded at 1 mL/min under 1 bar N_2 pressure, followed by elution with 0.4 M HNO_3 to recover Ho with its tracer ^{166}Ho then 1 M HNO_3 to recover ^{165}Er. Finally, the column was rinsed first with ~15 mL of 5 M HNO_3 to completely elute the last traces of ^{165}Er then with ~80 mL water to store the column in a neutral pH for next use and reused various times (8 - 10) after reconditioning.

^{165}Er radioactivity was measured by ionization chamber dose calibrator (Capintec CRC-15R, setting #187). The dose calibrator setting #187 was experimentally determined by cross-calibration with HPGe gamma spectrometry. The HPGe detector was calibrated with ^{133}Ba and ^{152}Eu solution on Tube 2G geometry homemade with certified standard radioactive sources (Cerca France) in energy and efficiency. For activity measurements, γ-ray spectrum analysis software package Genie 2000 (Canberra, USA) was used. An aliquot of ^{165}Er solution to quantify was prepared in Tube 2G geometry and counted in HPGe and ionization chamber dose calibrator.

- **Results**

Ho was eluted with recovery of 97.2 ± 1.7 % (n = 11) in ≈ 151 mL of 0.4 M HNO_3 then ^{165}Er was eluted in 1 M HNO_3. Elution with 1 M HNO_3 was divided into three parts (Table 5.5):

(1) final elution of Ho on column (1 - 3 %) and activation of ^{165}Er desorption (0 to 5 % eluted in ≈ 10 mL of 1 M HNO_3 whereas only 1 – 7 % of ^{165}Er was recovered in 150.6 ± 18.2 mL of 0.4 M HNO_3

(2) elution of the majority ^{165}Er, 76.7 ± 13.1 % (n = 11) in 16.7 ± 4.1 mL of 1 M HNO_3 with residual Ho quantity (0 – 2 %)

(3) elution of rest of ^{165}Er (1 – 25 %) in a reduced volume of 1 M HNO_3 (8.4 ± 1.8 mL) without detectable Ho (< 0.1%).

HNO_3	Volume (mL)			Er (%)			Ho (%)			SF Ho/Er
0.4 M	150.6	±	18.2	4.3	±	3,0	97.2	±	1.7	0
1 M (1)	9.7	±	1.6	5.4	±	5.3	2.0	±	1.4	3
1 M (2)	16.7	±	4.1	76.7	±	13.1	0.7	±	0.9	107
1 M (3)	8.4	±	1.8	12.8	±	11.8		< 0.1		> 127
5 M	17.0	±	7,0	0.7	±	1.1		< 0.1		> 7
Rinsing	80.2	±	17.2	0.1	±	0.1		< 0.1		> 1

Table 5.5: Distribution of ^{165}Er and ^{166}Ho during elution on LN2 resin (20 - 50 µm)

The volume of 1 M HNO_3 is crucial to the quality of separation. Looking for results in Table 5.5., the first ≈ 10 mL of elution with 1 M HNO_3 needs to be excluded for its low $SF_{(Ho/Er)}$ (3). But this volume needs to be increased until 12 mL (Figure 5.10, red line) to reduce residual Ho as low as possible in fraction (2) of 1 M HNO_3. The next 20 mL of 1 M HNO_3 will be sufficient to recover 80% of ^{165}Er fixed in column with an $SF_{(Ho/Er)}$ >> 127 because percent of residual Ho < 0.7%. These experimental conditions correspond to results with high uncertainty in Table 5.5 for fractions (1) and (2). Nevertheless, these results confirm a good reproducibility of radiochemical separation of Ho/Er by LN2 (20 – 50 µm) resin with $SF_{(Ho/Er)}$ >100. Optimization of 1 M HNO_3 volume in fractions (1) and (2) for a fixed 0.4 M HNO_3 volume will give benefit for automation of this separation. This result confirms the reproducibility of first-step separation on an EXC with LN2 (20 - 50 µm) resin. By adjusting the 1 M HNO_3 faction (1) volume to 12 mL will reduce the quantity of ^{165}Ho in the final ^{165}Er fraction (2) to less than 1 % and improve final $SF_{(Ho/Er)}$. This will come at the expense of some ^{165}Er yield, demonstrating the balance between yield of ^{165}Er recovery and Ho impurity as seen for CX with αHIBA.

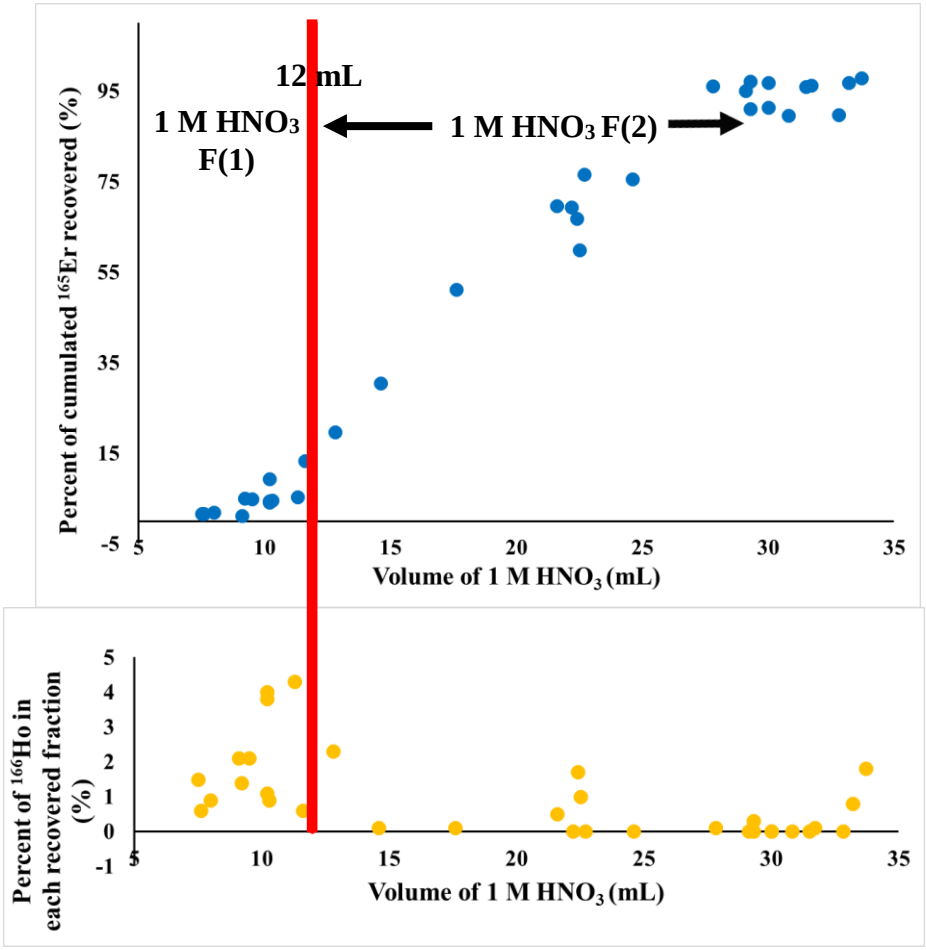

Figure 5.13: Relation between eluted 1 M HNO_3 volume, the quantity of cumulated ^{165}Er recovered (%), and percent of Ho in each fraction recovered

5.3.2.3 Conclusion

Similar results of ^{165}Er radiochemical separation from Ho were obtained using the CX or EXC column. In all cases, the sensitivity of methods has demonstrated the necessity to lose a quantity of ^{165}Er associated with the elution of Ho for higher $SF_{(Ho/Er)}$. A compromise must be made between a high yield of ^{165}Er recovery and quantity of Ho in the sample affecting $SF_{(Ho/Er)}$. In terms of timing, 1.5 - 2 hours are necessary for the first step for each resin. Moreover, EXC separation with LN2 (20 – 50 µm) resin is more useful to apply because no high pressure is needed, only low pressure of N_2 (1 bar) to fix flow on a column to 1 mL/min, no pH to fix, no quality and stability of complexant to manage. LN2 (20 -50 µm) extraction resins can be reused after conditioning whereas the CX column repacking was more time-consuming (Dowex 50W-X8). However, the CX method was completed automatized from dissolution of the target to recovery of ^{165}Er fraction for the second separation step. At the time, for EXC protocol, no automatic transfer from the dissolution bench to deposition of solution on top of the colunm was done. But the radiochemical separation of ^{165}Er from the Ho target was semi-automatized on the column using micropumps. After this first step, ^{165}Er fraction obtained from each method was treated by the EXC method using LN2 (20 – 50 µm) resin. For that, ^{165}Er eluted in 1 M HNO_3 solution from LN2 (20 – 50 µm) column must be diluted 10x before being used in the second step of separation, thus resulting in a similar volume (≈ 200 mL) to the CX method.

5.3.3 Step two: selectivity for high AMAs

The second separation step was designed to eliminate residual Ho in the ^{165}Er batch thus increasing $SF_{(Ho/Er)}$. This was accomplished through a smaller scale (~500 mg) extraction chromatography resin column. Various experimental tests optimized the choice of resin, dimensions of column, flow rate, elution volume, and erbium capacity of this separation step, as detailed below.

For experiments in this section three Ho targets (∅ 7.6 and 6.35 mm, 190 and 604 µm thickness, 70 - 174 mg, 100 or 600 ppm impurity Er) were irradiated at 11 MeV in CTI-RDS 112 cyclotron for 1 – 2 h at 20 µA producing 540 – 880 MBq (EoB). Then they were dissolved in 2 – 4 mL 10 M HCl, heated at 130° C to dryness, and dissolved in 2 mL of αHIBA 0.07 M to form a solution (S1). Then, for individual experiments, 23 – 30 µL (1 mg of Ho) of a S1 was added to 200 mL of αHIBA 0.07 M (average volume recovered from the first column). These 200 mL loading solutions (S2) were then acidified to 0.1 M with concentrated (15 M) HNO_3 to form the free species of holmium in the solution. S2 is a representative solution of Ho mass and volume and was used to test various resins and elution conditions for the second step of the ^{165}Er isolation process.

Solution of αHIBA (99 %, Sigma Aldrich or 98 %, Acros Organics) 0.07 M pH= 4.7 were freshly prepared, pH adjusted with 25% ammonia solution to 4.4 to 4.7 using pH strips). All diluted acids HNO_3 and HCl were prepared from high purity concentrated acid and using ultra purified (UP) 18 MΩ water.^{165}Er was measured by ionization chamber dose calibrator Capintec CRC-15R with coefficient #260 and Ho mass determined by MP-AES after a 10x dilution in 0.1 M HCl (limit of detection 1 ppm considering dilution). $SF_{(Ho/Er)}$ was calculated with equation (21). LN2 (20 - 50 µm) resins were reused after reconditioning if the same condition of diameter or mass (100 – 200 - 300 – 500 mg) were applied. For that, Ho MP-AES analysis was made on each 0.1 M HNO_3 conditioning column fraction, rinsing line of the column, and labware/glassware used to collect loaded fraction. Although the sensitivity of MP-AES was only at 1ppm, this technique was used to check all material: no traces of Ho were detected.

5.3.3.1 Other option than LN2 resin?

For comparison of their efficiency versus this one of LN2 (20 – 50 µm), some extraction resins available in the laboratory (Madison) were tested. They were all registered trademarks of TRISKEM:

- LN© [(50 – 100 µm) density: 0.38 g/mL; capacity: 0.16 mmol (trivalent actinides and lanthanides) / Conversion factor Dw/k': 1.75];
- LN2© [(20 – 50 µm), density: 0.37 g/mL; capacity: 0.16mmol (trivalent actinides and lanthanides)/ Conversion factor Dw/k' :1.75]
- TK211/212/213 (13 – 17 µm) (resin with larger particle size (20 – 50 µm) have been recently used in the production of ^{165}Er ^{211}).

➢ **Methods**

Fritted solid phase extraction (SPE) tubes (1 mL, 5.5 mm inner diameter) were used as column for extraction resins. 200 mg of resin was used giving a 20 mm bed height. Columns were conditioned with 5 mL of 5 M HNO_3, 40 mL of water (check pH neutral value), and 5 mL of 0.1 M HNO_3. For TK213, 0.01 M HNO_3 was used in the last step instead of 0.1 M due to its specifications of elution similar to LN3 (desorption at low acidity). According to the specifications of extraction resins, various elution gradients were applied:

1. LN and TK211: 0.8 M (15 mL) then 1 M (8 mL for LN, 5 mL for TK211), and 5 M (3 mL) HNO_3 to completely desorb ^{165}Er

2. LN2 and TK212: 0.4 M (15 mL) then 1 M (1 mL) and 5 M HNO_3 (5 mL) (in this case the stronger acid was more to reconditioning column for the next experiment)
3. TK213: 0.1 M (10 mL) then 0.4 M (5 mL) and 1 M HNO_3 (8 mL).

➢ **Results**

	Resin					Flow		Fraction of ^{165}Er with $SF_{(Ho/Er)} > 100$		
	Size particle	Bed Length	Time separation (min)	Method		(ml/min)		SF	(%)	Volume 1 M HNO_3
Type	(µm)	(mm)		F-F	F-S	Loading	Elution			(ml)
LN	50 - 100	20	63		X	10.4	0.6		no SF > 100	
LN2	20 - 50	19	50		X	8.7	0.8	121	55	2.7
TK211	13 - 17	22	131	X		2.7	0.4	127	77	7.4
TK212	13 - 17	22	123	X		3.2	0.3		no SF > 100	
TK213	13 - 17	22	106	X		2.9	0.6		no SF > 100	

Table 5.6: Comparison of 5 extraction resins for separation Ho/Er

Due to TK211/212/213 resin's very small size, the default flow mode F-S (see details on the flow method in section 5.3.3.3) was not applied due to the very low flow rate – the F-F method was used for their elution. Similar $SF_{(Ho/Er)}$ were obtained with TK211 resins (13 – 17 µm, $SF_{(Ho/Er)}$ = 127) and LN2 (20 – 50 µm, $SF_{(Ho/Er)}$ = 121) astonishing results because this resin is supposed to be similar to LN and not LN2[212]. However, 77 % of ^{165}Er were recovered in the case of TK211 whereas only 55% was recovered for LN2 resin (Table 5.6). However, for such results, the time of elution was more than twice (130 min against 50 min) in the case of ^{165}Er with a decay of 10.36 h, it's a crucial parameter. As expected, LN (50 – 100 µm) is not appropriate for this separation due to large particle size.

Due to our experience with Ho/Er separation, LN2 (20 – 50 µm) resin was chosen. TK resins with similar granulometry could be too as efficient as LN2 (20 – 50 µm) but more investigations on these resins will be necessary to confirm these preliminary results.

5.3.3.2 Dimensions of column

➢ **Methods**

Diameter and bed height have a significant impact on the efficiency of column separation: reducing the column diameter for an equal mass of used resin, will increase the number of theretical separation plates and therefore separation efficiency. To experimentally test this, the separation performance of an 200 mg LN2 (20 – 50 µm) columns will be compared for a ∅ 5.5 mm inner diameter (ID) column (19 mm bed height) and a home-made 3.8 mm ID glass column (42 mm bed height) (Figure 5.11).

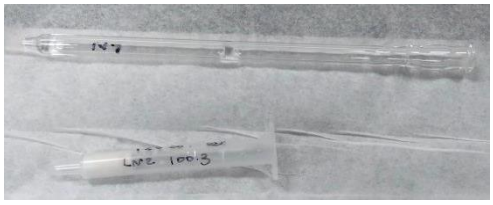

Figure 5.14: 3.8- and 5.5-mm column diameters

➢ **Results**

55 % of ^{165}Er were recovered with a 5.5 mm diameter ($SF_{(Ho/Er)}$ = 121) whereas 48 ± 34 % (n = 2) of ^{165}Er recovery yield was obtained with a 3.8 mm diameter for an $SF_{(Ho/Er)}$ = 224 ± 24 (n = 2). There was only a small difference in separation performance between the two column diameters, and a very large difference in the flow rates achievable. Therefore it was not worth using the smaller diameter column. Elution time increased significantly: 50 min for 5.5 mm diameter compared with an average of 90 min for 3.8 mm.

5.3.3.3 Variation of flow

➢ **Methods**

Two peristaltic pumps P1 and P2 are used. The first pump (P1) permits until 10.5 mL/min (depending on resin size and column diameter), named fast flow (F), whereas the second (P2) had a range of flow limited to 2 mL/min named slow flow (S). The elution step is especially sensitive to the flow in the separation of adjacent lanthanide. For elution, by default, a slow flow (S) = 0.6 to 1.6 mL/min was applied in all experiments of section 5.3.3. Step two: selectivity for high AMAs. Without any information about the flow method, a method noted F-S was used for separation meaning P1 used for loading column (F) and P2 used for elution (S).

Comparison of flow rate methods F-S and F-F were done on a 3.8 mm diameter glass column and a 5.5 mm diameter 1 mL polypropylene column with 200 mg (42 mm bed height) and 300 mg (31 mm bed height) of LN2 (20 – 50 µm), respectively(Table 5.7).

➢ **Results**

Weight	Diameter	Bed height	Flow				Fraction Er with $SF_{(Ho/Er)} > 100$		Fraction Er with $SF_{(Ho/Er)} > 500$	
			Method		Loading	Elution	SF	%	SF	%
(mg)	(mm)	(min)	F-F	F-S	(mL/min)		(Ho/Er)		(Ho/Er)	
200	3.8	42		X	4.2	1.1	249	64.8	535	37.8
200	3.8	42	X		3.9	1.7	109	31.9		
300	5.5	31		X	7.7	0.7	124	84.2	515	64.8
300	5.5	31	X		6.9	2.7	100	8.4		

Table 5.7: Influence of variation of elution flow on $SF_{(Ho/Er)}$

For a 3.8 mm diameter column, 64.4 % of ^{165}Er was recovered at 1.1 mL/min with a $SF_{(Ho/Er)}$ = 249 whereas, when eluting at 1.7 mL/min there was significantly more Ho/Er co-elution with a smaller ^{165}Er recovered with a lower SF. In the case of a 5.5 mm diameter column, 84.2 % of recovered ^{165}Er had an $SF_{(Ho/Er)} > 100$ when eluted at 0.7 mL/min, compared with only 8.4% when eluted at 2.7 mL/min. Moreover, with the slow flow, 64.8% of recovered ^{165}Er had an $SF_{(Ho/Er} = 515$. These experiments demonstrate the criticality of the slow flow rate during elution, which was utilized for the final separation procedure.

5.3.3.4 Variation of resin mass

➢ **Methods**

Resin mass is a critical chromatographic parameter. It was investigated: the used mass of LN2 resin was gradually increased from ≈ 100 mg (10 mm bed height), ≈ 300 mg (30 mm),

and ≈ 500 mg (50 mm, equal to the capacity limit of 1 mL fritted solid phase extraction tube). Three categories of $SF_{(Ho/Er)}$ were established to compare the percentage of recovered ^{165}Er: > (1) 100, (2) 500, (3) 1000. Around 1 mg of irradiated Ho target with 6 – 8 MBq (EoB) of ^{165}Er was diluted in 200 mL of 0.07 M αHIBA then the solution was acidified with 15 M HNO_3 to adjust solution acidity to 0.1 M HNO_3. This solution was loaded in each column with different resin masses.

- **Results**

Only 24% of ^{165}Er was able to be recovered with an $SF_{(Ho/Er)}$ = 122 with the 100 mg column, whereas 90% was recovered with an $SF_{(Ho/Er)}$ = 119 for a 500 mg column (Figure 5.12). While using 500 mg of resin increases time separation from 57 to 87 min, 51 % of ^{165}Er was recovered with $SF_{(Ho/Er)}$ = 1052: separation was improved by one decade with twice more activity recovered. Increasing LN2 (20 – 50 µm) resin mass significantly improves the separation between Ho and ^{165}Er (Figure 5.12) and significantly improves associated $SF_{(Ho/Er)}$ (Figure 5.13).

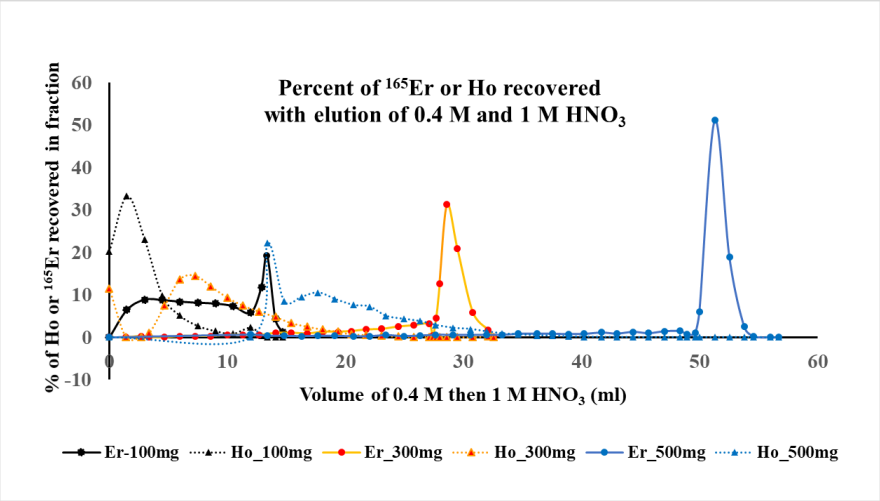

Figure 5.15: profile of elution in 0.4 M then 1 M HNO_3 for Ho and ^{165}Er in 100, 300, and 500 mg LN2 (20 – 50 µm) resin in a 5.5 mm diameter column

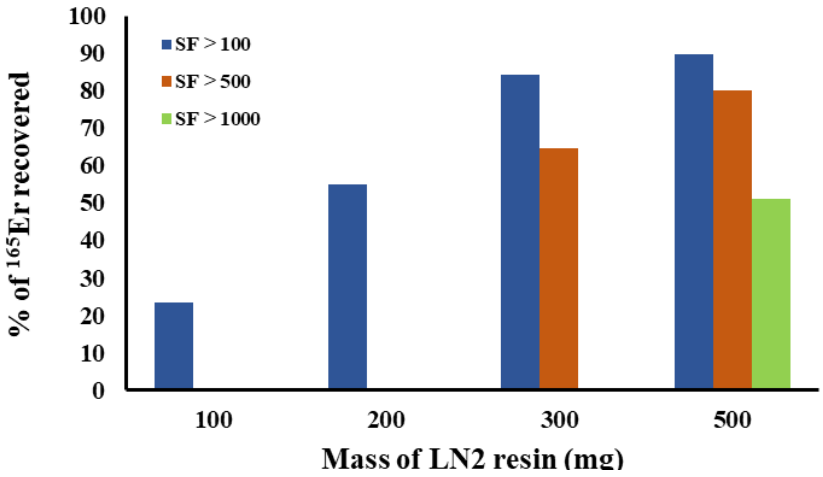

Figure 5.16: % of ^{165}Er recovered according to $SF_{(Ho/Er)}$ and resin mass used

The percentage of recovered Ho in ^{165}Er final fraction (1 M HNO_3) decreases from 3.1% for a100 mg column to 0.1% for a 500 mg (Table 5.8). Increasing the volume of 1 M HNO_3 (3.6 mL) in the case of 51 mm bed height column only led to 3% more ^{165}Er recovery but reducing the volume of 0.4 M HNO_3 could be more efficient. However, a balance between $SF_{(Ho/Er)}$, and the necessary 0.4 M HNO_3 volume to elute Ho needs to be done.

		HNO_3 (mL)		Ho (%)		Er (%)	
		0.4 M	1 M	0.4 M	1 M	0.4 M	1 M
100 mg	(a), (b)	10.5	4.2	76.6	3.1	53.1	42.3
200 mg	(a)	15.2	7.5	84.5	2.0	19.5	80.5
300 mg	(a)	27.4	5.2	88.0	0.5	23.0	77.0
500 mg	(a), (c)	49.0	3.6	99.7	0.1	20.0	77.3

(a) rest of Ho eluted during loading solution

(b) rest of ^{165}Er eluted during loading solution

(c) rest of ^{165}Er eluted in 5 M HNO_3

Table 5.8: Evolution of % of Ho and ^{165}Er in 0.4 M and 1 M HNO_3 fraction according to used LN2 (20 – 50 µm) resin mass

5.3.3.5 Optimization of 0.4 M HNO_3 volume

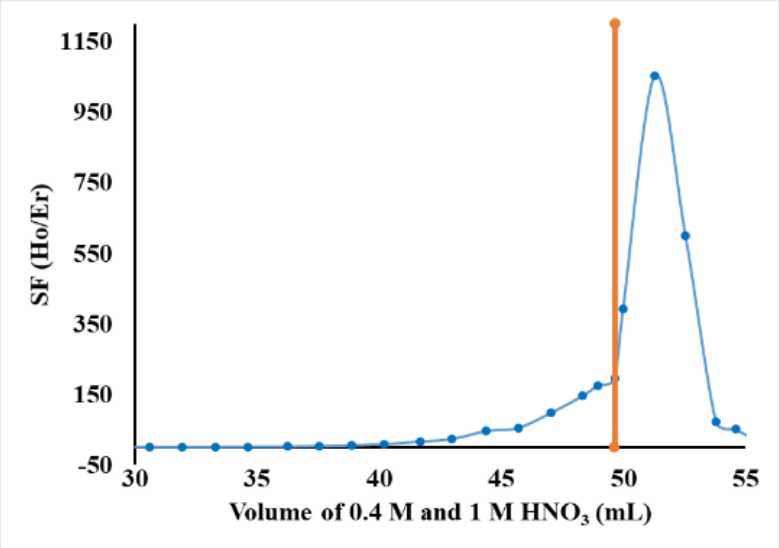

Figure 5.17: $SF_{(Ho/Er)}$ relative to volume of 0.4 M HNO_3 to elute Ho from a 500 mg LN2 column. Mobile phase switched to 1 M HNO_3 at the orange vertical line.

In Figure 5.14., the profile of 51 mm bed height column elution was presented for an elution with ≈ 50 mL of 0.4 M HNO_3. Then less than 10 mL of 1 M HNO_3 solution was used to recover 77.3 % of ^{165}Er (Table 5.8.). If only 31 mL of 0.4 M HNO_3 could be used 91.5 % of ^{165}Er would be recovered but with a very poor $SF_{(Ho/Er)}$ = 20 (Figure 5.15). At 45.7 mL, $SF_{(Ho/Er)}$ = 550 was obtained versus 764 for 49.7 mL.

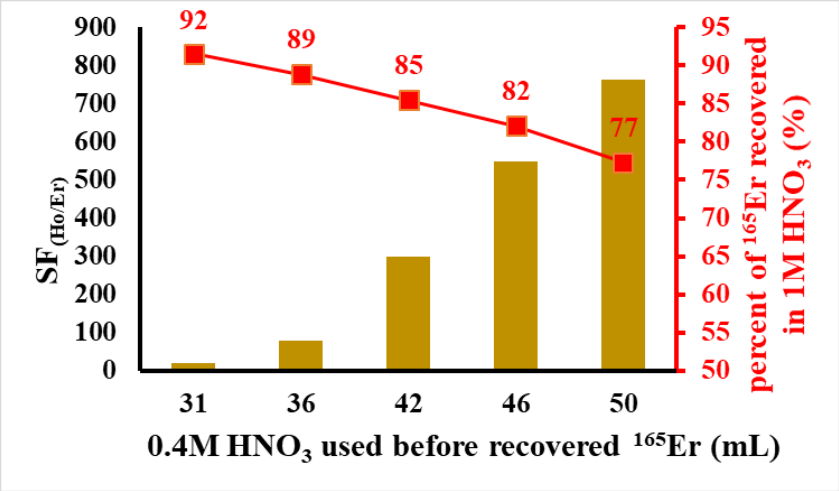

Figure 5.18: $SF_{(Ho/Er)}$ along the separation of ^{165}Er from Ho on 500 mg LN2 (20 – 50 µm) resin, 5.5 mm diam. column, 50 mL 0.4 M HNO_3 then 1 M HNO_3)

To confirm these calculations, three experiments with ≈ 30 mL of 0.4 M HNO_3 were done using a 500 mg LN2 column (Table 5.9.). These results confirmed estimation for 32 ± 3 mL, 93 ± 2 % of ^{165}Er was recovered in 5.2 ± 0.3 mL of 1 M HNO_3 for a $SF_{(Ho/Er)}$= 59 ± 10.

0.4 M HNO_3 volume (mL)	**$SF_{(Ho/Er)}$**	**^{165}Er (%)**	**1 M HNO_3 volume for ^{165}Er (mL)**
29.3	48	94.0	4.9
34.2	64	95.0	5.2
33.5	65	91.2	5.4

Table 5.9: Composition of ^{165}Er final batch when 30 mL of 0.4 M HNO_3 was used for elution of Ho

5.3.3.6 Capacity of LN2 resin

Increasing the column resin mass increases efficiency of column and obviously $SF_{(Ho/Er)}$. However, in this study, the same amount of Ho (about 1 mg) was put, whereas resin mass increased. That reduces the used % capacity of the resin. The capacity of LN2 resin (20 - 50µm) is equal to 0.16 mmol for Ln^{3+}. Assuming this specification, 1 mg of Ho represents 19 % of the resin capacity for the 10 mm bed height column (100 mg), whereas only 3 % for 50 mm (500 mg). Therefore, the impact of holmium loading mass on LN2 extraction chromatography columns was investigated.

- **Materials and Methods**

A holmium target (174 mg, outer diameter 6.35 mm, thickness 690 µm, Alfa Aesar, 99.9%, 0.06% Er content) was irradiated with a CTI-RDS-112 cyclotron at 11 MeV proton for 2 h with an average proton current of 14 µA. It was dissolved in 11 M HCl (2 mL) and dried with heat and argon flow. After cooling, the pink salts were dissolved in 0.07 M αHIBA (4 mL, pH = 4.7, Sigma Aldrich). This was the Ho/^{165}Er stock solution. 16 M HNO_3 (TraceSelect, Fluka) was used to acidify the solution or to prepare diluted nitric acid solutions (0.4 M and 1M) with 18 MΩ·cm ultrapure water (Milli-Q). LN2 resin from Triskem (20 - 50 µm) has a capacity of 0.16 mmol/mL of resin and a density of 0.37 g/mL. A 5.5 mm inner diameter polypropylene column filled with LN2 resin (300 mg) was used for all experiments. Before each attempt, LN2 resin had been preconditioned with 5 M HNO_3 (5 mL) then water (40 mL) and 0.1 M HNO_3 (5 mL). Separations were performed by loading 1 mg (5 % theoretical maximum capacity), 3 mg (14 %

capacity), and 10 mg (47 % capacity) holmium and 0.6 – 1.5 MBq ^{165}Er diluted in 0.1 M HNO_3 (200 mL), 0.07 M αHIBA to simulate recovered ^{165}Er-rich fraction from the CX/αHIBA separation. The column was loaded at 7.3 ± 0.4 mL/min (n = 3), followed by 28.6 ± 0.8 mL (n = 3) 0.4 M HNO_3 at 1.0 ± 0.2 mL/min (n = 3) to elute holmium before switching the eluent to 1 M HNO_3 to elute rest of ^{165}Er on resin.

For calculations of $SF_{(Ho/Er)}$, ^{165}Er was quantified by a radioactivity ionization chamber dose calibrator (Capintec CRC-15R, setting #260) and Holmium by MP-AES (Agilent MP4200). MP-AES was done on samples diluted 10 times in 0.1 M HCl. Under these conditions, the MP-AES limit of detection (LD) is 1 ppm. All measurements at LD were estimated as less than or equal to 1 ppm for $SF_{(Ho/Er)}$. To assess whether the increased loading mass affected chromatographic performance under the optimized conditions, the $SF_{(Ho/Er)}$ was measured based on the assumption that the column would be rinsed with 0.4 M HNO_3 until 20 % of the ^{165}Er had eluted, followed by the recovery of the remaining ^{165}Er for bDGA EXC work up. For each of these three experiments, the $SF_{(Ho/Er)}$ was calculated according to equation (21) based on the assumption that all fractions recovered after the elution of the first 20 % of ^{165}Er were pooled into a single fraction, resulting in ~ 80 % ^{165}Er recovery.

- **Results**

The elution profiles from the three LN2 EXC columns are shown in Figure 5.16. At the lowest loaded holmium mass (1 mg, 5% theoretical max capacity, Figure 5.16 top), the Ho/^{165}Er elution profile appears similar to those performed under optimized conditions (see Figure 5.12. blue curves (500 mg)). When recovering 80% of ^{165}Er by collecting all fractions after the vertical red arrow, the separation resulted in an $SF_{(Ho/Er)}$ = 140. Upon increasing the loaded Ho mass (3 mg, 14% max capacity, Figure 5.16 middle), the holmium and ^{165}Er were observed to elute significantly earlier. This resulted in a decrease in column $SF_{(Ho/Er)}$ = 11 for 80% ^{165}Er recovery. This trend continued when the column was loaded with 10 mg Ho (47 % max capacity, Figure 5.16 bottom) with the holmium and ^{165}Er eluting even earlier and a further decreased column $SF_{(Ho/Er)}$ = 4.5 for 80% ^{165}Er recovery. It is hypothesized that increasing Ho loading mass limits the number of free sites for extraction on the resin. This results in a significant breakthrough of both holmium and erbium, decreasing in chromatographic performance.

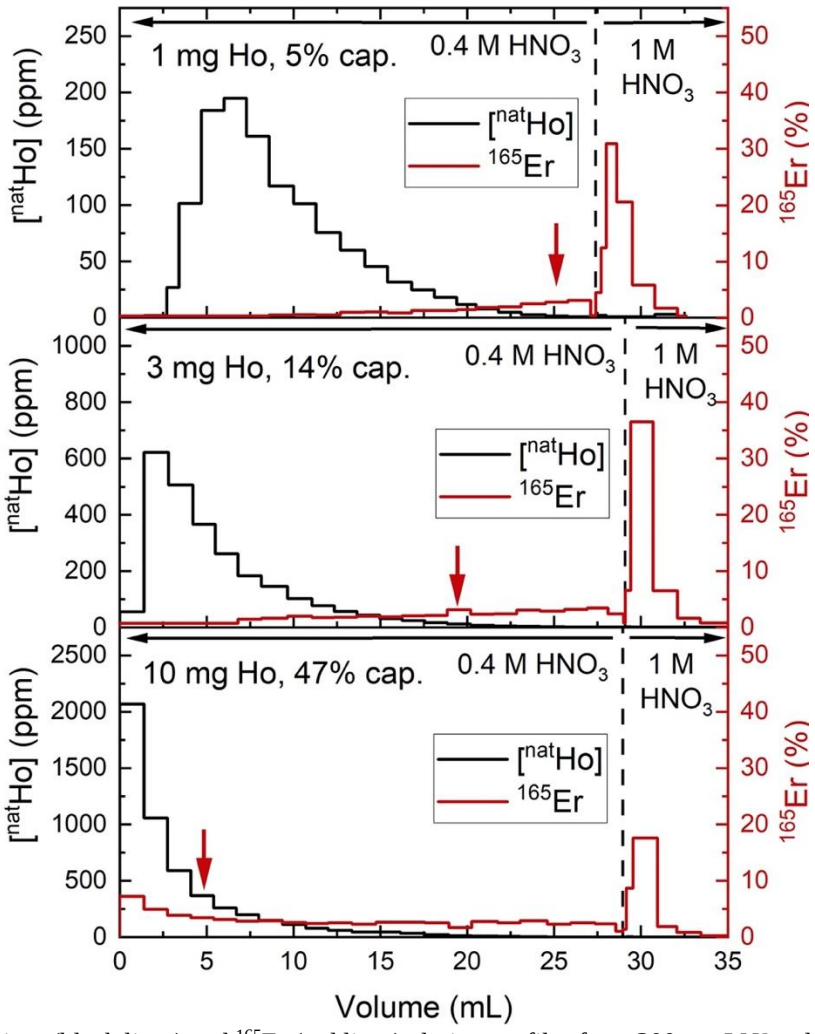

Figure 5.19: Holmium (black lines) and ^{165}Er (red lines) elution profiles from 300 mg LN2 columns loaded with 1 mg (top), 3 mg (middle) or 10 mg (bottom) holmium, 0.6 – 1.5 MBq ^{165}Er in 200 mL 0.1 M HNO_3, 70 mM αHIBA and eluted with ~29 mL 0.4 M HNO_3, followed by ~5 mL 1 M HNO_3. Red line denotes the volume where 20% of ^{165}Er had eluted from the column

These experiments demonstrate that under the investigated conditions the chromatographic performance of LN2 EXC columns is significantly decreased when holmium loading masses are increased from 5% theoretical maximum capacity to 14% to 47%. It conservatively limits the loading capacity of the 500 mg LN2 columns used in the bulk of this work to 1 – 2 mg (3 – 6% theoretical max capacity) of holmium.

5.3.3.7 Effect of dry loading conditions

Because of the high flow rate of the loading process, there have been incidences of the LN2 column going dry between the loading and rinsing steps. As column dryness could create channelling within the column resin that allows eluents to pass through with decreased interaction, this experiment compared two identical LN2 columns, one running dry and the other not, to determine if dryness during the loading step hindered Ho-Er separation.

- **Materials and Methods**

This testing of the LN2 column required the intermediate step of the full Ho-^{165}Er separation procedure. The columns were freshly dry packed using 500 mg of LN2 (20 - 50 µm, Triskem Int.) in a 1mL fritted polypropylene column. All columns were preconditioned with 1 M HNO_3 (5 mL) then 0.1 M HNO_3 (25 mL) with all nitric acid solutions made with 16 M HNO_3

(TraceSelect, Fluka) and 18 MΩ·cm ultrapure water (Milli-Q). Holmium was taken from a solution with a known concentration of 100 mg Ho in 0.07 M α-HIBA (44.4 mL), and the erbium from 10 mg of $ErCl_3$ dissolved in 10 mL of Milli-Q water. A loading solution of 0.07 M α-HIBA (220 mL, pH 2.6), 0.5 mg Ho (220 µL), and 0.5 mg $ErCl_3$ (500 µL) was used for each trial. A peristaltic pump (Welco Co. Ltd, WPM1-P1CA-WP) loaded the solution at a flow of 6 mL/min onto the LN2 column. Under one experimental condition, deemed 'wet', the column was loaded but still had liquid in the lines when switched to the rinsing phase. Under a second experimental condition, deemed 'dry', the column was loaded, and the pump ran until the loading solution had drained from the column and loading lines. Once loaded, another peristaltic pump (Welco Co. Ltd, Welco Co. Ltd, WPM1- P1BB-BP) rinsed the columns with 0.4 M HNO_3 (100 mL) at 1 mL/min collected in 5 mL fractions, followed by 5 M HNO_3 (4 mL). The conditioning, loading, and rinsing were repeated to obtain two identical replicates for each experimental condition. The amount of holmium and erbium in each fraction was quantified using MP-AES (Agilent MP4200). Holmium standard solutions of 0.05 – 50 ppm were made by dissolving holmium metal in 11 M HCl, followed by dilution in 0.1 M HCl. Similarly, erbium standards were created by dissolving erbium chloride in 0.1 M HCl and diluted to the necessary concentrations. From each fraction (one loading, twenty rinsing, and one elution), 100 µL was taken and diluted to 1 mL with 0.1 M HCl. The limit of detection for holmium and erbium was estimated to be ~1 ppm in these diluted sample solutions.

- **Results and Discussion**

The MP-AES data showed holmium and erbium following the expected elution pattern, though some fractions had below detection limit concentrations (Figure 5.17). Average and standard deviation error bars are reported for the duplicated experiments under each experimental condition. Even with values being recorded as the limit of detection, the columns that run dry appear to have a broader holmium elution peak along with erbium eluting sooner, therefore more peak overlap. As the goal of the LN2 column is to recover as much erbium and as little holmium as possible, the less these peaks overlap, the higher the erbium recovery while maintaining an adequate $SF_{(Ho/Er)}$. Though the MP-AES detection limit obfuscates any quantifiable difference between the two experimental conditions about $SF_{(Ho/Er)}$, the peak overlap with non-overlapping error bars supports the idea that running the column dry may lead to a less successful separation.

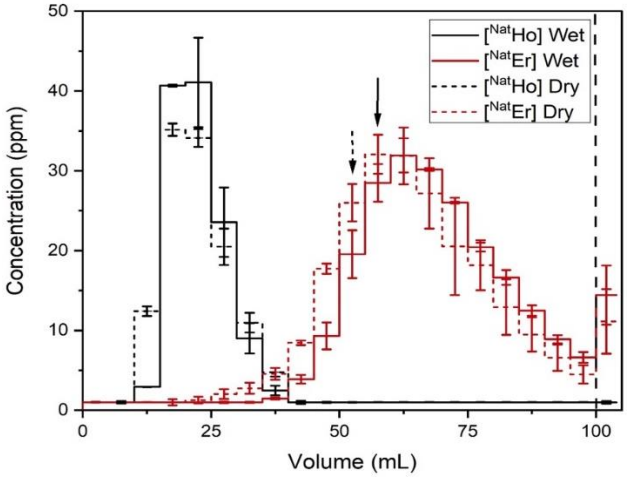

Figure 5.20: Elution profiles (n = 2 for each run type) for holmium (black) and erbium (red) eluted in rinse and elution fractions from 500 mg resin LN2 columns. The solid lines refer to the "wet run" trials where the column and lines were kept wet between the loading and rinsing stages. The dashed vertical line indicates the change between the rinsing (0.4 M HNO_3) and elution (1 M HNO_3) stage. The vertical black arrows indicate the fraction in which the threshold of 20 % erbium collection was reached. The error bars show the standard deviation between the two trials.

When using a freshly packed LN2 column, running the column dry may impact chromatographic performance. However, because the MP-AES quantified fraction concentrations in this experiment were near or below the limit of detection, the effect, if present, is only mild and does not render the separation useless if column dryness occurs.

5.3.3.8 Effect of column reuse and dry loading conditions

To expand on the impact of dryness on the LN2 column, an experiment explored if long durations of dry storage would cause changes in the resin thereby not allowing for reuse. This experiment took three columns stored dry from use in previous separations, ran them dry during the loading stage, and examined erbium and holmium concentrations of rinse fractions to determine if high-quality separation was achievable.

- **Materials and Methods**

Materials and methods are similar to the ones described in section 5.3.3.7. Several modifications have been made to adapt to the purpose of this study. The columns containing LN2 resin (500 mg, 20 - 50 µm, Triskem Int.) in a 1mL fritted polypropylene column were used at least once in previous ^{165}Er radioisolation chemistry, then stored dry for 20, 11, or 3 weeks. A peristaltic pump (Welco Co. Ltd, WPM1-P1CA-WP) loaded the solution at a rate of 6 mL/min onto the LN2 column until the solution was fully loaded and drained from the column and loading lines.

- **Results and Discussion**

Elution profiles for the three run-dry reused columns are shown in Figure 5.18. There was a marked difference in the elution patterns from both the standard LN2 performance (Figure 5.12 and 5.16 top) and from each other. Instead of a gradual peak of holmium elution followed by a peak of erbium elution, the elements washed out in unpredictable patterns, the erbium barely eluting until the elution fraction for two of the columns. Though this experiment did not repeat trials for each column, the varied elution patterns between dry columns preconditioned and run the same way made the results unpredictable and likely not repeatable. This evidence supports the idea that reusing columns stored dry and running them dry in the loading process causes significant separation issues.

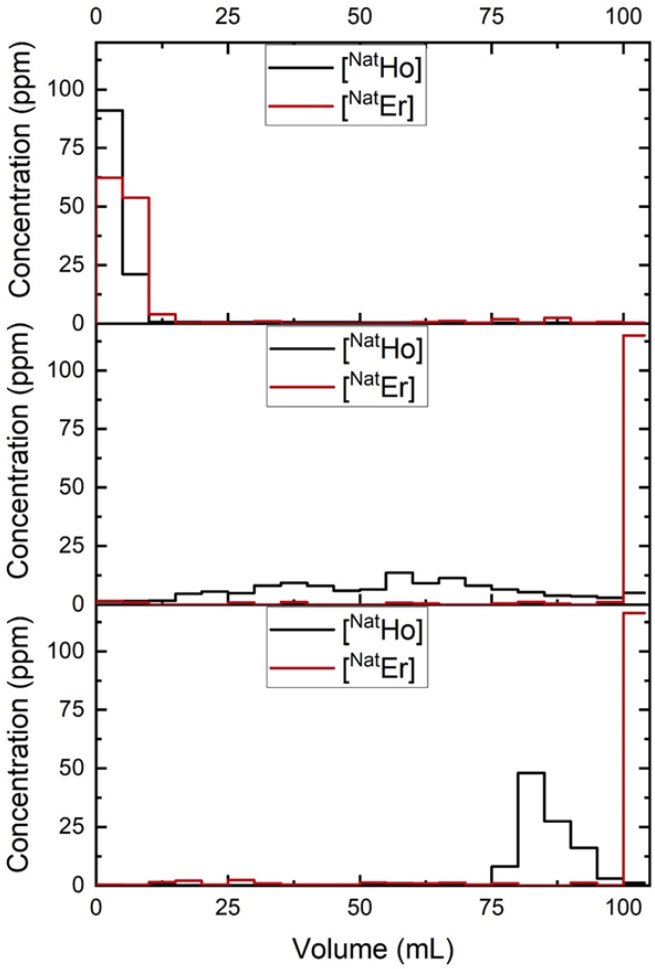

Figure 5.21: Elution profile for holmium (black) and erbium (red) eluted in rinse and elution fraction for reused 500 mg LN2 columns stored dry for 3 (top), 11 (middle), and 20 (bottom) weeks. The concentrations of Ho and Er for many of the fractions were near the detection limit. The dashed vertical line indicates the change between the rinsing (0.4 M HNO_3) and elution (1M HNO_3) stage. As can be seen, peaks are not shaped or ranged as in best practice separations (Figures 5.12. blue curves (500 mg). and 5.16. top).

Running the column dry with previously used, dry-stored columns is a combination that dramatically changes the chromatographic performance of LN2 columns. The resulting elution patterns are irreproducible and make proper cutoff between rinsing to waste and collecting for a large separation factor nearly impossible. Columns should not be dry-stored and reused from previous separations. Experiments on step 1 where used EXC LN2 (wet-stored in water between two uses), demonstrate that these resins stored in water could be reused after conditioning. In the case of a dried column, a repacking of the column allows its reuse.

5.3.3.9 Optimized step 2 EXC separation procedure

The second step of the ^{165}Er isolation procedure accomplishes a high $SF_{(Ho/Er)}$ while accommodating milligram quantity holmium masses through EXC using commercially available LN2 resin in a polypropylene column. When filled to maximum capacity (500 mg), the 1.3 mL column has a theoretical capacity of 36 mg of trivalent lanthanides according to the Triskem product sheet. However, a significant decrease in chromatographic performance was observed when loading more than 5 % theoretical capacity, limiting the LN2 column capacity to 1 – 2 milligrams of holmium. Following the CX/αHIBA column, the acidified Ho/^{165}Er solution was loaded onto the LN2 column, trapping both ^{165}Er and Ho. Based on previously published studies[102], the column was rinsed with 0.4 M HNO_3 to affect the differential elution

of holmium before erbium. As shown in Table 5.8., elution with 0.4 M HNO_3 (50 mL) removed > 99 % of the holmium, along with a cumulated ~20 % of the ^{165}Er. The remaining ^{165}Er was rapidly eluted with 1 M HNO_3 (~5 mL) (Figure 5.19). To avoid a moderate to severe decrease in chromatographic performance, care was taken to prevent the resin bed from going dry during use, and columns were freshly packed and conditioned before each experiment.

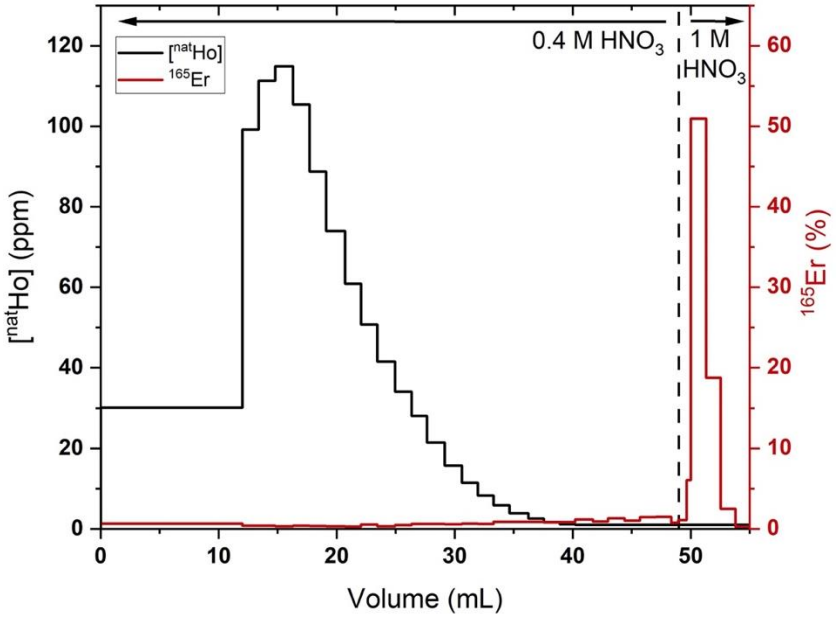

Figure 5.22: Holmium (black lines, quantified by MP-AES) and ^{165}Er (red lines, quantified by radioactivity dose calibrator) elution profiles from a representative 500 mg LN2 column loaded with ~1 mg holmium, ~2 MBq ^{165}Er in 0.1 M HNO_3 (200 mL), 70 mM αHIBA and eluted with 0.4 M HNO_3 (50 mL), followed by 1 M HNO_3 (5 mL). Fractions with Ho/^{165}Er below detection limits (Ho MP-AES: 1 ppm, ^{165}Er: 4 kBq) are shown as upper limits.

Fritted polypropylene columns (5.5 mm diameter, 1 mL, Supelco) were dry-packed with resin (500 mg) and preconditioned with 1 M HNO_3 (5 mL) followed by 0.1 M HNO_3 (25 mL). All nitric acid solutions were prepared using 16 M HNO_3 (TraceSelect, Fluka) and 18 MΩ·cm ultrapure water (Milli-Q). The ^{165}Er/Ho/αHIBA eluate from separation step 1 was acidified to 0.1 M HNO_3 using 16 M HNO_3 and passed through the EXC column at 5.8 ± 0.9 mL/min using a peristaltic pump (n = 10, Welco Co. Ltd, WPM1-P1CA-WP). With a lower flow rate of 1.2 ± 0.1 mL/min (n = 10, Welco Co. Ltd, WPM1-P1BB-BP), holmium was eluted with 0.4 M HNO_3 (40 – 60 mL), followed by ^{165}Er eluted with 1 M HNO_3 (4 – 6 mL).

For ^{165}Er fraction eluted in 1 M HNO_3 by EXC LN2 in step 1 (deuteron irradiation), the elution solution was diluted 10x in water before to being used in selectivity step 2. A similar protocol has been applied to for step 2 with the 500 mg LN2 column rinsed with 44 ± 2 mL (16.7 ± 5.8 %) and 6 ± 2 mL (6.5 ± 2.0 %) of 0.4 M HNO_3 before to recover 76.6 ± 7.4 % of ^{165}Er in 6 ± 1 mL of 1 M HNO_3.

In the optimized procedure, LN2 columns loaded with Ho (570 ± 370 µg), rinsed with 0.4 M HNO_3 (52 ± 9 mL) resulted in 78 ± 6 % ^{165}Er recovery and an $SF_{(Ho/Er)}$ = 1020 ± 320 (n = 4). The LN2 $SF_{(Ho/Er)}$ was estimated from the Ho mass in the final ^{165}Er solution, assuming no Ho/Er separation was achieved with the final bDGA column. Three additional replicates where holmium was below the MP-AES detection limit and four additional replicates with deviations from the above-described experimental procedure were excluded from this analysis. In two of these excluded replicates, a 0.4 M HNO_3 (42 mL) rinse resulted in 96% ^{165}Er recovery and a $SF_{(Ho/Er)}$ = 290 and a 0.4 M HNO_3 (52 mL) rinse resulted in a 63% ^{165}Er recovery and an $SF_{(Ho/Er)}$ > 2000. These results demonstrate the sensitivity of the procedure to HNO_3

concentration/volume and the interplay between $SF_{(Ho/Er)}$ and ^{165}Er recovery as demonstrated in step 1 for EXC separation. The latter of the two results indicates that simply using a set volume of 0.4 M HNO_3 to remove Ho may lead to irreproducible ^{165}Er recovery and $SF_{(Ho/Er)}$. To ensure a reproducible, optimal balance between recovery and $SF_{(Ho/Er)}$, the radioactivity in the 0.4 M HNO_3 eluant is quantified by dose calibrator as it is collected in 1 – 5 mL fractions. After ~ 20% of the loaded radioactivity had eluted, the mobile phase was changed to 1 M HNO_3 to elute the remaining high purity ^{165}Er with the optimized results reported above.

5.3.4 Third step: reduction of trace metal

The final step of the ^{165}Er isolation procedure reduced trace metals while concentrating the product into a small volume, low acidity solution suitable for radiolabeling using 100 mg of a commercially available bDGA resin (Triskem) (extractant: branched or *N,N,N',N'*-tetrakis-2-ethylhexyl-diglycolamide). A 1 mL, 5.5 mm ID fritted SPE tube was used as a column for extraction resins. The loading (5 M HNO_3, 5 mL) and rinsing (3 M HNO_3, 15 mL) solution concentrations were chosen due to literature studies showing high erbium and low transition metal (Fe, Co, Ni, Cu, Zn) affinities on a similar DGA resin[213]. This resin fixed element with charge 3+ at a high nitric acid concentration. A small volume rinse (0.5 M HNO_3, 2 mL) decreased column acidity and minimized subsequent ^{165}Er elution volume. Following this loading and rinsing routine, 97 ± 2 % of the loaded ^{165}Er was recovered in 0.01 M HCl (1.2 ± 0.2 mL) (n = 18) for proton 12.5 MeV irradiations at the University of Madison. Smaller elution volumes were attainable by fractionation of the 0.01 M HCl elution solution, with an optimized (n = 5) elution profile shown in Table 5.10. For 13 MeV deuteron irradiations, 91.5 ± 1.4 % of the loaded ^{165}Er was recovered in 0.01 mL HCl (1.0 ± 0.1 mL) (n = 10) (Table 5.10).

Table 5.10: Optimized ^{165}Er elution profile bDGA EXC column (proton and deuteron irradiations).

Irradiation	**Proton 12.5 MeV**						**Deuteron 13 MeV**					
Fraction	**Volume (µL)**			**^{165}Er Yield (%)**			**Volume (mL)**			**^{165}Er Yield (%)**		
1	210	±	20	0.1	±	0.2	0.1	±	0.1	0.8	±	1.1
2	390	±	30	88	±	4	1	±	0.1	91.5	±	1.4
3	420	±	10	9	±	4	0.5	±	0.1	4.3	±	1.9
4	490	±	30	1	±	0.3	0.6	±	0.2	1	±	0.4
Column		dry		1.8		0.5		dry		1.9		0.7

5.3.5 Overall radiochemical separation in three steps:

The overall chemical isolation procedure of 12.5 MeV proton irradiation from start-of-dissolution to final ^{165}Er isolation in 0.01 M HCl (~400 µL) was 4.9 ± 0.7 hours (n = 13) (Table 5.11). The optimized procedure had a decay-corrected ^{165}Er recovery of 64 ± 2 % and an $SF_{(Ho/Er)} = (2.8 \pm 1.1) \cdot 10^5$ and was validated for holmium target masses up to 180 mg, with the final ^{165}Er fraction containing 370 ± 180 ng of residual holmium after separation (n = 4).

	Madison (USA)	Orléans (FR)
Material Target	Ho spot welded target	
Ho	spot-welded target	
Er impurities	0.5 ppm	50 ppm
Size Target		
diameter	9.5 mm	
thickness	280 - 300 µm	127 µm
mass	180 mg (n = 5)	90 mg (n = 12)
Reaction	^{165}Ho(p,n)^{165}Er	^{165}Ho(d,2n)^{165}Er
Physical yield	24.1 ± 0.5 MBq.eµA^{-1}.h^{-1} (n = 5)	75.1 ± 10.1 MBq.eµA^{-1}.h^{-1} (n = 12)
Radiochemical Separation		
Step 1	Cation exchange Dowex 50W-X8 (200 - 400 mesh) 0.07 mM αHIBA ph = 4.7	Extraction exchange LN2 (20 - 50 µm) gradient HNO_3 (0.4 --> 1 M)
	≈ or > 90 % ^{165}Er recovered	
Step 2	LN2 (20 - 50 µm) 500mg 50 mL 0.4 M then 1 M HNO_3 ≈ 80 % ^{165}Er recovered	
Step 3	bDGA (50 - 100 µm) ≈ or > 90 % ^{165}Er recovered	
^{165}Er yield	64 ± 2 %	59.0 ± 9.7 %
Protocol time	4.9 ± 0.7 h (n = 13)	4 -5 h (n = 12)
$SF_{(Ho/Er)}$	(2.8 ± 1.1).10^5	(7.8 ± 3.7).10^4

Table 5.11: Comparison production of ^{165}Er by proton (Madison, biomedical cyclotron) and deuteron (Orleans, research cyclotron)

For 13 MeV deuteron irradiations, ~4 – 5 h were necessary from irradiation to recovery of 59.0 ± 9.7% (decay-corrected EoB) of ^{165}Er in 1 mL of 0.01 M HCl and a $SF_{(Ho/Er)}$ = (7.8 ± 3.7)·10^4 (n = 4), with ^{165}Er recovery measured via HPGe spectrometry measurements. It was validated for ≈ 90 mg of Ho target with a final ^{165}Er fraction containing 0.7 ± 0.3 µg of holmium and 1.1 ± 0.1 µg of erbium (ratio of Er estimated from ICP-OES and hypothesis of 50 ppm Er impurity in Ho foil). Assuming ICP-OES results and considering the uncertainty of 50% on the percent value of ppm Er impurity in Ho foil, a $SF_{(Ho/Er)}$ = (2.9 ± 2.0)·10^4 was estimated. $SF_{(Ho/Er)}$ was estimated using the equation (22) :

Equation (20)
$$SF(Ho/Er) = \frac{m \text{ or } A_{Ho,before} \Big/ m \text{ or } A_{Ho,after}}{A_{165Er,before} \Big/ A_{165Er,after}}$$

$SF_{(Ho/Er)}$ = (7.8 ± 3.7)·10^4 (n = 4) is a calculated value whereas $SF_{(Ho/Er)}$ = (2.9 ± 2.0)·10^4 is an estimated value based analysis certificate of Ho foil (<50 ppm). No exact level of Er in Ho foil (in ppm) was given and no analysis was done in the laboratory by ICP-MS. But if an estimation of 20 ppm Er impurity (with 20% of uncertainty), $SF_{(Ho/Er)}$ = (7.3 ± 3.7)·10^4 was obtained more in agreement with $SF_{(Ho/Er)}$ calculated without estimation of percent of Er impurity in Ho foil (Table 5.12).

	Ho (µg)	Er (µg)	Ho mass (mg)	Yield ^{165}Er (%)	SF calculated without Er impurity estimation	SF estimated with Er impurity at	
						50 ppm	20 ppm
Mean	0.7	1.1	92.1	61.5	77645	29166	72915
STD (%)	46.0	5.4	1.3	13.8	48.0	69.1	51.0

Table 5.12: $SF_{(Ho/Er)}$ calculated and estimated with variation of percentage (ppm) of Er impurity in Ho foil

5.3.6 DTPA/DOTA AMA determination

The AMA of the final ^{165}Er solution was determined by titration using tetraazacyclododecane-1,4,7,10-tetraacetic acid (DOTA, Macrocyclics Inc) and diethylenetriaminepentaacetic acid (DTPA, Acros Organics) as previously described[100]. To polypropylene tubes, 0.5 – 3 MBq (20 µL) of ^{165}Er in 0.01 M HCl, 1 M NaOAc (100 µL, pH 4.7, 99.995 % metal trace metal basis, Aldrich), and DOTA or DTPA (100 µL, 0.03 – 3 µg/mL) in 18 MΩ·cm water were added. Following incubation at 85 °C for DOTA and 21 °C for DTPA for 1 hour, each tube was assayed by thin layer chromatography (TLC) using silica-based stationary phase (J.T. Baker) and 0.05 M disodium ethylenediaminetetraacetic acid (EDTA, Fisher Scientific Co.) as mobile phase. Radioactivity distribution on the TLC plates was visualized using a Cyclone Plus phosphor plate reader (Perkin Elmer) (proton irradiation) (Figure 5.20) or miniGITA Star RadioTLC system (Elysia, Raytest, Belgium) (deuteron irradiation). Free ^{165}Er had an Rf of ~1, chelated [^{165}Er]Er-DOTA had an Rf of ~0.2, and [^{165}Er]Er-DTPA had an Rf of ~0.7. To compute the AMA, ^{165}Er activity in MBq was divided by twice the number of moles of DOTA/DTPA required to complex 50% of the radioactivity, and the value was reported as MBq of ^{165}Er per nmol of ligand, or MBq/nmol (mean ± standard deviation, SD)

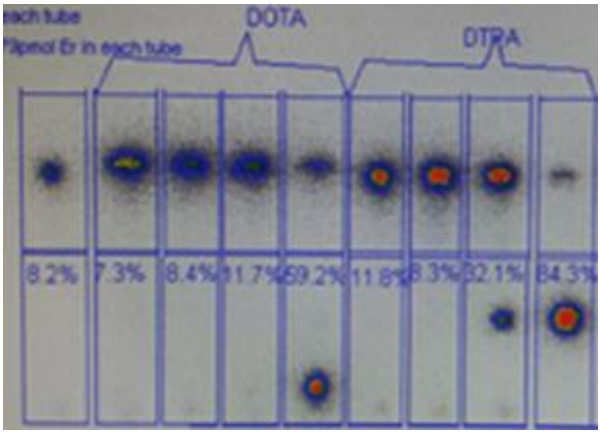

Figure 5.23: Determination of AMA by radio TLC with Cyclone Plus phosphor plate reader

Successful ^{165}Er isolation from low purity Ho foils (Alfa Aesar, <100 ppm Er (proton), <50 ppm (deuteron)) and high purity Ho foils (DOE Ames Laboratory MPC, 0.5 ppm Er), EoB-decay corrected AMA values determined by DTPA and DOTA titration are shown in Table 5.13.

Table 5.13.: Chelator-titration-based AMA results for ^{165}Er isolated from various qualities of Ho targets

Ho Target Er impurity (ppm)	AMA (MBq/nmol)[a]								n
	DOTA				DTPA				
< 100	11	±	4		10	±	4		5
< 50	3	±	2		36	±	16	(b)	9
0,5	20	±	24	(c)	92	±	97		4

(a) AMA decay corrected end of bombardment
(b) n= 8
(c) n = 3

Two main sources of erbium/holmium: cold erbium target impurity and residual holmium due to incomplete separation are the two dominating terms in the denominator of equation (21), which calculates a maximum achievable EoB AMA for a given ^{165}Er preparation. With the experimental ^{165}Er production and radiochemical separation results presented above in the case of proton irradiation, equation (21) yields a calculated EoB ^{165}Er AMA of 9.9 ± 0.5 MBq/nmol for a 1 hour, 12.5 MeV, 130 mg, 9.5 mm Ø, low purity (100 ppm Er) holmium target PETtrace irradiation. This calculated AMA (EoB) agrees with the measured DOTA/DTPA ^{165}Er AMAs (Table 5.13). In this case, the calculated AMA (EoB) is nearly entirely driven by the cold erbium impurity present in the holmium target material (second term in equation (21) denominator). This underscores that under the investigated irradiation conditions, utilization of holmium targets with high erbium impurity content will limit the molar activity of the resulting ^{165}Er to values lower than typically acceptable for therapeutic radiopharmaceutical research applications. Producing high AMA ^{165}Er via proton irradiation requires holmium with very low erbium content, such as target material that has been repurified from erbium or the DOE Ames Laboratory MPC metal used in this work.

For an identical irradiation of a high purity (0.5 ppm Er) holmium target, equation (21) yields an ^{165}Er AMA(EoB) of 240 ± 60 MBq/nmol, with this AMA being driven by cold holmium remaining in the ^{165}Er preparation after their separation by a $SF_{(Ho/Er)} = (2.8 \pm 1.1) \cdot 10^5$ (third term in equation (21) denominator). However, the ^{165}Er AMAs (EoB) (Table 5.11.) with DOTA (1.2 – 47 GBq/μmol$_{DOTA}$, n = 3) and DTPA (4.9 – 250 GBq/μmol$_{DTPA}$, n = 4) do not reflect this high value of an AMA. This disagreement may be a result of nanomole, sub-ppm metal trace metal (Zn, Fe, Cu) impurities in the radiolabeling reactions, which are not considered in equation (21). This hypothesis is supported by the fact that, for ^{165}Er isolated from high-purity holmium targets, the titration-based AMA measured using DTPA was 5 – 22 times higher than for DOTA (n = 3).

In the case of deuteron irradiation at 13 MeV (line < 50 ppm in table 5.13), the theoretical AMA of n Ho target of 90 mg (50 ppm Er impurities) with 9.5 mm diameter irradiated for 6 h at 6 μA is 92 MBq/nmole. AMA from titration with DTPA (36 ± 16 MBq/nmol) are 10 times higher than these ones obtained by DOTA (3 ± 2 MBq/nmol). DOTA AMA is very far from theoretical values in the case of DOTA. This difference in DTPA/DOTA AMA values, which has also been observed for cyclotron-produced ^{86}Y[214], is likely due to the non-selective nature of DOTA's metal binding properties. Compared with DTPA, DOTA binds 10.000 times stronger to Fe^{2+} ($LogK_{FeDOTA} = 20.22 \pm 0.07$ [215], $LogK_{FeDTPA} = 16.0 \pm 0.1$[216]), 100 times stronger to Zn^{2+} ($LogK_{ZnDOTA} = 20.8 \pm 0.2$, $LogK_{ZnDTPA} = 18.6 \pm 0.1$[216]), and 10 times stronger to Cu^{2+} ($LogK_{CuDOTA} = 22.3 \pm 0.1$, $LogK_{CuDTPA} = 21.5 \pm 0.1$[216]), causing these three common metal trace impurities to be significantly more problematic in DOTA versus DTPA radiochemical labelings as demonstrated in deuteron irradiation where DTPA results are on average 12 times higher than these ones of DOTA. Clearly, for these irradiations contamination by metals was a

possible explanation for the much lower AMA values. Thus, a systematically higher DTPA-based AMA compared with DOTA-based AMA is an indicator of contamination by Fe/Zn/Cu-based metal trace impurities in the radiolabeling solutions impacting the ^{165}Er AMA values (Table 5.13).

5.4 Applications of high ^{165}Er AMA: Auger therapy and in vivo MRI/SPECT imaging

5.4.1 Auger therapy: radiosynthesis of [^{165}Er]Er-PSMA-617

Receptor-targeted therapeutic radiopharmaceuticals for human use are radiolabeled using 10 – 40 GBq $^{177}LuCl_3$ with ~90% radiolabeling yield at ~60 MBq/nmol molar activity[201,202,217]. A clinically relevant DOTA-based radiopharmaceutical (PSMA-617) was radiolabeled with our high AMA ^{165}Er. PSMA-617 (MedChemExpress) was dissolved in 18 $M\Omega^{-1}\cdot$cm water to a concentration of 0.1 µg/µL and distributed into 10 aliquots that were stored at – 20 °C. A sodium acetate solution (1 M, 99.995% metal traces basis, Aldrich) was buffered with hydrochloric acid until a pH of 5.7. ^{165}Er (41 – 52 MBq in 70 – 80 µL 0.01 M HCl) was added to a solution of PSMA-617 in water (1 nmol in 10 µL, 2 nmol in 10 µL, or 5 nmol in 25 µL), NaOAc aq. (1 M, pH 5.7, 50 µL), and L-ascorbic acid (0.3 – 0.4 mg, 25 µL, ≥ 99.9998 % metal traces basis, Honeywell-Fluka) were added and the mixture reacted at 80 °C and 1000 rpm for 30 minutes. The reaction was diluted in 18 MΩ·cm water (10 mL) and loaded onto a pre-equilibrated C-18 Plus Light cartridge, rinsed with water (10 mL), and eluted with pure ethanol (700 µL). An aliquot (25 µL) was diluted with 18 MΩ·cm water (25 µL) and set aside for quality control analysis. Analytical HPLC was performed on [^{165}Er]Er-PSMA-617 using an Agilent 1260 Infinity II module coupled with an inline radioactivity detection system with an electronic analog pulse converted to voltage (Model 106, Lawson Labs Inc) and logged using an Agilent 1200 universal interface box. The separation was performed on a reverse-phase C18 column (Agilent InfinityLab Poroshell 120 EC-C18, 4.6 x 100 mm, 2.7 µm) using a linear gradient (95 to 20 % over 15 min) of 0.1% trifluoroacetic acid (Thermo Scientific in 18 $M\Omega^{-1}\cdot$cm water) in acetonitrile (Fisher Scientific, HPLC-grade) at 1 mL/min.

In vitro stability of [^{165}Er]Er-PSMA-617 was investigated in the presence of L-ascorbic acid and freshly prepared normal human serum prepared from lyophilized powder (009-000-001, Jackson Immuno Research Laboratories, Inc) reconstituted using phosphate buffered saline (2.0 mL, PBS, Lonza Bioscience). Dry [^{165}Er]Er-PSMA-617 (3.1 MBq) and L-ascorbic acid (0.6 mg) were dissolved in serum (300 µL) and incubated at 37 °C for 12 hours. Aliquots of the [^{165}Er]Er-PSMA-617 complex were assessed by analytical HPLC at t = 1 and 12 h. The chromatograms were analyzed by integration of the [^{165}Er]Er-PSMA-617 peak compared to all radioactive peaks (free erbium or decomposition products) in the chromatogram.

The distribution coefficient (log D value) of [^{165}Er]Er-PSMA-617 was determined using a 1:1 (v/v) solution of n-octanol (Alfa Aesar) and PBS according to previously reported methods[198]. A sample of [^{165}Er]Er-PSMA-617 (8.2 – 51 MBq, 2.8 – 8.4 MBq/nmol) was dried and diluted with PBS and n-octanol (700 µL each). The solution was vigorously agitated for 5 minutes before being centrifuged at 1000 rpm for 5 minutes. An aliquot of PBS and n-octanol was analyzed by HPGe gamma spectrometry under identical geometries and the ratio of decay-corrected net counts per minute was used to determine the distribution coefficient. The PBS aliquot required 4 – 5 days of decay before acquisition of an HPGe spectrum with acceptable (< 5%) dead-time. Uncertainty in the LogD value was calculated by the propagation of error associated with HPGe counting statistics and in the half-life of ^{165}Er (10.36 ± 0.04 h[218]). The

logD experiment was repeated for five independent preparations of [^{165}Er]Er-PSMA-617 and logD was reported as the average and standard deviation of results.

Following successful isolation, the [^{165}Er]Er-PSMA-617 was synthesized with labeling yields summarized in Table 5.14.

Table 5.14: [^{165}Er]PSMA-617 radiolabeling yields.

PSMA-617 (nmol)	^{165}Er activity† (MBq)	Labeling yield (%)	Labeled MA† (MBq / nmol)	n
1	170 ± 88	49 ± 7	82 ± 45	3
2	76	97	37	1
5	250	100	50	1

†Radioactivity and MA decay-corrected to end of bombardment

Radioanalytical HPLC showed [^{165}Er]Er-PSMA-617 (UV retention time (RT) = 6.45 min, radioactivity RT = 6.60), co-eluting with cold Er-PSMA-617 and Ho-PSMA-617 standards (230 nm RT = 6.45 min), shown in Figure 5.21. Radiochemical purity of the [^{165}Er]Er-PSMA-617 was > 95%.

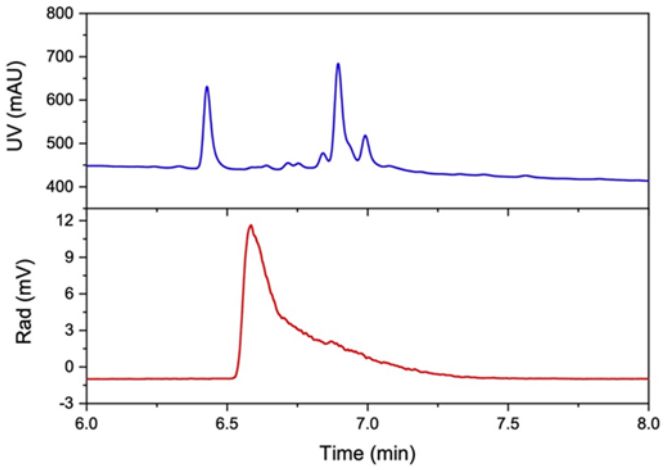

Figure 5.24: Analytical HPLC radiochromatograph (top: 230 nm absorbance, bottom: radiation detector) of representative purified [^{165}Er]Er-PSMA-617.

Also visible in the 230 nm absorbance chromatograph of the [^{165}Er]Er-PSMA-617 radiopharmaceutical were multiple mass peaks with RT = 6.8 – 7.0 min, retention times corresponding to [^{nat}Zn]PSMA-617 (230 nm RT = 6.90 min), [^{nat}Fe]PSMA-617 (230 nm RT = 6.80 min), and [^{nat}Cu]PSMA-617 (230 nm RT = 6.95 min), see Figure 5.22. The [^{165}Er]PSMA-617 radiochemical purity remained > 95 % after 12 hours of incubation in whole human serum, the longest time point assessed. The octanol-PBS distribution coefficient of [^{165}Er]Er-PSMA-617 was -3.3 ± 0.3 (n = 5).

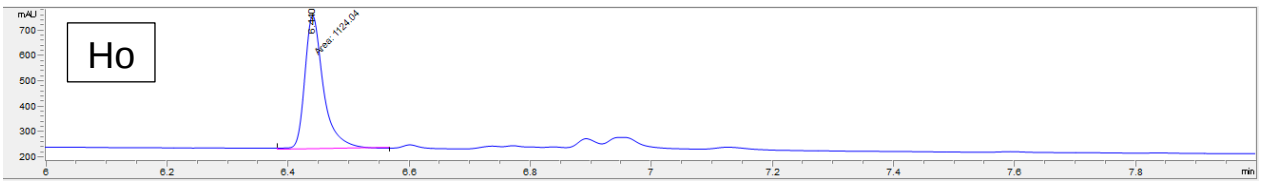

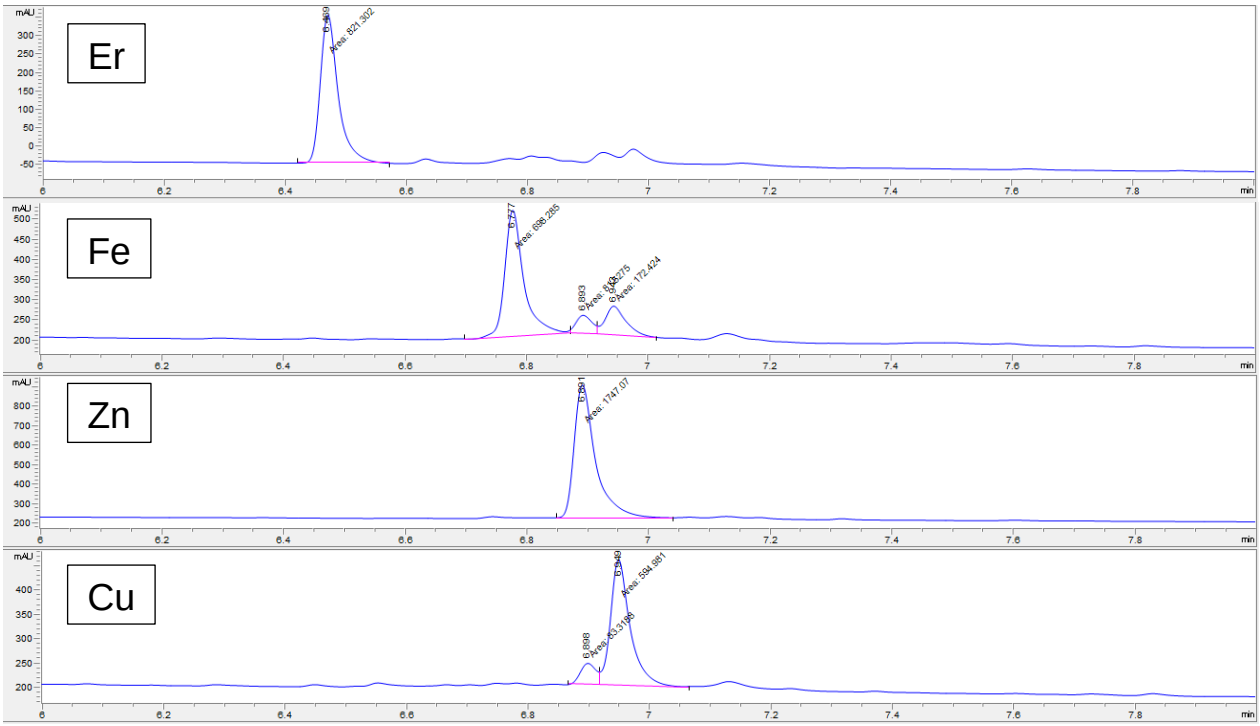

Figure 5.25: Analytical HPLC chromatograph (230 nm absorbance) of cold metal PSMA-617 compounds

Due to a high purity of ^{165}Er (AMA) produced in this work, a new radiopharmaceutical agent, [^{165}Er]PSMA-617, was successfully synthesized at biologically relevant molar activities. It will be utilized to understand the role of AEs in PSMA-targeted radionuclide therapy of prostate cancer in vitro and in vivo.

5.4.2 Toward "in vivo" bimodal MRI/SPECT imaging: Ligand P6

For in vitro use, a batch of ^{165}Er with low AMA values has been used to demonstrate proof of concept of bimodal MRI/SPECT imaging. With our developments, AMA values increase significantly due to the high purity of Ho foil (0.5 ppm impurity), higher product activity, or high $SF_{(Ho/Er)}$. Nevertheless, in the case of DOTA, presence of trace metal reduces AMA values drastically compared to theoretically expected values due to its slow kinetics of reaction compared to DTPA. In the case of deuteron irradiations, AMA with DTPA is 10 times higher than the ones obtained with DOTA with the same solution (Table 5.13.). For in vivo bimodal MRI/SPECT imaging, P6 ligand was a candidate for experiments.

P6 ligand (Figure 5.23) is supposed to have higher selectivity to lanthanides than transition metals. Conditions of radiolabeling are described in section 5.3.6. DTPA/DOTA AMA determination have been applied to determine AMA of ^{165}Er with P6.

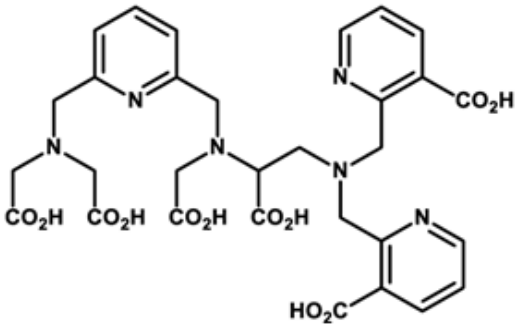

Figure 5.26: Ligand P6

An average P6 AMA of 19 ± 7 MBq/nmole (n = 6) (EoB) was obtained. This value confirmed the selectivity of P6 for lanthanides versus metals and could be applied to the investigation in vivo bimodality concept. At least ^{165}Er with high AMA > 10 MBq/nmole (EoB) was produced for bimodality MRI/SPECT and Auger therapy dosimetry applications. In the first case, its AMA has been determined with molecule P6: 19 ± 7 MBq/nnmol (n=6) (EoB). For the second application when ^{165}Er was produced by proton 12.5 MeV irradiation with a biomedical cyclotron, PSMA-617 was successfully radiolabeled for the first time with ^{165}Er with ≈ 100% with 37 - 50 MBq/nmole increasing to 82 ± 45 MBq/nmol for 49 ± 7 % of radiolabeling yield.

6. Outlooks and Conclusion

6.1 Outlooks

6.1.1 Outside production of radionuclides

Due to the lockdown of the cyclotron at CEMHTI in March 2023, one of the main challenges to continuing the activities related to the separation of radionuclides with different materials is to assure access to the radionuclides at Orleans. We demonstrate that ^{52}Mn could be produced by alpha irradiation and after 4 – 5 h of separation, this radionuclide is available for studies. Due to its long half-life ($T_{½}$ = 5.5 days), production at ARRONAX, where a 67 MeV alpha beam energy is available, will be logistically possible (production and transport). The cyclotron of ARRONAX is located approximately 4 h from Orleans. Exploring the area above 45 MeV makes sense but some traces of ^{54}Mn will be expected and physical yield will be similar.

For ^{165}Er, the delivery from other producing laboratories to Orleans encounters two main challenges : (1) its short half-life of 10.36 h prevents the possibility of ^{165}Er transportation from Roskilde (Denmark), only laboratory producing ^{165}Er in Europe, and (2) the long-time response for acquiring a new license at CEMHTI for receiving exotic radionuclides from external laboratories. Access to facilities that produce ^{165}Er and use it on-site is a good option. International organizations advocate exploring new ways and using new facilities to produce radioisotopes for medical purposes as a complementary option to conventional methods based on nuclear reactors[106,219]. In this context, PRISMAP, the European medical radionuclides program, was created. This network of world-leading European facilities, including nuclear reactors, medium- and high-energy accelerators, and radiochemical laboratories, has been established to offer the broadest catalogue of radionuclides for medical research. Development towards upscaling of novel radionuclide production will be explored with novel production technology, new purification methods, and proof-of-concept investigations showing the development of new treatments from test bench to patient care. It is the European equivalent of the U.S. Department of Energy's University Isotope Network (UIN), see section 2.1.3. University of Wisconsin-Madison's cyclotrons.

The International Fusion Materials Irradiation Facility - Demo Oriented NEutron Source (IFMIF-DONES) is set to become a facility aimed at irradiating materials with neutrons to characterize crucial components for future fusion reactors[220]. The expected outstanding characteristics of DONES in terms of neutrons and deuterons have pushed the complementary applications of radioisotope production for nuclear medicine[221]. Currently, the initial phase DONES is under design and construction in Granada[222], which will hold only one 40 MeV accelerator focusing deuterons onto the lithium jet target. The successful design of AE-emitting radiopharmaceuticals is based on consideration of all parameters, including decay properties, nuclear chemistry, radiochemistry, dosimetry, and radiobiology[223,224]. Access to a high deuteron beam (in energy) opens access to AE emitters such as ^{165}Er. A first collaboration around the AE topics with the group of J. Praena, from the University of Granada (Spain) (article in progress) drove us to determine the cross-section of nuclear reaction ^{165}Ho(d,2n)^{165}Er between 5 to 17.5 MeV at Orleans'cyclotron (Figure 6.1).

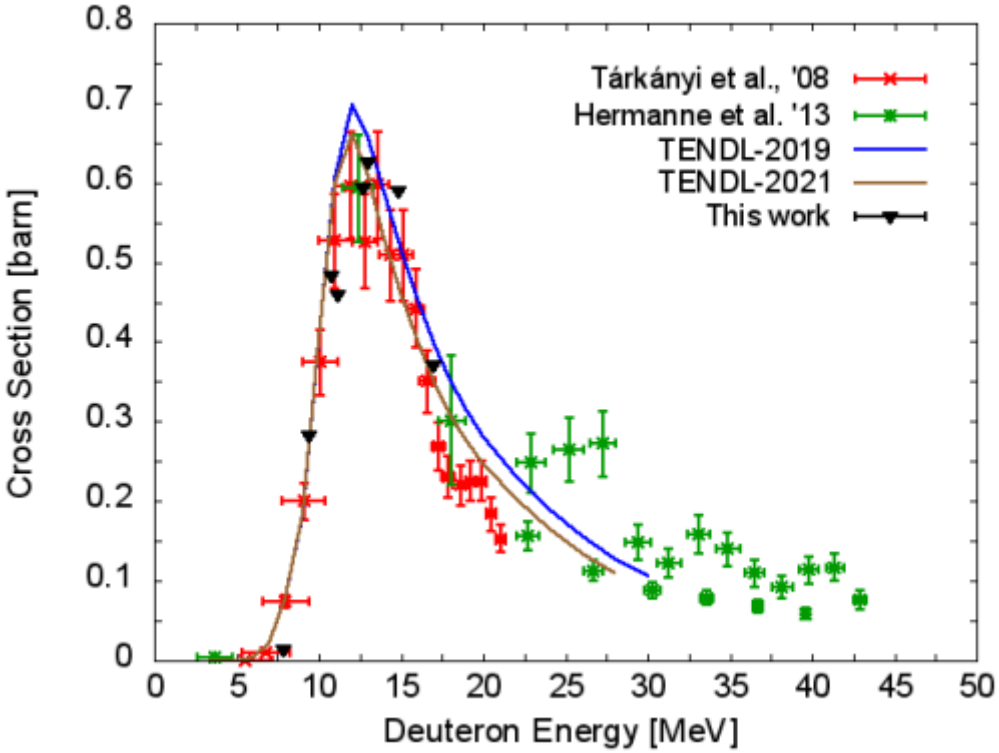

Figure 6.1: Excitation function for the ^{nat}Ho(d,2n)^{165}Er nuclear reaction.

These results have been used to calculate the expected ^{165}Er produced by a 1.25 mA, 40 MeV deuteron beam in DONES. Due to its high power, a realistic cooling system has been simulated[221] and evaluated on the production of ^{165}Er with the ^{nat}Ho(d,2n)^{165}Er reaction. Considering this device, our results show a superior activity to other direct and indirect routes. These results push further experimental studies that characterize possible contamination, as stable ^{164}Er and ^{166}Er, as the apparent molar activity after chemical separation.

Another pathway exists to produce ^{165}Er and use it for several days: a ^{165}Tm/^{165}Er generator, ^{165}Tm ($T_{½}$ = 30.06 h) decays to ^{165}Er ($T_{½}$ = 10.36 h) through electron capture.

6.1.2 ^{165}Tm/^{165}Er Generator

Preliminary results established by Van der Meulen's group in PSI (Paul Scherrer Institute) in 2020 have shown that irradiation of an erbium oxide ^{166}Er[Er_2O_3]target with proton beam at high energy (18 to 30 MeV) leads to ^{165}Tm[147] However, this process requires expensive enriched ^{166}Er targets[225]. For this reason, we are investigating two different ways to obtain ^{165}Tm:

1. Use of nuclear reaction ^{165}Ho(α,4n)^{165}Tm: preliminary irradiations of a Ho target with 45 MeV alpha beam have been performed on a spot-welded target prepared with Ho foil (127 µm thickness, Energy out = 34.7 MeV). About 3 MBq of ^{165}Tm ($T_{½}$ = 30.06 h) were produced in 15 min of irradiation at I = 1 eµA. Under these conditions, ^{166}Tm (30 MBq, $T_{½}$ = 7.7 hours) and ^{167}Tm (< 0.1 MBq, $T_{½}$ = 9.25 days) were coproduced (Figure 6.2). In collaboration with ARRONAX (Nantes) and Subatech laboratory, the cross-section of this nuclear reaction between 30 – 68 MeV will be determined.

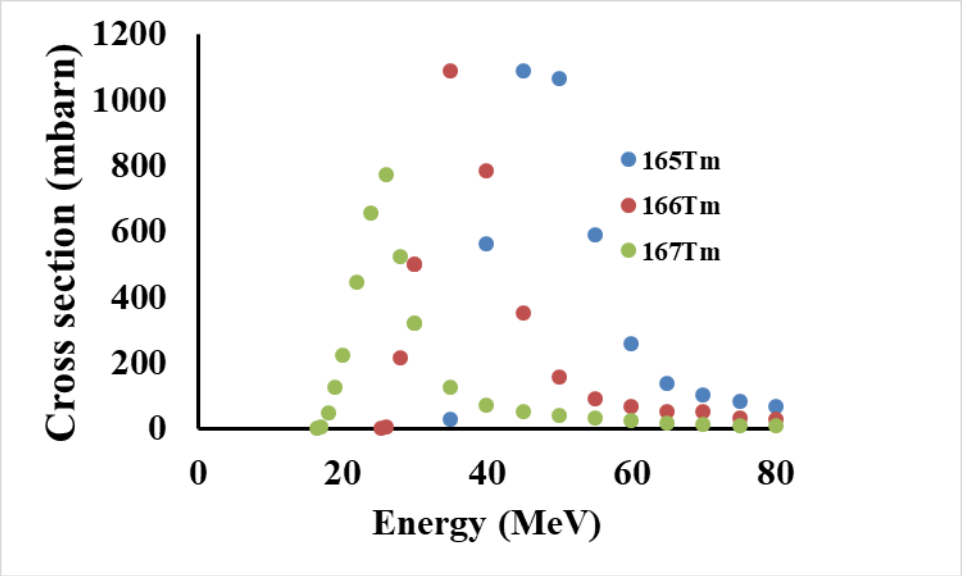

Figure 6.2: Cross section of nuclear reaction ^{165}Ho(α,xn)$^{165\text{-}166\text{-}167}$Tm according to TENDL 2021.

2. Spallation on a natural target of Ta: ISOLDE facility at CERN in Geneva (Switzerland)[226] uses high energy proton-induced spallation reactions to produce radioisotopes by the isotope separation on-line (ISOL) technique[227] on a natural target of Ta. By this process, ^{165}Tm is isolated. No supplementary purification of delivered ^{165}Tm is necessary. After a 17 – 20 h decay time, ^{165}Er could be separated from ^{165}Tm by extraction resin. However, in a generator ^{165}Tm/^{165}Er, ^{165}Tm (generator parent nuclide) is immobilized on a support by chemical bound whereas ^{165}Er (daughter parent nuclide, $^{165}Er^{3+}$) needs to be mobile.

6.1.3 Use porous carbon supports for radiolanthanide separation

6.1.3.1 Porous materials at CEMHTI

Access to ^{165}Er is necessary for application in Auger therapy dosimetry and bimodality use. However, the separation of adjacent lanthanides as Ho/Er is still a challenge. Bearing this in mind, we have investigated the use of porous carbons as supports for the separation of adjacent lanthanides. For this purpose, commercial materials are currently used, namely: AG®1-X8 anion exchange resin (Bio-Rad), Dowex 50W-X8 cation exchange resin (Sigma Aldrich), and LN2 (20-50µm) extraction resins (Triskem). The association of cation exchange materials (high capacity but low selectivity) with extraction resins (high selectivity but low capacity) seems to be a good compromise to separate lanthanides.

We start with a colleague Dr Conchi Ania, expert in the synthesis and applications of porous materials, to improve the separation efficiency of common materials using porous carbon supports with varied characteristics. The concept is based on the functionalization of the porous carbons with chelatants[228], to explore the role of the pore size of the carbon supports on the separation capacity and distribution ratio[180]. Indeed, recent works have highlighted the potential advantages of porous materials in this field due to their high stability under harsh irradiation conditions, easy functionalization, low cost, and versatility of pore architectures[229]. The choice of the carbon-based porous supports was based on their chemical resiliency to acidic conditions [230,231] and stability to radiation emissions[232].

For this, porous carbons with varied porosity and chemical composition were selected and functionalized with acidic organophosphorous extractants as bis (2-ethylhexyl) phosphoric acid (HDEHP) and 2-ethylhexyl phosphonic acid mono-2-ethylhexyl ester (HEHEHP). These

extracts are those used by Triskem to prepare respectively LN and LN2 extractive resins. Given the dimensions of the organophosphorus extractants, carbon materials with a well-developed mesoporosity (pores between 2 and 50 nm) were selected for this study.

6.1.3.2 Functionalization

Three porous carbon-based materials with microporous/mesoporous character were selected: sample CV (biomass-derived porous carbon, average particle size below 20 µm), sample MS (MAST® polymeric carbon, spherical particles of ca. 200 – 300 µm), and sample PG (polymeric resorcinol-formaldehyde xerogel, average particle size below 20 µm). The selected porous supports were functionalized according to the method described by Horwitz[180]. Briefly, ca. 10 g of extractant (bis (2-ethylhexyl) phosphoric acid HDEHP, (2-ethyl-1-hexyl) phosphonic acid mono 2-ethyl-1-hexyl ester (HEHEHP) were dissolved in 100 mL of methanol in a round flask. Then 15 g of the porous carbon was added and stirred for 1 hour at room temperature on a rotary evaporator (vacuum pressure). After that, the temperature was increased to 50 °C, and the solvent was evaporated. The resulting material was dried at 60 ºC and stored in a desiccator until further use. For comparison purposes, the commercial LN and LN2 resins from Triskem were also used. Additionally, a home-made LN resin was synthesized at CEMHTI following a similar protocol to that of Triskem (i.e., functionalization of Amberchrom CG-71 (25 – 53 µm) polymethacrylate polymer with HDEHP extractant).

The successful functionalization of the selected porous supports was investigated by gas adsorption and thermal analysis. The textural parameter evaluated from N_2 adsorption isotherms at 77 K of the samples revealed a sharp decrease in the specific surface area and total pore volumes of the samples, due to the immobilization of the extractant (Table 6.1). The thermogravimetric profiles of the samples also confirmed the immobilization inside the pore structure of the materials rather than on the external surface.

		S_{BET} (m^2/g)	V_{Pores} (cm^3/g)	V_{Micro} (cm^3/g)	V_{Meso} (cm^3/g)
(a)	**CV**	1280	1,06	0,41	0,64
	MS	1375	1,2	0,57	0,64
	PG	591	0,55	0,13	0,38
	Amberlite CG71	547	0,981	0,21	0,7
(b)	**CV-LN**	49	0,17	0,03	0,14
	MS-LN	34	0,29	0,13	0,07
	PG-LN	61	0,09	0,01	0,07
	LN (Triskem)	146	0,43	0,04	--

Table 6.1: Characterization of resin support before (a), and after incorporation (b) of extractant (bis (2-ethylhexyl) phosphoric acid HDEHP (LN)

6.1.3.3 Determination of Dw in static mode

Distribution coefficients Dw were studied according to (1) HNO_3 concentration (resin capacity fixed at 10%) and (2) resin capacity ($[HNO_3]$ = 0.5 M).

6.1.3.3.1 Variation of HNO_3 concentration

➢ **Materials and Methods**

The Ho target (Alfa Aesar, 99.9%, < 50 ppm of Er) was centered and spot welded to a 0.5 mm thick, 14.3 mm diameter Ta disc (Alfa Aesar, > 99.95%). The 37.9 mg Ho target (127 µm thick, 6.3 mm diameter) was assembled into the water-jet cooled transfer capsule and clamped to an aluminum piece (2 mm thickness) back cooled with an 11 mm apertured aluminum ring. The target was irradiated at 13 MeV deuteron beam 2 hours at I = 4 µA at the Orleans'cyclotron on the 60° incident angle CISCoTe targetry, producing ~785 MBq of ^{165}Er and ~150 MBq ^{166}Ho at the end of the bombardment.

For determination of distribution coefficients (Dw)**,** after irradiation, the Ho target was dissolved in 2 M HCl and heated at 130 °C until dry. The pink residue was dissolved in 12 mL of water to form the ^{165}Er/Ho stock solution. Then about 50 mg of resin (porous carbon materials, commercial resin LN, homemade LN resin, PG or MS resin) were weighed in a 2 mL Eppendorf tube (each weight was replicated three times) and 1.2 mL of nitric acid solutions (0.3 M – 5 M) were added (for CV carbon support point at 0.01 M and 0.1 M were added). Then 100 µL of stock solution (≈ 6.5 MBq of ^{165}Er (EoB), 1.25 MBq ^{166}Ho (EoB)) contained 0.32 mg of cold holmium (10 % of LN resin capacity)) were added. The suspensions were stirred over ½ hour at 850 rpm and then centrifuged for 10 min. An aliquot of 600 µL of each sample was taken, and 1.4 mL of water was added to obtain a counting sample with a calibrated geometry for HPGe spectrometry. ^{165}Er and ^{166}Ho activities were quantified by high-purity germanium (HPGe) gamma spectrometry (Canberra). HPGe detector was calibrated in energy and efficiency with ^{133}Ba certified standard source at a specific geometry (Cerca France). For activity analysis, γ-ray spectrum analysis software package, Genie 2000 (Canberra, USA) was used. Activities of ^{165}Er and ^{166}Ho were estimated following peaks centered at 47.5 keV for ^{165}Er and 80 keV for ^{166}Ho. Dw were calculated using equation (19) (see section 4.2.2.1.2.1. Concept of distributon coefficient: Dw).

➢ **Results:**

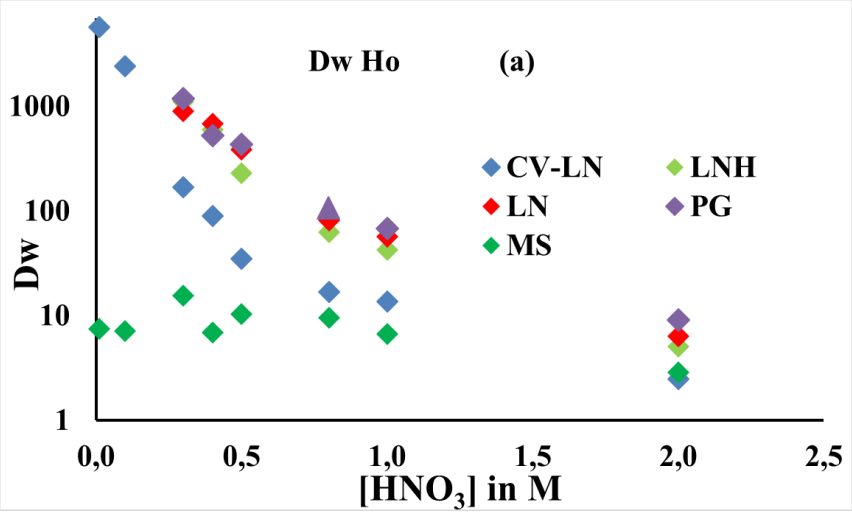

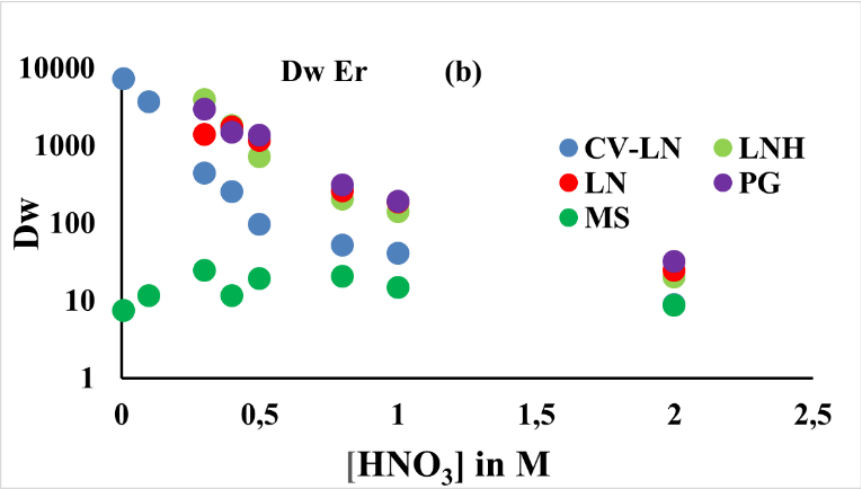

Figure 6.3: Dw of Ho (a) and Er (b) in samples CV, MS, PG, LN, and LNH for different [HNO_3].

Results of 5 M HNO_3 are not shown in graphs (Figure 6.3): values are weak, $Dw_{(Ho)} \approx 0$ and $Dw_{(Er)} \approx 3$ for all tested resin supports. Low retentions with Dw of ≈ 10 for Ho or Er were demonstrated for the sample MS. The large particle size of the MS sample (spheres of ca. 200 - 300 µm diameter) reduces specific surface area leading to low extraction efficiency. On the other hand, samples LNH, LN, and PG give similar Dw. ^{165}Er was slightly retained for 2 M HNO_3. In the case of sample PG, the suspensions in contact with nitric acid displayed different colors varying from transparent for the suspension (0.8 M HNO_3), yellow for 1 M and 2 M HNO_3, and orange for 5 M HNO_3. This suggests that the material is not stable under highly acidic conditions used for the Ho/Er separation. Indeed, the control experiments putting the resin in contact with nitric acid showed a similar trend regarding color change.
Furthermore, long-term exposure over 1 year of sample PG in 5 M HNO_3 confirmed the disintegration of the sample in an acidic medium. The addition of highly concentrated HNO_3 to sample PG generated a strong exothermic reaction. Based on this, sample PG was not further investigated. Regarding the Dw, sample CV displayed a similar parameter to commercial resin, although at lower nitric acid concentrations: ^{165}Er desorption started at 1 M instead of 2 M HNO_3. These values of Dw are more like those of commercial LN2 resin (Amberlite impregnated with HEHEHP extractant). Sample CV functionalized with the extractant was chemically stable during all the assays after one year of contact (this was verified by measuring any likely leaching of the material to the acid solution by UV-visible spectrophotometry).

6.1.3.3.2 Variation of resin capacity

- **Materials and Methods**

Some modifications were done to resin capacity tests. PG and MS supports were excluded from these experiments. The tests were evaluated at 0.5 M HNO_3. This concentration was an intermediary concentration between high retention of Ho/Er at lower [HNO_3] and desorption at higher concentration. A 347.9 mg Ho target (300 µm thick, 12.7 mm diameter) was irradiated for 4 hours at I = 10 µA (≈ 3300 MBq of ^{165}Er (EoB), ≈ 400 MBq ^{166}Ho (EoB)). Ho target was dissolved in 2 M HCl and heated at 130 °C until dry. The pink residue was recovered in 10 mL of 0.5 M HNO_3 producing the ^{165}Er/Ho stock solution. Then about 50 mg of resin (porous carbon materials (CV-LN), commercial resin LN or homemade LN resin (LNH)) were weighed in a 2 mL Eppendorf tube (each weight was replicated three times) then 20 µL (20%) – 50 µL (50%) – 100 µL (100%) – 200 µL (200%) – 400 µl (400%) of stock solution were added and

the solution completed to 1.5 mL with 0.5 M HNO_3. An aliquot of 20 – 600 µL of each sample was taken (dead time counting <7%) and completed to 2 mL with water for HPGe spectrometry.

➢ **Results**

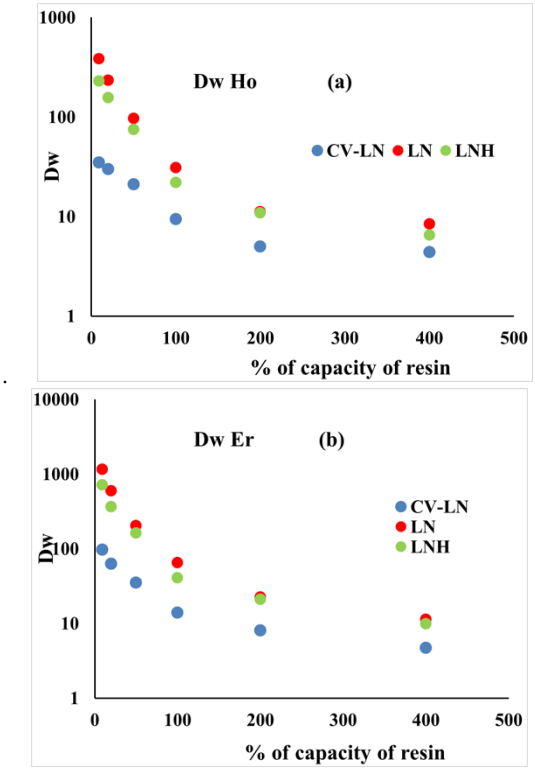

Figure 6.4: Dw of Ho (a) and Er (b) in samples CV, LN, and LNH for 0.5 M HNO_3 for various % capacity of resin

With a variation of the capacity of resin, the affinity of Er and Ho for resin was reduced due to the decreasing number of sites available to fix Ho/Er. The evolution of Dw (Ho and Er) for functionalized sample CV was like the commercial resin. No higher capacity of porous support was demonstrated in these experiments (Figure 6.4). Above 100%, Dw for Cv support was <10 for each element, Ho and Er. These results agree with the considerations exposed in section 5.4.3.5. The capacity of LN2 resin: increasing mass resin for equal Ho mass increases the separation efficiency. The number of extraction-free sites increases when the percentage of resin capacity is reduced.

In summary, after the determination of Dw in static mode, only the material prepared upon functionalization of CV carbon has been validated as a potential support. This functionalized material has proven to be stable at high nitric acid concentration and radiation during time (limited exposure) with a similar profile as LN2 resin. This is interesting since resin LN2 is synthesized with a different extractant (HEHEHP).

6.1.3.4 Dynamic profile of Ho/^{165}Er separation

➢ **Materials and Methods**

To further investigate the functionalization of carbon CV, a second functionalization of carbon CV (labeled CV-LN2) was carried out to incorporate extractant HEHEHP according to the process explained in section 6.4.2. preparation and characterization of the functionalized

porous carbons. The elution profile of resin LN (synthesized with extractant HDEHP, 50 – 100 µm), CV-LN (HDEHP, 20 – 50 µm), LN2 (HEHEHP 20 – 50 µm) and CV - LN2 (HEHEHP, 20 – 50 µm) were established. Set-up and elution conditions of step 2 (see section 5.3.3.9. Optimized step EXC separation procedure) were applied. A 1 mL, 5.5 mm diameter polypropylene column was filled with 500 mg of impregnated resins. Columns were pre-conditioned with 5 mL of 5 M HNO_3, 15 mL water and, finally, 5 mL of 0.1 M HNO_3. 2 mL of 4 MBq of ^{165}Er (the equivalent of 1 mg of holmium (3% of LN resin capacity)) in 0.1 M HNO_3 were deposited on top of column. Then columns were eluted with 50 mL of 0.4 M HNO_3, 8 mL of 1 M HNO_3, and finally, 4 mL of 2 M HNO_3. Each test was replicated three times with the same column and resin. The material after rinsed with 5 mL of 5 M HNO_3 was then reconditioned by repeating the procedure above-mentioned to achieve three extraction-elution cycles. No characterization of resins had been done between each test, only verification of the absence of radioactivity. The flow of the micro peristaltic pump for loading solution was regulated at 4 mL/min (10 V) and at 1 mL/min (4.5 V) for elution. In this set-up, the same micro peristaltic pump was used at low (1 mL/min) and high flow (4 mL/min) determined by variation of voltage of supply power in V. For dynamic column separation studies, an ionization chamber dose calibrator (Capintec CRC-15R, setting #187 experimentally determined by cross-calibration with HPGe gamma spectrometry) and HPGe spectrometry were used for ^{165}Er quantification activities. The mass of Ho was evaluated by ICP-OES to determine the $SF_{(Ho/Er)}$ for each material and fraction.

- **Results**

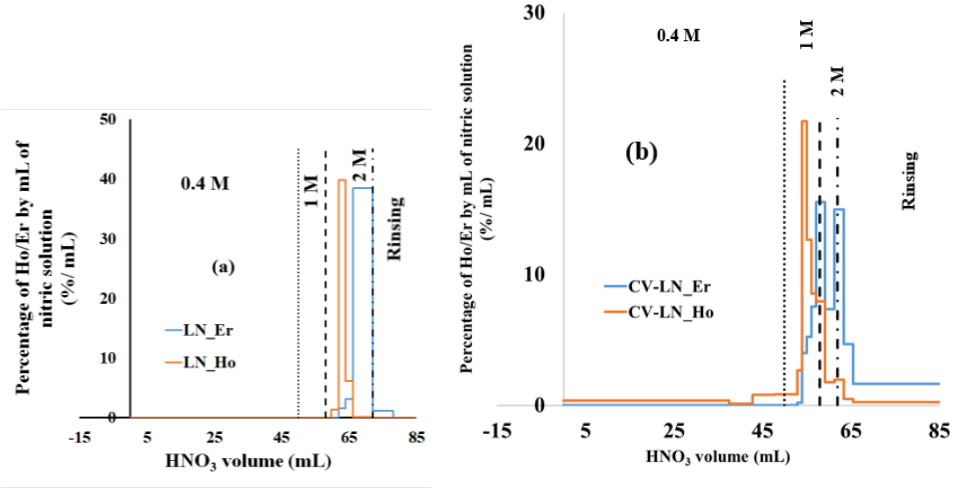

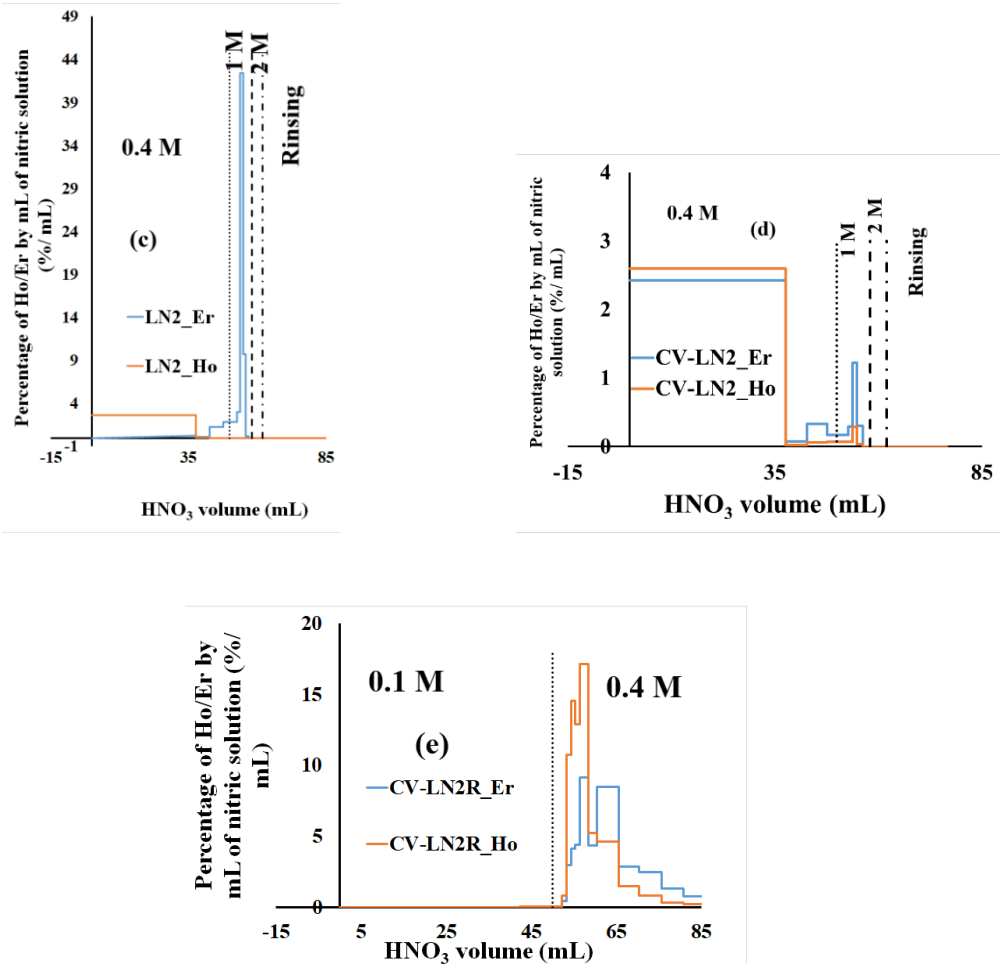

Figure 6.5: Comparison of elution profile of (a) LN resin (50 – 100 µm) (b) LN2 (20 – 50 µm) (c) CV - LN resin (20 – 50 µm) (d) CV - LN2 (20 – 50 µm) elution with 0.4 M HNO_3 in first 50 mL, and (e) (CV - LN2), elution with 0.1M HNO_3 in first 50 mL (for the test resin named CV - LN2R)

	SF	% ^{165}Er	^{165}Er Recovery volume (mL)	[HNO3] (M)
LN	184	90	12.1	2
LN 2	604	76	6.6	0.4 - 1
CV-LN	3	82	9.5	1 - 2
CV-LN2	4	4	2	1
CV-LN2R	3	66	25.5	0.4

Table 6.2: Comparison of specifications of ^{165}Er solution batch according to used resin.

The obtained results confirmed the influence of porosity on the behavior of the material used for the separation of Ho/Er. The functionalization of porous carbon CV with HDEHP (sample CV - LN) induced desorption of ^{165}Er at a lower concentration of HNO_3 as expected (2 M in the case of resin LN) (Figure 6.5). After elution of column of 500 mg of CV - LN2 with 0.4 M HNO_3, more than 90% of Ho and Er are recovered, thus no separation is produced. When the elution was done with 0.1 M HNO_3, no elution of each radiolanthanide ^{166}Ho and ^{165}Er before 40 mL. After eluted CV-LN2R resin with 50 mL of 0.1 M HNO_3, 0.4 M HNO_3 was used

and Ho was immediately desorbed whereas Er was more slowly. By comparison, extraction with resin LN2 (20 – 50 µm) renders >99 % of Ho recovered without Er elution (Figure 6.5c).

If the yield of ^{165}Er recovery was good for CV - LN (i.e. 80% of ^{165}Er recovered in 9.5 mL of 1 – 2 M HNO_3), the $SF_{(Ho/Er)}$ = 3 is very low compared to that of resin LN2 (20 – 50 µm, $SF_{(Ho/Er)}$ = 604) (Table 6.2). Thus, this parameter would need to be improved for a potential application of carbon CV support.

These preliminary results open new perspectives on the mesoporous carbons used for the radiochemical separation of lanthanides, as these results demonstrated for the pair Ho/^{165}Er. For these challenging separations, high $SF_{(Ho/Er)}$ are requested and the characteristics of the porous material need to be further investigated and optimized to attain this goal.

6.2 General conclusion

For the first time in France, ^{52}Mn and ^{165}Er were produced purified, and used in radiolabeling molecules. Moreover, ^{52}Mn and ^{165}Er were produced by various types of beam: ^{52}Mn was produced by irradiation of a 14 MeV proton beam on a Cr pellet or a 45 MeV alpha beam on a V foil. For ^{165}Er, a 16 MeV proton or a 13/17.5 MeV deuteron on a Ho target for ^{165}Er were used. Optimal conditions for a high AMA in MBq/nmol were defined according to target, conditions of irradiation (type of cyclotron, energy), and radiochemical separation. Thus, these radionuclides have been sufficiently isolated from irradiated bulk material with high activity to be used in radiolabeling molecules for bimodal MRI/PET or MRI/SPECT applications.

First, ^{52}Mn was produced by a 14 MeV proton irradiation of a 300 – 400 µm thick, 13 mm diameter sintered Cr pellet. The pellet was dissolved in 5 mL of 10 M HCl and put under reflux for 4 h. After cooling and adding ethanol, the Cr solution was dissolved in a mixture of 10 M HCl/ethanol (97/3 (v/v)), a radiochemical separation of ^{52}Mn from Cr target was performed using three anion exchange (AX) columns with 300 mg, 200 mg and 100 mg of AG®-1X8 200 – 400 mesh resin. 43 – 60 % of ^{52}Mn was recovered by a manual separation and 53 % was obtained using a homemade remote control system in the laboratory (ACCRA). The isolated ^{52}Mn was used to radiolabel several Mn-containing magnetic resonance imaging (MRI) contrast agent and some biodistributions of radiolabeled molecules were investigated. Finally, stability studies of [^{52}Mn]Mn-DOTA, [^{52}Mn]Mn-CDTA , and [^{52}Mn]-MnL6 demonstrated equivalent thermodynamic stability of [^{52}Mn]MnL6 and [^{52}Mn]Mn-DOTA complexes after various days in different conditions; solution of pH between 2 and 10, dissolution media (HSA, PBS, RPMI, MEM, Human serum), or in presence of Zn^{2+} or Cu^{2+} in solution.

Due to the presence of ^{54}Mn ($T_{½}$ = 312 days) in ^{52}Mn (< 1%) and a challenging target Cr target fabrication methodology for 14 MeV proton irradiation, the production of ^{52}Mn by alpha irradiation at high energy (45 MeV) was investigated. The cross-section of the ^{nat}V(α,x)^{52}Mn nuclear reaction was measured using V foils and two targetries available in Orleans'cyclotron: "hatch tip" (90° incident angle) and CiSCoTe (60° incident angle). ^{52}Mn production is effective for an energy beam > 30 MeV and no significant quantity of ^{54}Mn was detected. Irradiation of 9.5 mm diameter spot-welded vanadium targets with 75, 96, and 126 µm thicknesses gave physical yield of 2.5 ± 0.1 MBq·eµA^{-1}·h^{-1} (n = 4), 2.8 ± 0.3 MBq·eµA^{-1}·h^{-1} (n = 3) and 3.6 ± 0.7 MBq·eµA^{-1}·h^{-1} (n = 14), respectively. V target was dissolved in 0.7 mL of 15 M HNO_3 then complete to [HNO_3] ≈ 0.1 M with water. The solution was loaded on a cation exchange column (6.6 g Dowex 50Wx8) and was eluted with 0.5 M HNO_3 and 1.5 M HNO_3. 93 ± 6 % (n = 5) of ^{52}Mn were recovered in 19 ± 7 mL of 7 M HNO_3 in best conditions. A global vanadium/manganese separation factor of $SF_{(V/Mn)}$ = 423 ± 47 (n = 16) was obtained for the separation step 1 of V/^{52}Mn. For the second cation exchange purification step (500 mg of Dowex 50W-X8 200 - 400 mesh), 87.8 ± 11.8% (n = 11) of ^{52}Mn was recovered in 5.7 ± 1.0

mL of 10 M HCl. However, the $SF_{(V/Mn)} = 2$ was insignificant. For a final trace metal reduction step, AX and extraction chromatography (EXC) were tested: AX with resin AG® 1-X8 200 – 400 mesh (200 and 100 mg) with similar protocol applied to proton irradiation or EXC with AC resin 50 – 100 µm (250 and 150 mg). More than 90% of ^{52}Mn were recovered from each protocol, but low apparent molar activity (AMA) was measured by DOTA titration. However, weak AMAs were not associated with the efficiency of the metal traces protocol Origin of the used metal traces protocol applied on the ^{52}Mn batch didn't affect AMA values. Our radiochemical separation process in 4 steps (two CX columns and two columns for metal traces elimination) reduces significantly V: $SF_{(V/Mn)} \approx 800$ (obtained after the two first steps of separation). This $SF_{(V/Mn)}$ can be improved in different ways : (1) optimization of Dowex 50W-X8 column elution by V ICP – OES monitoring, (2) using one CX in step 1 and for steps 2 and 3, extraction AC resin, or (3) combination of option (1) and (2). Finally, recovery of ^{52}Mn in a highly concentrated solution of HCl (6 M) increases its AMA before its use. But assuming separation results, low produced ^{52}Mn activities (<50 MBq) is the most likely reason for low obtained ^{52}Mn AMA.

At least, the physical yield of 45 MeV alpha irradiation 3.6 ± 0.7 $MBq \cdot e\mu A^{-1} \cdot h^{-1}$ (n = 14) (37 to 97 mg) was equivalent to 14 MeV proton irradiation 4.5 ± 1.7 $MBq \cdot e\mu A^{-1} \cdot h^{-1}$ (n = 6) (266 ± 18 mg) with lower mass. However, by alpha irradiation higher radionuclidic purity from ^{54}Mn was obtained: 0.09 ± 0.02 % (n = 13) for 45 MeV alpha beam versus 0.39 ± 0.15% for proton beam.

In both cases, ^{54}Mn ($T_{½}$ = 312 days) will be produced. This is a significant drawback for two main reasons. First, because its half-life is > 100 days, French regulatory authorities require that ^{54}Mn-containing radioactive waste cannot be decayed in storage in the laboratory. Second, the presence of the long-lived ^{54}Mn will add an additional, no required dose burden to ^{52}Mn used in clinical studies. Thus, it is likely that ^{52}Mn produced via ^{nat}Cr(p,x) or ^{nat}V(α,x) could be used only in preclinical studies for the biodistribution of new Mn-labelled drugs. For ^{52}Mn, even if the radiochemical separation process is good, high AMA requires high activities, which requires an automatic process for regular manipulation to limit radiation to staff (operator, researcher). In our work, we demonstrate a reproducibility of ^{52}Mn production by proton and alpha beam.

In this context, this work makes ^{52}Mn available for its applications for example bimodality MRI/PET using pair ^{52}Mn/^{55}Mn.

In the second part of this work, ^{165}Er was produced initially for a proof of concept of bimodality MRI/SPECT application. ^{165}Er was chosen because it was a radioactive lanthanide with SPECT imaging capacity. A 100 mg Ho target was irradiated with a 16 MeV proton beam and dissolved in 15 M nitric acid. After evaporation and dissolution in 0.1M HNO_3, the solution was deposited in ≈ 4 g of extraction LN2 resin (20 – 50 µm) (Triskem). After elution of the column with ≈ 110 mL of 0.4 M HNO_3, and 40 mL of 1 M HNO_3, ^{165}Er was finally recovered in 1 M HNO_3. This ^{165}Er solution was used in the quantification of Zn^{2+} with a cocktail of the Zn^{2+}-responsive MRI agent GdL1 and its [^{165}Er]ErL1 analog. A cocktail with a known molar ratio ($1/2.4 \cdot 10^{-7}$) of Gd-to-^{165}Er was prepared in human serum albumin (HSA) solution (0.6 mM, physiological concentration) for successful proof of concept bimodal MRI/SPECT imaging. This validation was obtained with ^{165}Er purified only on one column of extraction LN2 resin (20 – 50 µm) for an $SF_{(Ho/Er)} > 1000$. However, for in vivo bimodal MRI/SPECT, $SF_{(Ho/Er)} > 10^5$ will be required to obtain a high and useful AMA. This requirement is also crucial for targeted Auger radiotherapy studies: ^{165}Er is a pure Auger emitter and is a perfect candidate for these studies.

To reach for higher ^{165}Er AMAs, three sensitive areas of radionuclide production have been investigated: target, targetry, and radiochemical separation according to tools and facilities

available in Orleans (France) for bimodal MRI/SPECT imaging and in Madison (Wisconsin, USA) for Targeted Auger Emitter Therapy (TAET).

First, the spot-welding method was applied to Ho foil to control target size and improve the water cooling system on target for high current intensity. Various parameters (thickness, diameter) and quality (< 100, < 50, 0.5 ppm Er impurities) were designed and spot welded on a Ta support (500 µm thickness). Through optimization of Ho target dimensions, (1) the quantity of Er impurity was limited to as low as possible, and (2) adaptation of Ho target mass to the radiochemical separation process.

Relative to targetry, as discussed with for ^{52}Mn production, higher activity product results in higher AMA. Theoretical physical yields of ^{165}Er by deuteron irradiation of Ho are 7 times higher than irradiation by proton. However, irradiation results with 17.5 MeV deuterons were not reproducible (some targets melted) at high-intensity current (> 10 µA). Decreasing the energy deuteron beam from 17.5 MeV to 13 MeV and limiting I = 6 µA, reduced power deposited on the Ho target and resulted in reproducible ^{165}Er yields from irradiations. In these conditions, Ho targets (mass = 90.4 ± 2.3 mg) have been 13 MeV deuteron irradiated during 6.0 ± 0.4 h at 6.0 ± 0.3 µA for a physical yield of 75.1 ± 10.1 MBq·eµA^{-1}·h^{-1}. At Madison, on GE PETtrace cyclotron, 13 MeV proton irradiation of 180 mg, 0.3 mm thick, 9.5 mm diameter Ho targets resulted in physical yields of 24 ± 1 MBq·eµA^{-1}·h^{-1} (n = 5). While this proton yield is 3 – 4 times lower than observed for deuteron irradiation at Orleans, such targets were irradiated at I = 40 µA without any disturbance or melted target for 1 – 2 h. In each case, the produced ^{165}Er activity was drastically increased – via deuteron irradiation at Orleans or by high current intensity at Madison.

Additionally, the radiochemical separation of ^{165}Er from Ho affects drastically the ^{165}Er AMA. In the case of ^{52}Mn, this point is not so crucial because separation V/Mn or Cr/Mn is less challenging than Ho/Er separation for a high AMA. A $SF_{(Ho/Er)} > 10^5$ was obtained with a three-step protocol. For the first step, at Orleans'cyclotron, using EXC with LN2 resin (20 – 50 µm) at low pressure (1 bar N_2), 76.7 ± 13.1 % (n = 11) of ^{165}Er was recovered in 16.7 ± 4.1 mL of 1 M HNO_3 with residual Ho quantity (< 0.7 %, $SF_{(Ho/Er)} >> 127$). This solution was diluted by 10 times for the second step of separation. In Madison, a CX column of Dowex 50W-X8 (200 - 400 mesh) was used for this first step with a high-pressure chromatography system using a freshly 70 mM αHIBA solution (pH = 4.7) for elution. This resulted in ~90% ^{165}Er recovery with $SF_{Ho/Er}$ = 320 ± 210 (n = 6) from an irradiated ~180 mg Ho and ~95% with $SF_{Ho/Er}$ = 250 ± 150 (n = 5) in case of ≤ 120 mg Ho target. The same protocol was applied to 200 – 300 mL of ^{165}Er in 0.1 M HNO_3 solution recovered from the extraction LN2 resin method or in 70 mM αHIBA solution (pH = 4.7). After optimization of various parameters (type of extractant, bed height column (mass resin), column capacity, 0.4 M HNO_3 volume, flow rate) for the second step, a 500 mg extraction LN2 resin (20 – 50 µm) column was used recovering > 75% of ^{165}Er in 1 M HNO_3 solution after elution of the column with 45 – 50 mL of 0.4 M HNO_3. Finally, ^{165}Er was concentrated and trace metal impurities were removed by using a 100 mg bDGA EXC resin (50 – 100 µm). The overall chemical isolation procedure in the case of 12.5 MeV proton irradiation from start-of-dissolution to final ^{165}Er isolation in 0.01 M HCl (~400 µL) was 4.9 ± 0.7 hours (n = 13). The optimized procedure had a decay-corrected ^{165}Er recovery of 64 ± 2%. The $SF_{(Ho/Er)}$ was equal to $(2.8 \pm 1.1)\cdot 10^5$ and was validated for holmium target masses up to 180 mg, with the final ^{165}Er fraction containing 370 ± 180 ng of residual holmium after separation (n = 4). For 13 MeV deuteron irradiation, ≈ 4 – 5 h were necessary from irradiation to recover 59.0 ± 9.7% (decay-corrected EoB) of ^{165}Er in 1 mL of 0.01 M HCl and a $SF_{(Ho/Er)} = (2.4 \pm 0.9)\cdot 10^5$ (n = 4). It was validated for ≈ 90 mg of Ho target with a final ^{165}Er fraction containing 0.7 ± 0.3 µg of holmium and 1.1 ± 0.1 µg of erbium.

Finally, high end-of-bombardment (EoB) decay-corrected AMA values were measured by titration with DTPA: 36 ± 16 MBq/nmol (n = 9) for Ho foil (from deuteron irradiation of Ho

with < 50 ppm Er impurity) and 92 ± 97 MBq/nmol (n = 4) (from proton irradiation of Ho with 0.5 ppm Er impurity). AMAs measured by DOTA titration were lower than DTPA, likely due to trace metal traces in the final batch. Significant variation of DTPA AMA to DOTA AMA indicated good separation factor $SF_{(Ho/Er)} \sim 10^5$.

In Madison, the isolated ^{165}Er was used to synthesize [^{165}Er]Er-PSMA-617 with EoB molar activities of 82 ± 45 MBq/nmol (n=3). This new radiopharmaceutical will be used in Auger Electron dosimetry studies to understand the role of AEs in PSMA-targeted radionuclide therapy of prostate cancer by comparison with agents such as [^{161}Tb]-PSMA-617 and [^{177}Lu]Er-PSMA-617. Finally, in Orleans, the isolated ^{165}Er radiolabeled the P6 ligand molecule with a high AMA 19 ± 7 MBq/nmole (n = 6) (EoB give access to the validation of in vivo bimodal MRI/SPECT applications).

Bibliography

1. Gudkov S V, Yu Shilyagina N, Vodeneev VA, Zvyagin A V, Chi-shing Cho W, Lemarié A. Targeted Radionuclide Therapy of Human Tumors. doi:10.3390/ijms17010033
2. Caravan P, Ellison JJ, McMurry TJ, Lauffer RB. Gadolinium(III) chelates as MRI contrast agents: Structure, dynamics, and applications. *Chem Rev*. 1999;99(9):2293-2352. doi:10.1021/cr980440x
3. Ndiaye D. Complexes de Manganese (II) Par Des Ligands de Type Bispidine Pour Des Applications En Iagerie Médicale (IRM, TEP). University of Orleans (France); 2021.
4. Dizeux A. Ultrasound Characterization of Tumor Angiogenesis, Stiffness and Microstructure under Conventional and Innovative Therapies. Université Pierre et Marie Curie, Paris VI; 2015.
5. Wang G, Zhang X, Liu Y, Hu Z, Mei X, Uvdal K. Magneto-fluorescent nanoparticles with high-intensity NIR emission T1- and T2-weighted MR for multimodal specific tumor imaging. *J Mater Chem B*. 2015;3(15):3072-3080. doi:10.1039/C5TB00155B
6. Grobner T. Gadolinium - A specific trigger for the development of nephrogenic fibrosing dermopathy and nephrogenic systemic fibrosis? *Nephrol Dial Transplant*. 2006;21(4):1104-1108. doi:10.1093/ndt/gfk062
7. Gale EM, Atanasova IP, Blasi F, Ay I, Caravan P. A Manganese Alternative to Gadolinium for MRI Contrast. *J Am Chem Soc*. 2015;137(49):15548-15557. doi:10.1021/jacs.5b10748
8. Molnár E, Váradi B, Garda Z, et al. Remarkable differences and similarities between the isomeric Mn(II)-cis- and trans-1,2-diaminocyclohexane-N,N,N′,N′-tetraacetate complexes. *Inorganica Chim Acta*. 2018;472:254-263. doi:10.1016/j.ica.2017.07.071
9. Di Gregorio E, Ferrauto G, Furlan C, et al. The Issue of Gadolinium Retained in Tissues: Insights on the Role of Metal Complex Stability by Comparing Metal Uptake in Murine Tissues Upon the Concomitant Administration of Lanthanum- and Gadolinium-Diethylentriamminopentaacetate. *Invest Radiol*. 2018;53(3):167-172. doi:10.1097/RLI.0000000000000423
10. Troughton JS, Greenfield MT, Greenwood JM, et al. Synthesis and evaluation of a high relaxivity manganese(II)-based MRI contrast agent. *Inorg Chem*. 2004;43(20):6313-6323. doi:10.1021/ic049559g
11. Wang S, Westmoreland TD. Correlation of relaxivity with coordination number in six-, seven-, and eight-coordinate Mn(ll) complexes of pendant-arm cyclen derivatives. *Inorg Chem*. 2009;48(2):719-727. doi:10.1021/ic8003068
12. Brandt M, Cardinale J, Rausch I, Mindt TL. Manganese in PET imaging: Opportunities and challenges. *J Label Compd Radiopharm*. 2019;62(8):541-551. doi:10.1002/jlcr.3754
13. Drahoš B, Lukeš I, Tóth É. Manganese(II) complexes as potential contrast agents for MRI. *Eur J Inorg Chem*. 2012;(12):1975-1986. doi:10.1002/ejic.201101336
14. Esteban-Gómez D, Cassino C, Botta M, Platas-Iglesias C. 17O and 1H relaxometric and DFT study of hyperfine coupling constants in [Mn(H2O)6]2+. *RSC Adv*. 2014;4(14):7094-7103. doi:10.1039/c3ra45721d
15. Pirko I, Gamez JD, Shearier ER, Raman MR, Johnson AJ, Macura SI. Manganese Enhanced MRI (MEMRI) in Murine CNS Inflammatory Disease Models (S21.007). *Neurology*. 2012;78. https://api.semanticscholar.org/CorpusID:76090066
16. Jacobs KE, Behera D, Rosenberg J, et al. Oral manganese as an MRI contrast agent for the detection of nociceptive activity. *NMR Biomed*. 2012;25(4):563-569. doi:10.1002/nbm.1773
17. Dubin AE, Patapoutian A, Dubin AE, Patapoutian A. Nociceptors : the sensors of the pain pathway Review series. 2010;120(11):3760-3772. doi:10.1172/JCI42843.3760
18. Lin YJ, Koretsky AP. Manganese ion enhances T1-weighted MRI during brain activation: An approach to direct imaging of brain function. *Magn Reson Med*. 1997;38(3):378-388. doi:10.1002/mrm.1910380305

19. Schima W, Függer R, Schober E, et al. Diagnosis and staging of pancreatic cancer: Comparison of mangafodipir trisodium-enhanced MR imaging and contrast-enhanced helical hydro-CT. *Am J Roentgenol*. 2002;179(3):717-724. doi:10.2214/ajr.179.3.1790717
20. Hu TCC, Pautler RG, MacGowan GA, Koretsky AP. Manganese-enhanced MRI of mouse heart during changes in inotropy. *Magn Reson Med*. 2001;46(5):884-890. doi:10.1002/mrm.1273
21. Crossgrove J, Zheng W. Manganese toxicity upon overexposure. *NMR Biomed*. 2004;17(8):544-553. doi:10.1002/nbm.931
22. Guhlke S, Verbruggen AM, Vallabhajosula S. Radiochemistry and Radiopharmacy. In: Biersack HJ, Freeman LM, eds. *Clinical Nuclear Medicine*. Springer Berlin Heidelberg; 2007:34-76. doi:10.1007/978-3-540-28026-2_2
23. Dickson J, Ross J, Vöö S. Quantitative SPECT: the time is now. *EJNMMI Phys*. 2019;6(1):4. doi:10.1186/s40658-019-0241-3
24. Lawrence EO, Livingston MS. The Production of High Speed Protons Without the Use of High Voltages. *Phys Rev*. 1931;38(4):834. doi:10.1103/PhysRev.38.834
25. Site AIP (American International Physic). Accessed February 13, 2024. https://history.aip.org/exhibits/lawrence/first.htm
26. Lawrence; E.O. ENE. On the Production of High Speed Protons. *Science (80-)*. Published online 1930. https://www.science.org/doi/10.1126/science.72.1867.372
27. Component of cyclotron. Accessed June 24, 2024. https://www1.grc.nasa.gov/historic-facilities/cyclotron/cyclotron-operation/
28. Site of cyclotron of Madison, University of Wisconsin. Accessed March 11, 2024. https://cyclotron.wisc.edu/
29. Site of National Isotope Development Center. Accessed March 11, 2024. https://www.isotopes.gov/production-network,
30. Greenwood NN, Earnshaw A, eds. 24 - Manganese, Technetium and Rhenium. In: *Chemistry of the Elements (Second Edition)*. Second Edi. Butterworth-Heinemann; 1997:1040-1069. doi:https://doi.org/10.1016/B978-0-7506-3365-9.50030-4
31. Andreini C, Bertini I, Cavallaro G, Holliday GL, Thornton JM. Metal ions in biological catalysis: From enzyme databases to general principles. *J Biol Inorg Chem*. 2008;13(8):1205-1218. doi:10.1007/s00775-008-0404-5
32. Carver PL, ed. Essential Metals in Medicine: Therapeutic Use and Toxicity of Metal Ions in the Clinic. De Gruyter; 2019. doi:doi:10.1515/9783110527872
33. Erikson KM, Aschner M. 10. Manganese: its role in disease and health In: Carver PL, ed. Essential Metals in Medicine: Therapeutic Use and Toxicity of Metal Ions in the Clinic. De Gruyter; 2019:253-266. doi:doi:10.1515/9783110527872-010
34. Zidenberg-Cherr S, Keen CL, Lönnerdal B, Hurley LS. Superoxide dismutase activity and lipid peroxidation in the rat: developmental correlations affected by manganese deficiency. *J Nutr*. 1983;113(12):2498-2504. doi:10.1093/jn/113.12.2498
35. No Title. Accessed February 5, 2024. https://www.inlissa.com/blogs/actifs/manganese
36. Liu Y, Mostafaei F, Sowers D, Hsieh M, Zheng W, Nie LH. Customized compact neutron activation analysis system to quantify manganese (Mn) in bone in vivo. *Physiol Meas*. 2017;38(3):452-465. doi:10.1088/1361-6579/aa577b
37. Raymond J, Blankenship RE. The origin of the oxygen-evolving complex. *Coord Chem Rev*. 2008;252(3-4):377-383. doi:10.1016/j.ccr.2007.08.026
38. Calne DB, Chu NS, Huang CC, Lu CS, Olanow W. Manganism and idiopathic parkinsonism. *Neurology*. 1994;44(9):1583. doi:10.1212/WNL.44.9.1583
39. Sánchez-Crespo A, Andreo P, Larsson SA. Positron flight in human tissues and its influence on PET image spatial resolution. *Eur J Nucl Med Mol Imaging*. 2004;31(1):44-51. doi:10.1007/s00259-003-1330-y
40. Graves S. Production and Applications of Long-Lived Positron-Emitting Radionuclides. University of Wisconsin (Madison); 2017.

41. Le Loirec C, Champion C. Track structure simulation for positron emitters of physical interest. Part II: The case of the radiometals. *Nucl Instruments Methods Phys Res Sect A Accel Spectrometers, Detect Assoc Equip*. 2007;582(2):654-664. doi:10.1016/j.nima.2007.08.179
42. Site NNDC. Accessed March 11, 2024. https://www.nndc.bnl.gov/nudat3/DecayRadiationServlet?nuc=52Mn&unc=NDS
43. De Nardo L, Ferro-Flores G, Bolzati C, Esposito J, Meléndez-Alafort L. Radiation effective dose assessment of [^{51}Mn]- and [^{52}Mn]-chloride. *Appl Radiat Isot*. 2019;153(April):108805. doi:10.1016/j.apradiso.2019.108805
44. Smith DS, Stabin MG. Exposure rate constants and lead shielding values for over 1100 radionuclides. *Health Phys*. 2012;102(3). https://journals.lww.com/health-physics/fulltext/2012/03000/exposure_rate_constants_and_lead_shielding_values.4.aspx
45. https://www.radiochemistry.org/periodictable/la_series/I1.html. 19/03/24.
46. T. Moeller. 2-Atomic Structure and its Consequences: The Dawn of Understanding,. In: The Chemistry of Lanthanides. Chapman an.; 1965.
47. Peters JA, Djanashvili K, Geraldes CFGC, Platas-Iglesias C. The chemical consequences of the gradual decrease of the ionic radius along the Ln-series. *Coord Chem Rev*. 2020;406:213146. doi:https://doi.org/10.1016/j.ccr.2019.213146
48. Jones CJ. D- and f- Block Chemistry. The Royal Society of Chemistry; 2001. doi:10.1039/9781847550682
49. Pearson RG. Hard and Soft Acids and Bases. *J Am Chem Soc*. 1963;85(22):3533-3539. doi:10.1021/ja00905a001
50. Charalampides G, Vatalis KI, Apostoplos B, Ploutarch-Nikolas B. Rare Earth Elements: Industrial Applications and Economic Dependency of Europe. *Procedia Econ Financ*. 2015;24:126-135. doi:https://doi.org/10.1016/S2212-5671(15)00630-9
51. Ren F, Liu H, Zhang H, et al. Engineering NIR-IIb fluorescence of Er-based lanthanide nanoparticles for through-skull targeted imaging and imaging-guided surgery of orthotopic glioma. *Nano Today*. 2020;34:100905. doi:https://doi.org/10.1016/j.nantod.2020.100905
52. Boyer M, Yang X, Fernández Carrión AJ, et al. First transparent oxide ion conducting ceramics synthesized by full crystallization from glass. *J Mater Chem A*. 2018;6(13):5276-5289. doi:10.1039/c7ta07621e
53. http ://nucleardata.nuclear.lu.se/toi/listnuc.asp?sql=&Z=64. 19/03/24.
54. Ghosh R, Badwar S, Lawriniang B, et al. Measurement of photo-neutron cross-sections of Gd and Ce using bremsstrahlung with an end-point energy of 10 MeV. *J Radioanal Nucl Chem*. 2017;314(3):1983-1990. doi:10.1007/s10967-017-5535-0
55. Soares DCF, de Barros Correia Menezes MÂ, Santos RG dos, Ramaldes GA. 159Gd: preparation and preliminary evaluation as a potential antitumoral radionuclide. *J Radioanal Nucl Chem*. 2010;284(2):315-320. doi:10.1007/s10967-010-0486-8
56. Simindokht SA, Somayeh G, Ali BS, Mojtaba SZ. Production, quality control, and bio-distribution studies of 159Gd-EDMP as a palliative agent for bone pain. *Electron physician*. 2015;7:977-984. https://api.semanticscholar.org/CorpusID:203778892
57. Buchholz M, Spahn I, Coenen HH. Cross section measurements of proton and deuteron induced reactions on natural europium and yields of SPECT-relevant radioisotopes of gadolinium. *Appl Radiat Isot*. 2014;91:8-16. doi:10.1016/j.apradiso.2014.04.022
58. Hermanne A, Tárkányi F, Takács S, et al. Excitation functions for production of medically relevant radioisotopes in deuteron irradiations of Pr and Tm targets. *Nucl Instruments Methods Phys Res Sect B Beam Interact with Mater Atoms*. 2009;267(5):727-736. doi:https://doi.org/10.1016/j.nimb.2008.12.017
59. https://en.wikipedia.org/wiki/Ytterby. 19/03/24.
60. Vereb M, Liepe K, Fischer M, Kaliska L, Noskovicova L, Balogova S. Radiosynoviorthesis of acromioclavicular joint using 169Er-citrate: prospective evaluation of efficacy. *Nucl Med Rev Cent East Eur*. 2018;21(1):26-31. doi:10.5603/NMR.a2018.0004

61. Vishnuvardhana Rao Dandamudi, Dover N. Radioactive erbium-165 complexes and methods of preparation and use thereof. Published online 1976:U.S. patent 580.210.
62. Kassis AI. Cancer therapy with Auger electrons: Are we almost there? *J Nucl Med*. 2003;44(9):1479-1481.
63. Gracheva N, Carzaniga TS, Schibli R, Braccini S, van der Meulen NP. 165Er: A new candidate for Auger electron therapy and its possible cyclotron production from natural holmium targets. *Appl Radiat Isot*. 2020;159:109079. doi:10.1016/j.apradiso.2020.109079
64. Zaman MR, Qaim SM. No Title. *Radiochim Acta*. 1996;75(2):59-64. doi:doi:10.1524/ract.1996.75.2.59
65. Avrigeanu M, Avrigeanu V, Bém P, et al. Low energy deuteron-induced reactions on Fe isotopes. *Phys Rev C*. 2014;89(4):44613. doi:10.1103/PhysRevC.89.044613
66. Valdovinos HF, Hernandez R, Graves S, et al. Cyclotron production and radiochemical separation of 55Co and 58mCo from 54Fe, 58Ni and 57Fe targets. *Appl Radiat Isot*. 2017;130:90-101. doi:https://doi.org/10.1016/j.apradiso.2017.09.005
67. Bianchi F, Marchi C, Fuad G, et al. On the production of 52gMn by deuteron irradiation on natural chromium and its radionuclidic purity. *Appl Radiat Isot*. 2020;166(July). doi:10.1016/j.apradiso.2020.109329
68. Topping GJ. Manganese Imaging with Positron Emission Tomography, Autoradiography, and Magnetic Resonance. 2014;(February):1-281. https://www.google.com/url?sa=t&rct=j&q=&esrc=s&source=web&cd=3&ved=0CDMQFjAC&url=https://circle.ubc.ca/bitstream/handle/2429/46045/ubc_2014_spring_topping_geoffrey.pdf?sequence=2&ei=2GcPVJjgO4mfyASCzoLoCw&usg=AFQjCNEfE3DY6Bz0mrtr9LlFL7fuqiIcSQ&sig2=vqSwM
69. Graves SA, Hernandez R, Fonslet J, et al. Novel Preparation Methods of 52Mn for ImmunoPET Imaging. *Bioconjug Chem*. 2015;26(10):2118-2124. doi:10.1021/acs.bioconjchem.5b00414
70. Fonslet J, Tietze S, Jensen AI, Graves SA, Severin GW. Optimized procedures for manganese-52: Production, separation and radiolabeling. *Appl Radiat Isot*. 2017;121(August 2016):38-43. doi:10.1016/j.apradiso.2016.11.021
71. Wooten AL, Lewis BC, Lapi SE. Cross-sections for (p,x) reactions on natural chromium for the production of 52,52m,54 Mn radioisotopes. *Appl Radiat Isot*. 2015;96:154-161. doi:10.1016/j.apradiso.2014.12.001
72. Pyles JM, Omweri JM, Lapi SE. Natural and enriched Cr target development for production of Manganese-52. *Sci Reports* |. 123AD;13:1167. doi:10.1038/s41598-022-27257-w
73. Shields WR, Murphy TJ, Catanzaro EJ, Garner EL. Absolute isotopic abundance ratios and the atomic weight of a reference sample of chromium. *J Res Natl Bur Stand Sect A Phys Chem*. 1966;70A(2):193. doi:10.6028/jres.070a.016
74. Brandes EA, Greenaway HT, Stone HEN. Ductility in Chromium. *Nature*. 1956;178(4533):587. doi:10.1038/178587a0
75. Brezovcsik K, Veres S, Molnár J, Fenyvesi A, Szűcs Z. Comparison of manganese uptake and transport of maize seedlings by mini-PET camera. *Appl Radiat Isot*. 2020;160(February). doi:10.1016/j.apradiso.2020.109127
76. Sciacca G, Martini P, Cisternino S, et al. A Universal Cassette-Based System for the Dissolution of Solid Targets. *Molecules*. 2021;26(20). doi:10.3390/molecules26206255
77. Westergaard HM. Stresses in concrete pavements computed by theoretical analysis. *Public roads*. Published online 1926. https://api.semanticscholar.org/CorpusID:107831384
78. Zaoui A., François D. PA. Comportement mécanique des matériaux. In: *Edition Hermes, Chap. 4.* ; 1995:402-437.
79. Zydorczak B, May PM, Meyrick DP, Bátka D, Hefter G. Dissolution of Cr2O3(s) and the Behavior of Chromium in Concentrated NaOH Solutions. *Ind Eng Chem Res*. 2012;51(51):16537-16543. doi:10.1021/ie302096e
80. Seo M, Furuichi R, Okamoto G, Sato N. Dissolution of Hydrous Chromium Oxide in Acid Solutions. *Trans Japan Inst Met*. 1975;16(8):519-525. doi:10.2320/matertrans1960.16.519

81. Site of National Physical Laboratory. Accessed June 22, 2018. http://resource.npl.co.uk/mtdata/phdiagrams/ccr.htm
82. Lahiri S, Nayak D, Korschinek G. Separation of no-carrier-added 52Mn from bulk chromium: A simulation study for accelerator mass spectrometry measurement of 53Mn. *Anal Chem*. 2006;78(21):7517-7521. doi:10.1021/ac0607459
83. Hevesy G. The Absorption and Translocation of Lead by Plants: A Contribution to the Application of the Method of Radioactive Indicators in the Investigation of the Change of Substance in Plants. *Biochem J*. 1923;17(4-5):439-445. doi:10.1042/bj0170439
84. Site of Nobel Prize. Accessed February 14, 2024. https://www.nobelprize.org/prizes/chemistry/1943/hevesy/facts/
85. Site of University of Missouri. Accessed February 14, 2024. https://archaeometry.missouri.edu/naa_technical.html
86. I. Da Silva, L. Frealle, P. Rifard WH. Automatisme & Contrôle Commande Radiochimie, a software for an automated radiometals separation, Erice (Italy) 2019.
87. Lacerda S, Zhang W, T. M. de Rosales R, et al. On the Versatility of Nanozeolite Linde Type L for Biomedical Applications: Zirconium-89 Radiolabeling and In Vivo Positron Emission Tomography Study. *ACS Appl Mater Interfaces*. 2022;14(29):32788-32798. doi:10.1021/acsami.2c03841
88. Ndiaye D, Sy M, Pallier A, et al. Unprecedented Kinetic Inertness for a Mn(2+) -Bispidine Chelate: A Novel Structural Entry for Mn(2+) -Based Imaging Agents. *Angew Chem Int Ed Engl*. 2020;59(29):11958-11963. doi:10.1002/anie.202003685
89. Bohnert T, Prakash C. ADME Profiling in Drug Discovery and Development: An Overview. In: *Encyclopedia of Drug Metabolism and Interactions*. John Wiley & Sons, Ltd; 2012:1-42. doi:https://doi.org/10.1002/9780470921920.edm021
90. Chandrasekaran B, Abed SN, Al-Attraqchi O, Kuche K, Tekade RK. Chapter 21 - Computer-Aided Prediction of Pharmacokinetic (ADMET) Properties. In: Tekade RK, ed. *Dosage Form Design Parameters*. Advances in Pharmaceutical Product Development and Research. Academic Press; 2018:731-755. doi:https://doi.org/10.1016/B978-0-12-814421-3.00021-X
91. Sy M, Ndiaye D, da Silva I, et al. 55/52Mn2+ Complexes with a Bispidine-Phosphonate Ligand: High Kinetic Inertness for Imaging Applications. *Inorg Chem*. 2022;61(34):13421-13432. doi:10.1021/acs.inorgchem.2c01681
92. Jin H, Varner J. Integrins: roles in cancer development and as treatment targets. *Br J Cancer*. 2004;90(3):561-565. doi:10.1038/sj.bjc.6601576
93. Man F, Gawne PJ, de Rosales RTM. Nuclear imaging of liposomal drug delivery systems: A critical review of radiolabelling methods and applications in nanomedicine. *Adv Drug Deliv Rev*. 2019;143:134-160. https://api.semanticscholar.org/CorpusID:174810395
94. Gillet R, Roux A, Brandel J, et al. A Bispidol Chelator with a Phosphonate Pendant Arm: Synthesis, Cu(II) Complexation, and (64)Cu Labeling. *Inorg Chem*. 2017;56(19):11738-11752. doi:10.1021/acs.inorgchem.7b01731
95. Ndiaye D, Sy M, Pallier A, et al. Unprecedented Kinetic Inertness for a Mn2+-Bispidine Chelate: A Novel Structural Entry for Mn2+-Based Imaging Agents. *Angew Chemie - Int Ed*. 2020;59(29):11958-11963. doi:10.1002/anie.202003685
96. Baranyai Z, Tircsó G, Rösch F. The Use of the Macrocyclic Chelator DOTA in Radiochemical Separations. *Eur J Inorg Chem*. 2020;2020(1):36-56. doi:https://doi.org/10.1002/ejic.201900706
97. Kálmán FK, Tircsó G. Kinetic inertness of the Mn2+ complexes formed with AAZTA and some open-chain EDTA derivatives. *Inorg Chem*. 2012;51(19):10065-10067. doi:10.1021/ic300832e
98. Coenen HH, Gee AD, Adam M, et al. Consensus nomenclature rules for radiopharmaceutical chemistry — Setting the record straight. *Nucl Med Biol*. 2017;55:v-xi. doi:https://doi.org/10.1016/j.nucmedbio.2017.09.004

99. Radioactivity. In: *Molecular Imaging: Radiopharmaceuticals for PET and SPECT*. Springer Berlin Heidelberg; 2009:35-43. doi:10.1007/978-3-540-76735-0_4
100. Aluicio-Sarduy E, Hernandez R, Olson AP, et al. Production and in vivo PET/CT imaging of the theranostic pair 132/135La. *Sci Rep*. 2019;9(1):1-6. doi:10.1038/s41598-019-47137-0
101. Byegård J, Skarnemark G, Skålberg M. The stability of some metal EDTA, DTPA and DOTA complexes: Application as tracers in groundwater studies. *J Radioanal Nucl Chem*. 1999;241(2):281-290. doi:10.1007/BF02347463
102. Vaudon J, Frealle L, Audiger G, et al. First Steps at the Cyclotron of Orléans in the Radiochemistry of Radiometals: 52Mn and 165Er. *Instruments*. 2018;2(3). doi:10.3390/instruments2030015
103. Kretowicz MN, Barrett KE, Barnhart TE, Engle JW. Recycling of 52Cr electroplated targets for 52gMn production. *Appl Radiat Isot*. 2023;200(January):110924. doi:10.1016/j.apradiso.2023.110924
104. Colombi A, Carante MP, Barbaro F, Canton L, Fontana A. Production of High-Purity 52gMn from natV Targets with Alpha Beams at Cyclotrons. *Nucl Technol*. 2022;208(4):735-752. doi:10.1080/00295450.2021.1947122
105. Koning AJ, Rochman D, Sublet JC, Dzysiuk N, Fleming M, van der Marck S. TENDL: Complete Nuclear Data Library for Innovative Nuclear Science and Technology. *Nucl Data Sheets*. 2019;155:1-55. doi:10.1016/j.nds.2019.01.002
106. *Nuclear Physics European Collaboration Committee*; 2014. https://www.nupecc.org/pub/npmed2014.pdf%0D
107. I Konstantinov, N Krasnov PD. Methods for producing the 52Mn isotope. *At Energiya*. 1969;26(5):467-469.https://link.springer.com/content/pdf/10.1007%2FBF01174115.pdf
108. Bowman WW, Blann M. Reactions of 51V and 27Al with 7–120 MeV α-particles (equilibrium and non-equilibrium statistical analyses). *Nucl Phys A*. 1969;131(3):513-531. doi:https://doi.org/10.1016/0375-9474(69)90592-2
109. Smend F, Weirauch W. Isomerenverhältnis für die Reaktion $^{51}V(\alpha,3n)^{52g,m}Mn$. *Zeitschrift für Phys*. 1969;219(5):467-474. doi:10.1007/BF01400823
110. Site NNDC exfor data. https://www-nds.iaea.org/exfor/servlet/X4sGetSubent?reqx=30986&subID=151214007
111. Michel R, Brinkmann G, Stück R. Measurement and Hybrid Model Analysis of Integral Excitation Functions for α-Induced Reactions on Vanadium and Manganese BT - Nuclear Data for Science and Technology. In: Böckhoff KH, ed. Springer Netherlands; 1983:599-602.
112. Rao JR, Rao AVM, Mukherjee S, et al. Non-equilibrium effects in alpha-particle-induced reactions in light, medium and heavy nuclei up to 120 MeV. *J Phys G Nucl Phys*. 1987;13(4):535-542. doi:10.1088/0305-4616/13/4/017
113. Singh NL, Agarwal S, Rao JR. Excitation function for α-particle-induced reactions in light-mass nuclei. *Can J Phys*. 1993;71(3-4):115-121. doi:10.1139/p93-017
114. Singh NL, Mukherjee S, Rao AVM, Chaturvedi L, Singh PP. Effects of pre-equilibrium nucleon emission on excitation functions of various reactions in vanadium induced by alpha particles. *J Phys G Nucl Part Phys*. 1995;21(3):399-410. doi:10.1088/0954-3899/21/3/014
115. Sonzogni AA, Romo ASMA, Mosca HO, Nassiff SJ. Alpha and deuteron induced reactions on vanadium. *J Radioanal Nucl Chem Artic*. 1993;170(1):143-156. doi:10.1007/BF02134585
116. Shu Q, Khayambashi A, Zou Q, et al. Studies on adsorption and separation characteristics of americium and lanthanides using a silica-based macroporous bi(2-ethylhexyl) phosphoric acid (HDEHP) adsorbent. *J Radioanal Nucl Chem*. 2017;313(1):29-37. doi:10.1007/s10967-017-5293-z
117. Kumar BB, Mukherjee S, Singh NL. Pre-equilibrium Model Analysis of Alpha Particle Induced Reactions up to 80MeV. *Phys Scr*. 1998;57(2):201-206. doi:10.1088/0031-8949/57/2/007

118. Ismail M. Measurement of excitation functions and mean projected recoil ranges of nuclei in α-induced reactions on F, Al, V, Co and Re nuclei. *Pramana*. 1993;40(3):227-251. doi:10.1007/BF02900190
119. Levkovskij. Act.Cs by Protons and alphas. Published 1991. https://www-nds.iaea.org/exfor/servlet/X4sGetEntry?acc=A0510&reqx=31045
120. Gantumur D, Aikawa M, Khishigjargal T. Production cross sections of natural vanadium Mn in alpha-particle-induced reactions on. *Appl Radiat Isot*. 2022;184(January):110204. doi:10.1016/j.apradiso.2022.110204
121. Barbaro F, Canton L, Carante M Pietro, et al. The innovative 52gMn for positron emission tomography (PET) imaging: Production cross section modeling and dosimetric evaluation. *Med Phys*. 2023;50(3):1843-1854. doi:10.1002/mp.16130
122. L. Frealle, A. Canizares, D. Zanghi , P. Rifard , I. Da Silva. CiSCoTe : Cible Solide Irradiée Contrôlée en Température (Solid Target irradiated under control temperature by thermocouple and pyrometer. In: *MEDICIS-Promed and Related Science Topics,* 2019 (Erice, Italy).
123. Weinreich R, Schult O, Stöcklin G. Production of ^{123}I via the ^{127}I(d,6n)^{123}Xe(β+,EC) ^{123}I process. *Int J Appl Radiat Isot*. 1974;25(11-12):535-543. doi:10.1016/0020-708X(74)90080-5
124. Blessing G, Bräutigam W, Böge HG, Gad N, Scholten B, Qaim SM. Internal irradiation system for excitation function measurement via the stacked-foil technique. *Appl Radiat Isot*. 1995;46(9):955-960. doi:10.1016/0969-8043(95)00179-H
125. Hermanne A, Ignatyuk A V., Capote R, et al. Reference Cross Sections for Charged-particle Monitor Reactions. *Nucl Data Sheets*. 2018;148:338-382. doi:10.1016/j.nds.2018.02.009
126. Tárkányi FT, Ignatyuk A V, Hermanne A, et al. Recommended nuclear data for medical radioisotope production: diagnostic gamma emitters. *J Radioanal Nucl Chem*. 2019;319(2):487-531. doi:10.1007/s10967-018-6142-4
127. Ziegler JF, Ziegler MD, Biersack JP. SRIM – The stopping and range of ions in matter (2010). *Nucl Instruments Methods Phys Res Sect B Beam Interact with Mater Atoms*. 2010;268(11):1818-1823. doi:https://doi.org/10.1016/j.nimb.2010.02.091
128. El Sayed R, Massicano AVF, Queern SL, Loveless CS, Lapi SE. Manganese-52 production cross-section measurements via irradiation of natural chromium targets up to 20 MeV. *Appl Radiat Isot*. 2019;147:165-170. doi:10.1016/j.apradiso.2019.02.017
129. Avila-Rodriguez MA, Rajander J, Lill JO, et al. Proton energy determination using activated yttrium foils and ionization chambers for activity assay. *Nucl Instruments Methods Phys Res Sect B Beam Interact with Mater Atoms*. 2009;267(10):1867-1872. doi:10.1016/j.nimb.2009.02.064
130. Gagnon K, Jensen M, Thisgaard H, et al. A new and simple calibration-independent method for measuring the beam energy of a cyclotron. *Appl Radiat Isot*. 2011;69(1):247-253. doi:10.1016/j.apradiso.2010.09.012
131. Da Silva I, Johnson TR, Mixdorf JC, et al. A high separation factor for ^{165}Er from Ho for targeted radionuclide therapy. *Molecules*. 2021;26(24):1-15. doi:10.3390/molecules26247513
132. Nielsen KM, Korpe E, Parker D, Blower P. Comparison of cyclotron produced manganese-52 from natural chromium and vanadium targets. *Nucl Med Biol*. 2022;108-109(2022):S171-S172. doi:10.1016/s0969-8051(22)00360-2
133. Ellison PA, Valdovinos HF, Graves SA, Barnhart TE, Nickles RJ. Spot-welding solid targets for high current cyclotron irradiation. *Appl Radiat Isot*. 2016;118:350-353. doi:10.1016/j.apradiso.2016.10.010
134. Sastri CS, Petri H, Kueppers G, Erdtmann G. Production of manganese-52 of high isotopic purity by 3He-activation of vanadium. *Int J Appl Radiat Isot*. 1981;32(4):246-247. doi:10.1016/0020-708X(81)90060-0
135. Saar G, Millo CM, Szajek LP, Bacon J, Herscovitch P, Koretsky AP. Anatomy, Functionality, and Neuronal Connectivity with Manganese Radiotracers for Positron Emission Tomography. *Mol IMAGING Biol*. 2018;20(4):562-574. doi:10.1007/s11307-018-1162-6

136. Korkisch J. Rare Earth Elements in Handbook of ion Exchange Resins: their application to inorganic analytical chemistry, CRC Press, 1, 1989, p.127, ISBN 0-8493-3191-9. Published online 1989:127.
137. Bio-Rad Laboratories I. AG® 50W-X8 Cation Exchange Resin Instruction Manual. Accessed May 6, 2024. https://www.bio-rad.com/webroot/web/pdf/lsr/literature/LIT203.pdf
138. J Johnson EL. *Handbook of Ion Chromatography*; 1986.
139. Davies CM. Determination of Distribution Coefficients for Cation Exchange Resin and Optimisation of Ion Exchange Chromatography for Chromium Separation for Geological Materials. Manchester (United Kingdom); 2012.
140. Svehla G, Tölg G. Talanta mini-review: the determination of vanadium. *Talanta*. 1976;23(11):755-768. doi:https://doi.org/10.1016/0039-9140(76)80085-9
141. Strelow FWE, Rethemeyer R, Bothma CJC. Ion Exchange Selectivity Scales for Cations in Nitric Acid and Sulfuric Acid Media with a Sulfonated Polystyrene Resin. *Anal Chem*. 1965;37:106-111. https://api.semanticscholar.org/CorpusID:93933914
142. Barrett KE, Aluicio-Sarduy E, Happel S, et al. Characterization of actinide resin for separation of 51,52gMn from bulk target material. *Nucl Med Biol*. 2021;96-97:19-26. doi:10.1016/j.nucmedbio.2021.02.005
143. McCarthy DW, Shefer RE, Klinkowstien RE, et al. Efficient production of high specific activity 64Cu using a biomedical cyclotron. *Nucl Med Biol*. 1997;24(1):35-43. doi:10.1016/S0969-8051(96)00157-6
144. Kraus KA, Moore GE. Anion Exchange Studies. VI.1,2 The Divalent Transition Elements Manganese to Zinc in Hydrochloric Acid. *J Am Chem Soc*. 1953;75(6):1460-1462. doi:10.1021/ja01102a054
145. Tárkányi F, Takács S, Hermanne A, et al. Investigation of production of the therapeutic radioisotope 165Er by proton induced reactions on erbium in comparison with other production routes. *Appl Radiat Isot*. 2009;67(2):243-247. doi:https://doi.org/10.1016/j.apradiso.2008.10.006
146. Zandi N, Sadeghi M, Afarideh H. Evaluation of the cyclotron production of 165Er by different reactions. *J Radioanal Nucl Chem*. 2013;295(2):923-928. doi:10.1007/s10967-012-2116-0
147. Gracheva N. Development of Terbium and Erbium Radiolanthanides for Radiopharmaceutical Application. Doctoral Thesis ETH Zurich; 2020. https://doi.org/10.3929/ethz-b-000398344
148. Tárkányi F, Hermanne A, Király B, et al. Study of activation cross-sections of deuteron induced reactions on erbium: Production of radioisotopes for practical applications. *Nucl Instruments Methods Phys Res Sect B Beam Interact with Mater Atoms*. 2007;259(2):829-835. doi:https://doi.org/10.1016/j.nimb.2007.01.287
149. Tárkányi F, Hermanne A, Király B, Takács S, Ignatyuk A V. Study of excitation functions of alpha-particle induced nuclear reactions on holmium for ^{167}Tm production. *Appl Radiat Isot*. 2010;68(3):404-411. doi:https://doi.org/10.1016/j.apradiso.2009.11.043
150. Usman AR, Khandaker MU, Haba H, Otuka N, Murakami M. Production cross sections of thulium radioisotopes for alpha-particle induced reactions on holmium. *Nucl Instruments Methods Phys Res Sect B Beam Interact with Mater Atoms*. 2020;469:42-48. doi:https://doi.org/10.1016/j.nimb.2020.02.036
151. Tárkányi F, Hermanne A, Takács S, et al. Experimental study of the ^{165}Ho(d,2n) and ^{165}Ho(d,p) nuclear reactions up to 20MeV for production of the therapeutic radioisotopes ^{165}Er and ^{166g}Ho. *Nucl Instruments Methods Phys Res Sect B Beam Interact with Mater Atoms*. 2008;266(16):3529-3534. doi:https://doi.org/10.1016/j.nimb.2008.05.123
152. Hermanne A, Adam-Rebeles R, Tarkanyi F, et al. Deuteron induced reactions on Ho and La: Experimental excitation functions and comparison with code results. *Nucl Instruments Methods Phys Res Sect B Beam Interact with Mater Atoms*. 2013;311:102-111. doi:https://doi.org/10.1016/j.nimb.2013.06.014

153. Beyer GJ, Zeisler SK, Becker DW. The Auger-electron emitter ^{165}Er: excitation function of the ^{165}Ho(p,n)^{165}Er process. *Radiochim Acta*. 2004;92(4-6):219-222. doi:doi:10.1524/ract.92.4.219.35608
154. Tárkányi F, Hermanne A, Takács S, et al. Experimental study of the ^{165}Ho(p,n) nuclear reaction for production of the therapeutic radioisotope ^{165}Er. *Nucl Instruments Methods Phys Res Sect B Beam Interact with Mater Atoms*. 2008;266(15):3346-3352. doi:10.1016/j.nimb.2008.05.005
155. Schmor P. Review of Cyclotrons for the Production of Radioactive Isotopes for Medical and Industrial Applications. *Rev Accel Sci Technol*. 2011;04(01):103-116. doi:10.1142/S1793626811000574
156. Choppin GR, Silva RJ. Separation of the lanthanides by ion exchange with alpha-hydroxy isobutyric acid. *J Inorg Nucl Chem*. 1956;3(2):153-154. doi:https://doi.org/10.1016/0022-1902(56)80076-6
157. Smith HL, Hoffman DC. Ion-exchange separations of the lanthanides and actinides by elution with ammonium alpha-hydroxy-isobutyrate. *J Inorg Nucl Chem*. 1956;3(3):243-247. doi:https://doi.org/10.1016/0022-1902(56)80025-0
158. Malikidogo KP, Da Silva I, Morfin JF, et al. A cocktail of ^{165}Er(iii) and Gd(iii) complexes for quantitative detection of zinc using SPECT and MRI. *Chem Commun*. 2018;54(55):7597-7600. doi:10.1039/C8CC03407A
159. Lehenberger S, Barkhausen C, Cohrs S, et al. The low-energy β− and electron emitter ^{161}Tb as an alternative to ^{177}Lu for targeted radionuclide therapy. *Nucl Med Biol*. 2011;38(6):917-924. doi:https://doi.org/10.1016/j.nucmedbio.2011.02.007
160. Gracheva N, Müller C, Talip Z, et al. Production and characterization of no-carrier-added ^{161}Tb as an alternative to the clinically-applied ^{177}Lu for radionuclide therapy. *EJNMMI Radiopharm Chem*. 2019;4(1):12. doi:10.1186/s41181-019-0063-6
161. Mocko V, Taylor WA, Nortier FM, et al. Isolation of ^{163}Ho from dysprosium target material by HPLC for neutrino mass measurements. *Radiochim Acta*. 2015;103(8):577-585. doi:doi:10.1515/ract-2014-2362
162. Schwantes JM, Taylor WA, Rundberg RS, Vieira DJ. Preparation of a one-curie ^{171}Tm target for the detector for advanced neutron capture experiments (DANCE). *J Radioanal Nucl Chem*. 2008;276(2):533-542. doi:10.1007/s10967-008-0538-5
163. Gharibyan N, Bene BJ, Sudowe R. Chromatographic separation of thulium from erbium for neutron capture cross section measurements—Part I: Trace scale optimization of ion chromatography method with various complexing agents. *J Radioanal Nucl Chem*. 2017;311(1):179-187. doi:10.1007/s10967-016-4926-y
164. Winchester JW. Rare earth chromatography using bis-(2-ethylhexyl) orthophosphoric acid. *J Chromatogr A*. 1963;10:502-506. doi:https://doi.org/10.1016/S0021-9673(01)92343-X
165. Pin C, Rodriguez J. 15.8 - Separation Methods Based on Liquid–Liquid Extraction, Extraction Chromatography, and Other Miscellaneous Solid Phase Extraction Processes. In: Holland HD, Turekian KK, eds. *Treatise on Geochemistry (Second Edition)*. Edi. Elsevier; 2014:147-170. doi:https://doi.org/10.1016/B978-0-08-095975-7.01409-1
166. Siekierski S, Sochacka RJ. Reversed-phase partition chromatography with di-(2-ethylhexyl) orthophosphoric acid as the stationary phase. Part II. Factors affecting the height of the plate. *J Chromatogr A*. 1964;16(C):385-395. doi:10.1016/s0021-9673(01)82502-4
167. Horwitz EP, Bloomquist CAA. Chemical separations for super-heavy element searches in irradiated uranium targets. *J Inorg Nucl Chem*. 1975;37(2):425-434. doi:https://doi.org/10.1016/0022-1902(75)80350-2
168. McAlister DR, Horwitz EP. Characterization of Extraction of Chromatographic Materials Containing Bis(2-ethyl-1-hexyl)Phosphoric Acid, 2-Ethyl-1-Hexyl (2-Ethyl-1-Hexyl) Phosphonic Acid, and Bis(2,4,4-Trimethyl-1-Pentyl)Phosphinic Acid. *Solvent Extr Ion Exch*. 2007;25(6):757-769. doi:10.1080/07366290701634594
169. Aziz A, Artha WT. Radiochemical Separation of ^{161}Tb from Gd/Tb Matrix Using Ln Resin Column. *Indones J Chem*. 2018;16(3):283-288. doi:0.22146/ijc.21143

170. Jiang J, Davies A V, Britton RE. Measurement of ^{160}Tb and ^{161}Tb in nuclear forensics samples. *J Radioanal Nucl Chem*. 2017;314(2):727-736. doi:10.1007/s10967-017-5468-7
171. Horwitz EP, McAlister DR, Bond AH, Barrans RE, Williamson JM. A process for the separation of ^{177}Lu from neutron irradiated ^{176}Yb targets. *Appl Radiat Isot*. 2005;63(1):23-36. doi:https://doi.org/10.1016/j.apradiso.2005.02.005
172. Tapio S. Studies towards Purification of Auger Electron Emitter 165Er - a Possible Radiolanthanide for Cancer Treatment. Masters Thesis, University of Helsinki; 2018.
173. Gracheva N, Carzaniga TS, Schibli R, Braccini S, van der Meulen NP. ^{165}Er: A new candidate for Auger electron therapy and its possible cyclotron production from natural holmium targets. *Appl Radiat Isot*. 2020;159:109079. doi:10.1016/j.apradiso.2020.109079
174. Kazakov AG, Aliev RA, Bodrov AY, Priselkova AB, Kalmykov SN. Separation of radioisotopes of terbium from a europium target irradiated by 27 MeV α-particles. *Radiochim ACTA*. 2018;106(2):135-140. doi:10.1515/ract-2017-2777
175. Hidaka H, Yoneda S. Sm and Gd isotopic shifts of Apollo 16 and 17 drill stem samples and their implications for regolith history. *Geochim Cosmochim Acta*. 2007;71(4):1074-1086. doi:10.1016/j.gca.2006.10.015
176. Xie F, Zhang TA, Dreisinger D, Doyle F. A critical review on solvent extraction of rare earths from aqueous solutions. *Miner Eng*. 2014;56:10-28. doi:10.1016/j.mineng.2013.10.021
177. Product sheets of serie LN from Triskem. ttps://www.triskem-international.com/scripts/files/60afaead91e3a2.51353659/PS_LN2-Resin_EN_200603.pdf
178. Reddy M., Prasada Rao T., Damodoran A., Liquid-Liquid Extraction Processes for the Separation and Purification of Rare Earths. *Miner Process Extr Metall Rev*. 1993;12(2-4):91-113. doi:10.1080/08827509508935254
179. Nicholas VDM. Ion Exchange Behaviour of 42 Selected Elements on AG MP-50 Cation Exchange Resin in Nitric Acid and Citric Acid Mixtures. 2003.
180. Horwitz EP, McAlister DR, Dietz ML. Extraction chromatography versus solvent extraction: How similar are they? *Sep Sci Technol*. 2006;41(10):2163-2182. doi:10.1080/01496390600742849
181. Ettre LS. Nomenclature for chromatography (IUPAC Recommendations 1993). *Pure Appl Chem*. 1993;65(4):819-872.doi:10.1351/pac199365040819
182. De Leon-Rodriguez L, Lubag AJM, Dean Sherry A. Imaging free zinc levels in vivo – What can be learned? *Inorganica Chim Acta*. 2012;393:12-23. doi:https://doi.org/10.1016/j.ica.2012.06.026
183. Kelleher SL, McCormick NH, Velasquez V, Lopez V. Zinc in Specialized Secretory Tissues: Roles in the Pancreas, Prostate, and Mammary Gland. *Adv Nutr*. 2011;2(2):101-111. doi:https://doi.org/10.3945/an.110.000232
184. Wijesekara N, Chimienti F, Wheeler MB. Zinc, a regulator of islet function and glucose homeostasis. *Diabetes, Obes Metab*. 2009;11(s4):202-214. doi:https://doi.org/10.1111/j.1463-1326.2009.01110.x
185. Faller P, Hureau C. Bioinorganic chemistry of copper and zinc ions coordinated to amyloid-β peptide. *Dalt Trans*. 2009;(7):1080-1094. doi:10.1039/B813398K
186. Frullano L, Catana C, Benner T, Sherry AD, Caravan P. Bimodal MR–PET Agent for Quantitative pH Imaging. *Angew Chemie Int Ed*. 2010;49(13):2382-2384. doi:https://doi.org/10.1002/anie.201000075
187. Gianolio E, Maciocco L, Imperio D, et al. Dual MRI-SPECT agent for pH-mapping. *Chem Commun*. 2011;47(5):1539-1541. doi:10.1039/C0CC03554H
188. Kyangwi Malikidogo Patrick. Agents de Contraste Pour La Détection Quantitative Du Zn(II) Par IRM. 2017.
189. Corsi DM, Platas-Iglesias C, Bekkum H van, Peters JA. Determination of paramagnetic

lanthanide(III) concentrations from bulk magnetic susceptibility shifts in NMR spectra. *Magn Reson Chem*. 2001;39(11):723-726. doi:https://doi.org/10.1002/mrc.922
190. Strosberg J, El-Haddad G, Wolin E, et al. Phase 3 Trial of ^{177}Lu-Dotatate for Midgut Neuroendocrine Tumors. *N Engl J Med*. 2017;376(2):125-135. doi:10.1056/NEJMoa1607427
191. Hofman MS, Emmett L, Sandhu S, et al. [^{177}Lu]Lu-PSMA-617 versus cabazitaxel in patients with metastatic castration-resistant prostate cancer (TheraP): a randomised, open-label, phase 2 trial. *Lancet*. 2021;397(10276):797-804. doi:https://doi.org/10.1016/S0140-6736(21)00237-3
192. Cornelissen B, Vallis KA. Targeting the nucleus: an overview of Auger-electron radionuclide therapy. *Curr Drug Discov Technol*. 2010;7(4):263-279. doi:10.2174/157016310793360657
193. Ku A, Facca VJ, Cai Z, Reilly RM. Auger electrons for cancer therapy – a review. *EJNMMI Radiopharm Chem*. 2019;4(1):27. doi:10.1186/s41181-019-0075-2
194. Pirovano G, Wilson TC, Reiner T. Auger: The future of precision medicine. *Nucl Med Biol*. 2021;96-97:50-53. doi:https://doi.org/10.1016/j.nucmedbio.2021.03.002
195. Kassis AI. Molecular and cellular radiobiological effects of Auger emitting radionuclides. *Radiat Prot Dosimetry*. 2011;143(2-4):241-247. doi:10.1093/rpd/ncq385
196. Grünberg J, Lindenblatt D, Dorrer H, et al. Anti-L1CAM radioimmunotherapy is more effective with the radiolanthanide terbium-161 compared to lutetium-177 in an ovarian cancer model. *Eur J Nucl Med Mol Imaging*. 2014;41(10):1907-1915. doi:10.1007/s00259-014-2798-3
197. Müller C, Reber J, Haller S, et al. Direct in vitro and in vivo comparison of ^{161}Tb and ^{177}Lu using a tumour-targeting folate conjugate. *Eur J Nucl Med Mol Imaging*. 2014;41(3):476-485. doi:10.1007/s00259-013-2563-z
198. Müller C, Umbricht CA, Gracheva N, et al. Terbium-161 for PSMA-targeted radionuclide therapy of prostate cancer. *Eur J Nucl Med Mol Imaging*. 2019;46(9):1919-1930. doi:10.1007/s00259-019-04345-0
199. Eckerman KF, Endo A. Nuclear decay data for dosimetric calculations. A report of ICRP Committee 2. *Ann ICRP*. 2008;38(3):7-96. doi:10.1016/j.icrp.2008.10.004
200. Van de Voorde M, Van Hecke K, Cardinaels T, Binnemans K. Radiochemical processing of nuclear-reactor-produced radiolanthanides for medical applications. *Coord Chem Rev*. 2019;382:103-125. doi:https://doi.org/10.1016/j.ccr.2018.11.007
201. Rahbar K, Bode A, Weckesser M, et al. Radioligand Therapy With ^{177}Lu-PSMA-617 as A Novel Therapeutic Option in Patients With Metastatic Castration Resistant Prostate Cancer. *Clin Nucl Med*. 2016;41(7):522-528. doi:10.1097/RLU.0000000000001240
202. Hennrich U, Kopka K. Lutathera®: The First FDA- and EMA-Approved Radiopharmaceutical for Peptide Receptor Radionuclide Therapy. *Pharmaceuticals*. 2019;12(3). doi:10.3390/ph12030114
203. Sietmann R. False Attribution. *Phys Bull*. 1988;39(8):316-317. doi:10.1088/0031-9112/39/8/017
204. Matsakis D, Coster A, Laster B, Sime R. A renaming proposal: "The Auger–Meitner effect." *Phys Today*. 2019;72(9):10-11. doi:10.1063/PT.3.4281
205. Lisa Meitner. https://en.wikipedia.org/wiki/Lise_Meitner
206. Mahnke HE. Lise Meitner, β-decay and non-radiative electromagnetic transitions. *Notes Rec R Soc J Hist Sci*. 2022;76(1):107-116. doi:10.1098/rsnr.2020.0036
207. Ellison PA, Olson AP, Barnhart TE, et al. Improved production of ^{76}Br, ^{77}Br and ^{80m}Br via CoSe cyclotron targets and vertical dry distillation. *Nucl Med Biol*. 2020;80-81:32-36. doi:https://doi.org/10.1016/j.nucmedbio.2019.09.001
208. Tárkányi F, Hermanne A, Takács S, et al. Experimental study of the ^{165}Ho(p,n) nuclear reaction for production of the therapeutic radioisotope ^{165}Er. *Nucl Instruments Methods Phys Res Sect B Beam Interact with Mater Atoms*. 2008;266(15):3346-3352. doi:10.1016/j.nimb.2008.05.005
209. Da Silva I. Developments of exotic Radionuclides at Orléans Cyclotron : ^{89}Zr, ^{165}Er and 52Mn. In: *17th Workshop on Targetry and Target Chemistry*-. 2018, Coimbra, Portugal

210. Chen XY, Goff GS, Ewing WC, Scott BL, Runde W. Solid-state and solution-state coordination chemistry of lanthanide(III) complexes with α-hydroxyisobutyric acid. *Inorg Chem*. 2012;51(24):13254-13263. doi:10.1021/ic301775d
211. Saghez BS, Yang H, Radchenko V. High Separation Factor, High Molar Activity, and Inexpensive Purification Method for the Production of Pure ^{165}Er. *Inorg Chem*. 2024;63(12):5330-5340. doi:10.1021/acs.inorgchem.3c03166
212. Happel S. Tk211/2/3 Resins. *Triskem Infos*. 2020;20:1-4. https://www.triskem-international.com/scripts/files/5f7489e5e56bd1.99690772/tki-20-tk211-13-resin-en-online.pdf
213. Pourmand A, Dauphas N. Distribution coefficients of 60 elements on TODGA resin: Application to Ca, Lu, Hf, U and Th isotope geochemistry. *Talanta*. 2010;81(3):741-753. doi:https://doi.org/10.1016/j.talanta.2010.01.008
214. Aluicio-Sarduy E, Hernandez R, Valdovinos HF, et al. Simplified and automatable radiochemical separation strategy for the production of radiopharmaceutical quality ^{86}Y using single column extraction chromatography. *Appl Radiat Isot*. 2018;142:28-31. doi:https://doi.org/10.1016/j.apradiso.2018.09.016
215. Chaves S, Delgado R, Da Silva JJRF. The stability of the metal complexes of cyclic tetra-aza tetra-acetic acids. *Talanta*. 1992;39(3):249-254. doi:https://doi.org/10.1016/0039-9140(92)80028-C
216. Anderegg G, Arnaud-Neu F, Delgado R, Felcman J, Popov K. Critical evaluation of stability constants of metal complexes of complexones for biomedical and environmental applications (IUPAC Technical Report): . *Pure Appl Chem*. 2005;77(8):1445-1495. doi:doi:10.1351/pac200577081445
217. Aslani A, Snowdon GM, Bailey DL, et al. Lutetium-177 DOTATATE Production with an Automated Radiopharmaceutical Synthesis System. *Asia Ocean J Nucl Med Biol*. 2015;3(2):107-115.
218. Jain AK, Ghosh A, Singh B. Nuclear Data Sheets for A = 165. *Nucl Data Sheets*. 2006;107(5):1075-1346. doi:https://doi.org/10.1016/j.nds.2006.05.002
219. *Nuclear Physics European Collaboration Committee*.; 2017.
220. Krolas W., Ibarra A. AF. The IFMIF-DONES ´ fusion oriented neutron source : evolution of the design. *Nucl Fusion 61 125002*. Published online 2021. https://www.esf.org/fileadmin/user_upload/%0Aesf/Nupecc-LRP2017.pdf
221. López-Melero E, de Saavedra FA, Da Silva I, Roldán A, Praena J. Production of ^{165}Er with deuterons at IFMIF-DONES. *Nucl Mater Energy*. 2024;39(April):101659. doi:10.1016/j.nme.2024.101659
222. *European Strategy Forum on Research Infrastructures, International Fusion Materials Irradiation Facility - DEMO Oriented NEutron Source*.; 2018.
223. Technical Meeting on Auger Electron Emitters for Radiopharmaceutical Developments. https://www.iaea.org/events/evt2103627
224. Bolcaen J, Gizawy MA, Terry SYA, et al. Marshalling the Potential of Auger Electron Radiopharmaceutical Therapy. *J Nucl Med*. 2023;64(9):1344-1351. doi:10.2967/jnumed.122.265039
225. Gracheva N. Development of Terbium and Erbium Radiolanthanides for Radiopharmaceutical Application. Published online 2020.
226. Duchemin C, Cocolios TE, Dockx K, et al. Production cross-section measurements of proton-induced reactions on natural tantalum in the 0.3 GeV–1.7 GeV energy range. *Appl Radiat Isot*. 2021;178(September). doi:10.1016/j.apradiso.2021.109983
227. Blumenfeld Y, Nilsson T, Van Duppen P. Facilities and methods for radioactive ion beam production. *Phys Scr*. 2013;(T152). doi:10.1088/0031-8949/2013/T152/014023
228. Nifant'Ev IE, Minyaev ME, Tavtorkin AN, Vinogradov AA, Ivchenko P V. Branched alkylphosphinic and disubstituted phosphinic and phosphonic acids: Effective synthesis based

on α-olefin dimers and applications in lanthanide extraction and separation. *RSC Adv*. 2017;7(39):24122-24128. doi:10.1039/c7ra03770h
229. Perreault LL, Giret S, Gagnon M, Florek J, Larivière D, Kleitz F. Functionalization of Mesoporous Carbon Materials for Selective Separation of Lanthanides under Acidic Conditions. *ACS Appl Mater Interfaces*. 2017;9(13):12003-12012. doi:10.1021/acsami.6b16650
230. El Mourabit S, Guillot M, Toquer G, Cambedouzou J, Goettmann F, Grandjean A. Stability of mesoporous silica under acidic conditions. *RSC Adv*. 2012;2(29):10916-10924. doi:10.1039/C2RA21569A
231. Zhang W, Ye G, Chen J. Study on the gamma-ray irradiation behavior of mesoporous silica adsorbents functionalized with phosphine oxide and phosphonic acid ligands. *J Radioanal Nucl Chem*. 2016;307(2):1445-1451. doi:10.1007/s10967-015-4249-4
232. Marsh SF., Pillay KK. Effects of ionizing radiation on modern ion exchange materials.1993; (October)

Summary in french of all chapters

Abréviations pour résumé en français

AMA: Activité Molaire Apparente

FDG: fluorodéoxyglucose

TEP : Tomographie par Emission de Positons

CDTA : Acide Cyclohexanediamine-1,2 N,N,N',N'-Tetraacétique (Trans-)

DOTA: acide 1,4,7,10-tétraazacyclododécane-1,4,7,10-tétraacétique

TEMP: Tomographie d'Emission MonoPhotonique

IRM: Imagerie par Résonance Magnétique

PSMA-617 : Prostate-Specific Membrane Antigen

MEMRI : Manganese-Enhanced Magnetic-Resonance Imaging

CEMHTI: Conditions Extrêmes et Matériaux: Haute Température et Irradiation

Dw : coefficient de distribution

CiSCoTe: Cible Solide irradiée Contrôlée en Température

$FS_{(Ho/Er)}$: Facteur de Séparation Ho/Er

ICP-OES : spectrométrie à plasma à couplage inductif par détection optique

Introduction

Le ^{18}F est un émetteur de position le plus utilisé dans les services de médecine nucléaire pour la détection des tumeurs cancéreuses. Il s'utilise principalement sous forme de [^{18}F]F-FDG (fluorodéoxyglucose) et est détecté par tomographie à émission de positons (TEP). Avec les développements des technologies en imagerie et l'explosion des cyclotrons biomédicaux dans les années 2000, de nouveaux émetteurs de positons sont apparus : ^{64}Cu ($T_{1/2}$ = 12.7h) ou ^{89}Zr ($T_{1/2}$ = 78.41 h). Leur demi-vie plus longue que celle du ^{18}F est un argument de poids pour les études de biodistribution lentes des anticorps ou des peptides. Ils sont produits par irradiation de cibles solides dans un cyclotron rendant leur production plus complexe que celle du ^{18}F. Néanmoins, leurs radiomarquages principalement avec l'agent de complexation DOTA (acide 1,4,7,10-tétraazacyclododécane-1,4,7,10-tétraacétique) sont plus simples à mettre en oeuvre que ceux avec le ^{18}F. Actuellement, des radionucléides sont étudiés pour des applications thérapeutiques (émission alpha, bêta, électron Auger). On parle de radiothérapie interne vectorisée. Cette évolution se fait en parallèle de l'utilisation de paires théranostiques: association de 2 radionucléides l'un à vocation imagerie, l'autre pour la partie thérapie.

Dans tous les cas, l'utilisation de ces radionucléides « imageurs » fait appel aux imageries nucléaires très sensibles que sont la TEP (Tomographie par Emission de Positrons) ou la TEMP (Tomographie d'Emission MonoPhotonique). En revanche, elles sont peu résolutives et doivent être associées à des techniques d'imagerie anatomiques, comme l'IRM (Imagerie par Résonance Magnétique), permettant une très bonne résolution. Les recherches en imagerie bimodale (TEP ou TEMP/IRM) s'accélèrent ces dernières années avec le développement des sondes moléculaires et des appareils d'imagerie bimodale de ce type.

En IRM, deux éléments sont très utilisés pour leurs propriétés paramagnétiques: manganèse et gadolinium. Sous forme libre, ils sont toxiques pour l'organisme et doivent être complexés avec des molécules. L'accès à une imagerie bimodale (TEP ou TEMP / IRM) pour ces deux éléments permettrait une détection très sensible sans injecter de fortes concentrations d'agents de contraste. La production de radionucléides associés au Gd et au Mn est requise pour ces imageries bimodales (TEP ou TEMP/IRM).

Dans ce contexte, cette thèse vise à la production de deux radionucléides « exotiques » ^{52}Mn et ^{165}Er à partir d'un cyclotron pour des applications d'imagerie (bimodalité) et thérapie.

Tout d'abord, le ^{52}Mn a été choisi parmi les isotopes du Mn pour ses émissions de positons rendant possible une bimodalité TEP/RM. Le ^{52}Mn a été produit de deux façons :

1) classique: irradiation d'une cible de Cr par un faisceau de protons à 14 MeV (préparation d'une cible rigide en Cr, séparation Cr/Mn et radiomarquage de DOTA, CDTA et dérivés de bispidines pour des études de stabilité),

2) innovante : irradiation d'une cible de vanadium par un faisceau d'alpha à 45 MeV (détermination de la section efficace de la réaction nucléaire $^{nat}V(\alpha,x)^{52}Mn$, séparation V/^{52}Mn par différentes résines et comparaison des deux protocoles de production). Mais le ^{52}Mn a une dosimétrie qui limite son utilisation aux études précliniques.

Concernant le Gd, étant donné que les lanthanides ont des chimies très similaires et selon nos critères de sélection, l'^{165}Er a été choisi comme radiolanthanide pour substituer le Gd pour l'imagerie nucléaire. L'^{165}Er a d'abord été produit par irradiation d'une cible de Ho par un faisceau de protons (16 MeV) puis purifié sur une résine d'extraction de type LN2®. Ensuite une sonde TEMP/IRM sensible aux concentrations de Zn a été validée in vitro. Cependant pour

valider le concept de bimodalité TEMP/IRM in vivo, une forte activité molaire apparente (AMA) est nécessaire comme pour des applications en thérapie Auger. Afin d'obtenir de hautes valeurs d'AMA, trois paramètres primordiaux en production de radionucléides influent l'AMA: 1) cible, 2) ciblerie, 3) séparation radiochimique. L'influence des dimensions de la cible ainsi que la qualité des feuilles de Ho ont été évaluées ensuite selon le cyclotron disponible (Orléans (F) ou Madison (USA)), différentes conditions d'irradiation en proton ou deutéron ont été étudiées. Enfin un protocole de séparation radiochimique a été optimisé en jouant sur la nature de la résine, ses dimensions et les éluants. De hautes AMA pour l'^{165}Er produit ont été obtenues permettant ainsi : 1) le premier radiomarquage de la PSMA-617 (Prostate-Specific Membrane Antigen) avec l'^{165}Er pour de futures études dosimétriques sur les électrons Auger, 2) validation in vivo du concept de bimodalité TEMP/IRM.

Chapitre 1: Avant propos

Des millions d'examens à travers le monde sont réalisés chaque année dont 40 % utilisent un agent de contraste. Après avoir rappelé le principe de l'IRM basé sur la relaxation longitudinale et transversale des spins, il est rappelé que le Gd est l'élément le plus utilisé pour les agents de contrastes. Néanmoins, son accumulation dans le cerveau ou les os sous forme libre lui confèrent des risques de toxicité. L'utilisation de complexes de Mn, un autre élément paramagnétique, semble une alternative plus sereine comme agent de contraste sur ce point.

Contrairement au Gd, le Mn est naturellement présent dans notre corps. Il est impliqué dans des phénomènes biologiques (assimilation des lipides, antioxydant, croissance des os, présence dans les plantes, bactéries et animaux). Cependant son excès dans le corps peut provoquer des complications comme le manganisme (« maladie des soudeurs »). Sous forme $MnCl_2$, il est utilisé en IRM pour faire des mesures in vivo de l'activité cérébrale et le traçage des voies neuronales (technique MEMRI (Manganese-Enhanced Magnetic-Resonance Imaging)) entre autres. Bien que prometteuse, cette technique pâtît du manque de sensibilité de l'IRM qui se limite à des injections millimolaires d'agents de contraste. Dans ce contexte, le principe des techniques nucléaires que sont la TEP ou la TEMP sont rappelées. Selon les caractéristiques du radionucléide, à savoir émission de positons ou émission monophonique, l'une ou l'autre de ces techniques d'imagerie pourra être utilisée en association avec une IRM afin de maintenir la résolution spatiale de l'IRM tout en diminuant les quantités injectées du fait de la forte sensibilité des imageries nucléaires.

Le Mn possède 5 radiosotopes dont les demi-vies sont supérieures à 2 min. Parmi eux, le ^{52}Mn (T ½= 5.5 jours) est le meilleur candidat en tant qu'émetteur de positon et une résolution (244.6 keV, 0.63 mm) équivalente à celle obtenue avec le ^{18}F (250 keV, 0.62 mm). Cependant sa dosimétrie très forte limite son usage à des expérimentations animales. Malgré cela, il possède des atouts pour son utilisation en PET : une demi-vie similaire au ^{89}Zr ($T_{1/2}$ = 3.3 jours) et plus longue que le ^{64}Cu ($T_{1/2}$ = 12.7 heures) compatible avec le suivi de métabolismes longs comme ceux des anti-corps. La haute sensibilité de l'imagerie TEP permet d'établir des biodistributions de molécules radiomarquées au ^{52}Mn à de très faibles concentrations (nM) bien loin des doses toxiques. Cela représente un atout majeur dans son exploitation en imagerie bimodale IRM/TEP.

La paire ^{52}Mn/^{55}Mn est donc un atout pour des applications de bimodalité TEP/IRM mais comment produire le ^{52}Mn ?

Chapitre 2: Production de ^{52}Mn par irradiation de protons

Le ^{52}Mn est produit le plus couramment par irradiation d'une cible de Cr avec un faisceau de 14 MeV proton selon la réaction nucléaire ^{52}Cr (p,n)^{52}Mn. En raison de sa friabilité, la préparation d'une cible de Cr est nécessaire. Une méthode de préparation a donc été développée conduisant à des pastilles de Cr de 13 mm de diamètre et de 300 – 400 µm d'épaisseur, obtenues après compression de 650 mg de Cr en poudre à 8.3 tonnes durant 30 minutes puis frittage à 800 °C et polissage.

Ensuite la méthode de Stephen Graves de séparation du ^{52}Mn d'une cible de Cr a été appliquée. Tout d'abord, les coefficients de distribution Dw du Cr et Mn au contact d'une résine anionique AG1-X8 en présence d'un mélange aux proportions variables d'éthanol (0; 93-98%)/HCl (1;4;8 et 12 M) ont été confirmés. Ensuite, le ^{52}Mn est séparé sur trois colonnes de résine AG1-X8 successives pour finalement être récupéré dans une solution de HCl 0.1 M d'abord manuellement puis en utilisant un dispositif automatisé ACCRA fait maison.

Enfin, des chélatants de type bispidine (Bisp1-3) sont radiomarqués avec le ^{52}Mn. Les études de stabilité des complexes de manganèse formés confirment ses propriétés sous leur forme radioactive. De plus, le complexe [^{52}Mn]Mn-Bisp3 a été comparé aux complexes [^{52}Mn]Mn-CDTA et [^{52}Mn]Mn-DOTA dans différentes conditions (pH, milieu de dissolution, présence de Cu ou Zn). Le complexe [^{52}Mn]Mn-Bisp3 est plus inerte que les complexes de [^{52}Mn]Mn-CDTA ou [^{52}Mn]Mn-DOTA.

Chapitre 3: Production de ^{52}Mn par irradiation de particules alpha

La production de ^{52}Mn par irradiation d'une cible vanadium V à 45 MeV avec un faisceau de particules alpha constitue une alternative à la voie classique exposée dans le chapitre 2. Cette voie présente deux avantages : la cible de V est commercialement disponible et le vanadium est une cible pratiquement monoisotopique (^{51}V 99.75 % and ^{50}V 0.25 %) contrairement au chrome naturel qui possède 4 isotopes (^{50}Cr 4.345 %, ^{52}Cr 83.790 %, ^{53}Cr 9.501 % and ^{54}Cr 2.365 %), dont le 54 est à l'origine de la production du ^{54}Mn par la voie proton.

Tout d'abord la section efficace de la réaction nucléaire ^{nat}V(α,3n)^{52}Mn a été déterminée par la technique des empilements de feuilles en sandwich sur deux cibleries utilisées au cyclotron d'Orléans : faisceau incident à 60° (CiSCoTe) et 90° (embout à trappe) par rapport à la cible. Les feuilles ont été irradiées durant 2 minutes à I = 200 – 500 nA. Les sections efficaces du ^{52}Mn obtenues sont en accord avec les résultats de la littérature pour la gamme d'énergie du faisceau alpha 30 – 45 MeV. Pas d'activité de ^{54}Mn détectée pour des énergies de faisceau > 30 MeV. Les dimensions de la cible (masse, épaisseur, pureté), l'activité produite et la présence d'impuretés métalliques influencent la valeur d'activité molaire apparente (AMA) finale du ^{52}Mn produit. Afin d'augmenter l'efficacité de refroidissement de la cible, les feuilles de vanadium sont soudées sur un support en Ta selon la technique de soudage par spot. Des conditions de production reproductibles ont été obtenues : cible de V soudée de diamètre = 9.5 mm pour une épaisseur de 126 µm et une masse de ≈ 54 mg pour un rendement physique de 3.6 ± 0.7 MBq·µA^{-1}·h^{-1} (n = 14). Ensuite l'extraction du ^{52}Mn est réalisé en deux étapes :

1) séparation radiochimique du ^{52}Mn de la cible de V par résine échangeuse de cations (Dowex 50W-X8),

2) élimination des éléments métalliques (Fe, Cu, Cr, Zn, Ni, Co) par échanges cationiques (résine AG1-X8) ou extraction (résine AC).

93 ± 6% de ^{52}Mn sont récupérés dans 19 ± 7 ml (n = 5) de HNO_3 7M pour un facteur de séparation $SF_{(V/Mn)}$ = 423 ± 47 (n = 15)) lors de l'étape 1). Pour l'élimination des métaux, les deux méthodes testées donnent des résultats comparables avec plus de 90 % de ^{52}Mn récupérés. Cependant la séparation par résine d'extraction (résine AC) conduit à des solutions de ^{52}Mn moins riches en métaux comparativement à la résine échangeuse d'anion (AG1-X8) sans doute dû à un protocole de séparation utilisant des solutions d'acide dilué et d'eau. Les AMA obtenues après ces deux étapes de séparation sont faibles : 20.9 ± 4.5 MBq/µmole pour une activité de ^{52}Mn de 30.2 ± 11.1 MBq (n = 7) et AMA = 3.1 ± 1.5 MBq/µmole pour 3.8 ± 1.1 MBq (n = 8) produits. Ces valeurs sont similaires à celles obtenues lors de la production de ^{52}Mn par voie proton. L'efficacité de séparation n'est pas en cause dans les faibles valeurs de AMA. Les activités faibles en ^{52}Mn sont dûes aux faibles activités en ^{52}Mn produites pour des raisons de radioprotection.

En termes de rendement, les voies par irradiation alpha ou proton sont équivalentes : 3.6 ± 0.7 MBq·µA^{-1}·h^{-1} (n = 14) pour une cible de V de 53.9 ± 2.8 mg irradiée en alpha alors qu'en proton 4.5 ± 1.7 MBq·µA^{-1}·h^{-1} (n = 6) pour une cible de Cr de 266 ± 18 mg. L'impureté ^{54}Mn est présente à 0.09 ± 0.02 % (n = 13) pour une irradiation alpha alors que cette valeur est de 0.39 ± 0.15 % (n = 3) pour une irradiation proton.

Pour la première fois le ^{52}Mn a été produit à la fois par la voie classique (proton) et une voie nouvelle (alpha). De plus, cette seconde voie a été explorée à la fois sur les aspects d'irradiation (section efficace) mais également sur le plan de la séparation radiochimique. Le

protocole de séparation radiochimique intégrant des résines d'échanges de cations (Dowex 50W-X8), d'anions (AG1-X8) et/ou d'extraction (résine AC) le rend facilement automatisable après quelques ajustements opératoires. Malgré tout ce ^{52}Mn produit présente des traces de ^{54}Mn et surtout possède une forte dosimétrie limitant son utilisation aux études précliniques. Pour une application bimodale avec IRM, il reste le choix du gadolinium mais quel radiogadolinium utiliser ?

Chapitre 4 : Production de ^{165}Er pour une bimodalité IRM/TEMP « in vitro »

Le Gd est un lanthanide très largement utilisé comme agent de contraste en Imagerie par Résonance Magnétique (IRM). Il serait intéressant de disposer d'un isotope radioactif dans la perspective d'imagerie bimodale. Le Gd possède 9 radionucléides avec des temps de demi-vie supérieures à 1 heure mais aucun ne présente une méthode de production par irradiation simple à partir d'une cible naturelle. Cependant les lanthanides dont le Gd fait partie possèdent une chimie très similaire tout au long de la série. Considérant les critères de demi-vie et les rendements de production ou émission (TEP ou TEMP), l'^{165}Er a été retenu comme traceur du Gd en imagerie nucléaire. Il a une demi-vie de 10,36 h., émet uniquement des rayons X (47 – 55 keV), mais avec une énergie suffisante pour une détection par l'imagerie TEMP.

Pour le produire, une cible de Ho naturel est irradiée au cyclotron d'Orléans par un faisceau de protons de 16 MeV(^{165}Ho(*p,n*)^{165}Er ou de deutons de 17.5 MeV (^{165}Ho(d,2n)^{165}Er). Ensuite, les coefficients de distribution Dw pour Ho et Er sur une résine d'extraction LN2 (20 – 50 µm) sont déterminés en présence d'acide nitrique à différentes concentrations puis une colonne avec cette résine est réalisée: l'Ho est élué avec l'acide nitrique 0.4 M puis 50 – 70 % de l'^{165}Er sont récupérés avec de l'acide nitrique 1M.

Cet ^{165}Er est ensuite utilisé pour des expériences de bimodalité IRM/TEMP. Des collaborateurs ont développés des sondes moléculaires en IRM dont le signal de relaxation est corrélé à la concentration en Zn dans le milieu (le Zn est un indicateur de cancer, diabète ou maladie dégénérative). Une étude in vitro « preuve de concept » a été réalisée : un cocktail de ^{55}GdL1/^{165}ErL1 est préparé selon un ratio molaire connu ($1/2.4 \times 10^{-7}$: entre le complexe formé par le ligand L1 avec ^{155}Gd (Gd naturel) et le complexe [^{165}Er]Er-L1 auquel on rajoute des concentrations inconnues de Zn. Le signal d'^{165}Er est mesuré dans l'échantillon avec une gamma caméra. Ensuite, connaissant le ratio [^{155}Gd]Gd-L1/[^{165}Er]Er-L1, la concentration de Gd est déterminée. Après décroissance, les échantillons sont mesurés en IRM associant une concentration de Gd à un signal de relaxation lié à la concentration de Zn à l'aide d'une courbe d'étalonnage. Les concentrations en Zn ainsi déterminées sont comparables à celles mesurées par ICP-OES. Le concept de mesure bimodale IRM/TEMP est validé « in vitro » avec le couple ^{55}Gd/^{165}Er.

Chapitre 5 : Haute activité molaire apparente pour l'^{165}Er

Pour une application bimodale IRM/TEMP « in vivo », une haute AMA est nécessaire. Pour cela plusieurs paramètres seront étudiés: cible, conditions d'irradiation et paramètres de séparation radiochimique. Ce besoin de haute AMA est encore plus crucial pour l'^{165}Er en tant que pur émetteur d'électrons Auger pour des études dosimétriques en thérapie Auger.

Pour une AMA élevée, la ciblerie (rendement, section efficace, refroidissement), la cible (qualité des feuilles de Ho, masse de Ho (épaisseur et diamètre)) et la séparation radiochimique (facteur de séparation Ho/Er, temps, impuretés métalliques) sont des facteurs déterminants.

Malgré un dispositif d'irradiation CiSCOTe adapté pour de fortes intensités de courant et un accès à des deutons de 17.5MeV (multipliant par 7 le rendement de production de l'^{165}Er par rapport à un faisceau de protons*)*, les irradiations d'une cible d'Ho ne sont pas répétables, certaines fondent. Des expériences ont donc été réalisées à Madison (USA) pour produire du ^{165}Er sur des cyclotrons médicaux avec des faisceaux de protons (11 - 12.5MeV). L'utilisation de particules proton est compensée par l'utilisation de courant de forte intensité 35 – 40 µA avec une cible d'Ho conçue par la méthode de « spot welding ». Des comparaisons de production d'^{165}Er sur 2 modèles de cyclotrons médicaux ont été réalisées pour une cible de diamètre 7.9 mm : le rendement avec le cyclotron RDS-112 (CTI Cyclotron Systems) est le double de celui du PET-Trace (GE) : 28.0 ± 1.8 MBq·µA^{-1}·h^{-1} (n = 5) contre 14.1 ± 1.4 MBq·µA^{-1}·h^{-1} (n = 3). Cependant le RDS-112 est limité en courant sur cible à 20 µA, en diamètre de cible (< 8 mm) et ne possède pas de système de recupération de cible automatisée. Néanmoins, des rendements similaires (24.1 ± 0.5 MBq·µA^{-1}·h^{-1} (n = 5)) sur le PET-Trace (GE) sont obtenus en augmentant le diamètre de la cible avec des courants de 40 µA. A Orléans, une répétabilité des irradiations (rendement de 75.1 ± 10.1 MBq·µA^{-1}·h^{-1} (n = 12)) a été obtenue en irradiant (6.0 ± 0.4 h à 6.0 ± 0.3 µA une cible de Ho "soudée par spot", masse = 90.4 ± 2.3 mg) à 13 MeV.

Le second point pour accroître les valeurs de AMA est liée aux caractéristiques physiques (masse (épaisseur et diamètre)) et chimiques (présence de Er naturel) de la cible d'Ho. Enfin, la séparation radiochimique Ho/^{165}Er constitue un point essentiel pour une haute AMA : un facteur de séparation de 10^5 entre Ho et Er est nécessaire. Elle est réalisée en trois étapes : 1) extraction d'un maximum de Ho, 2) séparation sélective afin d'accroître le facteur de separation ($FS_{(Ho/Er)}$), 3) élimination des traces métalliques de la solution. Pour la première étape, deux protocoles ont été utilisés selon le lieu de production de l'^{165}Er et son utilisation finale : résine échangeuse de cations Dowex 50W-X8 sous haute pression (Madison, thérapie Auger) ou résine d'extraction LN2® (20 - 50µm) (Orléans, bimodalité IRM/TEMP in vivo). Les rendements d'extraction sont > 80%. Des valeurs > 90% sont obtenues mais avec une baisse des $FS_{(Ho/Er)}$. Les étapes suivantes sont communes aux deux utilisations. Ensuite la solution de ^{165}Er est passée sur une colonne de 500 mg de résines d'extraction LN2® (20 – 50 µm), l'^{165}Er est récupéré dans 4 – 6 mL de HNO_3 1M. Un $FS_{(Ho/Er)} > 10^5$ est obtenu sur l'ensemble des 2 étapes. Enfin le passage sur 100 mg d'une résine d'extraction AC ® réduit les traces métalliques dans la solution finale de ^{165}Er. Les AMA minimales obtenues par titration DOTA (> 11 ± 4 MBq/nmol) ou DTPA (> 10 ± 4 MBq/nmol) sont suffisantes pour les applications de l'^{165}Er envisagées. Dans ces conditions, le [^{165}Er]Er-PSMA-617 a été synthétisé ouvrant des perspectives d'études comparatives avec le [^{177}Lu]Lu-PSMA-617 ou le [^{161}Tb]Tb-PSMA-617 sur les effets dosimétriques en thérapie Auger selon la source radiative.

En parallèle, la molécule [^{165}Er]Er-P6 a une AMA (19 ± 7 MBq/nmole (n = 6)) supérieure à [^{165}Er]Er-DOTA (3 ± 2 MBq/nmole (n = 9)). Ce résultat est prometteur pour des applications bimodales IRM/TEMP in vivo.

Perspectives et Conclusion générale

➢ Perspectives

Dans les perspectives d'une suite des travaux exposées dans cette thèse, la production de ^{52}Mn est soumise à deux contraintes : l'optimisation des protocoles de séparation V/Mn et l'utilisation de ^{52}Mn provenant d'un autre cyclotron, suite à la fermeture du cyclotron d'Orléans. ARRONAX (Nantes) est le seul cyclotron capable de produire le ^{52}Mn à partir de faisceaux alpha suffisamment énergétiques en France. Concernant les travaux sur l'^{165}Er à Orléans, leur poursuite est dépendante d'un accès viable à une source de ^{165}Er. En effet, l'^{165}Er provenant d'irradiation en proton ou deuton est une solution peu viable sur le plan logistique. L'accès à un générateur ^{165}Tm/^{165}Er serait une solution plus réaliste. Elle se base sur le principe de décroissance du ^{165}Tm ($T_{½}$ = 30.0 h) qui décroît en ^{165}Er ($T_{½}$ = 10.36 h).

Nous travaillons actuellement sur deux voies d'accès au ^{165}Tm : l'une par voie de spallation et la seconde par irradiation d'une cible de Ho par un faisceau de alphas à 45 MeV. L'idée de générateur suppose de fixer la source de ^{165}Tm sur une résine adaptée afin que seul l'^{165}Er soit élué alors que le ^{165}Tm reste sur la résine. Pour développer ces résines, des supports carbonés poreux seront fonctionnalisés. Des premiers essais ont été réalisés sans succès pour le moment.

Par ailleurs, l'utilisation de ces matériaux résultent d'essais encourageants sur la séparation de l'^{165}Er d'une cible de Ho selon le protocole établi pour l'étape 2 de séparation Ho/Er faite avec une résine d'extraction LN2®. Les supports polydivynilbenzène ont été remplacés par trois matériaux carbonés poreux de différente nature (granulométrie, polymère, porosité). Ils ont été fonctionnalisés avec les extractants acide phosphorique (bis(2-ethylhexyl) HDEHP et acide monophosphonique (2-ethyl-1-hexyl) mono 2-ethyl-1-hexyl ester (HEH[EHP]) respectivement contenus dans les résines LN1® et LN2®. Après les déterminations de $D_{W,}$ un seul support carboné (nommé) CV a été retenu pour les tests dans les conditions de production de l'^{165}Er. La séparation des deux lanthanides est bien obtenue mais les $FS_{(Ho/Er)}$ sont très inférieurs à ceux obtenus avec la résine d'extraction LN2® dans les mêmes conditions d'élution. Ces premiers résultats sont néanmoins encourageants car ils ont montré que pour un même extractant fonctionnalisé sur des supports différents, la séparation s'en trouve affectée : stabilité chimique, efficacité de séparation ou influence de la porosité.

La recherche de solutions de purification de radiolanthanides pour des applications médicales est actuellement un domaine en pleine croissance. L'utilisation de matériaux poreux peut contribuer à ces besoins par leur emploi à la fois sous forme de résine mais également dans la miniaturisation des dispositifs de séparation.

➢ Conclusion

Le ^{52}Mn et l'^{165}Er ont été produits et utilisés dans des radiomarquages de molécules pour la première fois en France. Le ^{52}Mn a été obtenu à Orléans par irradiation proton à 14 MeV d'une cible de Cr ou par alpha à 45 MeV d'une cible de V. Pour l'^{165}Er, sa production à Orléans provient d'irradiation à 16 MeV en proton ou 13 MeV / 17.5 MeV en deuton et pour celle à Madison, 11 ou 12.5 MeV en proton.

Pour la production de ^{52}Mn, dans un premier temps, des pastilles de Cr ont été préparées par compression, frittage et polissage : 13 mm de diamètre et 300 – 400 µm d'épaisseur ont été obtenues à partir de 650 mg de poudre de Cr pressés à 8.3 tonnes durant 30 minutes puis frittage

à 800°C avant un polissage pour réduire l'épaisseur des cibles et éliminer la surface oxydée des cibles. Après irradiation de ces cibles, du ^{52}Mn en solution est isolé par séparation chimique sur résine échangeuse d'anions AG1-X8 avec des rendements de 43 – 60 %. Différentes molécules dérivées de bispidines (Bisp1, Bisp2 et Bisp3) ont été radiomarquées au ^{52}Mn. Les études réalisées sur [^{52}Mn]Mn-Bisp1, [^{52}Mn]Mn-Bisp2 et [^{52}Mn]Mn-Bisp3 confirment la stabilité de ces complexes avec du radiomanganèse. [^{52}Mn]MnBisp3 possède une très grande stabilité en milieu acide fort ainsi que dans différents milieux de dissolution en comparaison avec le [^{52}Mn]Mn-DOTA ou le [^{52}Mn]Mn-CDTA. Néanmoins cette voie de production requière 2 jours de préparation à partir d'une cible de Cr et produit un ^{52}Mn contenant l'impureté ^{54}Mn ($T_{½}$ = 312 jours) pénalisante en termes de réglementation (< 0.4%). Afin de supprimer le ^{54}Mn, l'irradiation alpha a été étudiée d'abord en établissant la section efficace de la réaction nucléaire ^{51}V(α,x)^{52}Mn sur deux cibleries (angle à 90° et 60° par rapport au faisceau incident) puis en réalisant la séparation V/Mn en deux étapes : extraction du ^{52}Mn de la cible V par résines échangeuses de cations Dowex 50W-X8 puis élimination des traces métalliques soit par résine anionique AG1-X8 soit par résine d'extraction AC. 93 ± 6 % (n = 5) du ^{52}Mn sont récupérés dans HNO_3 7M lors de la première étape avec un $FS_{(Ho/Er)}$ de 423 ± 47 (n = 16). Une séparation complémentaire avec cette résine Dowex 50W-X8 s'avère décevante (FS = 2). Des améliorations doivent y être apportées. Pour les traces de métaux, les résultats des deux méthodes utilisées sont équivalents. De faibles AMA sont obtenues aussi bien par la voie proton qu'alpha provenant des faibles activités de ^{52}Mn mises en œuvre pour ces essais. Pour la manipulation de plus fortes activités, une automatisation de la méthode est nécessaire sur le plan radioprotection, facilitée par la répétabilité des protocoles aussi bien en proton qu'en alpha. Enfin, les rendements de production en alpha à 45 MeV (3.6 ± 0.7 $MBq \cdot \mu A^{-1} \cdot h^{-1}$ (n = 14) (37 to 97 mg)) sont équivalents à ceux de protons en 14 MeV (4.5 ± 1.7 $MBq \cdot \mu A^{-1} \cdot h^{-1}$ (n = 6) (266 ± 18 mg)). Pour le ^{54}Mn, 0.09 ± 0.02 % (n = 13) sont produits en alpha alors que cette quantité monte à 0.39 ± 0.15 % (n = 3) en mode proton. Ce travail sur la production de ^{52}Mn ouvre son développement en France pour des études bimodales IRM/TEP malgré sa dosimétrie qui est un handicap pour son utilisation en clinique.

Dans la seconde partie de cette thèse, l'^{165}Er a été produit pour des applications bimodales IRM/TEMP (in vitro puis in vivo) et dosimétriques en thérapie Auger. Tout d'abord, l'^{165}Er est produit par irradiation de protons à 16 MeV et la séparation Ho/^{165}Er est réalisée sur résine d'extraction LN2® (Triskem, 20 – 50 µm). Ensuite un cocktail de GdL/^{165}ErL est utilisé pour valider le concept de bimodalité IRM/TEMP in vitro avec l'^{165}Er sur des agents de contraste sensibles à la concentration de Zn dans le milieu. Pour des applications in vivo ou en thérapie Auger de l'^{165}Er, le $FS_{(Ho/Er)}$ = 1000 obtenu précédemment est insuffisant. La recherche d'une forte AMA (donc fort $FS_{(Ho/Er)}$) a donc été étudiée à Orléans (bimodalité IRM/TEMP, in vivo) et (Madison, thérapie Auger) sous trois angles : ciblerie, cible de holmium et séparation chimique. Un protocole en trois étapes a été établi incluant une séparation sélective sur résine d'extraction LN2® en étape 2 et une réduction des traces métalliques dans l'étape 3 avec une résine d'extraction bDGA® (Triskem, 50 – 100 µm). Pour l'étape 1, deux méthodes de séparation ont été utilisées : résine échangeuse de cations Dowex 50W-X8 sous haute pression en utilisant une solution d'acide α-isobutyrique à 70 mM (pH = 4.7) comme éluant à Madison et résine d'extraction LN2® avec désorption de l'^{165}Er avec une solution de 1 M HNO_3 à Orléans sous basse pression (azote à 1 bar).

64 ± 2% d'^{165}Er sont isolés avec un $FS_{Ho/Er}$ = (2.8 ± 1.1) · 10^5 dans le cas d'une irradiation à 12.5 Mev proton sur un cyclotron médical (Madison). Pour une irradiation en deuton à 13 MeV, 59.0 ± 9.7 % d'^{165}Er sont récupèrés dans 1 mL de HCl 0.01 M avec un $FS_{(Ho/Er)}$ = (2.4 ± 0.9). 10^5 (n = 4). Ces $FS_{(Ho/Er)}$ très élevées donnent accès à de hautes AMA (DOTA, DTPA ou P6). Pour des études de dosimétrie des électrons Auger, [^{165}Er]Er-PSMA-617 a été synthétisé.

L’AMA de 19 ± 7 MBq/µnmole (n = 6) obtenue avec la molécule P6 dérivée bispidine est supérieure à celle du DOTA (3 ± 2 MBq/µnmole (n = 9)) envisageant ainsi l’emploi de cet ^{165}Er dans la validation du concept de bimodalité IRM/TEMP in vivo.

Isidro Da Silva Colaço
Production de ^{52}Mn et ^{165}Er pour des applications en imagerie (bimodalité) et thérapie

L'utilisation de radiométaux s'est considérablement accrue notamment en imagerie bimodale. Dans notre cas, deux techniques d'imagerie sont associées : l'imagerie par résonance magnétique (IRM) apportant une meilleure résolution et la TEP (tomographie par émission de position) ou TEMP (tomographie par émission monophotonique), selon le radionucléide utilisé, accroissant la sensibilité de détection (pM-nM). L'utilisation de différents isotopes d'un élément paramagnétique est une méthode de choix de ces applications. Ainsi l'isotope 55 du manganèse est utilisé en IRM alors que l'isotope 52 (émetteur β^+) est parfait en TEP. Le ^{52}Mn a donc été produit au cyclotron d'Orléans durant cette thèse selon deux voies d'irradiation : 1) classique : pastilles de Cr et faisceau 14 MeV proton (réaction nucléaire ^{52}Cr (p,n)^{52}Mn), 2) nouvelle : cibles de V et faisceau d'alpha à 45 MeV (^{nat}V(α,3n)^{52}Mn). Ensuite le ^{52}Mn a été extrait des cibles et purifié en utilisant diverses résines (anioniques, cationiques ou d'extraction). Les deux voies de production du ^{52}Mn ont été comparées (Activité molaire apparente (AMA), impureté ^{54}Mn, facteur de séparation Mn/V ($FS_{(Mn/V)}$). Enfin des dérivés bispidines (Bisp1-3) ont été radiomarqués avec le ^{52}Mn. Cependant, le ^{52}Mn présente deux inconvénients majeurs : 1) forte dosimétrie 2) présence de ^{54}Mn (même avec la voie alpha). Le Gd est le cation métallique le plus utilisé en IRM, il fait partie de la famille des lanthanides. Ces éléments possèdent une chimie très similaire entre eux. De ce fait, l'^{165}Er (T½= 10,36h) lanthanide radioactif détectable par imagerie TEMP, a été associé au ^{155}Gd (IRM) pour une approche bimodale. L'^{165}Er a donc été produit dans une optique de forte AMA. Trois critères ont donc été étudiés : ciblerie, cible et séparation radiochimique. Pour cela des cibles de holmium ont été irradiées soit avec des faisceaux de protons (entre 11 et 16 MeV), soit par des faisceaux de deutons (13 ou 17.5 MeV). Ensuite l'^{165}Er a été extrait en 3 étapes par séparation radiochimique utilisant des résines cationiques ou d'extraction. Au final, les AMA obtenues (> 10 MBq/nmoles) sont adaptées pour de l'imagerie bimodale IRM/TEMP ou des études dosimétriques des électrons Auger en thérapie.

Mots clés : ^{52}Mn, ^{165}Er, lanthanides, cyclotron, séparation, résine

^{52}Mn and ^{165}Er production for bimodal imaging and therapy applications

The use of radiometals has grown considerably in recent years, in bimodal imaging. This associates two imaging techniques: Magnetic Resonance Imaging (MRI), for high image resolution, and PET (Position Emission Tomography) or SPECT (Single Photon Emission Computerized Tomography), depending on the radionuclide used detection sensitivity (pM-nM).

The use of different isotopes of a paramagnetic element is a good solution for these applications. Thus, the stable 55 isotope of manganese is used in MRI, while its β^+ emitter isotope 52 ($T_{½}$ = 5.5 d.) is perfectly suited for PET applications. ^{52}Mn was therefore produced at Orleans'cyclotron during this thesis, using two irradiation methods: 1) conventional: Cr pellets irradiated with a 14MeV proton beam (nuclear reaction ^{52}Cr (p,n)^{52}Mn), 2) new: V targets with an alpha beam at 45 MeV (^{nat}V(α,3n)^{52}Mn). Then ^{52}Mn was extracted from targets and purified using various resins (anionic, cationic, or extraction resins). The two ^{52}Mn production were compared (apparent molar activity (AMA), impurity ^{54}Mn, Mn/V separation factor ($SF_{(Mn/V)}$). Finally, bispidine derivatives (Bisp1-3) were radiolabeled with ^{52}Mn. However, ^{52}Mn has two major drawbacks 1) high dosimetry 2) presence of ^{54}Mn (even with alpha way).

Gd is the most widely used metal cation in MRI, belonging to the lanthanide family. The chemistry of these elements is very similar. As a result, ^{165}Er ($T_{½}$ = 10.36 h), a radioactive lanthanide detectable by SPECT imaging, was combined with ^{155}Gd (MRI) for a bimodal approach. The production of ^{165}Er was carried out to achieve a high AMA. Three criteria were studied: targeting, target, and radiochemical separation. Holmium targets were irradiated with either proton beams (between 11 and 16 MeV) or deuteron beams (13 or 17.5 MeV). Then ^{165}Er is extracted in 3 steps by radiochemical separation using cationic or extraction resins. Finally, the AMAs obtained (> 10 MBq/nmoles) are suitable for bimodal MRI/TEMP imaging or dosimetric studies of Auger electrons therapy.

Keywords: ^{52}Mn, ^{165}Er, lanthanides, cyclotron, separation, resin

CEMHTI Conditions Extrêmes et Matériaux :
Haute Température et Irradiation
UPR3079 CNRS Site Cyclotron
3A rue de la Férollerie
45071 Orléans Cedex 2 France